Perovskites as New Support Materials for the Iron Based Fischer-Tropsch Synthesis

Motlokoa Khasu

UNIVERSITY OF CAPE TOWN
IYUNIVESITHI YASEKAPA • UNIVERSITEIT VAN KAAPSTAD

c*change
DST-NRF Centre of Excellence in Catalysis

DSI-NRF Centre of Excellence in Catalysis c*change and Catalysis Institute, Department of Chemical Engineering

Submitted to the University of Cape Town in fulfilment of the requirements for the degree of

Doctor of Philosophy

2022

Acknowledgements

I would like to give my sincerest gratitude to all those who made this work a success:

- Above all, I would like to thank God for giving me the strength and helping me to grind away.
- A huge thank you goes out to my supervisors Assoc. Prof. Nico Fischer and Prof. Michael Claeys. Thank you for investing so much time into me and this project, for always making time available for valuable discussions, for countless corrections and recommendations to make this thesis a success.
- A big thank you to my colleagues for their support and friendly environment they provided, especially Shaine Raseale and Wijnand Marquart for assisting me with testing instruments and analysis of my data.
- Thank you to Mohamed Jaffer, Miranda Waldron and Nasheeta Hanief from Electron Microscope Unit, University of Cape Town, for making time to analyze my samples and to teach me how to operate TEM. I would also like to thank Sandeeran Govender for AAS/ICP and N_2 physisorption analysis, not forgetting Rachel Cupido, Waldo Koorts and Gideon Kaufmann, thank you for assistance in the laboratory. I would also like to acknowledge Dr. Simon Kondrat and Alex Mayer for their help to access the Core XAFS beamline B18 at Diamond Light source and the analysis of the data. A huge thank you also goes out to Dr. Jaco Olivier team at the Centre for High Resolution Transmission Electron Microscopy, Nelson Mandela University for the EDX-STEM measurements.
- I would also like to thank DST-NRF Centre of Excellence in Catalysis c*change, The Catalysis Institute and NRF - University of Cape Town for their financial support in my academic development.

Declaration

I, Motlokoa Khasu, hereby declare that the work on which this thesis is based is my original work (except where acknowledgements indicate otherwise) and that neither the whole work nor any part of it has been, is being, or is to be submitted for another degree in this or any other university. I authorize the University to reproduce for the purpose of research either the whole or any portion of the contents in any manner whatsoever.

Signature: Date: 11/02/2022

Synopsis

In the Fischer-Tropsch process, valuable products consisting mainly of long chain hydrocarbons and water as by-product are synthesized from the basic starting materials hydrogen and carbon monoxide, derived from sources such as coal, gas or biomass [1]. Iron catalysts and cobalt based systems are the preferred catalysts for the commercial Fischer-Tropsch synthesis (FTS) employed at PetroSA and Sasol in South Africa [2]. The use of iron catalysts is not only influenced by the low price of the active material compared Co and Ru, but also by higher activity and a wide window of FT operating conditions. Though the product selectivity of iron-based FT synthesis can, to a certain extent, be controlled by changing the process temperature, promoters are added to improve selectivity and activity of the catalyst by modifying structural and/or electronic properties of the active phase [3].

Potassium is the most used among alkali promoters in iron-catalyzed FTS because of its Lewis acid nature [4–6]. Alkali promoters simultaneously promote dissociative CO chemisorption and inhibit chemisorption of H_2 by a charge transfer to the surface of the iron based active phase, resulting in a higher C/H ratio on the catalyst surface and faster carburization rates, longer chain products and higher olefin content [5,7,8]. The addition of promoters is beneficial up to a certain amount, above which it becomes detrimental to the overall activity of the catalyst due to coverage of active sites and/or excessive coking [9–11]. Its mobility under reaction conditions is another challenge as it results in a highly dynamic system. The goal of the here proposed study is to investigate the possibility of using a new class of supports (perovskites) that do not only provide high surface area and enhance the dispersion of the active phase but also adopt the role currently played by promoting elements without suffering from the disadvantages reported above (mobility on catalyst, blocking active sites, etc.) [12].

Perovskites are mixed-metal oxides that have attracted much scientific attention due to their low price, adaptability and thermal stability. They generally have the formula ABO_3 or A_2BO_4 (A and B are cations of different sizes, and O is the anion that binds them), exhibiting a range of stoichiometries and crystal structures. Their structural features make it possible to accommodate around 90% of the metallic elements from the periodic table in positions A and/or B, without destroying the matrix structure. ‘A’ can be a rare earth alkali (La, Ce, Pr) or alkaline earth metals (Cs, K, Ca) of a larger diameter than ‘B’ which is normally a transition metal (Co, Fe, Cu, Mn, Cr) [13,14]. This study aims to incorporate selectivity and activity promoters into the perovskite structure, anchor iron particles on the perovskite and investigate the reducibility and activity/selectivity of the obtained model catalyst under Fischer-Tropsch conditions.

The model catalysts are developed by preparing a series of $LaAlO_3$ perovskites with partial substitution of lanthanum with 10 atom-% potassium, and 0, 10, 20, 60, and 100 atom-% substitution of aluminum with manganese. The performance of iron supported on these materials is compared with the one on $LaAlO_3$ support with potassium promotion via impregnation (2, 1 and 0.5 wt.-%). EDS-STEM and XANES results confirm the successful incorporation of potassium and manganese into the matrix of the $LaAlO_3$. *In situ* studies highlight the effect of potassium on the activation of the oxidic iron precursor. The iron supported on the potassium incorporated perovskite exhibits a lower reduction temperature and a faster subsequent formation of Hägg carbide (χ-Fe_2C_5). It is well reported that iron carbide is the active phase for the Fischer-Tropsch synthesis [15–17].

The Fischer-Tropsch activity of the iron supported on the unmodified $LaAlO_3$ perovskite support compares well with common supports such as SiO_2, Al_2O_3, ZrO_2 and TiO_2 in terms of CO conversion and selectivity towards FTS products. The incorporation of low concentrations of manganese into the perovskite support results in a slight decrease in CO conversion but no significant change of the product selectivity was observed. With a further increase in manganese concentration, CO conversion decreases accompanied by an increase in C_1 and C_2–C_4 product selectivity. The same phenomenon is observed with these high manganese containing samples when the perovskite support is further modified with potassium.

Incorporation of potassium into the $LaAlO_3$ and $LaMn_{0.2}Al_{0.8}O_3$ perovskites results in a substantial increase in CO conversion, beyond 70%. At a CO conversion comparable to the promoter free perovskite catalyst, the novel materials show a comparable CH_4 selectivity with lower CO_2 formation, resulting in a lower overall undesired C_1 product fraction suggesting a decoupling of the potassium enhancement of the FTS activity versus the enhancement of the water gas shift reaction. Additionally, these materials also show good stability under FT reaction conditions as no significant change is observed in the perovskite structure post reaction. It can therefore be confirmed that perovskites can double as both the support and electronic promoter via the incorporation of the known promoter elements within their structure, and their electronic effects can surpass those of conventional promoters.

References

[1] D.L. King, J.A. Cusumano, R.L. Garten, A Technological Perspective for Catalytic Processes Based on Synthesis Gas, Catalysis Reviews 23 (1-2) (1981) 233–263.

[2] P. Hilsenrath, The development of synthetic fuels in South Africa, The Journal of Energy and Development 14 (2) (1989) 269–283.

[3] Z. Liu, G. Jia, C. Zhao, Y. Xing, Selective Iron Catalysts for Direct Fischer-Tropsch Synthesis to Light Olefins, Industrial & Engineering Chemistry Research 60 (17) (2021) 6137–6146.

[4] M. Amoyal, R. Vidruk-Nehemya, M. Landau, M. Herskowitz, Effect of potassium on the active phases of Fe catalysts for carbon dioxide conversion to liquid fuels through hydrogenation, Journal of Catalysis 348 (2017) 29–39.

[5] L. Gavrilović, J. Save, E.A. Blekkan, The effect of potassium on cobalt-based Fischer-Tropsch catalysts with different cobalt particle sizes, Catalysts 9 (4) (2019) 351.

[6] W. Ma, E.L. Kugler, D.B. Dadyburjor, Potassium effects on activated-carbon-supported iron catalysts for Fischer− Tropsch synthesis, Energy Fuels 21 (4) (2007) 1832–1842.

[7] J. Chai, R. Pestman, W. Chen, A.I. Dugulan, B. Feng, Z. Men, P. Wang, E.J.M. Hensen, The role of H2 in Fe carburization by CO in Fischer-Tropsch catalysts, Journal of Catalysis 400 (2021) 93–102.

[8] A.P. Raje, R.J. O'Brien, B.H. Davis, Effect of Potassium Promotion on Iron-Based Catalysts for Fischer-Tropsch Synthesis, Journal of Catalysis 180 (1998) 36–43.

[9] D.P. Weber, Promoter Effects on Iron-Based, SBA-15 Supported Ultra-High Temperature Fischer-Tropsch Catalysts. Graduate Theses and Dissertations, 2018.

[10] F. Farias, R. Rabelo Neto, M. Baldanza, M. Schmal, F. Fernandes, Effect of K promoter on the structure and catalytic behavior of supported iron-based catalysts in Fischer-Tropsch synthesis, Brazilian Journal of Chemical Engineering 28 (2011) 495–504.

[11] N. Lohitharn, J.G. Goodwin, Effect of K promotion of Fe and FeMn Fischer-Tropsch synthesis catalysts: Analysis at the site level using SSITKA, Journal of Catalysis 260 (1) (2008) 7–16.

[12] G. Connell, J.A. Dumesic, Migration of potassium on iron and alumina surfaces as studied by Auger electron spectroscopy, Journal of Catalysis 92 (1) (1985) 17–24.

[13] M.A. Vannice, The catalytic synthesis of hydrocarbons from mixtures over the group VIII metals, Journal of Catalysis 37 (1975) 449–461.

[14] E.A. Lombardo, M.A. Ulla, Perovskite oxides in catalysis: Past, present and future, Research on Chemical Intermediates 24 (5) (1998) 581–592.

[15] Z. Tian, C. Wang, J. Yue, X. Zhang, L. Ma, Effect of a potassium promoter on the Fischer-Tropsch synthesis of light olefins over iron carbide catalysts encapsulated in graphene-like carbon, Catalysis Science & Technology 9 (11) (2019) 2728–2741.

[16] K. Opeyemi Otun, Y. Yao, X. Liu, D. Hildebrandt, Synthesis, structure, and performance of carbide phases in Fischer-Tropsch synthesis: A critical review, Fuel 296 (1) (2021) 120689.

[17] J.B. Butt, Carbide phases on iron-based Fischer-Tropsch synthesis catalysts part II: Some reaction studies, Catalysis Letters 7 (1990) 83–106.

Table of Contents

List of Figures

List of Tables

Nomenclature

Acronyms

3WV	three-way valve
AAS	atomic absorption spectroscopy
ASF	Anderson-Schulz-Flory (product distribution)
BET	Brunauer-Emmett-Teller
BPR	back pressure regulator
CSTR	continuously stirred tank reactor
DOR	degree of reduction
EDS	energy-dispersive X-ray spectroscopy
fcc	face-centered cubic
FIC	flow indicator and control
FID	flame ionization detector
FT	Fischer-Tropsch
FTS	Fischer-Tropsch synthesis
GC	gas chromatograph
HAADF	high-angle annular dark-field
GHSV	gas hourly space velocity
IWI	incipient wetness impregnation
MFC	mass flow controller
NTP	normal temperature and pressure (1 atm and 293 K)
NV	needle valve
O/P	olefin to paraffin ratio

PIC	pressure indicator and control
PRV	pressure relief valve
STEM	scanning transmission electron microscopy
STY	average space time yields
TCD	thermal conductivity detector
TEM	transmission electron microscopy
TGA	thermogravimetric analysis
TIC	temperature indicator and control
TPR	temperature-programmed reduction
WGS	water gas shift
XAS	X-ray Absorption Spectroscopy
XANES	X-ray absorption near edge spectroscopy
XRD	X-ray diffraction

Notations

α	chain growth probability
A_i	response area of component *i* in chromatogram
Å	Ångstrøm
C_{5+}	selectivity of hydrocarbons with a chain length $n \leq 5$ C_2–
C_4	Selectivity of hydrocarbons with a chain length $3 \leq n \leq 4$
f	response factor
KI	Kovats index
n_i	molar flow rate of component *i*
SV	space velocity (STP, per gram of catalyst)

W_n	mass fraction of a product consisting of carbon number n

Chemical formulas

Al_2O_3	aluminum oxide (alumina)
Ar	argon
C	carbon
CH_2	alkenyl group
CH_3	alkyl group
CH_4	methane
Co	cobalt
CO	carbon monoxide or carbonyl
CO_2	carbon dioxide
Co_3O_4	cobalt oxide
Fe	iron
Fe_2O_3	iron (III) oxide
Fe_3O_4	iron (II, III) oxide
χ-Fe_2C_5	Hägg carbide
γ-Fe_2O_3	maghemite
K_2CO_3	potassium carbonate

1 Introduction

Liquid transportation fuels and other hydrocarbon products of various molecular weights can be produced via a condensation polymerization reaction of CO. The process is a well-established catalytic reaction termed Fischer-Tropsch (FT) synthesis. The catalysts for the FT synthesis are metals such as iron, cobalt, nickel and ruthenium, because of their ability to form the carbon-carbon bond and support chain growth. However, only iron and cobalt based catalyst systems are commercially used. The use of iron catalysts is influenced by the low price when compared to Co, Ni and Ru, and by its high FT reaction as well as water-gas-shift activity. It is therefore more suitable for a hydrogen lean syngas such as when derived from coal gasification [1].

Though the product selectivity of iron-based FT can, to a certain extent, be controlled by changing the process temperature, space velocity and partial pressures, promoters can be added to increase olefin and long- chain hydrocarbon selectivity as well as FT and water gas shift activity by modifying structural and/or electronic properties of the active phase [2]. Promoter elements include the acids of the IA group metals like potassium and transition metals such as manganese, calcium, zinc, copper and magnesium. Compared with other promoters, potassium and manganese show complex structural and electronic effects [3]. Other promoters like copper as well as high surface area binders/supports such as silica and/or alumina are added mainly to facilitate iron reduction, stabilize a high metal surface area, and improve the mechanical properties. They also modify the selectivity, but their effects are usually small in comparison with that of potassium [4].

Alkali metal ions are the most used because of their acid nature, they regulate the acid/base sites on a catalytic surface and simultaneously promote the dissociative CO chemisorption and inhibit chemisorption of H_2, altering the surface concentration of desired adsorbates, leading to longer chain products and higher olefin content [5–8]. The addition of promoters is beneficial up to a certain amount (e.g. for potassium approximately 3 wt.-%) [9–11], above which it becomes detrimental to the overall activity of the catalyst due to coverage of active sites and/or excessive coking. Promoter mobility under reaction conditions is another challenge as it results in a highly dynamic system, making it difficult to know the amount and location of the promoter during FT [12,13]. For optimum catalyst performance it is important to achieve maximum promoter utilization. In the present work the possibility of using a new class of supports, lanthanum-based perovskites, which do not only provide surface area and enhance the dispersion of the catalyst but also adopt the role currently played by promoting elements without suffering from the disadvantages reported above (mobility on catalyst, blocking active sites, etc.) was studied.

Perovskites are compounds chemically represented by a formula ABO_3 or A_2BO_4 (A and B are cations of different sizes, and O is the anion), and therefore form a large variety of materials. The cation A usually has a bigger radius (1.0–1.9 Å) while the B cation has a smaller radius (0.5–1.2 Å). In the ideal perovskite structure, the 12-coordinated A cation may be rare-earth, alkaline-earth, alkali or other large ions and the 6-coordinated B cations are usually transition metals. The anion may be oxygen, chlorine, sulfur or fluorine [14,15]. The A site has a strong effect on stability of the matrix structure and can improve catalyst performance through synergetic interactions with cations at the B site [16–18]. In the present study, the perovskites are used as supports for iron catalysts empowered through the incorporation of selectivity and activity promoters into their matrix.

References

[1] M.E. Dry, Present and future applications of the Fischer-Tropsch process, Applied Catalysis A: General 276 (1-2) (2004) 1–3.

[2] M. Feyzi, M. Irandoust, A.A. Mirzaei, Effects of promoters and calcination conditions on the catalytic performance of iron–manganese catalysts for Fischer-Tropsch synthesis, Fuel Processing Technology 92 (5) (2011) 1136–1143.

[3] N.K. Jaggi, L.H. Schwartz, J. Butti, H.B. Papp, M. Baerns, Phase characterization of iron/manganese Fischer-Tropsch catalysts: effect of composition and reduction conditions, Applied Catalysis 13 (2) (1985) 347–361.

[4] B.B. Dragomir, M. Doble, S.A. Patel, Promoter effects on precipitated iron catalysts for Fischer-Tropsch synthesis, Industrial & Engineering Chemistry Research 29 (1990) 194–204.

[5] A.P. Raje, R.J. O'Brien, B.H. Davis, Effect of Potassium Promotion on Iron-Based Catalysts for Fischer-Tropsch Synthesis, Journal of Catalysis 180 (1998) 36–43.

[6] T. Riedela, H. Schulz, G. Schaub, K.W. Jun, J.S. Hwang, K.W. Lee, Fischer-Tropsch on iron with H_2=CO and H_2=CO_2 as synthesis gases: the episodes of formation of the Fischer-Tropsch regime and construction of the catalyst, Topics in Catalysis 26 (2003) 41–53.

[7] T. Riedel, M. Claeys, H. Schulz, G. Schaub, S.S. Nam, K.W. Jun, M.J. Choi, G. Kishan, K.W. Lee, Comparative study of Fischer-Tropsch synthesis with H_2/CO and H_2/CO_2 syngas using Fe and Co based catalysts, Applied Catalysis A: General 186 (1999) 201–213.

[8] R.W. Dorner, D.R. Hardy, F.W. Williams, H.D. Willauer, Heterogeneous catalytic CO_2 conversion to value-added hydrocarbons, Energy & Environmental Science 3 (7) (2010) 884–890.

[9] F. Farias, R.R. Neto, M. Baldanza, M. Schmal, F. Fernandes, Effect of K promoter on the structure and catalytic behavior of supported iron-based catalysts in Fischer-Tropsch synthesis, Brazilian Journal of Chemical Engineering 28 (2011) 495–504.

[10] N. Lohitharn, J.G. Goodwin, Effect of K promotion of Fe and FeMn Fischer-Tropsch synthesis catalysts: Analysis at the site level using SSITKA, Journal of Catalysis 260 (1) (2008) 7–16.

[11] M.E. Dry, The Fischer-Tropsch synthesis, in: J.R. Anderson, M. Boudart (Eds.): Catalysis Science and Technology 1, Springer Verlag, New York, USA, 1981.

[12] G. Connell, J.A. Dumesic, Migration of potassium on iron and alumina surfaces as studied by Auger electron spectroscopy, Journal of Catalysis 92 (1) (1985) 17–24.

[13] H.C. Chen, R.B. Anderson, Studies of a triply promoted ammonia synthesis catalyst with an electron probe microanalyzer, Journal of Catalysis 28 (1) (1973) 161–173.

[14] D. Leckel, Diesel Production from Fischer−Tropsch: The Past, the Present, and New Concepts, Energy Fuels 23 (5) (2009) 2342–2358.

[15] T. Nitadori, M. Misono, Catalytic Properties of $LaAFeO_3$ (A = Sr Ce) and $LaCeCoO_3$, Journal of Catalysis 93 (1985) 459–466.

[16] R.J.H. Voorhoeve, J.P. Remeika, P.E. Freeland, B.T. Matthias, Rare-Earth Oxides of Manganese and Cobalt Rival Platinum for the treatment of carbon monoxide in auto exhaust, Science 177 (1972) 353–354.

[17] B.P. Barbero, J.A. Gamboa, L.E. Cadús, Synthesis and characterization of $La_{1-x}Ca_xFeO_3$ perovskite-type oxide catalysts for total oxidation of volatile organic compounds, Applied Catalysis B: Environmental 65 (1-2) (2006) 21–30.

[18] M.A. Vannice, The catalytic synthesis of hydrocarbons from mixtures over the group VIII metals, Journal of Catalysis 37 (1975) 449–461.

2 Literature Review

2.1 Fischer-Tropsch Synthesis

2.1.1 Background to the Fischer-Tropsch Synthesis

The current global supply of fuels and chemicals is based largely on crude oil and the International Energy Agency (IEA) projected that the demand for liquid fuels will increase more rapidly in the transportation sector than in any other end-use sector [1]. The depleting reserves of oil and volatile prices have shifted interest to coal and methane with reserves exceeding that of oil by a factor of 2.5 and 1.5 respectively [2]. Methane, coal and biomass can be used to produce syngas, a mixture of gases containing mainly hydrogen and carbon monoxide, which can be converted into a range of fuels and chemicals using the Fischer-Tropsch process [3,4]. The Fischer-Tropsch process was first commercialized in Germany in the 1940s during World War II, and nine reactors with an annual capacity of over half a million tons of Fischer-Tropsch liquid were in operation to provide the needed fuels for the German war effort [5]. However, these plants were closed after the commercial viability waned with the end of the war and the restored access to crude oil. Worried about the possible hikes in oil prices due to depleting reserves, a methane syngas plant with a capacity of 360 000 tons per year was built in Brownsville Texas during the 1950s [6,7]. The plant was shut down in 1957 because of increases in methane prices and the discovery of oil fields in the Middle East [8]. In the same period, South Africa turned to the FT synthesis from coal gasification due to low cost and abundance of domestic coal, to supply significant quantities of its hydrocarbon fuel and chemical needs. The first coal-based plant was constructed 1955 in Sasolburg in South Africa [9,10]. To date, Germany produces no synthetic fuel anymore, while various FT plants are active worldwide, operated by Sasol in South Africa and Qatar, Sasol/Chevron in Nigeria, Shell in Malaysia and Qatar and several companies in China [11,12].

The FT technology is often referred to as coal-to-liquids (CTL) and/or gas-to-liquids (GTL) depending on the syngas source. Current operating CTL plants include Sasol's Sasolburg I and II plant. There are two GTL plants in operation in Qatar; Oryx GTL which is a joint venture between Qatar Petroleum and Sasol, and Pearl GTL which is a revenue sharing project between Qatar Petroleum and Shell [13]. Sasol also has GTL projects in Nigeria and Uzbekistan [14]. The world's first commercial GTL plant, Shell MDS is in Bintulu, Malaysia. In China, Synfuels China focuses on the technologies for indirect Coal Liquefaction or Coal-to-Liquids (CTL) processes [15].

The economic viability of the Fischer-Tropsch process is highly dependent on the cost of the feedstocks considering the depletion of fossil resources and the strong fluctuation of oil prices. The combustion of fossil fuels releases over seven gigatons of CO_2 annually, adding to the global greenhouse effect [16]. To meet the ambitious targets of the Paris agreement, governments have renewed the interest in FT synthesis to exploit the CO_2 content in air through direct air capture (DAC) or capture CO_2 at point sources and convert it into beneficial chemicals such as urea [17–19]. But the capture of CO_2 via DAC is very energy intensive. It requires the same amount of energy as contained in the fuels producing CO_2 [20]. CO_2 storage presents another challenge as geological formations like depleted oil and gas reservoirs are usually far from the CO_2 source. The development of new technologies to capture CO_2 have provided new ways of valorizing CO_2 providing an industry serving as a compliment to carbon capture and storage. These include the production of syngas for use in the FT synthesis from recycled CO_2 by means of green hydrogen to close the carbon loop and meeting the heat requirements by making use of heat released from the FT synthesis reaction [21–23, 307].

2.1.2 The Fischer-Tropsch reactions

The Fischer-Tropsch synthesis comprises a set of highly exothermic primary and secondary reactions in which CO and H_2 (synthesis gas) are catalytically converted into a mixture of linear and branched hydrocarbons, mainly n-paraffins and n-olefins, as well as some oxygenates and aromatics, with water as the main by-product [24]. The main reactions taking place in the FT synthesis, can be described by equations 2.1 and 2.2.

$$2nH_2 + nCO \rightarrow C_nH_{2n} + nH_2O \qquad 2.1$$

$$(2n+1)H_2 + nCO \rightarrow C_nH_{2n+2} + nH_2O \qquad 2.2$$

Where n is an integer. Thus, for n=1, the reaction (eqn. 2.2) represents the formation of methane, which in most applications is considered an undesirable product. Besides the formation of long chain hydrocarbons, several side reactions take place to a varying degree owing to the nature of the catalyst, chosen reaction temperature, and reactor configuration. The water-gas shift reaction (eqn. 2.3) takes place over iron catalysts and unlike other side reactions, it provides means to tune the H_2:CO feed ratio. This is of special interest if synthesis gas is sourced via coal gasification often yielding a H_2:CO ratio of below 2. The Boudouard

reaction (eqn. 2.4) produces carbonaceous deposits that can block the active sites, deactivating the catalyst [25].

$$CO + H_2O \leftrightarrow CO_2 + H_2 \quad 2.3$$

$$2CO \rightarrow CO_2 + C \quad 2.4$$

Synthesis of certain products and their average carbon number can be achieved by using a selectivity modified FT catalyst at a certain pressure and temperature. Industrial operation of the FT synthesis is categorized based on the operating temperature. Industrial Low Temperature Fischer-Tropsch Synthesis (LTFTS) takes place at typically 200–270 °C, 20–45 bar and H_2/CO = 1.7–2.15, and mainly produces long chain products and is thus predominantly employed for the production of diesel, kerosene and wax. Meanwhile the High Temperature Fischer-Tropsch Synthesis (HTFTS) takes place at temperatures of 300–350 °C, 20–40 bar and H_2/CO < 2. Higher temperatures limit chain growth and shift selectivity towards lower carbon number and more hydrogenated products. This may result in more branching and more secondary products such as aromatics and ketones (see Figure 2-1) [26–28]. Iron, cobalt, nickel and ruthenium have been found to be sufficiently active for the hydrogenation of carbon monoxide, however only iron catalysts are flexible towards low hydrogen to carbon monoxide ratios in the synthesis gas because of its water gas shift activity. Furthermore, iron catalysts can catalyze both HTFTS and LTFTS due to their limited selectivity to methane even at high temperature operating conditions [29].

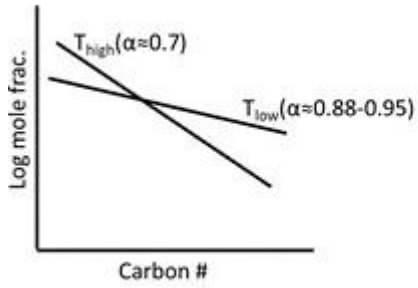

Low T	Sasol Arge	High T	Sasol Synthol
• low $C_1 - C_4$	13.3	• higher $C_1 - C_4$	43.0
• low $C_5 - C_{11}$	17.9	• higher $C_5 - C_{11}$	40.0
• low $C_{12} - C_{19}$	13.9	• less $C_{12} - C_{19}$	7.0
• 50 – 70% wax	51.7	• low wax	4.0
• 220 - 270°C		• 325 - 350°C	
• α ≈ 0.87+		• α ≈ 0.7+	
• gasoline/diesel: 1:2		• gasoline/diesel: 2:1	
• 80* Cetane #		• 50 – 60 Cetane #	
• 0 – 20 Octane #		• 0 – 60 Octane #	

Figure 2-1: Dependency of Fischer-Tropsch synthesis on reaction temperature. Product selectivity (in C-%) of the Sasol ARGE (220 °C) and Sasol Synthol (325 °C) processes. (from [28]).

2.1.3 Fischer-Tropsch Mechanisms

The FT reaction can be described as surface polymerization reaction, involving the following steps;

1. reactant adsorption on the surface of the catalyst
2. generation of a chain starter (chain initiation)
3. chain growth (propagation step)
4. chain termination and product desorption from the catalyst surface
5. re-adsorption of reactive products and further reaction

The first two steps of the FT reaction involve the adsorption and dissociation of CO on the catalyst surface, and the reaction with hydrogen to form surface methyl and methylene groups, monomers of the overall polymerization reaction [30]. During the chain growth, specific surface monomers polymerize to form long-chained hydrocarbons. In the termination step, the hydrocarbon chain is transformed into an adsorbed product on the surface of the catalyst. The product can subsequently desorb or further react [29,31].

The FT reaction mechanism has been under debate since its inception in the 1920s by Fischer and Tropsch. In practice, the most challenging aspect is understanding how to achieve a high yield of long chain hydrocarbons with low methane selectivity. Even though it is the simplest alkane formed during FT synthesis, the formation mechanism of CH_4 is still under debate [31]. It is therefore postulated that not a single pathway exists, but that there are several co-existing reaction pathways which occur with similar probability during FT synthesis to explain the observed product distribution [32,33]. More widely popularized pathways include the alkyl, alkenyl, enol and the CO-insertion mechanisms.

2.1.3.1 The alkyl mechanism

The alkyl mechanism is based on the classic carbide-mechanism originally proposed by Fischer and Tropsch [34] and has for a long time been the most accepted mechanism for the formation of long chain hydrocarbons in the FT synthesis. The proposed mechanism proceeds via the dissociative adsorption of CO and H_2 on the catalyst surface to form hydrogen and carbon species (see Figure 2-2). The surface oxygen

reacts with adsorbed carbon to form CO_2 or with surface hydrogen to form the by-product water via a multi-step reaction [33].

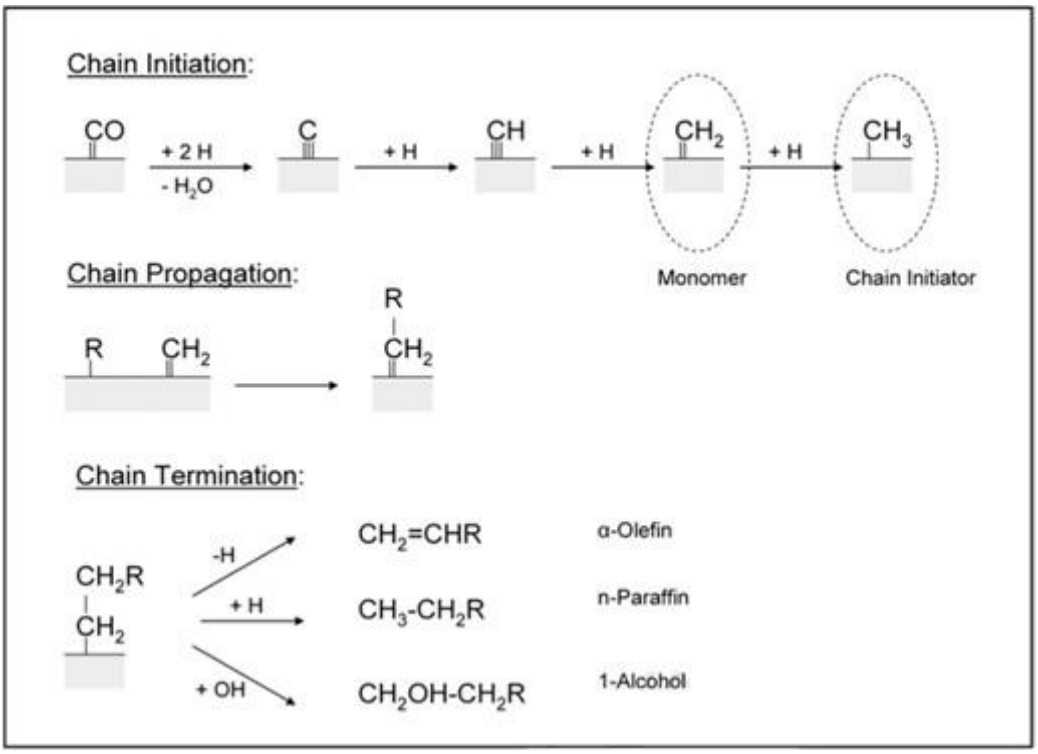

Figure 2-2: Reaction pathways proposed for the alkyl mechanism for the Fischer-Tropsch synthesis (from [33]).

The surface carbon is hydrogenated to form CH, CH_2 and CH_3 surface species. The methyl surface species are regarded as the chain growth initiator while the methylene, CH_2, surface species are regarded as the monomers. The actual chain propagation occurs through the insertion of the CH_2 monomer into a surface alkyl species. There are two possible desorption pathways. First the alkyl species can terminate through β-H-elimination yielding α-olefins, secondly through hydrogenation yielding n-paraffins. The incorporation of surface hydroxyl groups into the alkyl species yielding alcohols has been postulated [35], but there is no experimental evidence to support this reaction pathway. The desorbed olefins can re-adsorb onto the catalyst surface and further react to form longer chain hydrocarbons. The alkyl mechanism explains the formation of n-paraffins and α-olefins in the FT product spectrum [33,36].

The experimental evidence given by Brady and Pettit [37,38] supports the chain propagation step in the alkyl mechanism. They proved that the reaction between diazomethane and hydrogen over a FT catalyst produces a FT product spectrum, while in the absence of hydrogen, ethene is formed. This is an indication that CH_2 species are needed for chain formation in the presence of hydrogen. They can be a monomer or be part of monomer formation for long chain hydrocarbons.

The alkyl mechanism does not explain the formation of branched hydrocarbons. However, Schulz *et al*. [39,40] proposed a reaction pathway similar to the alkyl mechanism in which the formation of branched hydrocarbons proceeds via the reaction of surface alkylidene and a methyl species (see Figure 2-3). They also confirmed experimentally that olefins such as propene can reabsorb and react with CH_2 to form branched surface species. The termination of these species results in methyl branched product molecules [41]. This mechanism was also supported by work of Lee and Anderson [42].

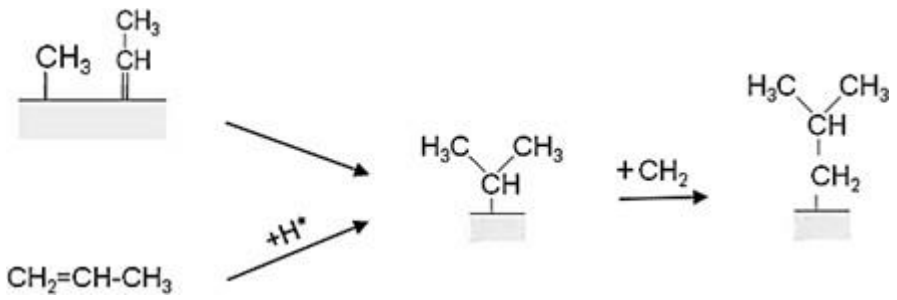

Figure 2-3: Reaction pathways proposed for the formation of branched hydrocarbons in the Fischer-Tropsch synthesis (from [33]).

2.1.3.2 The alkenyl mechanism

Maitlis *et al*. [43] proposed an alkenyl mechanism as an alternative reaction pathway for FT chain growth (see Figure 2-4). The monomer is the CH_2 species, same as for the alkyl mechanism, formed through the sequential hydrogenation of surface carbon. A vinyl surface species ($CH=CH_2$) is the chain initiator formed through the reaction between CH and CH_2 species. Chain growth is assumed to proceed by CH_2 insertion into a metal vinyl bond to form an allyl species, followed by a subsequent isomerization to give rise to a longer alkenyl species. Finally, hydrogen addition on the α-carbon results in chain termination in the form

of α-olefins. The alkenyl mechanism cannot explain the full mechanism of the Fischer-Tropsch products formation, as it describes a primary olefin selectivity of 100 mol.%, therefore an alternative co-existing reaction pathway would have to exist to describe the formation of other Fischer-Tropsch products [44].

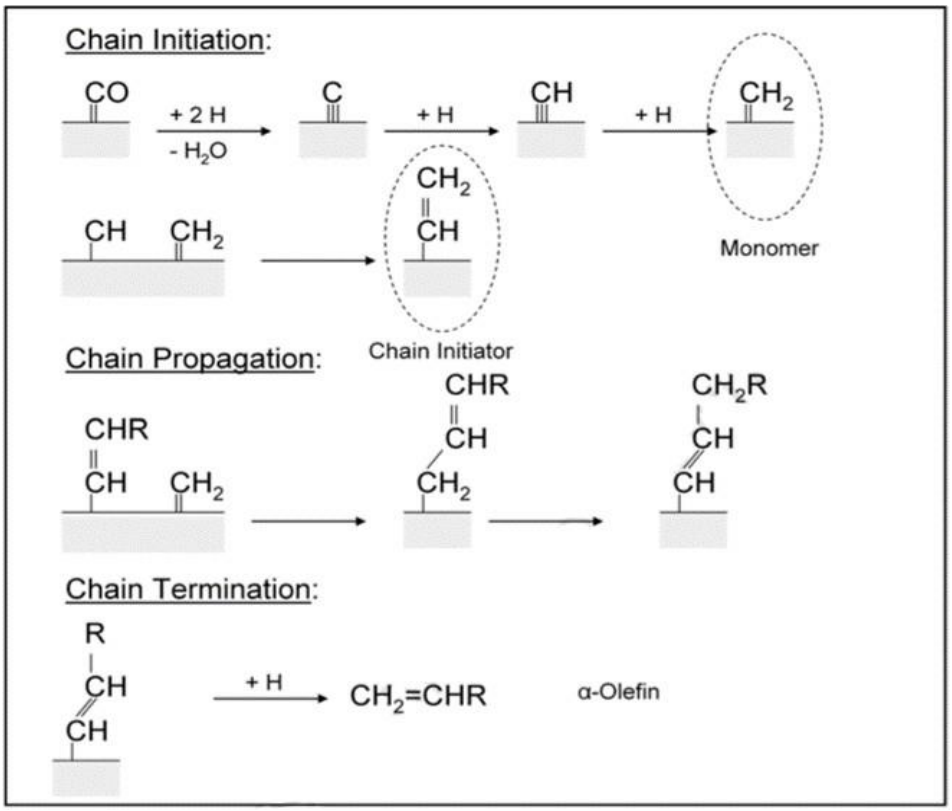

Figure 2-4: Reaction pathway proposed for the alkenyl mechanism in the Fischer-Tropsch synthesis (from [33]).

2.1.3.3 Enol mechanism

The enol mechanism describes a reaction pathway explaining the presence of oxygenates in the FT product (see Figure 2-5). This mechanism involves a relatively large enol surface species formed by hydrogenation of chemisorbed surface CO constituting both the monomer and the chain initiator [45]. The CO molecule does not dissociate. The chain growth occurs via an enol-condensation reaction, eliminating water followed

by the subsequent hydrogenation yielding oxygenates and α-olefins. n-paraffins are formed in secondary hydrogenation reactions of re-adsorbed olefins and their primary formation is not explained.

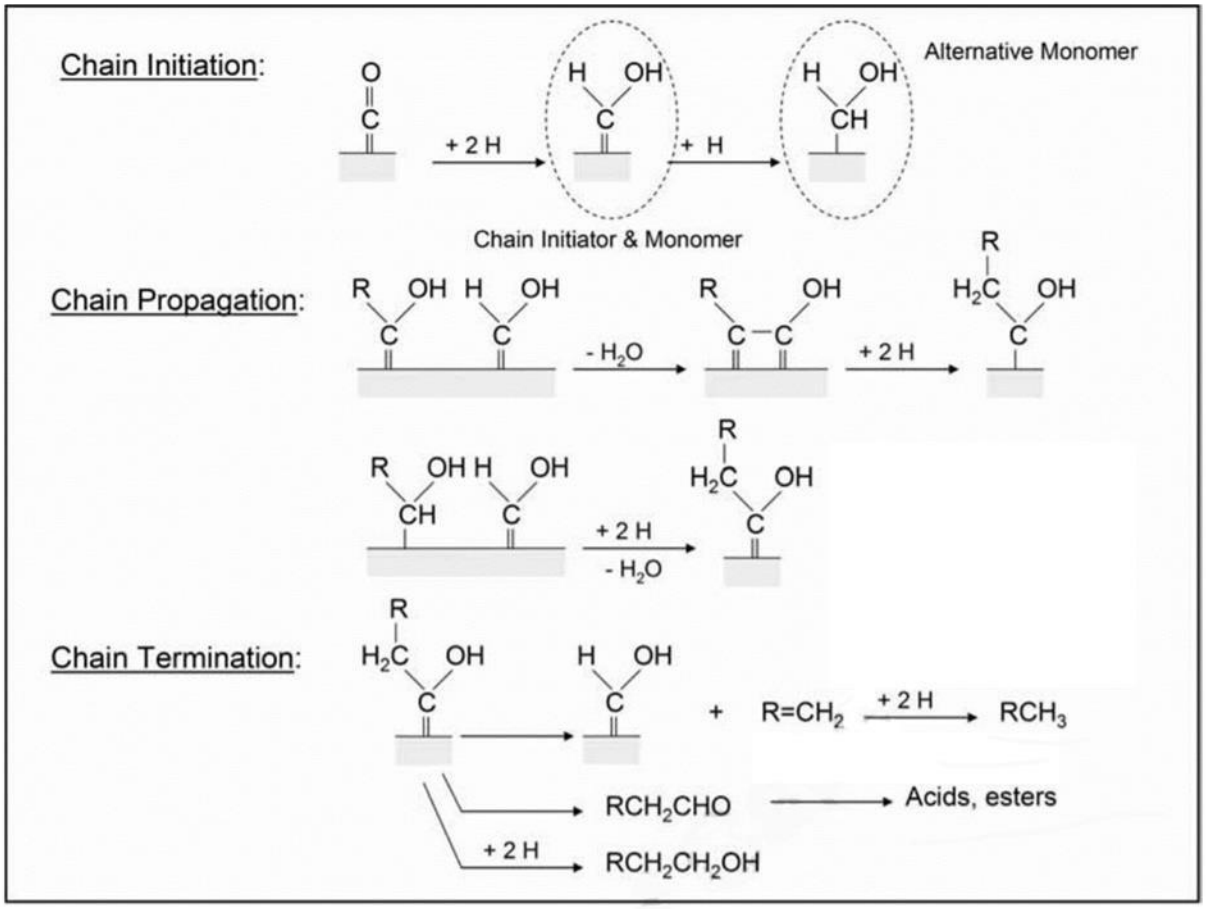

Figure 2-5: Reaction pathway proposed in the enol mechanism in the Fischer-Tropsch synthesis (from [33]).

2.1.3.4 CO-insertion mechanism

The CO insertion mechanism is the most probable and widely accepted mechanism for the formation of oxygenates in the Fischer-Tropsch synthesis (see Figure 2-6). Based on the CO insertion known from homogeneous catalysis, the mechanism was first proposed by Sternberg and Wender [46], and later fully refined by Pichler and Schulz [47]. The monomer is the chemisorbed CO while the chain initiator is a surface methyl species. CO is first hydrogenated and only then the C-O bond is broken to give the chain

initiator. The reaction between the monomer and the chain initiator results in chain propagation through the insertion of CO into a metal-alkyl (methyl or methylene) carbon bond leading to a surface acyl species, which can subsequently form longer alkyl species through the elimination of oxygen. The termination of chain growth proceeds in various pathways yielding either paraffins and olefins, or aldehydes and alcohols depending on the degree of hydrogenation of the alpha carbon [25].

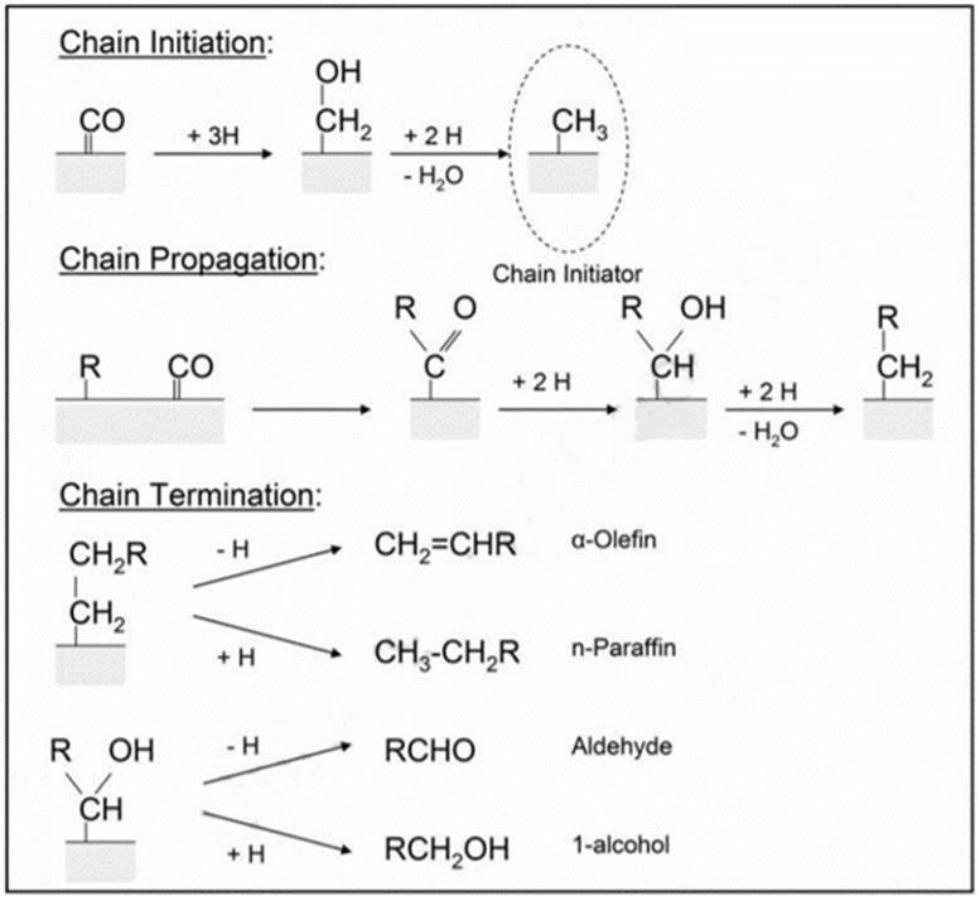

Figure 2-6: Reaction pathway proposed for the CO insertion mechanism in the Fischer-Tropsch (from [33]).

2.1.3.5 Recently proposed mechanisms

The four mechanisms described above do not fully describe the Fischer-Tropsch synthesis spectrum and are still not fully accepted. A lot of research and the advancement of characterization techniques have prompted the development of other potential mechanisms [48–50].

Using surface science data and DFT modelling, Weststrate *et al*. [50] proposed a chain growth mechanism for the close packed Co surface. In the alkyl mechanism mentioned above, the generation of a new chain starts by the surface reaction between the monomer CH_2 and the chain initiator CH_3 forming CH_2CH_3. In the proposed alkylidene mechanism, the monomer CH is described as the most stable C_1H_x species on several metal surfaces including Co (0001) [48]. The chain is initiated by CH + CH to form CH=CH, which is also the most stable adsorbed acetylene species. This step is concluded by the hydrogenation of acetylene to ethylidyne. The chain propagation is thought to proceed via the insertion of CH into the C_2H_3 to form propyne, which is the most stable C_3H_x species on Co (0001). The propyne can further react with hydrogen species to form propylidyne likely influenced by free surface species like CO (see Figure 2-7). Chain termination involves one or more hydrogenation steps, either the alkylidyne or the alkyne is thus hydrogenated to alkanes or alkenes [48–50].

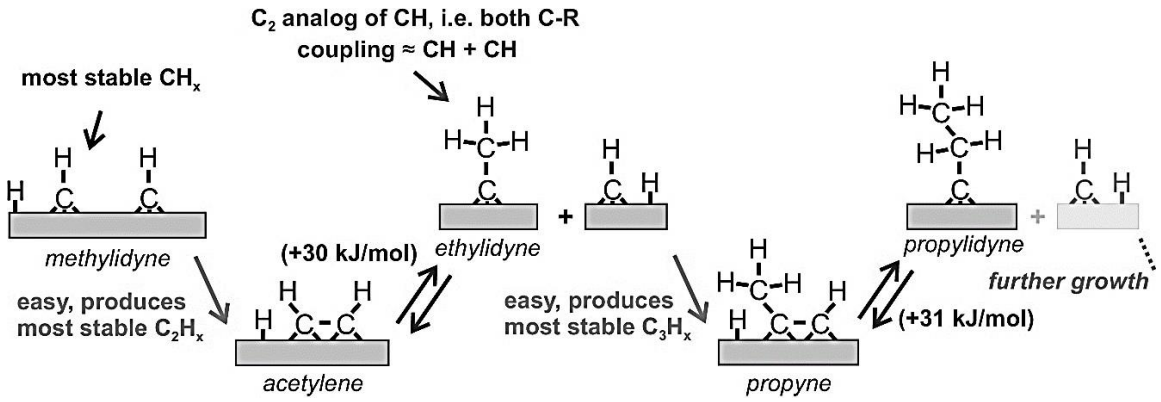

Figure 2-7: Proposed FTS chain growth mechanism on a close-packed Co surface (from [48]).

2.1.4 Fischer-Tropsch Product Distribution

Due to its polymerization nature, the Fischer-Tropsch reaction results in a wide variety of products. These mainly include n-olefins (primarily α-olefins and some olefins with internal double bond) and n-paraffins, with oxygenates (1-alcohols, aldehydes, ketones, carboxylic acids), branched compounds (mainly mono-methyl branched) and aromatics as side products [51]. The composition of the FT product spectrum is influenced by a number of variables including temperature, pressure, catalyst type, promoters and feed gas composition [52]. Irrespective of conditions, the FT synthesis product spectrum forms by a constant stepwise growth and desorption process.

The Anderson-Schulz-Flory (ASF) distribution, which can be applied due to the polymerization type nature of the FT reaction, suggests that the product formation follows an arithmetical distribution whereby C_1 units are successively added to the growing chains on the catalyst surface using carbon number parameters [40]. The synthesis proceeds through a constant stepwise growth and desorption process, over which the products can either desorb or continue in chain growth on the catalyst surface (see Figure 2-8).

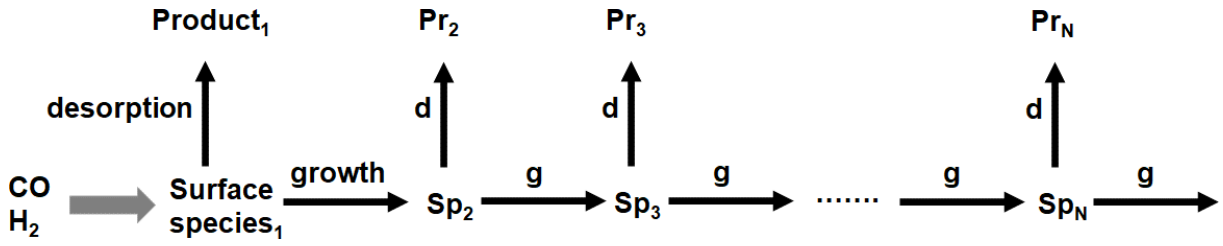

Figure 2-8: Fischer-Tropsch stepwise product growth process - a series of ideal chain growth and formation (from [40]).

The ideal ASF growth process shown in Figure 2-8 is however different from the product distribution observed in a real FT synthesis. For instance, it is widely reported that formed primary α-olefins can re-adsorb on the catalyst surface as a function of their carbon number [33,53], and form secondary products via chain growth, hydrogenation or double bond shift. Primary oxygenates like 1-alcohols and aldehydes [33] can also further react through re-adsorption on the catalyst surface (see Figure 2-9) [54–57]. These reactions can be summed up together with their chain length dependency in the proposed chain growth mechanism (not accounting for branched hydrocarbon formation and the fact that there may be different

surface species and different active sites) to give a model that explains some of the deviations from ideal ASF distribution experimentally observed, such as higher methane and lower C_2 content.

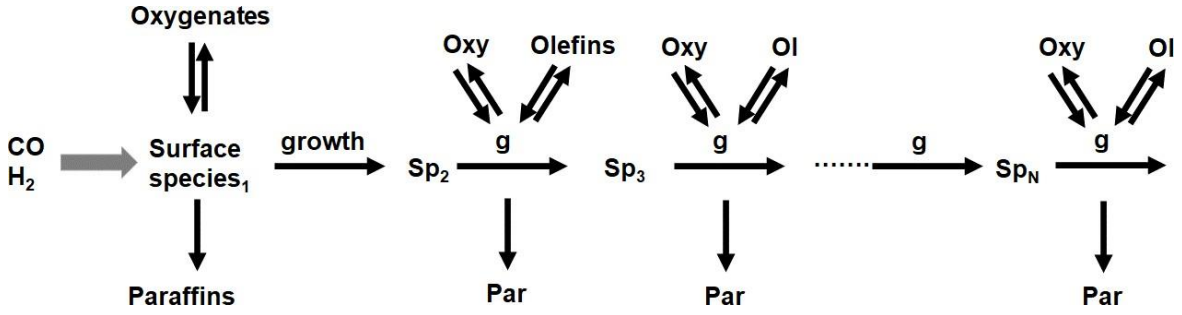

Figure 2-9: Mechanism for chain growth of paraffins, olefins and oxygenates as product classes and one class of surface species (Sp) (N: carbon number, g: growth) (from [33]).

The chain growth probability is described by the parameter α and is dependent of both the propagation and termination rates as shown in equation 2.5.

$$\propto = \frac{r_g}{r_g - r_d} \qquad 2.5$$

Where r_g and r_d are the propagation and termination rates respectively. According to the ASF distribution, the weight content of the products of a certain carbon number W_N as a function of carbon number N_C can be expressed as a linear equation.

$$log\frac{W_n}{N_C} = N_C.log\alpha + log\frac{1-\propto}{\propto} \qquad 2.6$$

The average chain length of the hydrocarbon product produced in the FT synthesis depends on the value of α. For the α value of zero, only methane is formed (see Figure 2-10). The maximum amount of C_5–C_9 hydrocarbons, for petrol production, that can theoretically be obtained is about 45% at an α- value of 0.75. At higher values of α (α approaching 1), the fraction of the more valuable hydrocarbons (C_{15}– C_{22}) in the product decreases sharply. Therefore, the best strategy to obtain the maximum amount of fuel fraction is to form longer

chain hydrocarbons (waxes) by maximizing α, and then hydrocrack them to the desired product chain length in a subsequent process [58].

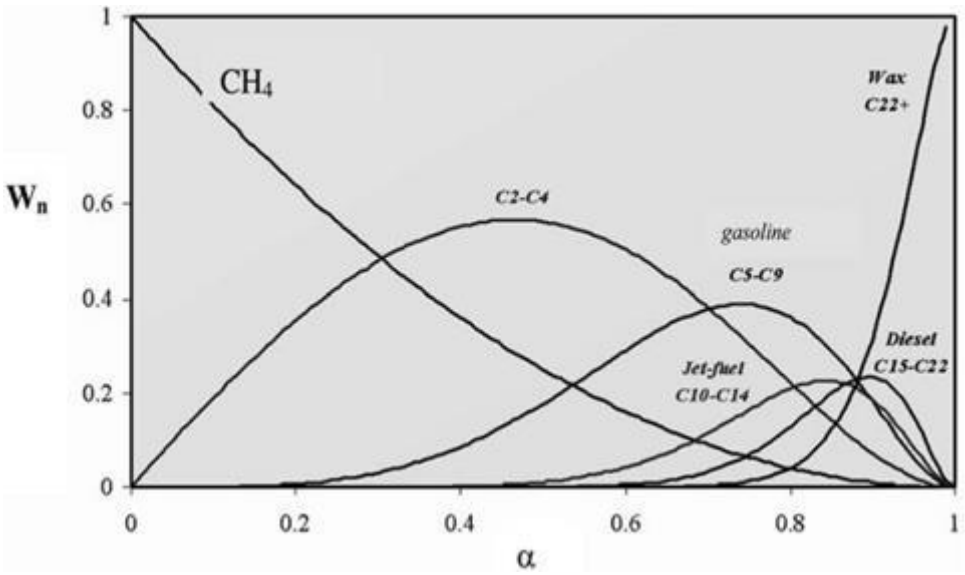

Figure 2-10: Concentration of different product slates according to theoretical ASF distributions at different chain growth probabilities (from [8]).

An increase in temperature increases the rate of desorption of surface species, shifting product selectivity towards short chain hydrocarbons and methane. Therefore, when targeting long chain products, the low temperature FT synthesis is beneficial. The effect of pressure is due to a combination of total pressure of the feed and product gases. Increasing the total pressure generally increases the probability of high molecular weight products. High H_2:CO ratios result in high hydrogen coverage on the catalyst surface (see Table 2-1). Hydrogen rich conditions increase the formation of hydrocarbons with high H:C ratio (CH_4 and paraffins), additionally, low olefin and oxygenate selectivity is observed due to increased secondary hydrogenation of these products. Increased residence times result in a higher methane selectivity [36].

Table 2-1: Effect of process conditions on product selectivity [59].

	Temperature	**Pressure**	**H_2:CO**	**Residence time**	**K[a]**
Methane selectivity	+	-	+	+	-
Chain growth	-	+	-	~	+
Chain branching	+	-	~	~	-
Olefin selectivity	~	~	-	-	+
Oxygenate selectivity	-	+	-	-	+
Carbon deposition	+	~	-	~	+

\+ increase with increasing parameter

\- decrease with decreasing parameter

~ no clear effect

[a] potassium loading for iron catalyst systems

2.1.5 Fischer-Tropsch Catalysts

Various transition metals (iron, cobalt, nickel, rhodium, and ruthenium) can be used as catalysts for the FT synthesis, but most are not commercially viable due to high cost, limited availability as well as poor selectivity and activity. Only iron and cobalt catalysts have successfully been used as commercial Fischer-Tropsch catalysts [52,52,60]. Nickel catalysts possess a high hydrogenation activity under practical conditions that leads to the formation of methane. Nickel also tends to form volatile nickel carbonyls under Fischer-Tropsch conditions [61]. Ruthenium is the Group VIII metal with the highest activity for FT synthesis forming high molecular weight products at very low temperatures. It is however not suited for commercialization because of its limited availability and associated high cost [62–64]. Apart from displaying good activity for FT synthesis, rhodium has very high selectivity towards oxygenates, preferentially ethanol over other alcohols [65,66]. However, commercialization of rhodium is impractical due to high costs of such catalysts, especially when high metal loadings are used [67].

Iron catalysts are reported to be more robust than cobalt catalysts, especially at more severe conditions (higher space velocities and at higher reactor pressures) [62,68]. They show activity for both the high and low temperature Fischer-Tropsch synthesis [52,69,70]. Iron catalysts are cheaper and more resistant to

sulfur poisoning than cobalt catalysts. Iron catalysts are also known to catalyze the water gas shift reaction (WGS), the conversion of CO and H_2O to form CO_2 and H_2, under Fischer-Tropsch conditions. In general, the water gas shift reaction is undesirable as it results in a low carbon efficiency due to some of the carbon being lost as CO_2. However, the WGS reaction has the advantage of producing H_2 that improves the H_2:CO ratio of hydrogen lean synthesis gas as is the case when derived from the gasification of coal. CO_2 is further produced by the Boudouard reaction. This disproportionation of CO to form CO_2 presents two problems, it increases the H_2:CO ratio which could potentially promote hydrogenation leading to a decrease in chain growth, and results in carbon deposition on the catalyst's surface blocking the active sites [62,70–72]. Although the iron-based Fischer-Tropsch catalysts are loaded into the reactor in their metallic form after hydrogen treatment at elevated temperatures, the catalyst is undergoing a phase change under Fischer-Tropsch conditions. The active phase consists of iron carbide, iron oxides and to some extent, metallic iron. At high FT synthesis conversions, the reaction mixture becomes oxidative due to the increased concentration of product water and a magnetite phase is formed [58,73]. Promoters are added to iron-based FT synthesis catalysts to enhance the catalytic performance, catalytic stability and selectivity towards certain products and will be discussed in detail in section 2.1.7.

Cobalt catalysts are more expensive and are usually synthesized in small crystallites supported on structural supports to maximize the available mass specific surface area. They have a very low WGS activity and are therefore more suitable for applications with hydrogen-rich synthesis gas, which is today mainly produced from natural gas [11]. Cobalt catalysts surpass iron catalyst in activity at low space velocities (high conversion) [62,74,75]. It is believed that nanoparticles of the metallic cobalt are the active phase in cobalt catalysts [52,62,70]. Cobalt catalysts have mainly been used commercially for the gas to liquids production of long chain saturated hydrocarbons. Promoters are reported for cobalt-based catalysts for the direct conversion of syngas to lower olefins, and for the suppression of methane and carbon dioxide [53,76,77]. Industrially, promoters are mainly employed to decrease the reduction temperature of the cobalt oxide precursor [78–80].

2.1.6 The active phase of iron-based FT catalysts

Iron based catalysts transform into several phases during FT synthesis depending on the chosen reaction conditions (see Figure 2-11). The higher the reduction temperature the higher the degree of reduction. The same result was observed at higher space velocities [81]. *In situ* Mössbauer spectroscopy showed that the level of CO conversion increased with the formation of carbides (ε'-$Fe_{2.2}C$ and χ-Fe_5C_2) on iron-based

catalysts. It was also observed that the metallic Fe catalysts showed no activity before the formation of surface carbides [82,83]. The carbide phases are usually intermetallic compounds made up of iron and carbon with the composition ranging from FeC to Fe_7C. During the Fischer-Tropsch synthesis, the iron catalyst goes through a number of phase changes in which the iron carbide phases are interconverted from one phase to another and oxidized (see Figure 2-12) [84]. Depending on the reduction conditions, these phases may be a mixture of metallic iron (α-Fe) and iron oxides (hematite, α-Fe_2O_3, magnetite Fe_3O_4), and different forms of iron carbides: monoclinic Hägg carbide (χ-Fe_5C_2), pseudo-hexagonal iron carbide (ἐ-$Fe_{2.2}C$), hexagonal iron carbide (ε-Fe_3C), cementite (θ-Fe_3C), and Eckstrom-Adcock iron carbide (Fe_7C_3) [85,86]. While it is well known that the active phase in cobalt catalyst to produce long chain hydrocarbons is metallic cobalt, the active phase of the iron catalyst is still not fully identified and might well be an interplay of different metastable phases.

Shroff *et al*. [87] confirmed that the formation of carbides is necessary for iron catalysts to be active in the FT synthesis by demonstrating that neither magnetite nor hematite displayed any FT activity. However, other researchers suggested that the observed FT activity may be due to metallic iron, Fe_3O_4 and traces of carbide phases [84,88,89].

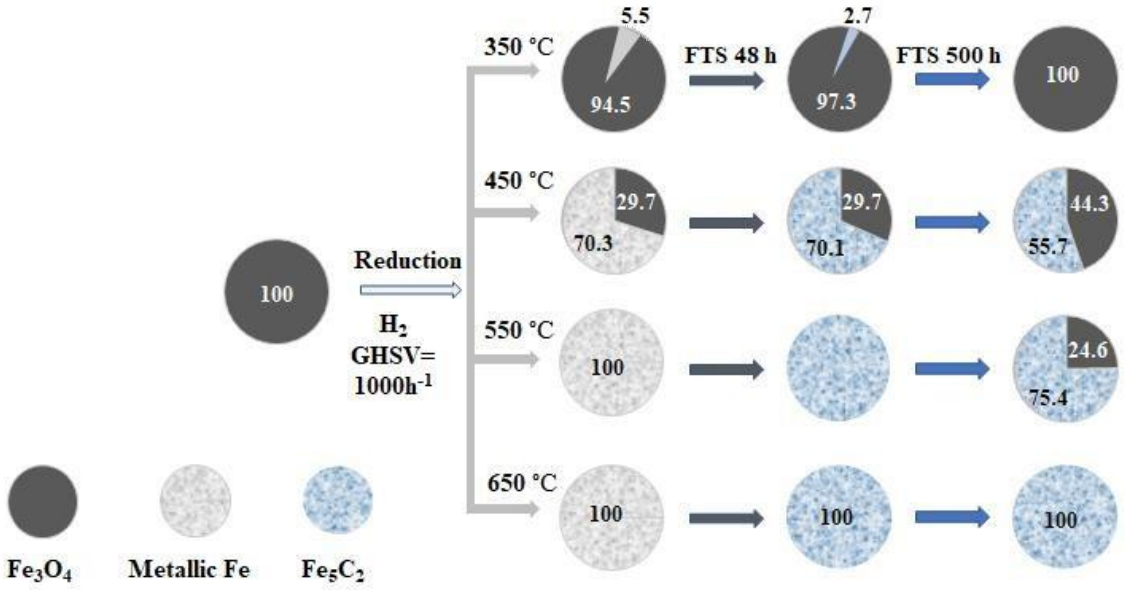

Figure 2-11: Evolution of iron phases in a fused iron catalyst during reduction and reaction (the content of the individual phases was calculated from XRD) (from [81]).

Different assumptions and hypotheses that exist today are based on the lack of surface sensitive *in situ* techniques in the early years of the FT synthesis which can monitor changes of the catalyst in real time and provide detailed information about the surface makeup. Today there are a number of powerful techniques that have led to the identification of several carbides mentioned above and the consensus among researchers is therefore that the carbidic phase of iron is the active phase [85,86,90], and to some extent metallic iron [91]. However, it is still difficult to pin point the exact phases of carbide responsible for improving activity or tuning selectivity towards certain products because of the parallel existence of carbidic phases which evolve under FT conditions [92]. But the tools have brought to light the understanding of the carbon species and their influence in catalyst performance. For instance, there are four kinds of carbon species identified, namely surface atomic carbon, oligomerized carbon species, graphitic surface carbon and iron carbide [93]. While it is strongly believed that iron surface carbides are active for CO activation and hydrogenation [94–97], bulk carbide does not really contribute to the FT synthesis [98,99]. Other carbon species are inactive or catalyst poisons [93].

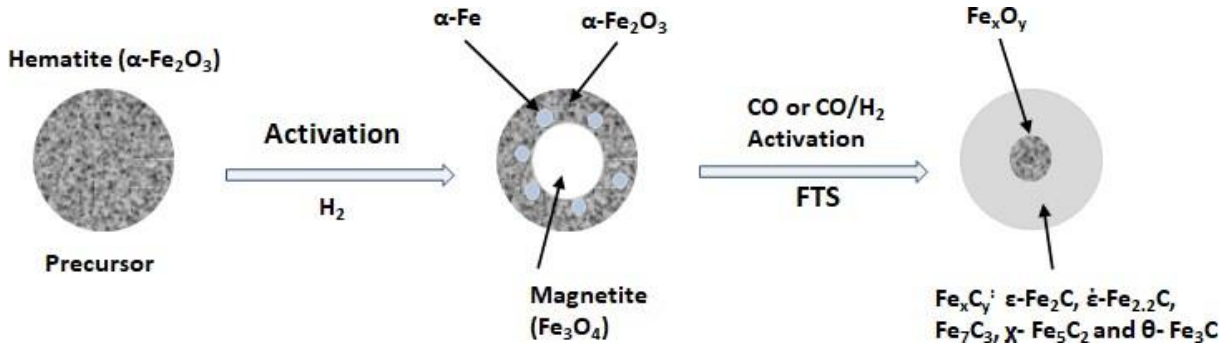

Figure 2-12: Evolution of iron carbide phases during pre-treatment and FT synthesis reaction conditions (from [84]).

2.1.7 Promoters in Fischer-Tropsch catalysts

The degree of reduction of the active phase plays an important role in optimizing catalyst performance. Small amounts of promoters (Cu, Pd, Pt, Ru) are usually added during the catalyst preparation to improve its reducibility. Additionally, the activity and selectivity can be improved by modifying the electronic character of the active phase using metal oxides (MnO and ZnO) and oxides or carbonates of alkali metals

(Na, K, Rb, Li) [100–102]. Positive effects of other non-common promoters such as La, Mo, Ta and V have been documented [103–106].

2.1.7.1 Promoters in iron-based Fischer-Tropsch catalysts

The following section discusses promoters reported for iron FT catalysts. They are classified as either chemical, reduction or structural promoters [107,108].

i. Chemical promoters

Almost all iron-based FTS catalysts are promoted with alkali metal salts to improve their activity and selectivity. Studies by Dry *et al*. [68] suggest that potassium promotes the chemisorption of CO by strengthening the metal carbon bond and weakening the carbon oxygen bond, while suppressing the chemisorption of hydrogen, which in turn leads to lower FT synthesis rates, a higher product molecular weight, and a greater olefin content [101]. Apart from promoting Fischer-Tropsch activity and selectivity, potassium is reported to promote the water gas shift activity by keeping the iron catalyst in the active carbide phase [109].

Despite the clear importance of potassium as a promoter for iron-based catalysts in the FT synthesis, it is unclear how the potassium compounds (mostly K_2CO_3) and iron carbide species interact on an atomic level to produce the proposed electronic effect. Van Steen and Claeys [110] argued, using molecular modelling, that the observed effect of potassium on CO conversion and selectivity is probably due to the electronic interactions between K and the surface of Fe. The authors looked at the state and interaction of K with χ-Fe_5C_2 carbide. However, under realistic FT synthesis conditions, there are other forms of carbide (θ and ε) and iron oxides that require understanding of their individual interaction with potassium.

Recently, Li *et al*. [90] explained the positive effects on activity and selectivity with regard to the electronegativity of the alkali promoters. It causes a charge transfer towards the transition metal, thereby simultaneously inhibiting adsorption of H_2 while enhancing adsorption and dissociation of CO [111,112]. Nørskov *et al*. [113] supported, based on DFT calculations, this type of long-range interaction. They observed that the main effect of the alkali metal is to transform the electrostatic potential of the surface atoms in the vicinity of the adsorbed potassium atom.

Ngantsoue-Hoc *et al*. [114] reported that K is the best performing promoter because of its ability to increase CO conversion at all conversion levels while lighter alkali promoters like Li and Na only show an

enhancement of CO conversion at low to moderate conversion levels relative to unpromoted catalysts. They are ineffective or even decrease CO conversion in the high conversion levels. Heavier alkalis like Rb and Cs result in lowered CO conversion over the entire conversion range [74,90,115]. An example of the effect of different promoter elements on the product distribution of hydrocarbons produced over Fe based catalysts is shown in Figure 2-13. Potassium promoted catalysts show the highest C_{5+} hydrocarbon and lowest CH_4 selectivity amongst the studied samples [90].

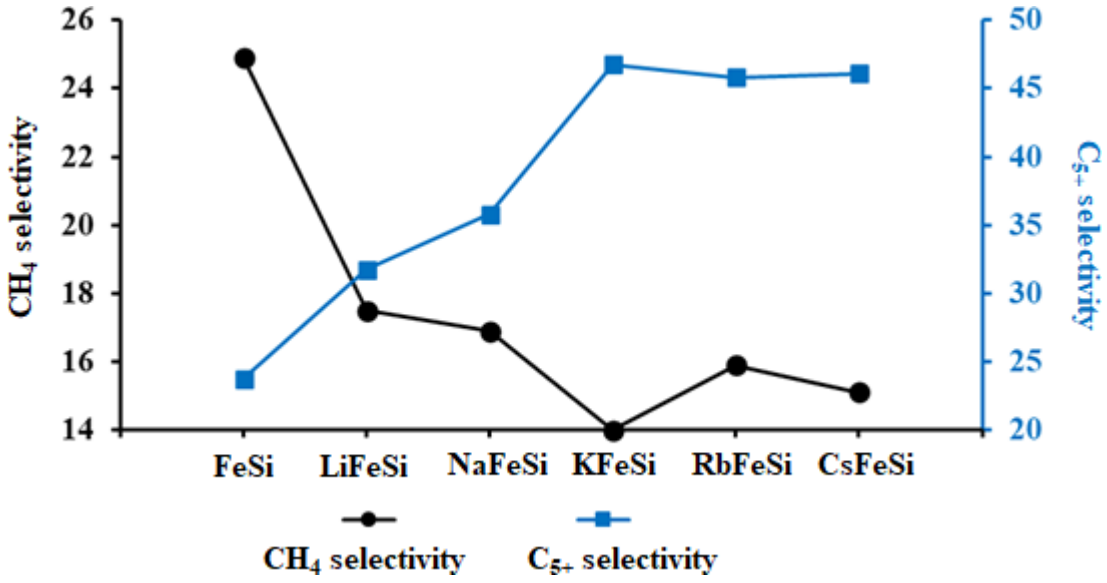

Figure 2-13: CH_4 and C_{5+} selectivity over alkali promoted iron catalysts. (from [116]).

Chemical promoters can seemingly enhance the reducibility of the iron catalyst or impede it depending on the loading of the promoter [117]. Jiang *et al* [118] demonstrated using *in situ* diffuse reflectance FT-IR that potassium species (potassium loading of 0.1 wt.-%) interact closely with the surface species of iron and aid in the reduction of iron to form fine metallic conglomerates after reduction. At higher loadings, potassium retards catalyst reduction due to a possible blockage of nucleation sites by the promoter [90]. Other studies also found that reduction of iron catalyst systems (Fe/SiO_2, precipitated Fe-Mn, etc.) was suppressed with an increasing amount of potassium [119–122]. Xiong *et al*. [123] studied the effect of three group I alkali metals (Li, Na, K) on Fe/CNT catalysts in the Fischer-Tropsch synthesis with promoter loadings of 0.04 wt.-% Li, 0.14 wt.-% Na and 0.23 wt.-% K. Li showed a slight improvement (reduction) of reduction temperature while Na and K increased the reduction temperature [121,124].

Chemical promoters are also reported to have influence on the active species (iron carbides, iron oxides and some metallic Fe) [125] of the working catalyst. The study of Li *et al*. [126] demonstrated that the presence of either potassium or copper promotes the abundance of small nuclei of Fe_3O_4 that form small crystallites leading to a quicker conversion of Fe_3O_4 to iron carbides due to shorter diffusion paths. Smaller iron particles (6.1–7.4 nm) are reported to be composed of mostly χ-$Fe_{2.2}C$, while larger particles around 10.1 nm are mostly χ-$Fe_{2.5}C$ [127]. Ribeiro *et al*. [128] used *in situ* TPR-XANES to study the influence of alkali promoters (Li, Na, K, Rb, and Cs) on the carburization rate of FeSi. They found that after 10 hours of CO treatment at 290 °C, the samples that are promoted with K, Rb and Cs were completely carburized while the unpromoted and Li containing samples still contained iron oxide.

The use of manganese oxide (MnO) as a promoter for iron-based Fischer-Tropsch synthesis catalysts has widely been reported. The reports show that manganese can decrease the selectivity to methane and have a higher light hydrocarbon fraction with more short-chain alkenes and less heavy wax even at a high Fe/Mn ratio. Lower yields of heavy wax are important for the industrial slurry phase reactors as they can operate continuously without the need to remove the wax during the reaction [129–131]. Manganese has also been reported to improve the dispersion of the active species of iron [132–134]. These observations seem to change depending on the amount of manganese loaded and reaction conditions. Yang *et al*. [135] studied the effect of Mn promoter on the Fe-Mn-K catalysts over a wide range of Mn concentrations. Their results show a low selectivity of light hydrocarbons at low Mn contents which increases with increasing Mn content. The promotional effects of manganese on iron catalysts are tightly linked to that of potassium except for the high evolution of CO_2 observed with potassium promoters. Storch *et al*. [45] promoted the iron catalyst with small amounts of manganese oxide and observed the same promoting effect as observed with potassium, with the olefin to paraffin ratio of both approximately three but methane and C_{5+} selectivities slightly higher for catalysts promoted with potassium [136,137]. Manganese oxide is also reported to possess similar surface basicity as alkali promoters, and the iron therefore also withdraws electron density from manganese [115,138,139].

Koelbel and Tillmetz [140] studied the co-precipitated iron-manganese catalyst with a Fe/Mn ratio of 1 and indicated in their patented literature that lower light olefins (C_2–C_4) would be formed in the fixed bed reactor with trace amounts of methane, and a chain growth of only up to C_6. Their later work on Fe/Mn ratios of up to 9 showed a significant decrease in light olefins selectivity and a shift to C_{5+} selectivity in a slurry reactor. A combinatory effect of K and Mn promotion has also been reported [141–143]. The results show that the addition of MnO to a potassium-promoted iron catalyst improved the selectivity to lower olefins, although these results were not confirmed by van Dijk [144] who did not observe any reportable changes

in selectivity. According to Wang *et al*. [145], the increase in MnO content changes the morphology of the samples. With increasing MnO content, cubic structures which are visible in TEM are formed. In the FT synthesis, these catalysts show a lowered CO conversion and light alkene selectivity. The poor performance is believed to be due to the cubic crystallites in the catalyst. It was also evidenced that catalysts with the same Mn content but prepared with different methods exhibit different catalytic activities. Coprecipitated catalysts showed a twofold increase of C_2–C_4 light alkenes while the sol-gel prepared MnO containing catalyst did not show any notable increase when compared with a pure iron catalyst [145,146].

Studies on the phase composition of Fe/Mn catalysts with different manganese content show that a single-phase solid solution of Mn was formed in α-$(Fe_{1-x}Mn_x)_2O_3$ during calcination at 500 °C. The same observation was found in coprecipitated FeMn and FeMnK catalysts systems [141,145,146]. Several studies also indicated that, depending on the amount of manganese oxide in the catalyst, manganese has the propensity to migrate to the surface of the catalyst system during calcination or reduction [147–149]. According to Kreitman *et al*. [148], the co-feeding of water assists the segregation of MnO towards the catalyst surface. The manganese enrichment on the catalyst surface is reported to be beneficial to the reduction of Fe_3O_4 to metallic Fe. Hughes *et al*. [149] used X-ray photoelectron spectroscopy and temperature-programmed reduction to study the differences between unpromoted Fe and manganese promoted Fe catalyst (l–4 wt.-% Mn) in reducing atmospheres. They demonstrated that Mn promoted catalysts with Mn surface enrichment achieved full reduction from Fe_3O_4 to Fe in H_2. But at higher concentrations of manganese, Leith and Howden [150] reported that the presence of manganese retards the reduction of iron, yielding intermediates of mangano-wüstite phases (cubic $FeMnO_3$ or γ-$FeMnO_3$) before the reduction to metallic iron [151,152].

Jensen and Massoth [136] studied the carburization of a pure Fe_3O_4 catalyst and a series of manganese promoted iron catalysts with 15 to 40 mol.% Mn in a flow microbalance reactor. The pre-reduced catalysts were carburized at 225 °C and 300 °C in a flow of H_2/CO. The researchers observed that all catalysts in the series carburized at the same rate at 300 °C, but at lower temperatures of 225 °C the carburization proceeded at a lower rate in the presence of MnO. The catalysts were also decarburized in H_2 and the MnO containing catalyst decarburized faster than the unpromoted catalyst. Catalyst with low Mn content showed a higher mass specific activity for CO and hexene hydrogenation. Wang *et al*. [145] investigated the carburization of pre-reduced iron catalysts and catalysts promoted with 1–4 wt.-% Mn prepared by coprecipitation and sol-gel synthesis using temperature programmed surface carburization (TPSC) tests in a CO atmosphere. Co-precipitated MnO containing catalysts had finer particles than pure iron catalysts prepared by the same method or MnO containing catalysts prepared via the sol-gel technique. The results show that the samples

prepared via the sol-gel route suppressed carburization, but ultrafine particles prepared via coprecipitation carburized easily. It has been demonstrated that reduction and carburization proceed via diffusion of oxygen in the bulk lattice [96,153]. The shorter the diffusion path, the faster the reduction or carburization.

La_2O_3 has been reported to have an effect on iron-based Fischer-Tropsch catalysts both regarding activity and selectivity. Zhao *et al*. [103] studied the effect of La_2O_3 at different loadings on unsupported precipitated iron catalysts. The XRD patterns showed a crystalline α-Fe_2O_3 phase that did not change upon addition of La_2O_3 as no lanthanum-containing phase was detected. The only noticeable change was the decrease in crystallite size at lower loadings from 21.6 nm (Fe_2O_3) to 16.8 nm (Fe2La). The CO conversion increased with increasing La_2O_3 content, reaching a maximum at a La/Fe ratio of 0.01, above which the CO conversion dropped sharply. With the increase in conversion, the selectivity towards light olefins (C_2–C_4) and CO_2 increased, as well as the formation of methane. C_{5+} hydrocarbons were suppressed except for a higher lanthanum loading of Fe2La. The group reported that iron carbide formation was favored at low loadings of La_2O_3 and suppressed at higher loadings. The presence of the carbide was also linked to the dispersion of the catalysts owed to the addition of small amounts of La_2O_3 [154–157]. Zamani *et al*. [158] investigated the effect of La and Ba promoters on nanostructured iron catalyst in the Fischer-Tropsch synthesis. The catalysts prepared by a microemulsion technique were 100Fe/4Cu, 100Fe/4Cu/2La, 100Fe/4Cu/1La/1Ba, and 100Fe/4Cu/2Ba with compositions in terms of the atomic ratios. The BET results showed that the surface area decreased with the addition of the promoters. The addition of lanthanum suppressed CH_4 selectivity and increased CO_2 selectivity, C_2–C_4 light hydrocarbons decreased while C_5–C_{12} increased, implying that the addition of the promoter improved the chain growth probability and suppressed hydrogenation similar to the effects observed with alkali promoters. The results are somewhat contradictory to results obtained by Zhao *et al*. [103], probably due to the presence of Cu and Ba.

A handful of researchers have shown the promoting capabilities of sulfur in low concentrations for iron catalysts in FT synthesis. However, such studies are limited due to the reported poisonous nature of sulfur for FT catalysts, whether the mode of poisoning is electronic or purely geometric [159–162]. The majority of these reports on sulfur compounds as poisons for FT synthesis catalysts are filled with contradictions and ambiguities [6,163], prompting the need to look into positive effects sulfur might have on the FT synthesis. Chaffee *et al*. [162] investigated catalysts whose general behavior had already been established and used industrially (Co/ThO_2/MgO/Kieselgel, Magnetite (fused iron), Fe/Cu/K_2O/waterglass, Fe/Cu/K_2O, Fe/Mn and Co/ThO_2/MgO/Aerosil) for their ability to resist sulfur. The catalysts were found to be tolerant to sulfur in a hydrogen lean synthesis gas (H_2/CO = 0.5) and performed poorly in the hydrogen rich synthesis gas (H_2/CO = 2). The most promising of these catalysts was the Fe/Mn, with two orders of

magnitude more sulfur tolerance than other catalysts, rationalized by a rapid reaction of sulfur with manganese.

Amid these reports focusing on how sulfur acts as a poison for FT catalysts, there are growing numbers of studies that show that sulfur can have a promoting effect. Several reports show that improved performance of using catalysts that have been subjected to sulfur [164–166]. It is reported that with small amounts of sulfur, the catalyst showed improved selectivity towards olefins, but at higher sulfur concentrations, the catalyst is poisoned [167]. Galvis *et al*. [168] used the combination of sodium and sulfur (Na_2S) on Fe/α-Al_2O_3 to investigate the promotional effects of sulfur on the lower olefin (C_2–C_4) selectivity. From the free sulfur catalyst (10Fe0.8Na), the addition of sulfur (10Fe0.8Na0.1S) increased the CO conversion from 31.3 to 42.2%. The selectivity towards lower olefins improved from 8.7 to 30.9% with no significant change on the selectivity towards methane and C_2–C_4 paraffins. The increase in C_2–C_4 selectivity is the result of a decrease in chain growth probability seen by the parallel decrease in C_{5+} selectivity from 67.2 to 53.0%. With further addition of sulfur (S/Fe = 0.56/10), the CO conversion dropped from 49.9 to 12.1%.

ii. Reduction Promoters

The freshly prepared catalyst systems are usually in their oxidic form. They are therefore exposed to a reductive pre-treatment in H_2 and/or CO at elevated temperatures to form the active phase, be it either in metallic or carbidic form. Under hydrogen, hematite (Fe_2O_3) first reduces to magnetite (Fe_3O_4), followed by the formation of metallic iron (Fe) [169]. In carbon monoxide atmosphere, Fe_2O_3 reduces to Fe_3O_4 followed by subsequent reduction and carbidization to predominantly Hägg carbide (Fe_5C_2) [169]. At the employed elevated temperatures, the risk of particle sintering increases, resulting in loss of active surface area.

In commercial catalysts, copper is added as a promoter to decrease the required maximum reduction temperature to facilitate the conversion to a zero valent iron in both a hydrogen rich and carbon monoxide rich atmosphere [74,133,170,171]. This can reduce unwanted sintering during catalyst activation and corresponding loss of catalyst activity, which is more relevant when activating in hydrogen as reduction in the presence of CO leads to the formation of iron carbides that are not prone to sintering [172].

In a hydrogen rich atmosphere, the initial facile reduction of the copper promoter is very important for the reduction of iron oxide as it can assist in hydrogen dissociation. The dissociation of hydrogen provides the much needed atomic hydrogen for the reduction of iron oxide to metallic iron, in a type of hydrogen spillover [173,174]. In carbon monoxide, copper assists in the reduction of iron oxide via the activation of

CO on the surface of the reduced copper and reaction of oxygen from the metal oxide to form CO_2 and metallic iron. The introduction of potassium to the iron-copper catalyst is believed to improve the rate of carburization as potassium promotes the activation of CO [174].

iii. Structural Promoters

Structural promoters are well known as supports and are mainly used as a dispersing or spacing agent of the active metal to avoid or minimize sintering and ensure maximum utilization of the costly metal catalysts. Structural promoters can modify the surface properties by affecting the metal-support interaction, thus improving the metal dispersion and number of active metals. They are usually high surface area microporous metal oxide structures with a combination of high thermal and chemical stability (see Figure 2-14). They include but are not limited to Al_2O_3, Cr_2O_3, zeolites, activated carbon, SiO_2, TiO_2 and perovskites [175,176].

Fischer-Tropsch catalyst particles are well known to undergo changes by physical attrition and chemical stresses because of phase transformations that occur during formation and reaction [177]. Attrition resistant iron catalysts are crucial, especially for slurry bubble column reactors or stirred tank slurry reactors that are now being used industrially because of their lower capital and operating costs, capability of on-line catalyst addition and removal and ability to efficiently remove the heat generated by the FT reaction. Vigorous movements and collisions of particles in the slurry reactors result in fine catalyst particles that may contaminate the product and limit the mass and heat transfer due to increased viscosity [178,179]. Structural promoters also play an important role in attrition resistance of the active phase of the metal within the catalyst. Silica has been widely used as a binder for many catalysts systems prepared using spray drying methods. Silica is usually used with K and Cu because it hinders the reducibility and carburization of the catalyst. [180–182]. Bukur *et al*. [183] prepared two catalysts with nominal compositions: 100Fe/3Cu/5K/16SiO_2 and 100Fe/5Cu/6 K/24SiO_2 and tested them for attrition. Compared with the silica free catalysts, the two catalysts showed high attrition resistance. It is believed that silica (optimum content: 10–12 wt.-%) provides strong interlocking forces between primary particles [181,184,185].

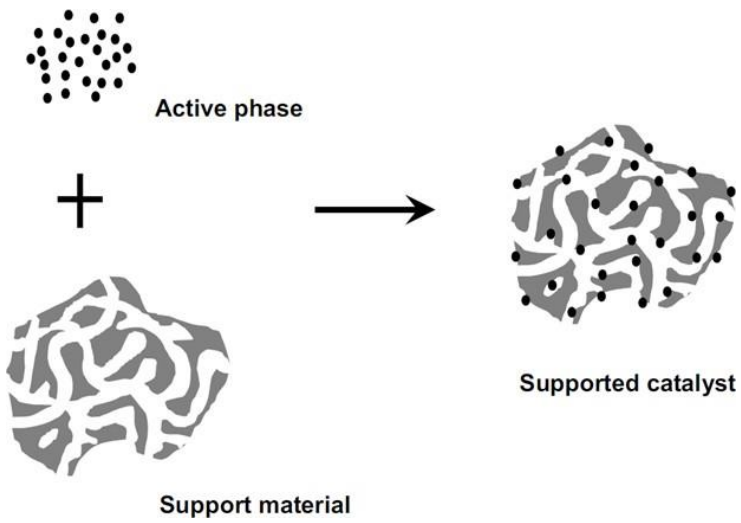

Figure 2-14: Schematic representation of a support and catalyst particles.

2.1.7.2 Promoters in the cobalt-based Fischer-Tropsch catalysts

The performance of cobalt based catalysts in the Fischer-Tropsch synthesis can be improved by the addition of promoters such as rare metal oxides like La, Zr and Ce, and noble metals (Pt, Ru, Pd, Ir, Au, Ag, etc.) [80,186–189]. Noble metals are usually used in very low concentrations (0.1–0.5 wt.-%), not only because of their high cost but also to avoid site blockage. Zhang *et al*. [80] investigated the effects of platinum and ruthenium on carbon nanotube supported cobalt catalysts. They found that the addition of small amounts of ruthenium and platinum (0.2 wt.-% each) lowered the reduction temperature and improved the degree of reduction, but there was no significant improvement of the catalytic activity. Ruthenium is regarded as both an electronic and structural promoter [190,191]. As a reduction promoter, ruthenium is reported to increase the number of active sites on the Co surface by facilitating hydrogen spill-over from ruthenium to cobalt [188,190,192]. Many studies showed that the reducibility of Co promoted by noble metals proceeds either via H_2 dissociation (H_2 spill-over mechanism) on the promoter surface and then spilled to the cobalt oxide nanoparticles [193–197] or a direct interaction between the Co and the noble metal to produce a facile Co reduction [198,199].

The crystallite size of the Co_3O_4 nanoparticles was also not affected by the promoters, the effect on size seemed to come from the interaction between cobalt and the carbon nanotube support during the synthesis. The results of Chu *et al*. [198] further confirmed that the promotion with small amounts of Pt on cobalt-

alumina catalyst had no effect on the crystallite size. The size was only influenced by the support pore diameter. The promoting effect of rare earth metals on the selectivity towards longer chain hydrocarbons using cobalt catalyst was reported by several authors [200–203].

Haddad *et al*. [204] studied the promotional effect of La_2O_3 on Co/SiO_2. The addition of La_2O_3 reduced the reduction temperature which was attributed to the fact that La_2O_3 moderates the strong synergistic interactions between Co and SiO_2. The observed increase in activity was linked to the increase in Co active sites created during reduction. The results obtained from steady-state isotopic transient kinetic analysis (SSITKA) showed that the residence times of CO on Co for both unpromoted and promoted catalyst were similar. Thus, it can be concluded that La_2O_3 did not have any effect on the nature of the active sites, just their concentration.

Alkali metals generally used for iron catalysts were also investigated for cobalt catalysts. Alkali metals salts (Li, Na, K, Rb, and Cs) generally have a negative effect on CO conversion, increase olefinicity of the product, promote the WGS reaction and increase the C_{5+} selectivity when employed for Co based catalysts. The decrease in activity is thought to be due to the strong adsorption of reactants on the catalyst surface caused by the promoters. CO conversion decreased in the following order: un-promoted>Rb>Li>Na>K≈Cs, while olefin to paraffin ratio increased in the following order: un-promoted<Li<Na<K [205–207].

2.1.8 Potassium mobility

Potassium is commonly utilized as a promoter of heterogeneous catalysts in a variety of reactions, including the FT synthesis, ammonia synthesis and the water gas shift reaction among others [74,208,209]. Because potassium atoms have a large radius, they do not dissolve in the iron crystal lattice and remain on the catalyst's surface. As a result, potassium surface diffusion is a critical mechanism, especially important when it comes to catalyst activation. Auger electron spectroscopy was used to investigate potassium migration on model iron/alumina catalyst surfaces by Connell and Dumesic [210]. In a 3 wt.-% ammonium tartrate solution, polished Al_2O_3 films were generated anodically on high purity aluminum foils. The samples were calcined in oxygen for 24 hours at 600 °C to transform the amorphous alumina layer to γ-Al_2O_3. Finally, using a vacuum metal evaporator, a 20 nm iron overlayer was formed on one half of the surface. Potassium was deposited by atomizing an aqueous solution containing 1.1 wt.-% KOH both on the iron overlayer as well as the bare alumina. The sample was then treated in H_2O/H_2, H_2, H_2O/O_2 and O_2 at

400 °C for 72 hrs. The authors confirmed potassium mobility at 400 °C on the iron and the alumina surfaces. This migration appears to be more extensive in hydrogen than in oxygen, and water has been found to boost potassium mobility in both gases [211]. The method of transport is thought to be dependent on potassium dispersion and crystallite size, with bigger sizes being more prone to gas phase transfer.

According to the authors, the poor mobility of potassium in O_2 indicates higher surface bonding under oxidizing circumstances. Iron, potassium, and aluminum are all present as oxides during the O_2 treatment. Activation reduces the strength of potassium attaching to the surface of the metallic iron. A strong tendency of potassium to segregate on the surface of the catalyst was reported by several authors [111,212,213]. Emmet and Brunauer [214] also indicated that at higher loadings, K_2O promoter covers a large fraction of the catalyst surface blocking the active sites.

2.2 Catalyst Deactivation

Deactivation of heterogeneous catalysts is a ubiquitous problem that causes loss of catalytic activity and/or selectivity with time. It can be very costly commercially, as the deactivated catalyst must be replaced or reactivated resulting in a process shutdown. Deactivation times vary. For instance, the lifetime of a cracking catalysts is a few seconds while iron catalysts in the ammonia synthesis are operated from 5 up to 10 years. Mechanisms of deactivation described in literature can be divided into six categories [30]:

- thermal degradation
- poisoning (mainly sulfur)
- fouling (carbon deposition)
- attrition/crushing
- vapor-solid and/or solid-solid reactions
- vapor compound formation accompanied by transport

2.2.1 Thermal degradation

Thermal degradation is more commonly known as sintering. It typically results from loss of catalytic surface area through structural modification of the catalyst. It is a thermally assisted process that takes place at high temperatures and is physical in nature [215]. Sintering can manifest itself as a of loss of catalytic surface area due to crystallite growth of the active phase or as collapse of the pore structure of the carrier (support) [216]. Sintering can occur during the synthesis stage (calcination), activation (reduction) and during the reaction and regeneration stages [217].

Figure 2-15 schematically shows the sintering of highly dispersed crystallites. The growth of crystallites through sintering is the most occurring form of thermal degradation in heterogeneous catalysis. There are two types of sintering proposed: particle migration and coalescence (PMC) [218] and Ostwald ripening (OR) [219]. In PMC, particles move on the support surface in a Brownian-like motion (random, uncontrolled movement of particles as they constantly collide with other molecules) followed by a subsequent coalescence leading to crystallite growth. In OR, mobility of particles is largely driven by the difference in free energy and local adatoms concentrations on the support surface. It has been suggested that particle migration occurs with smaller particles and the operative mechanism changes to OR when the particles become large and effectively immobile [220,221].

Sintering is dependent on a number of variables such as temperature, gas atmosphere, support surface area, promoters and metal dispersion. Among all these variables, temperature has the highest impact as sintering rates increase exponentially with temperature. Sintering was observed to occur at temperatures associated with the melting point (T_{mp}) of the metals. These temperatures are defined as the Hüttig or the Tamman temperatures. As the temperature increases and the Hüttig temperature is reached, atoms at the defect sites or kinks become mobile. At the Tamman temperature strongly bound atoms in the bulk become mobile. Consequently, metal or metal oxide sintering is more prevalent at temperatures above Hüttig and near the Tamman temperature. As the temperature increases and reaches melting point, the atoms become highly mobile and liquid phase behavior is observed [217,222] and sintering of crystallites becomes possible through surface diffusion and crystallite growth. The surface diffusion will result in the formation of two-dimensional clusters and subsequently 3D structures [217]. At even higher temperatures, crystallites/particles can travel and coalesce with other crystallites through surface migration. The presence of water vapor is known to enhance sintering processes. [216]. Table 2-2 shows the Hüttig, Tamman and melting temperatures of some metals and support structures. Semi-empirical relations for Hüttig and

Tamman temperatures are provided in equations 2.7 and 2.8.

$$T_{Hüttig} = 0.3T_{melting} \quad 2.7$$

$$T_{Tamman} = 0.5T_{melting} \quad 2.8$$

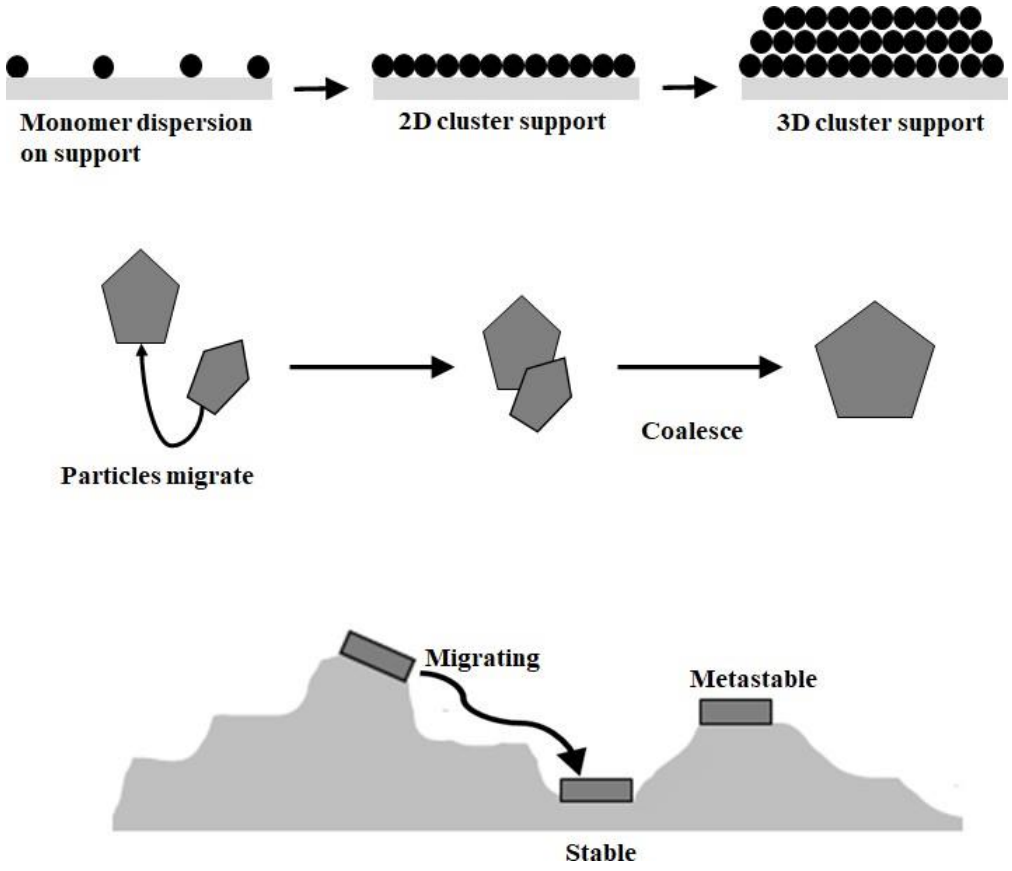

Figure 2-15: Schematic of various pathways for the formation and growth of crystallites (from [217]).

Bartholomew *et al*. [223] reviewed the effects of sintering on catalytic activity with respect to the crystallite size. While small crystallites sizes can be advantageous to activity of the catalyst system by providing a higher mass specific surface area, they are often associated with higher mobility. This can be explained with a decreasing melting temperature of crystallites in the nanometer regime compared to bulk characteristics [217]. Generally, it has been reported that the surface area decreases due to sintering with increasing temperature [224].

Table 2-2: Melting, Huettig and Tamman Temperatures for common metal and metal oxides [225,226].

Compound	$T_{melting}$ K	$T_{Hüttig}$ K	T_{Tamman} K
Fe	1808	542	904
Co	1753	526	877
$LaAlO_3$	2031–2049	609–615	1015–1024
Al_2O_3	2318	695	1159
SiO_2	1986	596	993
ZrO_2	2988	896	1494
TiO_2	2113	634	1057

2.2.2 Poisoning

Poisoning refers to the strong chemisorption of reactants, products and impurities on the active sites of a catalyst causing deactivation [215,217,227,228]. Apart from poisons blocking the catalytically active sites, reactants and products may also adsorb onto the catalyst surface inhibiting the reaction through the process termed competitive adsorption. Competitive adsorption differs from poisoning in that it is a relatively weak and reversible interaction with the catalytically active surface, while in poisoning the adsorbents have a strong and permanent interaction with the surface. Furthermore, poisoning has a possibility of reconstructing the active surface leading to a permanent change in catalytic activity/selectivity. There are two different types of poisoning, namely selective and non-selective poisoning [217] (see Figure 2-16). Selective poisoning describes the adsorption of the poison solely or predominantly on the active phase or even active site. Non-selective poisons adsorb on all available surfaces of the catalyst equally. For non-

selective poisons, the loss of catalytic activity and or selectivity is directly proportional to the concentration of the poison in the feed stream [159,217,222].

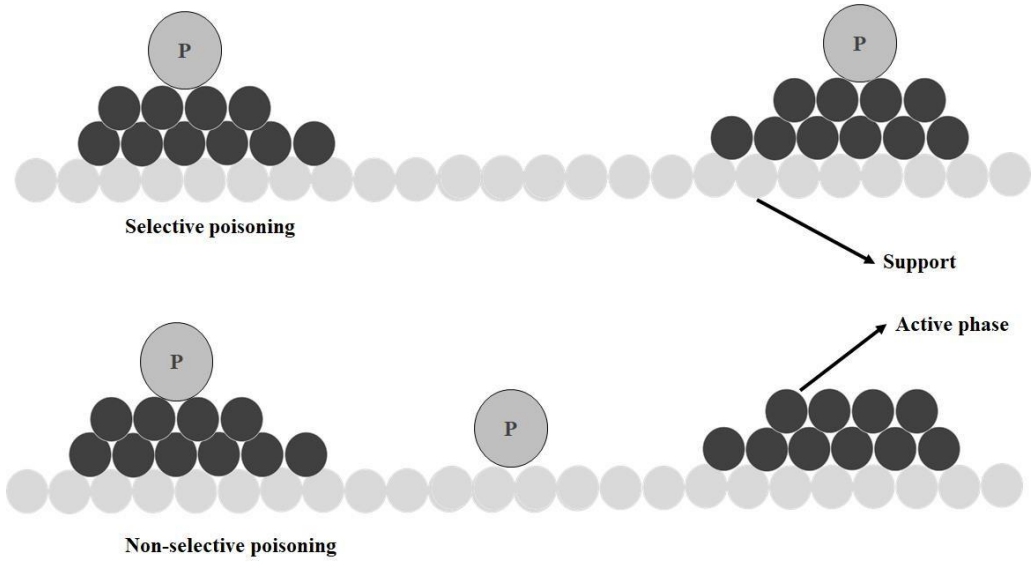

Figure 2-16: Schematic representation of selective and non-selective poisoning on a metal surface; P: poison (from [217,229]).

Commonly known poisons listed in Table 2-3 are divided into four groups according to the origin and the modes of interaction with the catalytically active surface. The most common poisons known in FT are H_2S, NH_3, metal carbonyls, carbonyl sulfide (COS) and arsenic [230]. The main source of the sulfur containing compounds is coal from which the synthesis gas is derived [159]. It is reported that a part per billion concentration of sulfur in the feed gas causes loss of activity and shortens the life of the catalyst. It is therefore crucial to remove sulfur from the synthesis gas prior to the FT reaction [74,159,231]. Anderson *et al*. [164] investigated the effects of sulfur compounds on fused iron catalyst in the FT synthesis. The results showed that the severity of poisoning increased in the following order: $COS < C_2H_5SH < H_2S < SO_2$. There are a number of industrial processes in which catalysts are intentionally poisoned in order to improve their selectivity. In the case of the FT synthesis, Wu *et al*. [232] demonstrated that iron catalysts containing small amounts of sulfur show an exceptionally high olefin.

Table 2-3: Common catalyst poisons classified according to chemical structure [216].

Chemical Type	Examples	Type of interaction with metals
Groups VA and VIA	N, P, As, Sb, O, S, Se, Te	Through s- and p-orbitals; shielded structures are less toxic[a]
Group VIIA	F, Cl, Br, I	Through s- and p-orbitals; formation of volatile bases
Toxic heavy metals and ions	As, Pb, Hg, Bi, Sn, Zn, Cd, Cu, Fe	Occupy d-orbitals; may form alloys
Molecules which adsorb with multiple bonds	CO, NO, HCN, benzene, acetylene, other unsaturated hydrocarbons	Chemisorption through multiple bonds and back bonding

[a] decreasing toxicity for poisoning of a given metal by different sulfur species is H_2S, SO_2, SO_4^{2-}, i.e., in the order of increased shielding by oxygen.

2.2.3 Fouling

Fouling refers to the deposition of carbonaceous or any foreign material on the catalyst surface leading to deactivation by loss of surface area due to blocking of active sites [216]. Even though the formation of carbonaceous deposits proceeds via a chemical reaction, fouling is physical or mechanical in nature. Apart from the carbonaceous deposits, blocking of active sites may be due to dust or other residues introduced with reactants or found/formed in the reactor. Coking is the most widely reported form of fouling, also prevalent in the potassium promoted iron-based FT synthesis. It originates from dissociative adsorption of carbon monoxide on the catalyst surface [33,233,234]. Agrawa *et al*. [235] investigated the effect of deactivation on Al_2O_3-supported Ni, Co, Fe, and Ru catalysts. The deactivation was worst on the industrially employed active phases of Co and Fe, decreasing the activity by around 100-fold without being regenerable in H_2. Graphitic carbon and bulk formation of carbide was observed using atomic emission spectroscopy [98,99]. Carbon containing species can completely encapsulate a metal/active phase particle or block the pores of the catalyst structure introducing severe mass transfer limitations. Deposits may also

be due to the formation of filamentous carbon which is known to plug catalyst pores and, if allowed, to accumulate in the pores even collapsing them [236–239].

2.2.4 Attrition

Attrition refers to the mechanical reduction of catalyst particle size, or breakup of catalyst pellets producing fines [216]. This challenge is specifically prevalent in catalyst systems where moving/ fluidized bed or slurry reactors are used [240]. Small spherical particles are reported to be more resistant to attrition compared to other morphologies. In fixed bed reactors, expansion and swelling of catalysts due to thermal expansion, fouling or phase changes, as is the case in the iron-based FT synthesis, can lead to attrition [216].

Slurry bubble column reactors are used extensively in the Fischer-Tropsch synthesis due to their excellent heat removal capabilities, which solves reaction control problems caused by the highly exothermic CO hydrogenation. However, attrition of the catalyst particles can cause filter plugging problems and lower product quality because of catalyst fines being carried out with the product stream [241]. Spray drying has been implemented in preparation of FT catalysts to improve their strength [184]. The strength of the catalyst can also be enhanced by using stronger supports (γ-Al_2O_3) or binders, changing of the catalyst loading on the support and modifying the catalyst with promoters [242].

2.2.5 Vapor-solid and solid-solid reactions

In vapor-solid and solid-solid reactions, the active phase reacts either with gaseous species or solid components (such as the catalyst's support) forming less active and/or selective species. In the FT synthesis for example, the active iron species have been reported to undergo an oxidation to FT inactive species if the concentration of product water is high, i.e. at high CO conversion [26,51,74,97,125,243,244].

For cobalt based FT catalysts, the oxidation of bulk and nanocrystalline cobalt to CoO or Co_3O_4 was evaluated using theoretical thermodynamic [245] and experimental studies [53,246–248]. These studies proved that metallic fcc cobalt crystallites can be oxidized in the presence of water at 220 °C [245]. Moreover, it was proved that with increasing water partial pressure, the probability that metallic cobalt will oxidize increases. The reoxidation of cobalt occurs readily at smaller crystallites sizes of about 4 nm at FT conditions of 170–240 °C, 20 bar, H_2:CO = 2, X_{CO+H2} = 50–70% [249,250].

Strong metal support interaction formed by solid-solid reactions also play an important role in catalyst deactivation. This type of phenomenon is prevalent in cobalt nanoparticles supported on alumina [249,251]. For the catalyst to lose activity, the cobalt atoms/ions get embedded into the support matrix (Al_2O_3) forming cobalt aluminates in the presence of water [195,252–254], although they are not kinetically favorable under FT synthesis conditions [233].

2.3 Perovskites

Perovskites are compounds having a crystal structure related to the mineral calcium titanium oxide $CaTiO_3$, the first-discovered perovskite crystal. The mineral perovskite was named after the Russian statesman and mineralogist Count von Perovski after being discovered by German scientist Gustav Rose in 1839 in the Ural Mountains. Ideal perovskite compounds have the chemical formula ABX_3, where A and B represent cations and X is an anion (see Figure 2-17).

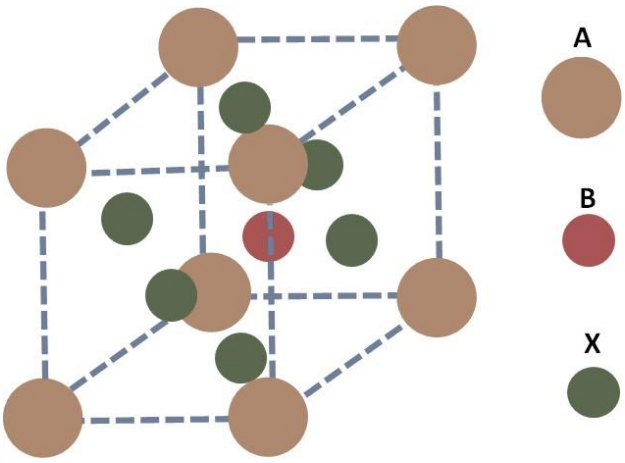

Figure 2-17: Ideal perovskite structure with A and B cations and X anion.

The inevitable rise of perovskites materials has been fueled by their robust chemical and structural flexibility together with their physical and chemical stability [255]. Many compositions are possible from combinations of cations on the two lattice sites. Researchers have been able to take advantage of this flexibility to design a variety of materials for use in catalytical, optical and electrical applications. They can

be modified by partial substitution of A and/or B cations forming an isostructural $A_{1-x}A'_xB_{1-y}B'_yO_3$ [256]. A downside is their generally low surface area. Researchers have explored many synthesis methods, including solid-state reaction, coprecipitation, freeze-drying, flame-hydrolysis, sol-gel processes, and nano-casting [257] to increase surface area. As a result Brunauer-Emmett-Teller (BET) surface areas of 100 to 270 m^2/g [257–259] have now been reported.

The traditional view of the perovskite lattice is that it consists of small B cations within oxygen octahedra with a coordination number of 6 and larger A cations which are twelve-fold coordinated by oxygen. The structure of an ideal perovskite is cubic, where the A cations are located at the corners of the cube, and the B cation in the center with oxygen ions in the face-centered positions. The radius of the A cation ranges between 1.0–1.9 Å whereas the radius of cation B is between 0.2–0.5 Å. The anion may be oxygen, sulfur, chlorine or fluorine [260].

The stability of the perovskite structure can be predicted using the Goldschmidt tolerance factor based on the formula ABX_3, and the ionic radii, R_j. The tolerance factor, t, is given by:

$$R_A + R_X = t\sqrt{2}(R_B + R_X) \qquad 2.9$$

The ionic radius of the cations A, B and an anion X are R_A, R_B and R_X respectively [261]. If the tolerance factor is exactly equal to unity, the packing of the perovskite structure is said to be ideal. If it is greater than unity, then there will be a large void for the B anion, causing distortions from the cubic structure. Depending on the extend of the distortion, the resulting compound can be a perovskite or non-perovskite structure [262–264].

2.3.1 Structural properties of $LaAlO_3$

Lanthanum aluminate, $LaAlO_3$, gained a lot of interest because of its variety of physical and mechanical properties and perfect perovskite-type structure. The structure of the bulk $LaAlO_3$ is rhombohedral at room temperature with the space-group *R-3m*. Luo and Wang [265] have confirmed that the rhombohedral allotrope is energetically most stable using first-principles linearized augmented plane wave calculations. It is reported that $LaAlO_3$ undergoes a phase change from rhombohedral (*R-3m)* to cubic (*PM-3m)* phase at

elevated temperatures (T > 435 °C) [266] or with a volume change of 1% due to strain caused by applied hydrostatic pressure of 154000 bar [265], agreeing closely with the experimentally determined value of 140000 bar [267] (see Figure 2-18). The transition pressure from one phase to another and the relationship between pressure and volume are shown in Figure 2-18 C. When cooled, the phase transformation is reversed [266,268]. Geller and Bala [268] investigated the phase changes between temperatures ranging from 125 to 650 °C. They observed a gradual change from rhombohedral to a cubic structure with increasing temperature up to 350 °C. No further phase changes were detected at higher temperatures.

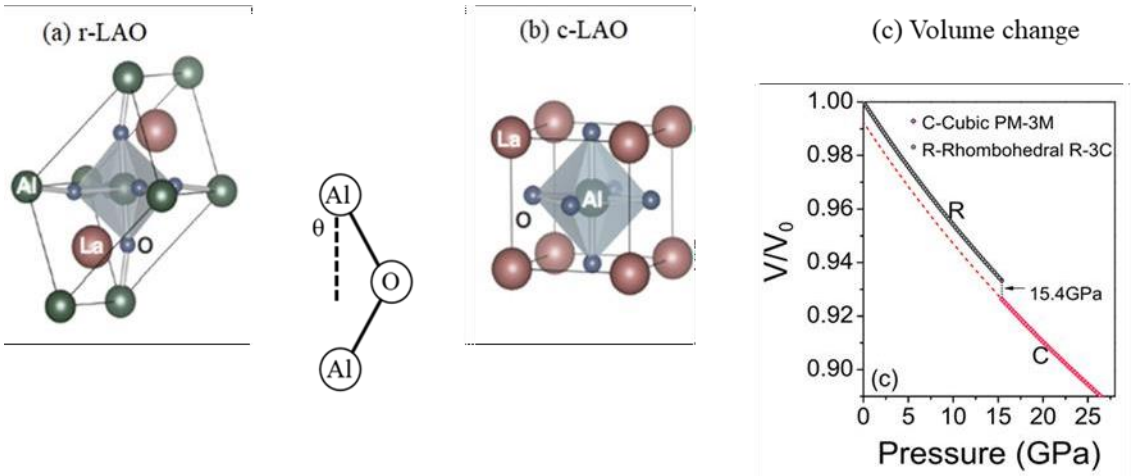

Figure 2-18: The crystal structure of rhombohedral $LaAlO_3$ (a) and the cubic structure (b) (from [260]). (c) Relationship between pressure and volume for the two phases of $LaAlO_3$ (from [265]).

2.3.2 Perovskites as catalysts in the Fischer-Tropsch synthesis

La-based perovskites have attracted significant research interest in recent years as cheap and efficient catalyst in various applications [269–273]. In the FT synthesis a number of studies and patents report on the use of mainly La based perovskites as component of catalyst formulations [25,270,274–291].

2.3.2.1 Perovskites as catalyst precursor

Kiennemann *et al*. [25,274–279] published a series of studies focusing on $La(Co,Fe)O_3$ perovskites as catalyst precursors for the FT synthesis. A series of perovskites with varying Co and Fe concentrations from pure Co to pure Fe in the B site were synthesized via the decomposition of the respective metal propionates

through boiling and evaporation followed by calcination in air at 600 to 1000 °C [274]. According to SEM EDXS the targeted concentrations were achieved. Expectedly, the BET surface area was low ranging from 3.9 to 8.8 m^2g^{-1} with a near linear decrease with decreasing Fe content. From literature, it is known that $LaFeO_3$ crystallizes in an orthorhombic space group, while $LaCoO_3$ crystallizes with a rhombohedral space group. The difference between these two is limited to a distortion of the B site in the case of Fe. XRD analysis confirmed a transition from orthorhombic to rhombohedral when the Co occupancy of the B site increased over 50% (see Figure 2-19).

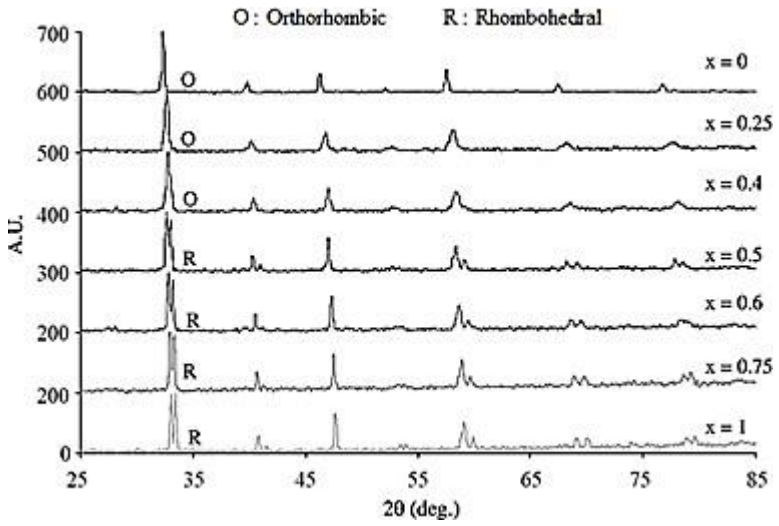

Figure 2-19: XRD diffraction patterns of the as prepared samples. X is the atom fraction of Co in the B site (from [274]).

TPR analysis of the samples evidences an increased low temperature reduction event (300–500 °C) with increasing Co content and a high temperature reduction above 570 °C. In the absence of Co, reduction is only recorded at temperatures exceeding 750 °C. The near linear relationship between H_2 consumption and Co content suggests that only Co was reduced. Magnetic studies confirm the evolution of metallic cobalt at the low temperature H_2 consumption range in the case of the orthorhombic perovskite (Co<50% of B site) while for the rhombohedral samples, the observed low temperature reduction is apparently only a reduction from Co^{+III} to Co^{+II}. Perovskites calcined at 600 °C showed higher degrees of exsolution and in the sample with the lowest Co content and lowest calcination temperature some fraction of the Fe also exsoluted forming a CoFe alloy. No analysis of the phase stability of the perovskite during or after the TPR treatment

is provided. CO dissociation activity increases with increasing metallic Co content, with the alloy showing lower activity compared to pure Co.

Under FTS conditions, at relatively low conversion (<10%), a very primary product slate, i.e. high olefin content, was observed. Interesting is also a high WGS reaction (S_{CO2} from 12.5 to 23.7%) and oxygenate selectivity (S_{oxy} from 17.3 to 7.9%, dominated by ethanol) which is related to the level of conversion (X_{CO} from 2.4 to 6.1% at 240 to 260 °C). Whether the presence of oxidized iron species in the perovskite played a role in this is not discussed in detail. Again, no phase information was provided after reduction and reaction, only that no metallic Co phase was detected in XRD which was attributed to a small crystallite size rather than low levels of exsolution (2 to 8.6 wt.-% Co^0).

In an attempt to increase the amount of exsoluted metal, a La deficiency was introduced in the synthesis. A reduction of La content (up to 40%) resulted in a cubic crystallographic structure of the perovskite and maghemite (γ-Fe_2O_3, only visible in XRD at the lowest concentrations of La) [276,280]. It was proposed that the iron oxide forms a core on which perovskite crystallites grow epitaxially forcing the cubic structure. During reduction, the iron oxide cores reduced in part and formed an alloy with exsoluted Co. Another part replaces the cation vacancy left by the exsoluted Co resulting in a cubic Fe enriched perovskite. Compared with the non-La deficient catalysts, these systems exhibited a higher activity in the FTS and at iso conversion (but lower reaction temperature) a lower CO_2 selectivity (still over 19%), a coupled higher oxygenate selectivity (maximum of 12%) and a higher olefin to paraffin ratio in the short chain product. If the reported effects are solely based on the new catalyst composition or at least in part affected by the range in reaction temperature (280 to 230 °C) chosen to achieve iso-conversion is unclear.

A very similar set of catalysts, without La deficiency and with B site Co contents of ≤50% were prepared by Escalona *et al*. [270] using the citrate method (calcination was conducted at 700 °C). The resulting BET surface areas were relatively constant at 12 to 15 m^2g^{-1}. In sharp contrast to the studies by the group of Kiennemann *et al*. [274] the researchers concluded from TPR analysis that only the $LaCoO_3$ sample exhibits exsolution of metallic Co. In all other samples, only a partial reduction was reported. It was however hypothesized that under reaction conditions (FTS with biogas feed) metallic Co is formed, although XRD after reduction did not provide any evidence of a segregated Co^0 phase. FTIR was used to identify the presence of rhombohedral species at Co concentrations as low as 0.3. The presence of this crystal structure was also associated with the observed very low conversion levels. For the purely orthorhombic perovskites (Co = 0, 0.1 and 0.2) CO conversion increased with Co content.

The approach to improve exsolution by tuning the allotrope of $LaCoO_3$ was further studied by displacing up to 40% of La with Sr [281]. The perovskite precursors were prepared via co-precipitation from the

nitrates with ammonia followed by drying and calcination at 800 °C. The resulting catalyst precursors all had a low surface area below 6 m^2g^{-1}. After calcination all samples showed the presence of small amounts of Co_3O_4. It has to be noted that the concentration of the cobalt oxide was not calculated but only assumed based on the low intensity of the XRD reflexes not accounting for amorphous or very small particles. Up to a Sr concentration in the A site of 10%, the perovskite structure was rhombohedral, previously reported to be stable and suppressing exsolution. At higher concentrations, the allotrope changed gradually to a cubic space group. After reduction in a diluted H_2 stream at 450 °C the rhombohedral structures remained intact with some peak broadening which might be an indication of exsolution and structural collapse. At higher Sr contents, the cubic phase was decomposed yielding La_2O_3, $LaSrO_x$ and Co^0 (after FT reaction even $SrCO_3$). This decomposition was accompanied with sintering as evidenced by SEM.

The catalysts were tested at high reaction temperatures of 300 to 350 °C and 30 bar. While the selectivity remained relatively stable, at a high CO_2 formation rate, the CO conversion peaked at a Sr content of 10% which was rationalized with the potential presence of small Co^0 entities after reduction compared to relatively large (unquantified) metallic cobalt crystallites after decomposition of the perovskites with higher Sr content. In an attempt to modify the selectivity of the best performing catalyst, Co on the B site was replaced by Ni at 10, 50 and 100% [282]. After the synthesis, traces of Co_3O_4, $NiCoO_x$ and NiO were detected in the XRD patterns for a theoretical Ni occupancy of the B-site of 10, 50 and 100% respectively (see Figure 2-20). The authors concluded that Ni can only partially be incorporated into the perovskite structure. After reduction at 450 °C only the perovskite samples with 100% Co or Ni retained their structure albeit Ni^0 was detected, and the reflexes of $LaCoO_3$ suggest a partial collapse of the structure. The samples containing mixtures or Co and Ni collapsed fully yielding a Co-Ni alloy, La_2O_3 and $LaSrO_x$. After the FTS (T = 275 °C, H_2:CO = 2, P = 30 bar) no perovskite structure remained with $LaCO_3OH$ as only phase besides the metallic Co, Ni and the alloy. The highest CO conversion was recorded for the $Co_{0.9}Ni_{0.1}$ catalyst. Regarding selectivity the authors only focused on the alcohol fraction and tried to increase specifically the fraction of C_{2+} alcohols. It is therefore not possible to conclude on the overall product spectrum. The authors reported optimum performance at a reaction temperature of 320 °C with over 70% of the alcohol fraction C_{2+}. Based on the provided space time yield (STY), gas hourly space velocity (GHSV) and X_{CO}, a carbon-based selectivity to alcohols of approximately 62% could be extracted.

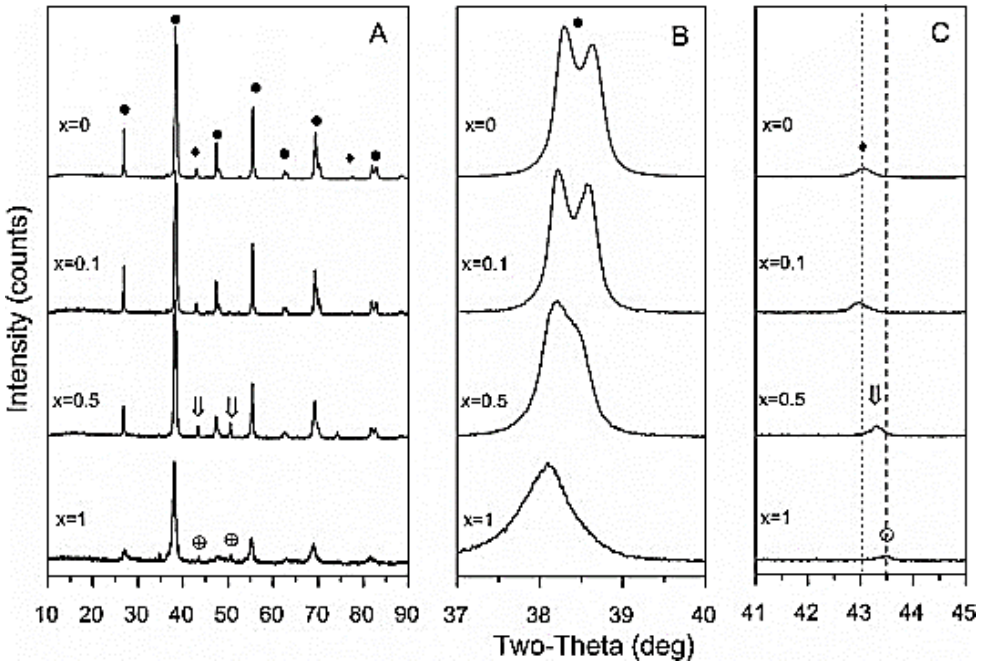

Figure 2-20: XRD diffraction patterns of $La_{0.9}Sr_{0.1}Co_{1-x}Ni_xO_3$ perovskite catalysts (A) complete pattern, (B) zoom in on the peak range and (C) zoom in on the Co-Ni oxide peak range. Phases: (•) perovskite (including $La_{0.9}Sr_{0.1}CoO_3$ and $La_{0.9}Sr_{0.1}NiO_3$), (♦) Co_3O_4, (⊕) NiO and (⇓) Co-Ni oxide ([282]).

In an attempt to further increase the selectivity to higher alcohols, 0.1 atom% of Co was replaced with the more traditional alcohol synthesis catalyst metal Cu [283]. In addition, the perovskite was impregnated by incipient wetness impregnation (IWI) with K or Na carbonate solution (targeted concentration of alkali 0.5 wt.-%). All resulting surface areas were below 3.5 m^2g^{-1}. Addition of the alkali did not affect the rhombohedral structure of the perovskite displaying only minor amounts of Co_3O_4. However, the presence of K/Na increases the observed reduction temperature in TPR experiments and decreases the overall H_2 consumption, i.e. the extend of reduction. After reduction at 450 °C the perovskite phase was decomposed and only La_2O_3, $LaSrO_x$ for the unpromoted sample, La_2O_3 for the Na promoted and $LaSrO_x$ for the K promoted sample remained besides a potential trimetallic alloy. From the intensity of the alloy reflexes the authors proposed an increased dispersion with alkali promotion. After CO hydrogenation at 325 °C $LaCO_3OH$ is identified as reported in previous studies. In addition, $La_2O_2CO_3$ is found in the K promoted sample as dominating phase. A transition from the carbonate to the carbonate hydrate is proposed via a reaction with CO_2 and steam which appeared to be suppressed in the presence of K. The trimetallic alloy, partially converted to CoC_2. This formation seems to be enhanced in the presence of the alkali, as is widely reported for iron based FT catalysts as well [284].

Under high temperature FT conditions (T = 340 °C, H_2:CO = 2, P = 30 bar), alkali promoted catalysts slightly decreased in CO conversion but the unpromoted catalyst suffered from severe deactivation. The methane selectivity was unchanged with an increased CO_2 formation. At the highest reaction temperature, the deposition of C was identified as deactivating mechanism, which is suppressed by the presence of K, to a much lesser extend by Na. It was hypothesized that K stirs the perovskite decomposition towards $La_2O_2CO_3$ which can in turn react with C to lanthanum oxide and CO. The carbonate was regenerated by the subsequent reaction of the oxide with CO_2. At reaction temperatures above 300 °C, the alcohol fraction produced over the K promoted catalyst contained approximately 80% $C_{2+}OH$. Again, little information is provided on the overall C-selectivity of alcohols but based on the selectivity of CH4 and CO2, it must be below 60 and 30% at conversions between 15 and 40% at reaction temperatures of 310 and 340 °C respectively.

Liu *et al*. [285–287] also targeted the synthesis of higher alcohols starting from $La(Co,Cu)O_3$ supported on mesoporous SiO_2 and ZrO_2. By using the perovskite as pure catalyst precursor to yield a CoCu alloy and depositing it on a high surface area material, the commonly encountered challenge of low surface area was overcome. Nitrate salt solutions of the metals La, Co and Cu together with citrate acid and glycol were impregnated onto the support (IWI), dried and calcined at 600 °C. The perovskite had a targeted composition of $LaCo_{0.7}Cu_{0.3}O_3$ and no 'free' Co or Cu species were observed. The perovskite was formed in 20 nm crystallites outside the pores of the SiO_2. To force exsolution, the samples were exposed to a hydrogen treatment at 600 °C yielding monometallic phases of Cu and Co as well as La_2O_3. HAADF-STEM-EDS confirmed that a Cu shell around a Co core were formed when the sample was heated in inert before switching to H_2. When already heated in hydrogen, a Cu core with a Co shell is formed due to the higher reducibility of Cu. The Co shell catalyst outperformed the Cu shell catalyst in the HAS, unfortunately no catalyst characterization of the spent materials is provided. On the ZrO_2 support, no core shell structures but a uniform mixture of Co and Cu is reported. Overall, Cu based systems from perovskites are described by various other research groups as precursor for a bimetallic catalyst for the MeOH or HA synthesis [288–290,292].

Looking at perovskites in the Fischer-Tropsch synthesis, Goldwasser *et al*. [291] synthesized $La_{1-x}K_xMn_yFe_{1-y}O_3$ (x=0, 0.1 and 0.2 and y=0.1 and 0.2) to produce short chained alkenes. Perovskites were prepared via co-precipitation and yielded BET surface areas of 3–13 m^2g^{-1} (one sample with 0.2 Mn and 0 K yielded 37 m^2g^{-1} no explanation is provided). The concentration of K and Mn in the calcined samples was always lower than expected which they attributed, for K, to the volatility of K_2O. Shifts in the IR bands were used as indicator that doping of the B site was successful. Additional La oxide and hydroxide were

Table 2-4: Mössbauer hyperfine parameters. (P): perovskite; (AS): as-synthesized; (Red): reduced; (R): reacted; (CR): carburated-reacted [291].

Solid	DI (mm s−1)	QS (mm s−1)	Hpf (kG)	Phase	Percentage
LaFe (AS)	0.36	−0.08	519	Fe (P)	100
LaFe (R)	0.36	−0.09	526	Fe (P)	89
	0.25	0.09	213	χ-Fe_5C_2	11
LaKFe 1 (Red)	−0.36	−0.07	522	Fe (P)	74
	−0.01	0	329	α-Fe	26
LaKFe 1 (CR)	0.36	0.09	529	Fe (P)	74
	0.25	0.09	213	χ-Fe_5C_2	26
LaKFe 2 (Red)	0.36	−0.07	525	Fe (P)	59
	−0.01	0	330	α-Fe	49
LaKMnFe (R)	0.34	−0.05	503	Fe (P)	100
LaKMnFe (Red)	0.38	−0.10	511	Fe (P)	39
	0.32	−0.13	483	Fe (P)	25
	−0.01	0	324	α-Fe	36
LaKMnFe (CR)	0.25	0.1	213	χ-Fe_5C_2	37
	0.38	0.1	520	Fe (P)	34
	0.32	0.13	490	Fe_3O_4	23
	0.4	0.2	460	Fe_3O_4	6

observed at increased levels of doping. The cell volume of the perovskite decreased although the doping metals have larger diameters. This was attributed to a Mn redox couple and/or oxygen vacancies. No

additional proof was provided that the promoting species, K and Mn, are confined to the perovskite structure and not also present as free species on the surface of the materials. All samples were subjected to a H_2 reduction at 450 °C to exsolute the iron followed by a carburization in pure CO at 350 °C. In the absence of a dopant, only 11% of the Fe exsolutes during reduction/carburization/reaction and was identified as Hägg carbide. In the presence of Mn, no Fe was reduced. In the presence of K, 26% of the Fe phase was reduced and subsequently carburized. When both Mn and K are present, 36% of Fe was reduced and subsequently carburized (see Table 2-4). It appears that during reaction even more Fe exsolutes and forms Fe_3O_4, probably in an equilibrium with the carbide phase. The location of K and Mn after reduction was not studied. In the FTS, K enhances CO conversion significantly, reduces the WGS activity and shifts the selectivity in favor of longer chains and away from methane. In the presence of both K and Mn, the activity is still enhanced, but to a lower extent. However, the WGS was suppressed significantly and the selectivity to short alkenes was hugely enhanced.

Amongst a variety of iron oxide matrices, the team of Landau investigated $LaFeO_3$ prepared via combustion synthesis as potential catalyst for the direct hydrogenation of CO_2 to fuels and chemicals [293]. The orthorhombic structure had to be activated at 900 °C in H_2 to exsolute some iron before carburization in a diluted 1:1 H_2:CO stream. After this treatment, a mixture of wüstite, lanthanum oxide and iron carbide were reported with some residual perovskite. Unsurprisingly after these pre-treatments, the catalyst hardly exhibits any chain growth activity and only limited reverse WGS activity and was not further considered. The perovskite was prepared from the nitrates of the precursors via the citrate method with a calcination temperature between 700 and 900 °C. K was subsequently impregnated.

Most work in the field is concentrating on developing perovskite materials as catalyst precursors and facilitating exsolution of Co, Ni and/or Fe through doping which in turn influences the crystal structure rendering the material less stable against reduction. No attempts were found in the field of Fischer-Tropsch catalysis to increase the generally low surface area of the perovskite. The work by Goldwasser *et al*. [291] is the only study identified, incorporating common iron FTS promoters into the perovskite structure. However, the active phase iron, was also incorporated and exsoluted during activation. The effect of this drastic change in phase/structure on the location and speciation of the promoters was not investigated. Whether the promoting element in the perovskite structure can act as a promoter during FTS therefore remains unanswered.

2.3.2.2 Patent literature

In a US patent application, the use of $LaX_{0.5}Fe_{0.5}O_3$ is described as support for impregnated iron nitrate (20 wt.-%). X being Ti, V, Cr, Mn and Zr [294]. The perovskite was prepared via mixing and heating the solid starting material to 900 °C for extended periods of time. It can therefore be assumed that the obtained surface area is very low. The catalysts were activated in H_2 at 500 °C and then exposed to FTS conditions at 320 and 340 °C, 20 bar and a H_2:CO ratio of 1. In comparison to iron supported on La_2O_3 and $LaFeO_3$, the inventive catalyst compositions were reported to have a significantly increased CO conversion, but for the Mn bearing sample. Selectivity remained relatively stable with some inconsistencies in the reported alcohol fraction. It has to be noted that no CO_2 is reported. At 320 °C, the Mn sample shows a slightly reduced activity compared to the reference formulations but a significantly higher alcohol and lower methane selectivity. At 340 °C, the Mn sample was not tested, but the Cr sample displayed a significant increase in alcohol and a decrease in methane selectivity, which was not at all observed in the 320 °C performance data. If the perovskites remain stable under reduction and reaction was not reported.

A World Intellectual Property Organization patent application by Shell claimed a wide variety of $X_aY_bO_c$ structures to act as support and/or precursor for cobalt based FTS catalysts, but the actual examples only describe stabilization of a common support, TiO_2 through incorporation of Co^{2+} forming a titanate [295]. These approaches had previously been reported several times in literature to avoid loss of active species through the uncontrolled formation of metal support compounds [296].

A whole series of patents describing and claiming perovskites in the Fischer-Tropsch synthesis are jointly published by the Fushun Research Institute of Petroleum and Petrochemicals and the China Petroleum and Chemical Corp. in 2014 [297–302]. In applications from 2015, Sinopec appears as additional assignee [303–305]. While all applications seem to be granted in China, none was submitted to any other national patent office.

In other patents seemingly granted in China, an iron based FTS catalyst for high per pass conversion with low CO_2 selectivity is claimed [297]. To this end, an ABO_3 perovskite structure where A is mostly Ba but can be any other alkaline earth metal and B is 85 to 95% Fe with the balance Mn (but can be Pt, Co, Ni, Cu, Zn, Cr, V, Ti, Mo or Zr). 5–10% K was added outside the perovskite structure as promoter via impregnation. The catalyst was reduced at 500 to 700 °C in hydrogen or preferably in a mixture of C_1–C_3 hydrocarbons. Under MTFTS conditions (T = 280 °C, P = 20 bar, H_2:CO = 2), after reduction at 650 °C at 10 bar in hydrogen or ideally in methane (highest conversion, lowest CH_4 and CO_2 selectivity), CO conversions of 70 to 83% were achieved at a methane selectivity of below 4% and a CO_2 selectivity between 10 and 23%. The claims encompassed the catalyst composition and reduction process. A

subsequent patent describes the same process of catalyst preparation, replacing Ba in the A site with neodymium (Nd) and Mn with Ni [298]. Under MTFTS conditions (T = 260 to 280 °C, P = 20 bar, H_2:CO = 1.5 to 2) conversion levels of 84 to 94%, methane selectivity was as low as 4 to 6% and the CO_2 selectivity between 22 and 29%. Again, activation in methane was advantageous.

A similar perovskite system, but Co based, was also described with Ba or Ca in the A site and Co with 5–10% Mo in the B site to optimize diesel fractions [299,300]. The catalyst was also promoted by impregnation with K. Reduction was carried out initially in H_2 between 300 and 450 °C and subsequently for a shorter period with CH_4 between 500 and 700 °C. LTFTS was conducted between 200 and 230 °C at 10 to 20 bar. Conversions between 60 and 83% yielded a consistently low methane selectivity with C_{5+} selectivity around 80% and the C_{12}–C_{18} (diesel) fraction up to 62%. A Ce, La and Nd, Co perovskite with some displacement of the B site with Ti is also described [306]. Additional promotion was achieved by Zn or Mo impregnation. Activation was again achieved by subsequent treatment with hydrogen and methane. $LaNi_{1-x}Co_xO_3$ [301] and $LaCu_{1-x}Co_xO_3$ [302] were subsequently described. For both, only reduction in H_2 was proposed, albeit at 10 bar. Under LTFTS (T = 200 °C, P = 20 bar, H_2:CO = 2) at CO conversions of over 85% a methane selectivity of below 4% and C_{5+} selectivity of over 85% was reported.

A $LaZr_xCo_{1-x}O_3$ (with $x<0.2$) and a $La_{1-y}K_yNi_xCo_{1-x}O_3$ (with $y<0.3$ and $x<0.35$) were synthesized using the citrate method and subsequently reduced initially in H_2 at 300–350 °C and 10 bar followed by an activation in a H_2/CH_4 mixture (H_2 rich) closer to reaction temperature [303,304]. Under FTS conditions (T = 220 °C, P = 20 bar, H_2:CO = 2) and CO conversions of 90 to 95%, a C_{5+} selectivity of over 92% at a CH_4 selectivity of 2–4% was achieved. In a recent different approach, a Co based LTFTS process was described in which cobalt nitrate and a Pt precursor was impregnated onto a $LaNiO_3$ perovskite only acting as carrier [305]. If any exsolution of Ni proceeded under a pure H_2 activation is unknown, but it can be expected as the degree of reduction of Co was significantly enhanced.

The absence of reliable characterization data makes the evaluation of the patent literature challenging, as actual catalyst compositions/structures under working conditions are not known. However, the majority of the publications [288,297–304,306] rely on the perovskite structure as catalyst precursor and are using exsolution of iron or cobalt to yield the active phase. Promoters are sometimes incorporated in the structure, sometimes added externally. The internal promoters are not expected to exsolute, if they are actually fully incorporated in the perovskite structures, and still provide the desired activity. The specification of these species after reduction is totally unavailable. Only once, was the perovskite used as support, with potential slight ‘promoting’ activity through the exsolution of Ni [305]. However, no effort is apparent to increase

the surface areas of the perovskite structures. Most efficient seems to be the activation in hydrogen followed by methane, which is claimed to increase the catalytic performance and stability.

References

[1] M. Iglesias Gonzalez, B. Kraushaar-Czarnetzki, G. Schaub, Process comparison of biomass-to-liquid (BtL) routes Fischer-Tropsch synthesis and methanol to gasoline, Biomass Conversion and Biorefinery 1 (4) (2011) 229.

[2] D.L. King, J.A. Cusumano, R.L. Garten, A Technological Perspective for Catalytic Processes Based on Synthesis Gas, Catalysis Reviews 23 (1-2) (1981) 233–263.

[3] M.E. Dry, Present and future applications of the Fischer-Tropsch process, Applied Catalysis A: General 276 (1-2) (2004) 1–3.

[4] H. Xiong, Y. Zhang, S. Wang, J. Li, Fischer-Tropsch synthesis: The effect of Al_2O_3 porosity on the performance of Co/Al_2O_3 catalyst, Catalysis Communications 6 (8) (2005) 512–516.

[5] R.B. Anderson, Kinetics and reaction mechanism of the Fischer-Tropsch synthesis, in Catalysis, Emmet, P.H; Ed. Von Norstand, –Reinhold, New Jersey, 4 (1956) (257–371).

[6] Anderson R.B., Forty Years with The Fischer-Tropsch Synthesis 1944-1984, Editor(s): S. Kaliaguine, A. Mahay, Studies in Surface Science and Catalysis, Elsevier, 19 (1984) 457−461.

[7] A.N. Stranges, A history of the Fischer-Tropsch synthesis in Germany 1926−45, in Studies in Surface Science and Catalysis, Editors: B.H. Davis, and M.L. Occelli, 163 (2000) 1−27.

[8] J.A. Moulijn, M. Makkee, A.E. van Diepen, Chemical Process Technology, Catalysis Engineering, Department of Chemical Engineering, Delft University of Technology, The Netherlands Wiley, (2013).

[9] M.E. Dry, Catalytic aspects of industrial Fischer-Tropsch synthesis, Journal of Molecular Catalysis 17 (1982) 133–144. suser_36

[10] F. Morales, M.B. Weckhuysen, Promotion Effects in Co-based Fischer– Tropsch Catalysis, Catalysis 19 (2006) 1–40.

[11] SyngasChem. News, Synfuels China demonstrates First Fischer-Tropsch products from the new Shenhua Ningxia Coal-to-Liquids plant, (2016).

[12] A. Mallik, V. Mantri, Gas-to-liquids plants face challenges in the U.S. market, (2014).

[13] Qatar Petroleum Marketing, Regulated Products - Gas to Liquids (GTL), n.d.

[14] Sasol North America, Gas-to-Liquids Facility, page 66.: Sasol Integrated, (2017) (accessed 30 June 2021).

[15] Synfuels China, Group profile, Company profile. http://www.synfuelschina.com.cn/en/about/

(accessed 6 March 2021).

[16] R. Sims, R. Schaeffer, F. Creutzig, X. Cruz-Núñez, M. D'Agosto, D. Dimitriu, M.J. Meza, L. Fulton, S. Kobayashi, O. Lah, A. Mckinnon, P. Newman, M. Ouyang, J.J. Schauer, D. Sperling, G. Tiwari, Transport. In: Climate Change 2014: Mitigation of Climate Change. Contribution of Working Group III to the Fifth Assessment Report of the Intergovernmental Panel on Climate Change, in: (2014).

[17] D.W. Keith, Why Capture CO_2 from the Atmosphere? Science 325 (5948) (2009) 1654–1655.

[18] F.D. Meylan, V. Moreau, S. Erkman, CO_2 utilization in the perspective of industrial ecology, an overview, Journal of CO_2 Utilization 12 (2015) 101–108.

[19] M. Fasihi, O. Efimova, C. Breyer, Techno-economic assessment of CO_2 direct air capture plants, Journal of Cleaner Production 224 (2019) 957–980.

[20] L. Collins, The amount of energy required by direct air carbon capture proves it is an exercise in futility, 2021. https://www.rechargenews.com/energy-transition/the-amount-of-energy-required-by-direct-air-carbon-capture-proves-it-is-an-exercise-in-futility/2-1-1067588 (accessed 19 October 2021).

[21] M. Aresta, Carbon dioxide as chemical feedstock, Wiley-VCH: Weinheim, Germany, (2010).

[22] M.M. Halmann, Chemical Fixation of Carbon Dioxide Methods for Recycling CO_2 into Useful Products, CRC press, (1993).

[23] M.M. Halmann, M. Steinberg, Greenhouse gas carbon dioxide mitigation: Science and technology, CRC press, (1998).

[24] G.L. Bezemer, J.H. Bitter, H.P.C.E. Kuipers, H. Oosterbeek, J.E. Holewijn, X. Xu, F. Kapteijn, A.J. van Dillen, K.P. de Jong, Cobalt particle size effects in the Fischer-Tropsch reaction studied with carbon nanofiber supported catalysts, Journal of the American Chemical Society 128 (12) (2006) 3956–3964.

[25] J.P. Hindermann, G.J. Hutchings, A. Kiennemann, Mechanistic Aspects of the Formation of Hydrocarbons and Alcohols from CO Hydrogenation, Catalysis Reviews 35 (1) (1993) 1–127.

[26] B. Jager, R. Esponoza, Advances in low temperature Fischer-Tropsch synthesis, Catalysis Today 23 (1995) 17–28.

[27] A.P. Steynberg, R.L. Espinoza, B. Jager, A.C. Vosloo, High temperature Fischer-Tropsch synthesis in commercial practice, Applied Catalysis A: General 186 (1999) 41–54.

[28] M. Crocker, Thermochemical Conversion of Biomass to Liquid Fuels and Chemicals, Royal Society of Chemistry, Thomas Graham House, Cambridge, (2010).

[29] A.P. Steynberg, M. Dry, Fischer-Tropsch Technology, Study of Studies in Surface Science and Catalysis, Elsevier Science, Amsterdam, The Netherlands, 152 (2004).

[30] F.A.N. Fernandes, Polymerization Kinetics of Fischer-Tropsch Reaction on Iron Based Catalysts and Product Grade Optimization, Chemical Engineering & Technology 28 (8) (2005) 930–938.

[31] W. Chen, I. Filot, R. Pestman, E. Hensen, Mechanism of Cobalt-Catalyzed CO Hydrogenation: 2. Fischer-Tropsch Synthesis, ACS Catalysis 7 (2017).

[32] P.K. Basu, Production of Synthetic Fuels and Chemicals from Biomass, (2010) 301–323.

[33] M. Claeys, E. van Steen, Fischer-Tropsch Technology: Studies in Surface Science and Catalysis, (2004).

[34] F. Fischer, H. Tropsch, The Synthesis of Petroleum at Atmospheric Pressures from Gasification Products of Coal, Brennstoff-Chemie 7 (1926) 299.

[35] P. Johnston, R.W. Joyner, Structure-Function Relationships in Heterogeneous Catalysis: The Embedded Surface Molecule Approach and Its Applications, in: L. Guczi, F. Solymosi, P. Tétényi (Eds.), New Frontiers in Catalysis - Proceedings of the 10th International Congress on Catalysis, Budapest, 19-24 July 1992, Elsevier, (1993) 165–180.

[36] H. Schulz, G. Schaub, M. Claeys, T. Riedel, Transient initial kinetic regimes of Fischer-Tropsch synthesis, Applied Catalysis A: Genera 186 (1999) 215–227.

[37] R.C. Brady, R. Pettit, Mechanism of the Fischer-Tropsch reaction. The chain propagation step, Journal of the American Chemical Society 103 (5) (1981) 1287–1289.

[38] R.C. Brady, R. Pettit, Reactions of diazomethane on transition-metal surfaces and their relationship to the mechanism of the Fischer-Tropsch reaction, Journal of the American Chemical Society 102 (19) (1980) 6181–6182.

[39] H. Schulz, E. Erich, H. Gorre, E. van Steen, Regularities of selectivity as a key for discriminating FT-surface reactions and formation of the dynamic system, Catalysis Letters 7 (1) (1990) 157–167.

[40] H. Schulz, K. Beck, E. Erich, D. Bibby, C. Chang, R. Howe, S. Yurchak, Mechanism of the Fischer-Tropsch process, Studies in surface science and catalysis 36 (1988) 457.

[41] H. Schulz, B.R. Rao, M. Elstner, Carbon-14-studies for the evaluation of the reaction mechanism of the Fischer-Tropsch synthesis: 1970. 23(10): 651-655., Erdoel & Kohle, Erdgas, Petrochemie 23 (10) (1970) 651–655.

[42] C.B. Lee, R.B. Anderson, Proceedings of the 8th International Congress on Catalysis, Bruxelles, Belgium, (1985).

[43] B.E. Mann, M.L. Turner, R. Quyoum, N. Marsih, P.M. Maitlis, Demonstration by 13 C NMR Spectroscopy of Regiospecific Carbon−Carbon Coupling during Fischer−Tropsch Probe Reactions, Journal of the American Chemical Society 121 (27) (1999) 6497–6498.

[44] S.B. Ndlovu, N.S. Phala, M. Hearshaw-Timme, P. Beagly, J.R. Moss, M. Claeys, E. van Steen, Some evidence refuting the alkenyl mechanism for chain growth in iron-based Fischer-Tropsch synthesis, Catalysis Today 71 (2002) 343–349.

[45] H.H. Storch, N. Golumbric, R.B. Anderson, The Fischer-Tropsch and Related Syntheses Including a Summary of Theoretical and Applied Contact Catalysis, John Wiley & Sons, Inc, (1951).

[46] H.W. Sternberg, I. Wender, Metal carbonyls and related compounds as catalytic intermediates in organic syntheses, Special publication - Chemical Society, London 13 (1959) 35–55.

[47] H. Pichler, H. Schulz, Neuere Erkenntnisse auf dem Gebiet der Synthese von Kohlenwasserstoffen aus CO und H_2, Chemie Ingenieur Technik 42 (18) (1970) 1162–1174.

[48] C.J. Weststrate, I.M. Ciobîcă, A.M. Saib, D.J. Moodley, J.W. Niemantsverdriet, Fundamental issues on practical Fischer-Tropsch catalysts: How surface science can help, Catalysis Today 228 (2014) 106–112.

[49] C.J. Weststrate, J. van de Loosdrecht, J.W. Niemantsverdriet, Spectroscopic insights into cobalt-catalyzed Fischer-Tropsch synthesis: A review of the carbon monoxide interaction with single crystalline surfaces of cobalt, Journal of Catalysis 342 (2016) 1–16.

[50] C.J. Weststrate, P. van Helden, J.W. Niemantsverdriet, Reflections on the Fischer-Tropsch synthesis: Mechanistic issues from a surface science perspective, Catalysis Today 275 (2016) 100–110.

[51] R.B. Anderson, Forty Years With The Fischer-Tropsch Synthesis 1944-1984: Studies in Surface Science and Catalysis, (1984).

[52] M.E. Dry, The Fischer-Tropsch process: 1950–2000, Catalysis Today 71 (2002).

[53] E. Iglesia, Design, synthesis, and use of cobalt-based Fischer-Tropsch synthesis catalysts, Applied Catalysis A: General 161 (1-2) (1997) 59–78.

[54] L.M. Tau, R. Robinson, R.D. Ross, B.H. Davis, Oxygenates formed from ethanol during Fischer-Tropsch synthesis, Journal of Catalysis 105 (2) (1987) 335–341.

[55] M. Claeys, E. van Steen, F. Roessner, A. Rausch WO2009127950A2, (2009).

[56] T. Sango, Nitrogen-containing compounds from ammonia co-feed to the Fischer-Tropsch synthesis: Nitrogen-containing compounds from ammonia co-feed to the Fischer-Tropsch synthesis, University of Cape Town, (2013).

[57] M. Claeys, H. Schulz, Effects of internal mass transfer on activity and selectivity in iron-based Fischer-Tropsch synthesis, Preprints-American Chemical Society. Division of Petroleum Chemistry 49 (2) (2004) 195–199.

[58] R.B. Anderson, R.A. Friedel, H.H. Storch, Fischer-Tropsch Reaction Mechanism Involving Stepwise Growth of Carbon Chain, The Journal of Chemical Physics 19 (3) (1951) 313–319.

[59] H.H. Starch, N. Golumbic, R.B. Anderson, The Fischer-Tropsch and Related Syntheses, John Wiley & Sons, Inc., New York, (1951).

[60] J.G. Speight, Handbook of Industrial Hydrocarbon Processes, Gulf Professional, USA, (2010).

[61] W.M. Shen, J.A. Dumesic, C.G. Hill, Criteria for stable Ni particle size under methanation reaction conditions: Nickel transport and particle size growth via nickel carbonyl, Journal of Catalysis 68 (1) (1981) 152–165.

[62] H. Schulz, Short history and present trends of Fischer-Tropsch synthesis, Applied Catalysis A: General 186 (1) (1999) 3–12.

[63] M.A. Vannice, The catalytic synthesis of hydrocarbons from H_2CO mixtures over the Group VIII metals: V. The catalytic behavior of silica-supported metals, Journal of Catalysis 50 (2) (1977) 228–236.

[64] M.A. Vannice, The catalytic synthesis of hydrocarbons from mixtures over the group VIII metals, Journal of Catalysis 37 (1975) 449–461.

[65] M. Ojeda, S. Rojas, F. García-García, M. Granados, P. Terreros, J. Fierro, Inhibition of oxygenated compounds formation during CO hydrogenation over $Rh/\gamma\text{-}Al_2O_3$ catalysts calcined at high temperature, Catalysis Communications 5 (2004) 703–707.

[66] M.M. Bhasin, W.J. Bartley, P.C. Ellgen, T.P. Wilson, Synthesis gas conversion over supported rhodium and rhodium-iron catalysts, Journal of Catalysis 54 (2) (1978) 120–128.

[67] R.C. Brown, Thermochemical Processing of Biomass: Conversion into Fuels, Chemicals and Power, Wiley Series, (2019).

[68] M.E. Dry, T. Shingles, L.J. Boshoff, Rate of the Fischer-Tropsch Reaction Over Iron Catalysts, Journal of Catalysis 25 (1971) 99–104.

[69] M.E. Dry, A.P. Steynberg, Chapter 5 - Commercial FT Process Applications, in: André Steynberg, Mark Dry (Eds.), Fischer-Tropsch Technology, Elsevier, (2004) 406–481.

[70] H. Schulz, Comparing Fischer-Tropsch Synthesis on Iron- and Cobalt Catalysts: The dynamics of structure and function, in: B.H. Davis, M.L. Occelli (Eds.), Fischer-Tropsch Synthesis, Catalyst and

Catalysis, Elsevier (2007) 177–199.

[71] M.E. Dry, Fischer-Tropsch synthesis over iron catalysts, Catalysis Letters 7 (1) (1990) 241–251.

[72] R.B. Anderson, L.J.E. Hofer, E.M. Cohn, B. Seligman, Studies of the Fischer—Tropsch Synthesis. IX. Phase Changes of Iron Catalysts in the Synthesis, Journal of the American Chemical Society 73 (3) (1951) 944–946.

[73] T. Riedel, M. Claeys, H. Schulz, G. Schaub, S.S. Nam, K.W. Jun, M.J. Choi, G. Kishan, K.W. Lee, Comparative study of Fischer-Tropsch synthesis with H_2/CO and H_2/CO_2 syngas using Fe- and Co-based catalysts, Applied Catalysis A: General 186 (1999) 201–213.

[74] M.E. Dry, The Fischer-Tropsch synthesis, in: J.R. Anderson, M. Boudart (Eds.): Catalysis Science and Technology 1, Springer Verlag, New York, USA, (1981).

[75] B.H. Davis, Fischer-Tropsch Synthesis: Comparison of Performances of Iron and Cobalt Catalysts, Industrial & Engineering Chemistry Research 46 (26) (2007) 8938–8945.

[76] A.A. Mirzaei, M. Faizi, R. Habibpour, Effect of preparation conditions on the catalytic performance of cobalt manganese oxide catalysts for conversion of synthesis gas to light olefins, Applied Catalysis A: General 306 (2006) 98–107.

[77] E.Ø. Pedersen, I.H. Svenum, E.A. Blekkan, Mn promoted Co catalysts for Fischer-Tropsch production of light olefins – An experimental and theoretical study, Journal of Catalysis 361 (2018) 23–32.

[78] R. Phienluphon, L. Shi, J. Sun, W. Niu, P. Lu, P. Zhu, T. Vitidsant, Y. Yoneyama, Q. Chen, N. Tsubaki, Ruthenium promoted cobalt catalysts prepared by an autocombustion method directly used for Fischer-Tropsch synthesis without further reduction, Catalysis Science & Technology 4 (2014).

[79] K.M. Cook, H.D. Perez, C.H. Bartholomew, W.C. Hecker, Effect of promoter deposition order on platinum-, ruthenium-, or rhenium-promoted cobalt Fischer-Tropsch catalysts, Applied Catalysis A: General 482 (2014) 275–286.

[80] H. Zhang, W. Chu, C. Zou, Z. Huang, Z. Ye, L. Zhu, Promotion Effects of Platinum and Ruthenium on Carbon Nanotube Supported Cobalt Catalysts for Fischer-Tropsch Synthesis, Catalysis Letters 141 (3) (2011) 438–444.

[81] J. Zhang, M. Abbas, J. Chen, The evolution of Fe phases of a fused iron catalyst during reduction and Fischer-Tropsch synthesis, Catalysis Science & Technology 7 (16) (2017) 3626–3636.

[82] B. Wu, L. Tian, H. Xiang, Z. Zhang, Y.W. Li, Novel precipitated iron Fischer-Tropsch catalysts with Fe3O4 coexisting with α-Fe_2O_3, Catalysis Letters 102 (3-4) (2005) 211–218.

[83] S. Li, W. Ding, G.D. Meitzner, E. Iglesia, Spectroscopic and Transient Kinetic Studies of Site Requirements in Iron-Catalyzed Fischer−Tropsch Synthesis, The Journal of Physical Chemistry B 106 (1) (2001) 85–91.

[84] K. Opeyemi Otun, Y. Yao, X. Liu, D. Hildebrandt, Synthesis, structure, and performance of carbide phases in Fischer-Tropsch synthesis: A critical review, Fuel 296 (1) (2021) 120689.

[85] K. Liang, C.H. Zhang, H.W. Xiang, Y. Yong, Y.W. Li, Effects of modified SiO_2 on H_2 and CO adsorption and hydrogenation of iron-based catalysts, Journal of Fuel Chemistry and Technology 47 (7) (2019) 769–779.

[86] B. Liang, H. Duan, T. Sun, J. Ma, X. Liu, J. Xu, X. Su, Y. Huang, T. Zhang, Effect of Na promoter on Fe-based catalyst for CO_2 hydrogenation to alkenes, ACS Sustainable Chemistry & Engineering 7 (1) (2018) 925–932.

[87] M.D. Shroff, Kalakkad. D.S., K.E. Coulter, S.D. Kohler, M.S. Harrington, N.B. Jackson, A.G. Sault, A.K. Datye, Activation of Precipitated Iron Fischer-Tropsch Synthesis Catalysts, Journal of Catalysis 156 (2) (1995) 185–207.

[88] D. Mahajan, P. Gütlich, J. Ensling, K. Pandya, U. Stumm, P. Vijayaraghavan, Evaluation of Nanosized Iron in Slurry-Phase Fischer−Tropsch Synthesis, Energy Fuels 17 (5) (2003) 1210–1221.

[89] J.B. Butt, Carbide phases on iron-based Fischer-Tropsch synthesis catalysts part II: Some reaction studies, Catalysis Letters 7 (1990) 83–106.

[90] J. Li, X. Cheng, C. Zhang, Q. Chang, J. Wang, X. Wang, Z. Lv, W. Dong, Y. Yang, Y. Li, Effect of alkalis on iron-based Fischer-Tropsch synthesis catalysts: Alkali-FeO_x interaction, reduction, and catalytic performance, Applied Catalysis A: General 528 (2016) 131–141.

[91] R.P. Mogorosi, M. Claeys, E. van Steen, Enhanced Activity via Surface Modification of Fe-Based Fischer-Tropsch Catalyst Precursor with Titanium Butoxide, Topics in Catalysis 57 (6-9) (2014) 572–581.

[92] O. Zhuo, L. Yang, F. Gao, B. Xu, Q. Wu, Y. Fan, Y. Zhang, Y. Jiang, R. Huang, X. Wang, Stabilizing the active phase of iron-based Fischer-Tropsch catalysts for lower olefins: Mechanism and strategy, Chemical science 10 (24) (2019) 6083–6090.

[93] C. Zhang, G. Zhao, K. Liu, Y. Yang, H. Xiang, Y. Li, Adsorption and reaction of CO and hydrogen on iron-based Fischer-Tropsch synthesis catalysts, Journal of Molecular Catalysis A: Chemical 328 (1) (2010) 35–43.

[94] J.F. Shultz, W.K. Hall, T.A. Dubs, R.B. Anderson, Studies of the Fischer-Tropsch Synthesis. XV. Cementite as Catalysts, Journal of the American Chemical Society 78 (2) (1956) 282–285.

[95] R.A. Dictor, A.T. Bell, Fischer-Tropsch synthesis over reduced and unreduced iron oxide catalysts, Journal of Catalysis 97 (1) (1986) 121–136.

[96] S. Li, G.D. Meitzner, E. Iglesia, Structure and site evolution of iron oxide catalyst precursors during the Fischer−Tropsch synthesis, The Journal of Physical Chemistry B 105 (24) (2001) 5743–5750.

[97] L.D. Mansker, Y. Jin, D.B. Bukur, A.K. Datye, Characterization of slurry phase iron catalysts for Fischer-Tropsch synthesis, Applied Catalysis A: General 186 (1) (1999) 277–296.

[98] J.T. Kummer, T.W. DeWitt, P.H. Emmett, Some Mechanism Studies on the Fischer-Tropsch Synthesis Using C14, Journal of the American Chemical Society 70 (11) (1948) 3632–3643.

[99] D.M. Stockwell, D. Bianchi, C.O. Bennett, Carbon pathways in methanation and chain growth during the Fischer-Tropsch synthesis on $FeAl_2O_3$, Journal of Catalysis 113 (1) (1988) 13–24.

[100] E. Iglesia, S.C. Reyes, R.J. Madon, S.L. Soled, Selectivity Control and Catalyst Design in the Fischer-Tropsch Synthesis: Sites, Pellets, and Reactors, in: D.D. Eley, H. Pines, P.B. Weisz (Eds.), Academic Press, (1993) 221–302.

[101] S.L. Soled, E. Iglesia, S. Miseo, B.A. DeRites, R.A. Fiato, Selective synthesis of α-olefins on Fe-Zn Fischer-Tropsch catalysts, Topics in Catalysis 2 (1) (1995) 193–205.

[102] A.P. Raje, R.J. O'Brien, B.H. Davis, Effect of Potassium Promotion on Iron-Based Catalysts for Fischer-Tropsch Synthesis, Journal of Catalysis 180 (1998) 36–43.

[103] L. Zhao, G. Liu, J. Li, Effect of La_2O_3 on a Precipitated Iron Catalyst for Fischer-Tropsch Synthesis, Chinese Journal of Catalysis 30 (7) (2009) 637–642.

[104] X. Ma, G. Lin, H. Zhang, Co-Mo-K Sulfide-Based Catalyst Promoted by Multiwalled Carbon Nanotubes for Higher Alcohol Synthesis from Syngas, Chinese Journal of Catalysis 27 (11) (2006) 1019–1027.

[105] M. Feyzi, M. Irandoust, A.A. Mirzaei, Effects of promoters and calcination conditions on the catalytic performance of iron–manganese catalysts for Fischer-Tropsch synthesis, Fuel Processing Technology 92 (5) (2011) 1136–1143.

[106] X. Dai, C. Yu, R. Li, Deactivation of CeO_2-Promoted Co/SiO_2 Fischer-Tropsch Catalysts, Chinese Journal of Catalysis 28 (12) (2007) 1047–1052.

[107] J.T. Richardson, Principles of Catalyst Development (Fundamental and Applied Catalysis), Springer, (1989).

[108] P. Forzatti, M. Borghesi, I. Pasquon, E. Tronconi, hermal desorption from heterogeneous surfaces; Thermal desorption from heterogeneous surfaces; normalized curve treatment, Surface Science 137 (2-3) (1984) 595–606.

[109] E. de Smit, B.M. Weckhuysen, The renaissance of iron-based Fischer-Tropsch synthesis: On the multifaceted catalyst deactivation behavior, Chemical Society Reviews 37 (12) (2008) 2758–2781.

[110] E. van Steen, M. Claeys, Proceedings of Syngas Convention, Cape Town, 1–4 April 2021 (2012).

[111] G. Ertl, S.B. Lee, M. Weiss, Adsorption of nitrogen on potassium promoted Fe(111) and (100) surfaces, Surface Science 114 (2) (1982) 527–545.

[112] D.C. Sorescu, Adsorption and activation of CO coadsorbed with K on Fe(100) surface: A plane-wave DFT study, Surface Science 605 (3) (2011) 401–414.

[113] J.K. Nørskov, S. Holloway, N.D. Lang, Microscopic model for the poisoning and promotion of adsorption rates by electronegative and electropositive atoms, Surface Science 137 (1984) 65–78.

[114] W. Ngantsoue-Hoc, Y. Zhang, R.J. O'Brien, Fischer-Tropsch synthesis: activity and selectivity for Group I alkali promoted iron-based catalysts, Applied Catalysis A: General 236 (2002) 77–89.

[115] M.E. Dry, G.J. Oosthuizen, The correlation between catalyst surface basicity and hydrocarbon selectivity in the Fischer-Tropsch synthesis, Journal of Catalysis 11 (1) (1968) 18–24.

[116] J. Li, X. Cheng, C. Zhang, J. Wang, W. Dong, Y. Yang, Y. Li, Alkalis in iron-based Fischer-Tropsch synthesis catalysts: Distribution, migration and promotion, Journal of Chemical Technology & Biotechnology 92 (6) (2017) 1472–1480.

[117] J. Folke, K. Dembélé, F. Girgsdies, H. Song, R. Eckert, S. Reitmeier, A. Reitzmann, R. Schlögl, T. Lunkenbein, H. Ruland, Promoter effect on the reduction behavior of wuestite-based catalysts for ammonia synthesis, Catalysis Today (2021).

[118] M. Jiang, N. Koizumi, M. Yamada, Characterization of potassium-promoted iron–manganese catalysts by *in situ* diffuse reflectance FTIR using NO, CO and $CO+H_2$ as probes, Applied Catalysis A: General 204 (1) (2000) 49–58.

[119] J.L. Rankin, C.H. Bartholomew, Effects of potassium and calcination pretreatment on the adsorption and chemical/physical properties of $FeSiO_2$, Journal of Catalysis 100 (2) (1986) 533–540.

[120] Y. Yang, H.W. Xiang, Y.Y. Xu, L. Bai, Y.W. Li, Effect of potassium promoter on precipitated iron-manganese catalyst for Fischer-Tropsch synthesis, Applied Catalysis A: General 266 (2) (2004) 181–194.

[121] W. Ma, E.L. Kugler, D.B. Dadyburjor, Potassium effects on activated-carbon-supported iron catalysts for Fischer− Tropsch synthesis, Energy Fuels 21 (4) (2007) 1832–1842.

[122] A. Chen, M. Kaminsky, G.L. Geoffroy, M.A. Vannice, Carbon monoxide hydrogenation over carbon-supported iron-cobalt and potassium-iron-cobalt carbonyl cluster-derived catalysts, The Journal of Physical Chemistry 90 (20) (1986) 4810–4819.

[123] H. Xiong, M.A. Motchelaho, M. Moyo, L.L. Jewell, N.J. Coville, Effect of Group I alkali metal promoters on Fe/CNT catalysts in Fischer-Tropsch synthesis, Fuel 150 (2015) 687–696.

[124] H. Xiong, M. Moyo, M. Am Motchelaho, L.L. Jewell, N.J. Coville, Fischer-Tropsch synthesis over model iron catalysts supported on carbon spheres: The effect of iron precursor, support pretreatment, catalyst preparation method and promoters, Applied Catalysis A: General 388 (1-2) (2010) 168–178.

[125] E. de Smit, A.M. Beale, S. Nikitenko, B.M. Weckhuysen, Local and long range order in promoted iron-based Fischer-Tropsch catalysts: A combined in situ X-ray absorption spectroscopy/wide angle X-ray scattering study, Journal of Catalysis 262 (2) (2009) 244–256.

[126] S. Li, W. Ding, G.D. Meitzner, E. Iglesia, Spectroscopic and Transient Kinetic Studies of Site Requirements in Iron-Catalyzed Fischer−Tropsch Synthesis, The Journal of Physical Chemistry B 106 (1) (2002) 85–91.

[127] H. Jung, W.J. Thomson, Dynamic X-ray diffraction study of an unsupported iron catalyst in Fischer-Tropsch synthesis, Journal of Catalysis 134 (2) (1992) 654–667.

[128] M.C. Ribeiro, G. Jacobs, B.H. Davis, D.C. Cronauer, A.J. Kropf, C.L. Marshall, Fischer−Tropsch Synthesis: An In-Situ TPR-EXAFS/XANES Investigation of the Influence of Group I Alkali Promoters on the Local Atomic and Electronic Structure of Carburized Iron/Silica Catalysts, The Journal of Physical Chemistry C 114 (17) (2010) 7895–7903.

[129] R. Malessa, M. Baerns, Iron/manganese oxide catalysts for Fischer-Tropsch synthesis. 4. Activity and selectivity, Industrial & Engineering Chemistry Research 27 (2) (1988) 279–283.

[130] L. Bai, H.W. Xiang, Y.W. Li, Y.Z. Han, B. Zhong, Slurry phase Fischer-Tropsch synthesis over manganese-promoted iron ultrafine particle catalyst, Fuel 81 (11) (2002) 1577–1581.

[131] Y. Soong, V.U.S. Rao, R.J. Gormley, B. Zhong, Temperature-programmed desorption study on manganese-iron catalysts, Applied Catalysis 78 (1) (1991) 97–108.

[132] B. Büssemeier, C.D. Frohning, B. Cornils, Lower olefins via Fischer-Tropsch, Hydrocarbon Process 105 (11) (1976) 55.

[133] W.D. Deckwer, Y. Serpemen, M. Ralek, B. Schmidt, Fischer-Tropsch synthesis in the slurry phase on manganese/iron catalysts, Industrial & Engineering Chemistry Process Design and Development 21 (2) (1982) 222–231.

[134] J. Barrault, C. Forquy, V. Perrichon, Effects of manganese oxide and sulphate on olefin selectivity of iron supported catalysts in the Fischer-Tropsch reaction, Applied Catalysis 5 (1) (1983) 119–125.

[135] T. Li, Y. Yang, C. Zhang, X. An, H. Wan, Z. Tao, H. Xiang, Y. Li, F. Yi, B. Xu, Effect of manganese on an iron-based Fischer-Tropsch synthesis catalyst prepared from ferrous sulfate, Fuel 86 (7) (2007) 921–928.

[136] K.B. Jensen, F.E. Massoth, Studies on iron-manganese oxide carbon monoxide catalysts: II. Carburization and catalytic activity, Journal of Catalysis 92 (1) (1985) 109–118.

[137] C.H. Yang, Ph.D. dissertation, University of Utah, Salt Lake City, Utah (1979).

[138] K.B. Jensen, F.E. Massoth, Studies on iron-manganese oxide carbon monoxide catalysts: I. Structure of reduced catalyst, Journal of Catalysis 92 (1) (1985) 98–108.

[139] T. Herranz, S. Rojas, F.J. Pérez-Alonso, M. Ojeda, P. Terreros, J.L.G. Fierro, Hydrogenation of carbon oxides over promoted Fe-Mn catalysts prepared by the microemulsion methodology, Applied Catalysis A: General 311 (2006) 66–75.

[140] H. Koelbel, K.D. Tillmetz US 4177203, (1979).

[141] C.K. Das, N.S. Das, D.P. Choudhury, G. Ravichandran, D.K. Chakrabarty, Hydrogenation of carbon monoxide on unsupported Fe-Mn-K catalysts for the synthesis of lower alkenes: Promoter effect of manganese, Applied Catalysis A: General 111 (2) (1994) 119–132.

[142] J.J. Venter, M. Kaminsky, G. Geoffroy, M. Vannice, Carbon-supported FeMn and KFeMn clusters for the synthesis of C_2C_4 olefins from CO and H_2: II. Activity and selectivity maintenance and regenerability, Journal of Catalysis 105 (1987) 155–162.

[143] Xu-Longya, Wang-Qingxia, Xu-Yide, Huang-Jiasheng, Promotion effect of K_2O and MnO additives on the selective production of light alkenes via syngas over Fe/silicalite-2 catalysts, Catalysis Letters 31 (2) (1995) 253–266.

[144] W.L. van Dijk, J.W. Niemantsverdriet, A.M.D. van Kraan, H.S. van der Baan, Effects of manganese oxide and sulphate on the olefin selectivity of iron catalysts in the Fischer-Tropsch reaction, Applied Catalysis 2 (4) (1982) 273–288.

[145] C. Wang, Q. Wang, X. Sun, L. Xu, CO Hydrogenation to Light Alkenes Over Mn/Fe Catalysts Prepared by Coprecipitation and Sol-gel Methods, Catalysis Letters 105 (1) (2005) 93–101.

[146] N.K. Jaggi, L.H. Schwartz, Butti. J., H. B. Papp, M. Baerns, Phase characterization of iron/manganese Fischer-Tropsch catalysts: effect of composition and reduction conditions, Applied Catalysis 13 (2) (1985) 347–361.

[147] T. Grzybek, H. Papp, N. Baerns, Fe/Mn oxide catalysts for Fischer-Tropsch synthesis: Part V XPS surface characterization of calcined and reduced samples, Applied Catalysis 29 (2) (1987) 335–350.

[148] K.M. Kreitman, M. Baerns, J.B. Butt, Manganese-oxide-supported iron Fischer-Tropsch synthesis catalysts: Physical and catalytic characterization, Journal of Catalysis 105 (2) (1987) 319–334.

[149] I.S.C. Hughes, J.O.H. Newman, G.C. Bond, The characterization of unsupported iron and manganese-promoted iron catalysts by X-ray photoelectron spectroscopy and temperature-programmed reduction, Applied Catalysis 30 (2) (1987) 303–311.

[150] I.R. Leith, M.G. Howden, Temperature-programmed reduction of mixed iron—manganese oxide catalysts in hydrogen and carbon monoxide, Applied Catalysis 37 (1988) 75–92.

[151] J. Barrault, C. Renard, L.T. Yu, J. Gal, Proceeding of 8th International Congress of Catalysis (Berlin West) 2 (1984) 101.

[152] G.C. Maiti, R. Malessa, M. Baerns, Iron/manganese oxide catalysts for Fischer-Tropsch synthesis: Part I: structural and textural changes by calcination, reduction and synthesis, Applied Catalysis 5 (2) (1983) 151–170.

[153] R. Kapoor, S.T. Oyama, Measurement of solid state diffusion coefficients by a temperature-programmed method, Journal of materials research 12 (2) (1997) 467–473.

[154] J.S. Ledford, M. Houalla, L. Petrakis, D.M. Hercules, Influence of Lanthanum Oxide on the Surface Structure and Co Hydrogenation Activity of Supported Cobalt Catalysts, in: B. Delmon, P. Grange, P.A. Jacobs, G. Poncelet (Eds.), Preparation of Catalysts IV, Elsevier, (1987) 433–442.

[155] R.B. Anderson, Catalysis IV (1956) PH Emmett, Ed, Rheinhold Publishing Company, New York.

[156] G.A. Hadjigeorghiou, J.T. Richardson, Promotion of nickel catalysts for Fischer-Tropsch reactions, Applied Catalysis 21 (1) (1986) 37–45.

[157] K.B. Mok, J.R.H. Ross, R.M. Sambrook, Thermally and Mechanically Stable Catalysts For Steam Reforming And Methanation. A New Concept in Catalyst Design, in: G. Poncelet, P. Grange, P.A. Jacobs (Eds.), Preparation of Catalysts III, Elsevier, (1983) 291–299.

[158] Y. Zamani, M. Bakavoli, M. Rahimizadeh, A. Mohajeri, S.M. Seyedi, Synergetic Effect of La and Ba Promoters on Nanostructured Iron Catalyst in Fischer-Tropsch Synthesis, Chinese Journal of Catalysis 33 (7) (2012) 1119–1124.

[159] T.C. Bromfield, N.J. Coville, The effect of sulfide ions on a precipitated iron Fischer-Tropsch catalyst, Applied Catalysis A: General 186 (1999) 297–307.

[160] H.M.T. Galvis, A.C.J. Koeken, J.H. Bitter, T. Davidian, M. Ruitenbeek, A.I. Dugulan, K.P. de Jong, Effects of sodium and sulfur on catalytic performance of supported iron catalysts for the Fischer-Tropsch synthesis of lower olefins, Journal of Catalysis 303 (2013) 22–30.

[161] C.H. Bartholomew, R.M. Bowman, Sulfur poisoning of cobalt and iron Fischer-Tropsch catalysts, Applied Catalysis 15 (1) (1985) 59–67.

[162] A.L. Chaffee, I. Campbell, N. Valentine, Sulfur Poisoning of Fischer-Tropsch Synthesis Catalysts in a Fixed-Bed Reactor, Applied Catalysis 47 (2) (1989) 253–276.

[163] R.J. Madon, H. Seaw, Effect of Sulfur on the Fischer-Tropsch Synthesis, Catalysis Reviews 15 (1) (1977) 69–106.

[164] F.S. Karn, J.F. Schultz, R.E. Kelly, R.B. Anderson, Fischer-Tropsch Synthesis. Poisoning of Iron Catalysts by H_2S in Synthesis Gas, I&EC Product Research and Development 2 (1) (1963) 43–47.

[165] F.S. Karn, J.F. Shultz, R.E. Kelly, R.B. Anderson, Hydrogen Sulfide Poisoning of Nitrided and Carbided Iron Catalysts in the Fischer-Tropsch Synthesis, I&EC Product Research and Development 3 (1) (1964) 33–38.

[166] R.B. Anderson, F.S. Karn, J.F. Shultz, Factors in sulfur poisoning of iron catalysts in Fischer-Tropsch synthesis, Journal of Catalysis 4 (1) (1965) 56–63.

[167] J.A. Kritzinger, The role of sulfur in commercial iron-based Fischer-Tropsch catalysis with focus on C_2-product selectivity and yield, Catalysis Today 71 (3) (2002) 307–318.

[168] H.M.T. Galvis, A.C.J. Koeken, J.H. Bitter, T. Davidian, M. Ruitenbeek, A.I. Dugulan, K.P. de Jong, Effects of sodium and sulfur on catalytic performance of supported iron catalysts for the Fischer-Tropsch synthesis of lower olefins, Journal of Catalysis 303 (2013) 22–30.

[169] D.B. Bukur, K. Okabe, M.P. Rosynek, C.P. Li, D.J. Wang, K.R.P.M Rao, G.P. Huffman, Activation Studies with a Precipitated Iron Catalyst for Fischer-Tropsch Synthesis., Journal of Catalysis 155 (2) (1995) 353–365.

[170] R.J. O'Brien, L. Xu, R.L. Spicer, S. Bao, D.R. Milburn, B.H. Davis, Activity and selectivity of precipitated iron Fischer-Tropsch catalysts, Catalysis Today 36 (3) (1997) 325–334.

[171] H. Wan, B. Wu, C. Zhang, H. Xiang, Y. Li, Promotional effects of Cu and K on precipitated iron-based catalysts for Fischer-Tropsch synthesis, Journal of Molecular Catalysis A: Chemical 283 (1) (2008) 33–42.

[172] R. O'Brien, B. Davis, Impact of Copper on an Alkali Promoted Iron Fischer-Tropsch Catalyst, Catalysis Letters 94 (2004) 1–6.

[173] Y. Jin, A.K. Datye, Phase transformations in iron Fischer-Tropsch catalysts during temperature-programmed reduction, Journal of Catalysis 196 (1) (2000) 8–17.

[174] S. Li, A. Li, S. Krishnamoorthy, E. Iglesia, Effects of Zn, Cu, and K Promoters on the Structure and on the Reduction, Carburization, and Catalytic Behavior of Iron-Based Fischer-Tropsch Synthesis Catalysts, Catalysis Letters 77 (4) (2001) 197–205.

[175] K. Keyvanloo, M.K. Mardkhe, T.M. Alam, C.H. Bartholomew, B.F. Woodfield, W.C. Hecker, Supported Iron Fischer-Tropsch Catalyst: Superior Activity and Stability Using a Thermally Stable Silica-Doped Alumina Support, ACS Catalysis 4 (4) (2014) 1071–1077.

[176] F. He, F. Li, Perovskite promoted iron oxide for hybrid water-splitting and syngas generation with exceptional conversion, Energy & Environmental Science 8 (2) (2015) 535–539.

[177] C. Zhou, Q. Lin, The State of the art review of Fischer-Tropsch Synthesis Technology [J], Shenhua Science and Technology 4 (2010).

[178] D.B. Bukur, V.H. Carreto-Vazquez, W. Ma, Catalytic performance and attrition strength of spray-dried iron catalysts for slurry phase Fischer-Tropsch synthesis, Applied Catalysis A: General 388 (1-2) (2010) 240–247.

[179] D.B. Bukur, W.P. Ma, V. Carreto-Vazquez, L. Nowicki, A.A. Adeyiga, Attrition Resistance and Catalytic Performance of Spray-Dried Iron Fischer−Tropsch Catalysts in a Stirred-Tank Slurry Reactor, Industrial & Engineering Chemistry Research 43 (6) (2004) 1359–1365.

[180] H.N. Pham, A. Viergutz, R.J. Gormley, A.K. Datye, Improving the attrition resistance of slurry phase heterogeneous catalysts, Powder technology 110 (3) (2000) 196–203.

[181] R. Zhao, J.G. Goodwin, K. Jothimurugesan, S.K. Gangwal, J.J. Spivey, Spray-dried iron Fischer−Tropsch catalysts. 1. Effect of structure on the attrition resistance of the catalysts in the calcined state, Industrial & Engineering Chemistry Research 40 (4) (2001) 1065–1075.

[182] R. Zhao, J.G. Goodwin, K. Jothimurugesan, S.K. Gangwal, J.J. Spivey, Spray-Dried Iron Fischer−Tropsch Catalysts. 2. Effect of Carburization on Catalyst Attrition Resistance, Industrial & Engineering Chemistry Research 40 (5) (2001) 1320–1328.

[183] D.B. Bukur, W.P. Ma, V. Carreto-Vazquez, Attrition studies with precipitated iron Fischer-Tropsch catalysts under reaction conditions, Topics in Catalysis 32 (3) (2005) 135–141.

[184] K. Jothimurugesan, J.G. Goodwin Jr., S.K. Gangwal, J.J. Spivey, Syngas Conversion to Fuels and Chemicals, American Chemical Society (1999).

[185] K. Sudsakorn, J.G. Goodwin, K. Jothimurugesan, A.A. Adeyiga, Preparation of attrition-resistant spray-dried Fe Fischer−Tropsch catalysts using precipitated SiO_2, Industrial & Engineering Chemistry Research 40 (22) (2001) 4778–4784.

[186] E. Rytter, Ø. Borg, N.E. Tsakoumis, A. Holmen, Water as key to activity and selectivity in Co Fischer-Tropsch synthesis: Γ-alumina based structure-performance relationships, Journal of Catalysis 365 (2018) 334–343.

[187] J.L. Casci, C.M. Lok, M.D. Shannon, Fischer-Tropsch catalysis: The basis for an emerging industry with origins in the early 20th Century, Catalysis Today 145 (1-2) (2009) 38–44.

[188] W. Ma, G. Jacobs, R.A. Keogh, D.B. Bukur, B.H. Davis, Fischer-Tropsch synthesis: Effect of Pd, Pt, Re, and Ru noble metal promoters on the activity and selectivity of a 25% Co/Al_2O_3 catalyst, Applied Catalysis A: General 437 (2012) 1–9.

[189] L. Wang, E. Guan, J. Zhang, J. Yang, Y. Zhu, Y. Han, M. Yang, C. Cen, G. Fu, B.C. Gates, Single-site catalyst promoters accelerate metal-catalyzed nitroarene hydrogenation, Nature communications 9 (1) (2018) 1–8.

[190] K. Shimura, T. Miyazawa, T. Hanaoka, S. Hirata, Fischer-Tropsch synthesis over TiO_2 supported cobalt catalyst: Effect of TiO_2 crystal phase and metal ion loading, Applied Catalysis A: General 460 (2013) 8–14.

[191] M. Mehrbod, M. Martinelli, A.G. Martino, D.C. Cronauer, A.J. Kropf, C.L. Marshall, G. Jacobs, Fischer-Tropsch synthesis: Direct cobalt nitrate reduction of promoted Co/TiO_2 catalysts, Fuel 245 (2019) 488–504.

[192] M. Mehrbod, M. Martinelli, A.G. Martino, D.C. Cronauer, A.J. Kropf, C.L. Marshall, G. Jacobs, Fischer-Tropsch synthesis: Direct cobalt nitrate reduction of promoted Co/TiO_2 catalysts, Fuel 245 (2019) 488–504.

[193] S.A. Hosseini, A. Taeb, F. Feyzi, Evaluation of Ru-promoted $Co/\gamma\text{-}Al_2O_3$ catalysts in Fischer-Tropsch synthesis in a CSTR, Catalysis Communications 6 (3) (2005) 233–240.

[194] A. Kogelbauer, J.G. Goodwin JR., R. Oukaci, Ruthenium Promotion of Co/Al_2O_3 Fischer-Tropsch Catalysts, Journal of Catalysis 160 (1) (1996) 125–133.

[195] T.K. Das, G. Jacobs, P.M. Patterson, W.A. Conner, J. Li, B.H. Davis, Fischer-Tropsch synthesis: Characterization and catalytic properties of rhenium promoted cobalt alumina catalysts, Fuel 82 (7) (2003) 805–815.

[196] Q. Cai, J. Li, Catalytic properties of the Ru promoted Co/SBA-15 catalysts for Fischer-Tropsch synthesis, Catalysis Communications 9 (10) (2008) 2003–2006.

[197] G. Jacobs, Y. Ji, B.H. Davis, D. Cronauer, A.J. Kropf, C.L. Marshall, Fischer-Tropsch synthesis: Temperature programmed EXAFS/XANES investigation of the influence of support type, cobalt loading, and noble metal promoter addition to the reduction behavior of cobalt oxide particles, Applied Catalysis A: General 333 (2) (2007) 177–191.

[198] W. Chu, P.A. Chernavskii, L. Gengembre, G.A. Pankina, P. Fongarland, A.Y. Khodakov, Cobalt species in promoted cobalt alumina-supported Fischer-Tropsch catalysts, Journal of Catalysis 252 (2) (2007) 215–230.

[199] W. Chu, L.N. Wang, P.A. Chernavskii, A.Y. Khodakov, Glow-Discharge Plasma-Assisted Design of Cobalt Catalysts for Fischer-Tropsch Synthesis, Angewandte Chemie International Edition 47 (27) (2008) 5052–5055.

[200] S. Vada, B. Chen, J.G. Goodwin, Isotopic Transient Study of La Promotion of Co/Al_2O_3 or CO Hydrogenation, Journal of Catalysis 153 (2) (1995) 224–231.

[201] S. Vada, A.M. Kazi, F.K. Bedu-Addu, B. Chen, J.G. Goodwin, Jr., in "Natural Gas Conversion" (H. E. Curry-Hyde, and R. F. Howe, Eds.), Elsevier Science 2 (1994).

[202] J. Barrault, A. Guilleminot, Hydrogenation of Carbon Monoxide on Carbon Supported Cobalt Rare Earth Catalysts, Applied Catalysis 21 (1986) 307.

[203] J.S. Ledford, M. Houalla, A. Proctor, D.M. Hercules, L. Petrakis, Influence of lanthanum on the surface structure and carbon monoxide hydrogenation activity of supported cobalt catalysts, The Journal of Physical Chemistry 93 (18) (1989) 6770–6777.

[204] G.J. Haddad, B. Chen, James G. Goodwin JR., Effect of La^{3+} Promotion of Co/SiO_2 on CO Hydrogenation, Journal of Catalysis 161 (1) (1996) 274–281.

[205] O.L. Eliseev, M.V. Tsapkina, O.S. Dement'eva, P.E. Davydov, A.V. Kazakov, A.L. Lapidus, Promotion of cobalt catalysts for the Fischer-Tropsch synthesis with alkali metals, Kinetics and Catalysis 54 (2) (2013) 207–212.

[206] L. Gavrilović, J. Save, E.A. Blekkan, The effect of potassium on cobalt-based Fischer-Tropsch catalysts with different cobalt particle sizes, Catalysts 9 (4) (2019) 351.

[207] Y. Dai, F. Yu, Z. Li, Y. An, T. Lin, Y. Yang, L. Zhong, H. Wang, Y. Sun, Effect of Sodium on the Structure-Performance Relationship of Co/SiO_2 for Fischer-Tropsch Synthesis, Chinese Journal of Chemistry 35 (6) (2017) 918–926.

[208] D.R. Strongin, G.A. Somorjai, The effects of potassium on ammonia synthesis over iron single-crystal surfaces, Journal of Catalysis 109 (1) (1988) 51–60.

[209] D.S. Newsome, The Water-Gas Shift Reaction, Catalysis Reviews 21 (2) (1980) 275–318.

[210] G. Connell, J.A. Dumesic, Migration of potassium on iron and alumina surfaces as studied by Auger electron spectroscopy, Journal of Catalysis 92 (1) (1985) 17–24.

[211] J.G. van Ommen, W.J. Bolink, J. Prasad, P. Mars, The nature of the potassium compound acting as a promoter in iron-alumina catalysts for ammonia synthesis, Journal of Catalysis 38 (1) (1975) 120–127.

[212] Z. Paál, G. Ertl, S.B. Lee, Interactions of potassium, oxygen and nitrogen with polycrystalline iron surfaces, Applications of Surface Science 8 (3) (1981) 231–249.

[213] G. Pirug, G. Brodén, H.P. Bonzel, Coadsorption of potassium and oxygen on Fe(110), Surface Science 94 (2) (1980) 323–338.

[214] P.H. Emmett, S. Brunauer, The use of low temperature van der Waals adsorption isotherms in determining the surface area of iron synthetic ammonia catalysts, Journal of the American Chemical Society 59 (8) (1937) 1553–1564.

[215] P. Forzatti, L. Lietti, Catalyst deactivation, Catalysis Today 52 (2) (1999) 165–181.

[216] C.H. Bartholomew, Mechanisms of catalyst deactivation, Applied Catalysis A: General 212 (1) (2001) 17–60.

[217] J.A. Moulijn, A.E. van Diepen, F. Kapteijn, Catalyst deactivation: is it predictable?: What to do? Applied Catalysis A: General 212 (2001) 3–16.

[218] C.G. Granqvist, R.A. Buhrman, Statistical model for coalescence of islands in discontinuous films, Applied Physics Letters 27 (12) (1975) 693–694.

[219] T.W. Hansen, A.T. DeLaRiva, S.R. Challa, A.K. Datye, Sintering of Catalytic Nanoparticles: Particle Migration or Ostwald Ripening? Accounts of Chemical Research 46 (8) (2013) 1720–1730.

[220] P. Wynblatt, N.A. Gjostein, Supported metal crystallites, Progress in solid state chemistry 9 (1975) 21–58.

[221] D.D. Beck, C.J. Carr, A study of thermal aging of PtAl2O3 using temperature-programmed desorption spectroscopy, Journal of Catalysis 110 (2) (1988) 285–297.

[222] M. Argyle, C. Bartholomew, Heterogeneous Catalyst Deactivation and Regeneration: A Review, Catalysts 5 (1) (2015) 145–269.

[223] C.H. Bartholomew (Ed.), Catalyst deactivation 1997: Proceedings of the 7th International Symposium, Cancun, Mexico, October 5 - 8, 1997, Elsevier, Amsterdam, 1997.

[224] S. Wanke, P. Flynn, The Sintering of Supported Metal Catalysts, Catalysis Reviews 37 (1975) 432.

[225] J.J. Kingsley, K. Suresh, K.C. Patil, Combustion synthesis of fine particle rare earth orthoaluminates and yttrium aluminum garnet, Journal of Solid State Chemistry 88 (2) (1990) 435–442.

[226] R. Guo, P. Ravindranathan, U. Selvaraj, A.S. Bhalla, L.E. Cross, R. Roy, Modified mixed oxide perovskites $0.7Sr(Al_{12}B_{12})\ O_3\ 3LaAlO_3$ and $0.7Sr(Al_{1.2}B_{12})O_3\ 3NdGaO_3$ (BTa^{5+} or Nb^{5+}) for high-Tc superconductor substrate applications., Journal of Materials Science 29 (19) (1994) 5054–5058.

[227] J. Oudar, H. Wise, Deactivation and poisoning of catalysts, Marcel Dekker, New York, NY, (1985).

[228] W.G. Frankenburg, V.I. Komarewsky, E.K. Rideal, P.H. Emmett, H.S. Taylor (Eds.), The Poisoning of Metallic Catalysts, Academic Press, (1951).

[229] C.H. Bartholomew, R.J. Farrauto (Eds.), Fundamentals of industrial catalytic processes, 2nd ed., Wiley, Hoboken N.J., (2006).

[230] K. Bartholomew, L.M. Horowitz, Attachment styles among young adults: A test of a four-category model, Journal of Personality and Social Psychology 61 (2) (1991) 226–244.

[231] J.F. Shultz, L.J.E. Hofer, F.S. Karn, R.B. Anderson, Studies of the Fischer-Tropsch synthesis. prepoisoning of iron catalysts by sulfur compounds, The Journal of Physical Chemistry 66 (3) (1962) 501–506.

[232] B. Wu, L. Bai, H. Xiang, Y.W. Li, Z. Zhang, B. Zhong, An active iron catalyst containing sulfur for Fischer-Tropsch synthesis, Fuel 83 (2) (2004) 205–212.

[233] A.M. Saib, D.J. Moodley, Im Ciobîcă, M.M. Hauman, B.H. Sigwebela, C.J. Weststrate, J.W. Niemantsverdriet, J. van de Loosdrecht, Fundamental understanding of deactivation and regeneration of cobalt Fischer-Tropsch synthesis catalysts, Catalysis Today 154 (3-4) (2010) 271–282.

[234] N.E. Tsakoumis, M. Rønning, Ø. Borg, E. Rytter, A. Holmen, Deactivation of cobalt-based Fischer-Tropsch catalysts: A review, Catalysis Today 154 (3) (2010) 162–182.

[235] P.K. Agrawal, W.D. Fitzharris, Katzer, JR (Eds.), Catalyst Deactivation, (1980).

[236] J.R. Rostrup-Nielsen, Steam reforming catalysts: Investigation of catalysts for tubular steam reforming of hydrocarbons (1975).

[237] J.R. Rostrup-Nielsen, Coking on nickel catalysts for steam reforming of hydrocarbons, Journal of Catalysis 33 (2) (1974) 184–201.

[238] E.J. Erekson, E.L. Sughrue, C.H. Bartholomew, Catalyst degradation in high temperature methanation, Fuel Processing Technology 5 (1-2) (1981) 91–101.

[239] C.H. Bartholomew, Carbon deposition in steam reforming and methanation, Catalysis Reviews Science and Engineering 24 (1982) 67–112.

[240] C. Perego, R. Bortolo, R. Zennaro, Gas to liquids technologies for natural gas reserves valorization: The Eni experience, Catalysis Today 142 (1) (2009) 9–16.

[241] B.L. Bhatt, E.C. Heydorn, P.J.A. Tijm, in "Proceeding of the 1997 coal liquefactoin & solid fuels contractors review conference": US Department of Energy, Federal Energy Technology Center, Pittsburg, Pynnsylvania (1997) 41.

[242] D. Wei, J. Goodwin, R. Oukaci, A. Singleton, Attrition resistance of cobalt FT catalysts for slurry bubble column reactor use, Applied Catalysis A: General 210 (2001) 137–150.

[243] J. Li, G. Jacobs, T. Das, Y. Zhang, B. Davis, Fischer-Tropsch synthesis: Effect of water on the catalytic properties of a Co/SiO_2 catalyst, Applied Catalysis A: General 236 (1) (2002) 67–76.

[244] D.J. Duvenhage, N.J. Coville, Deactivation of a precipitated iron Fischer-Tropsch catalyst—A pilot plant study, Applied Catalysis A: General 298 (2006) 211–216.

[245] E. van Steen, M. Claeys, M.E. Dry, J. van de Loosdrecht, E.L. Viljoen, J.L. Visagie, Stability of Nanocrystals: Thermodynamic Analysis of Oxidation and Re-reduction of Cobalt in Water/Hydrogen Mixtures, The Journal of Physical Chemistry B 109 (8) (2005) 3575–3577.

[246] D. Schanke, A. Hilmen, E. Bergene, K. Kinnari, E. Rytter, E. Adnanes, A. Holmén, Study of the deactivation mechanism of Al_2O_3-supported cobalt Fischer-Tropsch catalysts, Catalysis Letters 34 (1995) 269–284.

[247] D.B. Bukur, Z. Pan, W. Ma, G. Jacobs, B.H. Davis, Effect of CO Conversion on the Product Distribution of a Co/Al_2O_3 Fischer-Tropsch Synthesis Catalyst Using a Fixed Bed Reactor, Catalysis Letters 142 (11) (2012) 1382–1387.

[248] M. Wolf, N. Fischer, M. Claeys, Water-induced deactivation of cobalt-based Fischer-Tropsch catalysts, Nature Catalysis 3 (12) (2020) 962–965.

[249] J. van de Loosdrecht, B. Balzhinimaev, J.A. Dalmon, J.W. Niemantsverdriet, S.V. Tsybulya, A.M. Saib, P.J. van Berge, J.L. Visagie, Cobalt Fischer-Tropsch synthesis: Deactivation by oxidation? Catalysis Today 123 (1) (2007) 293–302.

[250] N. Fischer, B. Clapham, T. Feltes, E. van Steen, M. Claeys, Size-dependent phase transformation of catalytically active nanoparticles captured in situ, Angewandte Chemie International Edition 53 (5) (2014) 1342–1345.

[251] A. Tavasoli, R.M.M. Abbaslou, A.K. Dalai, Deactivation behavior of ruthenium promoted Co/γ-Al_2O_3 catalysts in Fischer-Tropsch synthesis, Applied Catalysis A: General 346 (1) (2008) 58–64.

[252] G. Jacobs, T.K. Das, Y. Zhang, J. Li, G. Racoillet, B.H. Davis, Fischer-Tropsch synthesis: Support, loading, and promoter effects on the reducibility of cobalt catalysts, Applied Catalysis A: General 233 (1) (2002) 263–281.

[253] G. Jacobs, T.K. Das, P.M. Patterson, J. Li, L. Sanchez, B.H. Davis, Fischer-Tropsch synthesis XAFS: XAFS studies of the effect of water on a Pt-promoted Co/Al_2O_3 catalyst, Applied Catalysis A: General 247 (2) (2003) 335–343.

[254] G. Jacobs, P.M. Patterson, Y. Zhang, T. Das, J. Li, B.H. Davis, Fischer-Tropsch synthesis: Deactivation of noble metal-promoted Co/Al_2O_3 catalysts, Applied Catalysis A: General 233 (1) (2002) 215–226.

[255] J.P. Attfield, P. Lightfoot, R.E. Morris, Perovskites, Dalton Trans. 44 (23) (2015) 10541–10542.

[256] E.A. Lombardo, M.A. Ulla, Perovskite oxides in catalysis: Past, present and future, Research on Chemical Intermediates 24 (5) (1998) 581–592.

[257] Y. Wang, J. Ren, Y. Wang, F. Zhang, X. Liu, Y. Guo, G. Lu, Nanocasted Synthesis of Mesoporous $LaCoO_3$ Perovskite with Extremely High Surface Area and Excellent Activity in Methane Combustion, The Journal of Physical Chemistry C 112 (39) (2008) 15293–15298.

[258] R.K.C.D. Lima, M.S. Batista, M. Wallau, E.A. Sanches, Y.P. Mascarenhas, E.A. Urquieta-González, High specific surface area LaFeCo perovskites—Synthesis by nanocasting and catalytic behavior in the reduction of NO with CO, Applied Catalysis B: Environmental 90 (3) (2009) 441–450.

[259] Y. Wang, X. Cui, Y. Li, Z. Shu, H. Chen, J. Shi, A simple co-nanocasting method to synthesize high surface area mesoporous $LaCoO_3$ oxides for CO and NO oxidations, Microporous and Mesoporous Materials 176 (2013) 8–15.

[260] M. Rizwan, S. Gul, T. Iqbal, U. Mushtaq, M.H. Farooq, M. Farman, R. Bibi, M. Ijaz, A review on perovskite lanthanum aluminate ($LaAlO_3$), its properties and applications, Materials Research Express 6 (11) (2019) 112001.

[261] V.M. Goldschmidt, Die Gesetze der Krystallochemie, Naturwissenschaften 14 (1926) 477–485.

[262] M. Becker, T. Klüner, M. Wark, Formation of hybrid ABX_3 perovskite compounds for solar cell application: First-principles calculations of effective ionic radii and determination of tolerance factors, Dalton Trans. 46 (11) (2017) 3500–3509.

[263] H. Zhang, N. Li, K. Li, D. Xue, Structural stability and formability of ABO_3-type perovskite compounds, Acta Crystallographica Section B 63 (Pt 6) (2007) 812–818.

[264] C. Li, X. Lu, W. Ding, L. Feng, Y. Gao, Z. Guo, Formability of ABX_3 (X = F, Cl, Br, I) halide perovskites, Acta Crystallographica Section B 64 (Pt 6) (2008) 702–707.

[265] X. Luo, B. Wang, Structural and elastic properties of $LaAlO_3$ from first-principles calculations, Journal of Applied Physics 104 (7) (2008) 73518.

[266] E.A. Wood, A high temperature stage for the polarizing microscope, Mineralogical Society of America, (1951).

[267] P. Bouvier, J. Kreisel, Pressure-induced phase transition in $LaAlO_3$, Journal of Physics: Condensed Matter 14 (15) (2002) 3981–3991.

[268] S. Geller, V.B. Bala, Crystallographic studies of perovskite-like compounds. II. Rare earth alluminates, Acta crystallographica 9 (1956) 1019.

[269] U. Megha, K. Shijina, G. Varghese, Nanosized $LaCo_{0.6}Fe_{0.4}O_3$ perovskites synthesized by citrate sol gel auto combustion method, PAC 8 (2) (2014) 87–92.

[270] N. Escalona, S. Fuentealba, G. Pecchi, Fischer-Tropsch synthesis over $LaFe_{1-x}Co_xO_3$ perovskites from a simulated biosyngas feed, Applied Catalysis A: General 381 (1) (2010) 253–260.

[271] J. Zhu, D. Xiao, J. Li, X. Yang, Y. Wu, Effect of Ce on NO direct decomposition in the absence/presence of O_2 over $La_{1-x}Ce_xSrNiO_4$ ($0 \leq x \leq 0.3$), Journal of Molecular Catalysis A: Chemical 234 (1-2) (2005) 99–105.

[272] X. Yang, L. Luo, H. Zhong, Structure of $La_{2-x}Sr_xCoO_{4\pm\lambda}$ (x=0.0–1.0) and their catalytic properties in the oxidation of CO and C_3H_8, Applied Catalysis A: General 272 (1) (2004) 299–303.

[273] Y. Nishihata, J. Mizuki, T. Akao, H. Tanaka, M. Uenishi, M. Kimura, T. Okamoto, N. Hamada, Self-regeneration of a Pd-perovskite catalyst for automotive emissions control, Nature 418 (6894) (2002) 164–167.

[274] L. Bedel, A.C. Roger, C. Estournes, A. Kiennemann, Co^0 from partial reduction of La(Co,Fe)O_3 perovskites for Fischer-Tropsch synthesis, Catalysis Today 85 (2) (2003) 207–218.

[275] L. Bedel, A.C. Roger, C. Estournes, A. Kiennemann, in 219th ACS National Meeting. PETR-100 (American Chemical Society).

[276] L. Bedel, A.C. Roger, J.L. Rehspringer, Y. Zimmermann, A. Kiennemann, $La_{(1-y)}Co_{0.4}Fe_{0.6}O_{3-\delta}$ perovskite oxides as catalysts for Fischer-Tropsch synthesis, Journal of Catalysis 235 (2) (2005) 279–294.

[277] L. Bedel, A.C. Roger, A. Kiennemann, C. Estournès, Combined use of TPR and magnetic measurements under H_2 to determine the reduction process of a La(Co,Fe)O_3 perovskite series to be active in Fischer-Tropsch synthesis, American Chemical Society, Division of Petroleum Chemistry, Preprints 45 (2000) 236–239.

[278] C. Estournès, H. Provendier, L. Bedel, C. Petit, A.C. Roger, A. Kiennemann, Reducibility study of the $LaM_xFe_{1-x}O_3$ (M = Ni, Co) perovskites, MRS Online Proceedings Library 658 (1) (2001) 622.

[279] A. Kiennemann, C. Petit, A.C. Roger, V. Pitchon, Perovskites: a versatile material in heterogeneous catalysis, Current Topics in Catalysis 3 (2002) 147–160.

[280] L. Bedel, A.C. Roger, J.L. Rehspringer, A. Kiennemann, (eds Xinhe Bao & Yide Xu), Studies in surface science and catalysis 147 (2004) 319–324.

[281] M. Ao, G.H. Pham, V. Sage, V. Pareek, Structure and activity of strontium substituted $LaCoO_3$ perovskite catalysts for syngas conversion, Journal of Molecular Catalysis A: Chemical 416 (2016) 96–104.

[282] M. Ao, G.H. Pham, V. Sage, V. Pareek, Selectivity enhancement for higher alcohol product in Fischer-Tropsch synthesis over nickel-substituted $La_{0.9}Sr_{0.1}CoO_3$ perovskite catalysts, Fuel 206 (2017) 390–400.

[283] M. Ao, G.H. Pham, J. Sunarso, F. Li, Y. Jin, S. Liu, Effects of alkali promoters on tri-metallic Co-Ni-Cu-based perovskite catalyst for higher alcohol synthesis from syngas, Catalysis Today 355 (2020) 26–34.

[284] N. Fischer, R. Henkel, B. Hettel, M. Iglesias, G. Schaub, M. Claeys, Hydrocarbons via CO_2 Hydrogenation Over Iron Catalysts: The Effect of Potassium on Structure and Performance, Catalysis Letters 146 (2) (2016) 509–517.

[285] G. Liu, Y. Geng, D. Pan, Y. Zhang, T. Niu, Y. Liu, Bi-metal Cu–Co from $LaCo_{1-x}Cu_xO_3$ perovskite supported on zirconia for the synthesis of higher alcohols, Fuel Processing Technology 128 (2014) 289–296.

[286] G. Liu, T. Niu, D. Pan, F. Liu, Y. Liu, Preparation of bimetal Cu–Co nanoparticles supported on meso–macroporous SiO_2 and their application to higher alcohols synthesis from syngas, Applied Catalysis A: General 483 (2014) 10–18.

[287] G.L. Liu, T. Niu, A. Cao, Y.X. Geng, Y. Zhang, Y. Liu, The deactivation of Cu–Co alloy nanoparticles supported on ZrO_2 for higher alcohols synthesis from syngas, Fuel 176 (2016) 1–10.

[288] H. Zhan, F. Li, P. Gao, N. Zhao, F. Xiao, W. Wei, L. Zhong, Y. Sun, Methanol synthesis from CO_2 hydrogenation over La–M–Cu–Zn–O (M = Y, Ce, Mg, Zr) catalysts derived from perovskite-type precursors, Journal of Power Sources 251 (2014) 113–121.

[289] N. Tien-Thao, H. Alamdari, S. Kaliaguine, Characterization and reactivity of nanoscale $La(Co,Cu)O_3$ perovskite catalyst precursors for CO hydrogenation, Journal of Solid State Chemistry 181 (8) (2008) 2006–2019.

[290] N. Tien-Thao, M.H. Zahedi-Niaki, H. Alamdari, S. Kaliaguine, Conversion of syngas to higher alcohols over nanosized $LaCo_{0.7}Cu_{0.3}O_3$ perovskite precursors, Applied Catalysis A: General 326 (2) (2007) 152–163.

[291] M.R. Goldwasser, V.E. Dorantes, M.J. Pérez-Zurita, P.R. Sojo, M.L. Cubeiro, E. Pietri, F. González-Jiménez, Y.N. Lee, D. Moronta, Modified iron perovskites as catalysts precursors for the conversion of syngas to low molecular weight alkenes, Journal of Molecular Catalysis A: Chemical 193 (1) (2003) 227–236.

[292] T.W. Kim, F. Kleitz, J.W. Jun, H.J. Chae, C.U. Kim, Catalytic conversion of syngas to higher alcohols over mesoporous perovskite catalysts, Journal of Industrial and Engineering Chemistry 51 (2017) 196–205.

[293] N. Utsis, R. Vidruk-Nehemya, M. Landau, M. Herskowitz, Novel bifunctional catalysts based on crystalline multi-oxide matrices containing iron ions for CO_2 hydrogenation to liquid fuels and chemicals, Faraday discussions 188 (2016).

[294] P.F. Meier, Preparation of a perovskite-like Fischer-Tropsch catalyst composition for the manufacture of C_2–C_4. US20040024071A1 (2004).

[295] M.J. Reynhout, Fischer-tropsch catalyst support and catalyst. WO2008087147A1 (2008).

[296] L. Fratalocchi, C.G. Visconti, L. Lietti, N. Fischer, M. Claeys, A promising preparation method for highly active cobalt-based Fischer-Tropsch catalysts supported on stabilized Al_2O_3, Applied Catalysis A: General 556 (2018) 92–103.

[297] C. Yuan, *et al*. Low carbon dioxide selectivity Fischer-Tropsch catalyst and preparation method and application. CN103586034A (2014).

[298] C. Yuan, *et al*. Method for preparing liquid hydrocarbons by iron-based Fischer-Tropsch synthesis catalyst system. CN103589446A (2014).

[299] X. Gui, R. Jiang, Fischer-Tropsch synthesis method. CN103589447A (2014).

[300] J. Li, S. Zhang, X. Ni, Z. Yin, Q. Liu, Cobalt-based catalyst for synthesizing liquid hydrocarbons and its preparation method and application. CN103623828A (2014).

[301] X. Ni, X. Zhang, S. Zhang, J. Li, High-activity Fischer-Tropsch catalyst and preparation and application of the same. CN103785391A (2014).

[302] X. Ni, X. Zhang, S. Zhang, J. Li, Fischer-Tropsch catalyst and preparation and application of the same. CN103785392A (2014).

[303] X. Ni, S. Zhang, Z. Yin, J. Li, N. Chen, High-activity Fischer-Tropsch synthesis catalyst, and preparation method and application thereof 2 (2015).

[304] X. Ni, S. Zhang, Z. Yin, J. Li, N. Chen, High-activity Fischer-Tropsch synthesis catalyst, and preparation method and application thereof. CN104588022A (2015).

[305] X. Ni, S. Zhang, Z. Yin, J. Li, N. Chen, Slurry reactor Fischer-Tropsch synthesis catalyst, and preparation method and application thereof. CN104588033A (2015).

[306] C. Yuan, *et al*. Cobalt-based catalyst for CO hydrogenation and its preparation method and application. CN103599788A (2014).

[307] M. Marchese, G. Buffo, M. Santarelli, A. Lanzini, CO_2 from direct air capture as carbon feedstock for Fischer-Tropsch chemicals and fuels: Energy and economic analysis, Journal of CO_2 Utilization, 46 (2021) 101487.

3 Scope and objectives

The Fischer-Tropsch synthesis is a well-established route to convert syngas (H_2 and CO) derived from coal or natural gas to liquid fuels and petrochemical substitutes [1,2]. The iron-based catalysts are preferentially used in commercial operations, especially for coal derived syngas with low H_2/CO ratio, due to their water gas shift (WGS) activity, low cost, flexible operation conditions as well as reasonable products distribution [3–5]. To improve FTS performances (activity, selectivity and stability) of iron-based catalyst, promoters are normally added to the catalyst in form of chemical or electronic promoters [6]. The effects of potassium are explained in terms of electropositivity. The potassium is believed to transfer a charge to the metal surface, thereby enhancing CO adsorption and dissociation but inhibiting H_2 adsorption [7]. The addition of promoters is beneficial up to a certain amount (eg. Potassium $\leq$ 3 wt.-%), above which it becomes detrimental to the overall activity of the catalyst due to coverage of active sites. Excessive concentration of promoters can facilitate carbon deposition and induce catalyst deactivation [8,9]. Their mobility under reaction conditions is another challenge as it results in a highly dynamic system [10]. It is therefore hypothesized that incorporation of the promoter(s) into a perovskite like structure will result in a well-defined chemical speciation of the promoter species, contact with the catalytically active material, and will suppress promoter mobility. More importantly, inclusion of the promoter elements in the perovskite like structure will not change its promoting activity.

The objective of this study is to develop an empowered oxidic matrix material namely a perovskite, that doubles as a catalyst support and promoter for iron catalysts in the Fischer-Tropsch synthesis. This is achieved by incorporating promoters like potassium and manganese into the perovskite matrix to achieve and hopefully surpass known performance enhancement abilities in common synthesis techniques. Perovskites (ABO_3) exhibit a range of stoichiometries and crystal structures, and can accommodate around 90% of the metallic elements from the periodic table in positions A and/or B, without destroying the matrix structure [11,12]. Due to this flexibility, it is therefore expected that the incorporation of the promoter into the perovskite matrix can be achieved by changing the composition of the perovskite [13]. A successful incorporation of the promoters (K and Mn) in the perovskite structure will solve the long-standing problem of promoter mobility.

A facile technique for the synthesis of iron oxide nanoparticles with a mean crystallite size of 22 nm was followed as described in literature [14]. The empowered support material was prepared via a citrate sol gel auto combustion method [15]. The success of these synthesis method was determined by evaluating the nature, composition, stability and reactivity of the prepared materials using characterization techniques such

as X-ray diffraction (XRD), transmission/scanning electron microscopy (TEM/SEM), inductively coupled plasma spectroscopy (ICP), atomic absorption spectrometry (AAS), temperature programmed reduction (TPR) and X-ray absorption spectroscopy (XANES and EXAFS). The performance of the prepared model catalysts was evaluated using a laboratory continuous stirred tank reactor under low temperature Fischer-Tropsch reaction conditions. The deciding factor on good performance was the effect of the promoter on CO conversion and selectivity towards the various Fischer-Tropsch product classes compared with the promotion achieved via impregnation. The stability of the perovskites was also determined by characterization of the spent catalyst.

Due to the low surface area of the bulk perovskites, an attempt was made to prepare three dimensionally ordered mesoporous perovskites by filling in the voids of the template with the precursors of the target perovskite materials. The subsequent removal of the template reproduces their replica. The synthesis technique outlined by Arandiyan *et al*. [16] was adopted.

References

[1] O.O. James, A.M. Mesubi, T.C. Ako, S. Maity, Increasing carbon utilization in Fischer-Tropsch synthesis using H_2-deficient or CO_2-rich syngas feeds, Fuel Processing Technology 91 (2) (2010) 136–144.

[2] Q. Zhang, J. Kang, Y. Wang, Development of Novel Catalysts for Fischer-Tropsch Synthesis: Tuning the Product Selectivity, ChemCatChem 2 (9) (2010) 1030–1058.

[3] W. Ngantsoue-Hoc, Y. Zhang, R.J. O'Brien, Fischer-Tropsch synthesis: activity and selectivity for Group I alkali promoted iron-based catalysts, Applied Catalysis A: General 236 (2002) 77–89.

[4] S. Li, S. Krishnamoorthy, A. Li, G.D. Meitzner, E. Iglesia, Promoted Iron-Based Catalysts for the Fischer-Tropsch Synthesis: Design, Synthesis, Site Densities, and Catalytic Properties, Journal of Catalysis 206 (2) (2002) 202–217.

[5] T.R. Motjope, H. Dlamini, G.R. Hearne, N.J. Coville, Application of *in situ* Mössbauer spectroscopy to investigate the effect of precipitating agents on precipitated iron Fischer-Tropsch catalysts, Catalysis Today 71 (2002) 335–341.

[6] D.B. Bukur, D. Mukesh, S.A. Patel, Promoter effects on precipitated iron catalysts for Fischer-Tropsch synthesis, Industrial & Engineering Chemistry Research 29 (2) (1990) 194–204.

[7] M. Luo, B.H. Davis, Fischer-Tropsch synthesis: Group II alkali-earth metal promoted catalysts, Applied Catalysis A: General 246 (1) (2003) 171–181.

[8] Y. Yang, H.W. Xiang, Y.Y. Xu, L. Bai, Y.W. Li, Effect of potassium promoter on precipitated iron-manganese catalyst for Fischer-Tropsch synthesis, Applied Catalysis A: General 266 (2) (2004) 181–194.

[9] H.W. Pennline, M.F. Zarochak, J.M. Stencel, J.R. Diehl, Activation and promotion studies in a mixed slurry reactor with an iron-manganese Fischer-Tropsch catalyst, Industrial & Engineering Chemistry Research 26 (3) (1987) 595–601.

[10] M.E. Dry, Present and future applications of the Fischer-Tropsch process, Applied Catalysis A: General 276 (1-2) (2004) 1–3.

[11] D. Leckel, Diesel Production from Fischer-Tropsch: The Past, the Present, and New Concepts, Energy Fuels 23 (5) (2009) 2342–2358.

[12] T. Nitadori, M. Misono, Catalytic Properties of $LaAFeO_3$ (A = Sr Ce) and La -$CeCoO_3$, Journal of Catalysis 93 (1985) 459–466.

[13] M. Bradha, S. Hussain, S. Chakravarty, G. Amarendra, A. Ashok, Synthesis, structure and total conductivity of A-site doped $LaTiO_{3-\delta}$ perovskites, Journal of Alloys and Compounds 626 (2015) 245–251.

[14] X.C. Yang, Y.L. Shang, Y.H. Li, J. Zhai, N.R. Foster, Y.X. Li, D. Zou, Y. Pu, Synthesis of Monodisperse Iron Oxide Nanoparticles without Surfactants, Journal of Nanomaterials 2014 (2) (2014) 1–5.

[15] U. Megha, K. Shijina, G. Varghese, Nanosized $LaCo_{0.6}Fe_{0.4}O_3$ perovskites synthesized by citrate sol gel auto combustion method, PAC 8 (2) (2014) 87–92.

[16] H. Arandiyan, Y. Wang, J. Scott, S. Mesgari, H. Dai, R. Amal, *In Situ* Exsolution of Bimetallic Rh–Ni Nanoalloys: A Highly Efficient Catalyst for CO_2 Methanation, ACS Applied Materials & Interfaces 10 (19) (2018) 16352–16357.

4 Research Approach and Experimental Methodology

A series of $LaAlO_3$ based perovskites with a fixed amount of K and varying amounts of Mn were prepared using the polymeric precursor method. The perovskites were synthesized in bulk and with an elevated surface area, namely as three dimensionally ordered mesoporous (3DOM) perovskites using a templating technique. Iron oxide (maghemite γ-Fe_2O_3) with an average crystallite size of 22 nm was synthesized using a coprecipitation method and supported on the prepared perovskites. The composition of perovskites was analyzed using inductively coupled plasma spectroscopy (ICP) and atomic absorption spectrometry (AAS). Structure and particle sizes were extracted from transmission electron microscopy (TEM) and scanning electron microscope (SEM). X-ray diffractometry (XRD) and absorption spectroscopy (XAS) were used to study the crystalline phase and chemical state of the samples. In the following, a comprehensive description of the techniques employed in the synthesis, characterization and testing of the model catalyst is outlined.

4.1 Synthesis of La based perovskites

The polymeric precursor method for the synthesis of bulk perovskites was first outlined by Pichini [1] as an alternative to the commonly used ceramic method. The resulting materials from this method showed considerably smaller particle size and higher porosity. The method used here is a citrate sol gel auto combustion method fully described by Megha *et al*. [2] based on the polyesterification of citric acid and ethylene glycol to synthesize the perovskite. Compared to conventional methods, this synthesis route is relatively easy and allows good control of the product stoichiometry.

4.1.1 Synthesis of bulk perovskites

The $La_{1-x}K_xMn_yAl_{1-y}O_3$ perovskite of the ABO_3 structure was prepared using $La(NO_3)_3{\cdot}6H_2O$, $Al(NO_3)_3{\cdot}9H_2O$, KNO_3, $Mn(NO_3)_2{\cdot}4H_2O$, citric acid (all Sigma Aldrich), ethylene glycol and nitric acid (Kimix) and deionized water without any further purification. The precursor solution was first prepared by mixing equimolar amounts of precursor salts, 5 g $La(NO_3)_3{\cdot}6H_2O$ and 4.33 g $Al(NO_3)_3{\cdot}9H_2O$, with 4.83 g citric acid, 1.5 ml nitric acid (assay min. 60%), and 150 ml deionized water. Citric acid acts as a chelating agent and organic fuel during the calcination process. Nitric acid is used as a catalytic medium. The solution

was ultra-sonicated to completely dissolve the salts followed by heating to 60 °C under stirring on a magnetic stirrer at which point 4.28 g ethylene glycol was added. Ethylene glycol is used as a stabilizing and capping agent to facilitate the control of particle size by retarding the particle growth after nucleation. The solution was heated to 90 °C and held for 1 hr to allow for polyesterification, and then transferred to a hot mantle at 100 °C for another hour to dehydrate and form a gel. The resulting gel was heated to 350 °C on a hot mantle resulting in swelling, foaming and auto combustion, yielding a black powder. The powder was well ground in a mortar and calcined at 800 °C for 6 hrs in static air in a Labofurn furnace (Kiln Contracts) to produce the perovskite.

For compounds $La_{0.9}K_{0.1}Mn_yAl_{(1-y)}O_3$ (y = 0, 0.2, 0.4, 0.8), the same method was used with equimolar amounts of metal cations on the A and B site of the perovskite structure (A = $La_{0.9}K_{0.1}$, B = $Mn_xAl_{(1-x)}$). For instance, in the synthesis of $La_{0.9}K_{0.1}Mn_{0.2}Al_{0.8}O_3$, 4.33 g $La(NO_3)_3{\cdot}6H_2O$, 0.116 g KNO_3, 3.5 g $Al(NO_3)_3{\cdot}9H_2O$ and 0.412 g $Mn(NO_3)_2{\cdot}4H_2O$ were used. Figure 4-1 illustrates schematically the steps followed to synthesize bulk perovskites.

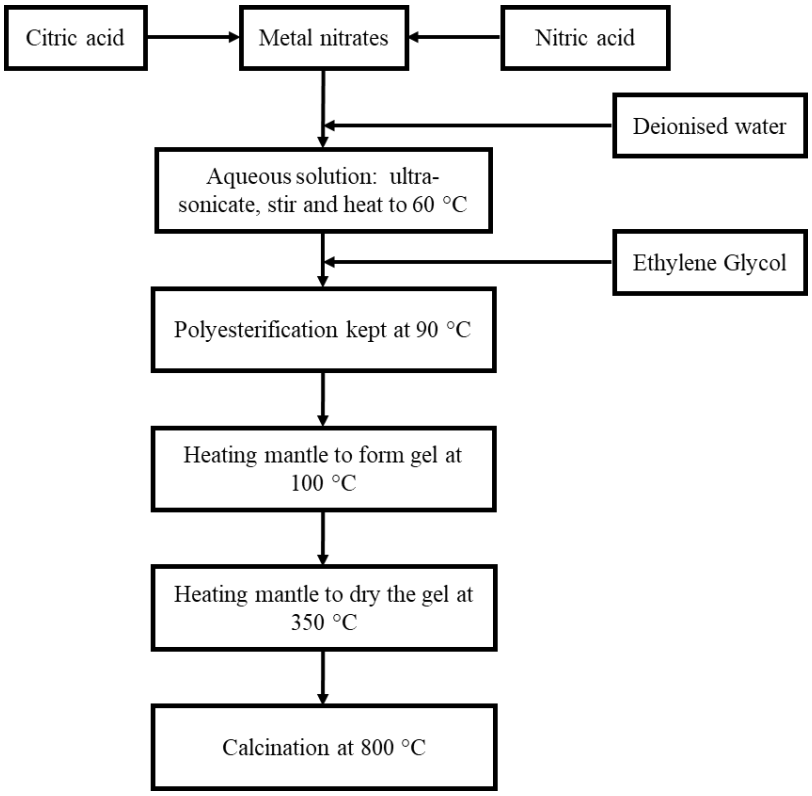

Figure 4-1: Flow chart for the preparation of perovskites by the citrate sol gel auto combustion method.

4.1.2 Synthesis of high surface area perovskites

The 3DOM perovskites were synthesized by infiltration of the target perovskite precursor solution into the interstitial void spaces of the three dimensionally aligned monodisperse poly-methyl methacrylate (PMMA) microspheres. The PMMA colloid consists of monodispersed spheres with face-centered (fcc) closed packing. When the 3D network of the resulting voids is infiltrated with the perovskite precursor and subsequently the PMMA spheres are removed, their replica is reproduced [3–6].

Well-arrayed colloidal template PMMA microspheres with an average diameter of approximately 250 nm were synthesized by adopting the procedures described by Arandiyan *et al*. [7]. The chemicals used were potassium persulfate ($K_2S_2O_8$) and methyl methacrylate $(C_5O_2H_8)_n$ (all Sigma Aldrich). 3 mmol of $K_2S_2O_8$ was mixed with 1500 ml of deionized water under stirring (400 rpm) and heated to 70 °C while degassing with nitrogen. $K_2S_2O_8$ was used as an initiator to synthesize the PMMA seed latex. After about thirty minutes at 70 °C, 115 ml of methyl methacrylate was poured into the flask, and the resulting suspension was stirred at 70 °C for 1 hr. The deionized water was evaporated in an oil or water bath at 80 °C to obtain a wet dense material which was dried at room temperature for two days. The slow evaporation is essential to obtain a packed colloidal crystal. The obtained template was ground with an agate mortar.

The diameter of the PMMA microspheres can be controlled by adjusting a number of variables. Increasing the amount of the monomer or $K_2S_2O_8$ increases the microsphere diameter, while increasing the temperature of the polymerization reaction or N_2 flow decreases the microsphere diameter. The particles obtained after grinding can also be adjusted to a desired size using testing sieves.

3DOM perovskites structures are achieved by filling in the voids of the template with the precursors of the target materials. The process of filling in the voids with the precursor solution is purely driven by capillary forces [8–10]. The synthesis method uses an ethylene glycol – methanol mixed solution of the metal nitrates as a precursor solution for the 3DOM perovskites. 10.0 g of $LaNO_3.6H_2O$ and 8.66 g $Al(NO_3)_3{\cdot}9H_2O$ (equimolar) was dissolved in 5 ml ethylene glycol by very slow stirring in a 100 ml beaker at room temperature (slow stirring overnight is essential to ensure a homogeneous solution). The produced ethylene glycol solution was transferred into a 25 ml volumetric flask, to which 10 ml methanol and 10 ml ethylene glycol were added. The crashed colloidal crystals were soaked in the solution and infiltration of the precursor solution into the particles was observed. The process took between 24 and 48 hours and was terminated once the color of the spheres changed to the color of the solution. The excess solution was separated from the impregnated PMMA colloidal crystals by vacuum filtration. The obtained sample was

allowed to dry in air at room temperature overnight. About 0.5 g of the sample was mixed with 2.5 g of silicon carbide (10–15 mesh) and calcined at 800 °C for 5 hours in a glass tube reactor in an air flow of about 50 ml/min. Removal of spheres in oxygen is an exothermic reaction so slow heating, high air flowrates and dilution with SiC have proven to be very important for rapid heat removal to avoid the collapse of the porous structure (see Figure 4-2) [11,12] .

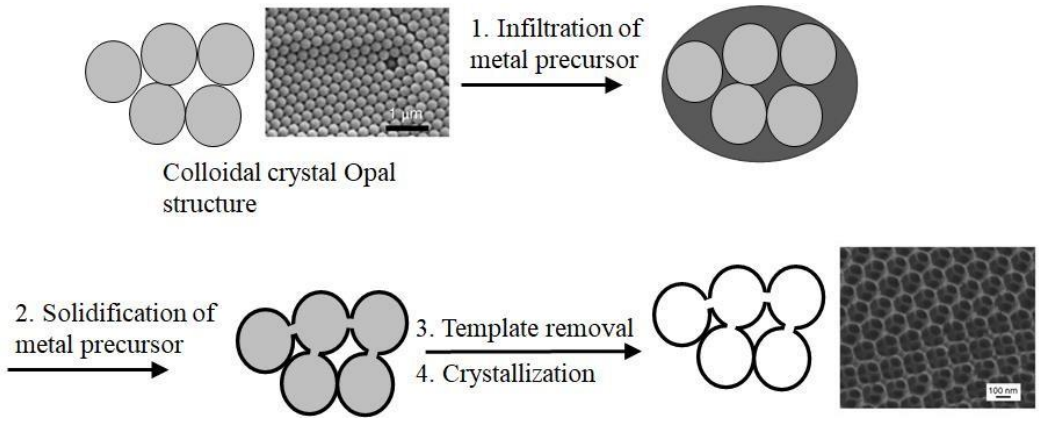

Figure 4-2: Preparation of 3DOM materials using colloidal crystal templates (from [13]).

4.2 Synthesis of iron oxide nanoparticles

The method for the preparation of iron oxide nanoparticles of around 22 nm was reported by Yang *et al*. [14]. The coprecipitation method described was based on a number of previous publications [15–18]. pH played a very important role to obtain a stable system for the synthesis of iron oxide nanoparticles. $FeCl_2 \cdot 4H_2O$, hydrochloric acid (HCl) (Sigma Aldrich), and ammonium hydroxide $NH_3 \cdot H_2O$ (Kimix) were used for the synthesis. A 0.25 M $FeCl_2 \cdot 4H_2O$ solution, a 5.4 M NaOH solution, a 1.34 M $NH_3 \cdot H_2O$ solution, and a 0.1 M HCl solution were first prepared with deionized water. 40 ml of each of 0.25 M of $FeCl_2 \cdot 4H_2O$, 5.4 M NaOH and 1.34 M $NH_3 \cdot H_2O$ solutions were mixed together (see Figure 3). The mixture was stirred on a magnetic stirrer in the fume hood and heated up to 90 °C under an inert atmosphere of nitrogen. The solution was kept at the temperature for 1.5 hours after which the pH was adjusted to 2.5 by dropwise addition of 40 ml of 0.1 M HCl solution. The slurry was then washed 20 times with boiling deionized water to remove residual chloride ions (see Figure 4-3) [19].

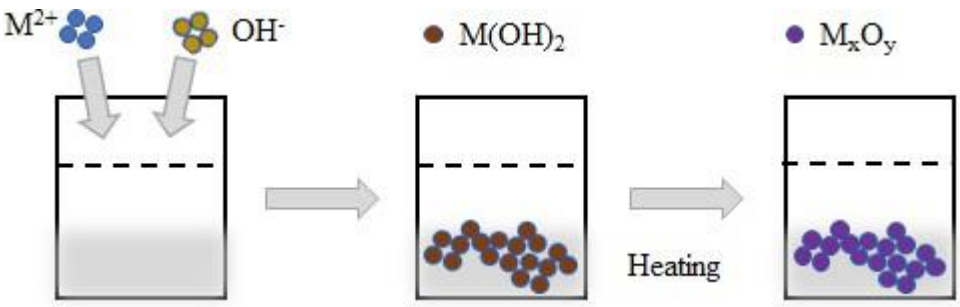

Figure 4-3: Schematic representation of iron oxide nanoparticle synthesis (from [14]).

4.3 Preparation of model catalysts

4.3.1 Preparation of model catalyst using conventional supports

Four supports, γ-alumina (Puralox SCCa 5–150, Sasol Technology), TiO_2 (P25) (from Evonik Industries), ZrO_2 (US Nano) and SiO_2 (Sigma-Aldrich, particle size 60–100 mesh, surface area 300 m^2/g, pore diameter 150 Å) were used to prepare baseline model catalysts. Before anchoring iron oxide on the support, the powders were first calcined at 300 °C in a Labofurn furnace in stagnant air for 5 hrs to remove adsorbed surface water and other contaminants. After cooling down to room temperature, the supports were removed from the furnace and used immediately for model catalyst synthesis. To prepare a model catalyst of 20 wt.-% Fe_2O_3, 1.43 g of Fe_2O_3 was sonicated in 500 ml of deionized water for 1 hr to disperse the nanoparticles. The support material was then placed in the suspension and further sonicated for 1hr. The nanoparticle support mixture was subsequently dried in a rotary evaporator at 80 °C and 150 mbar. The catalyst was finally dried on a watch glass at 120 °C in a Memmert oven overnight.

4.3.2 Preparation of model catalyst using bulk perovskites

After calcination at 800 °C (described in section 4.1.1), the perovskite supports were either used immediately for catalyst synthesis or stored in a closed crucible at 120 °C in a Memmert oven. The supporting method outlined in section 4.3.1 was followed to deposit the iron oxide nanoparticles.

To develop a system to compare the promoted perovskites by incorporation with traditionally promoted systems, a $LaAlO_3$ perovskite was impregnated with KNO_3. In this synthesis, 0.38 g of KNO_3 was dissolved

in 100 ml of deionised water and poured into a $LaAlO_3$ powder in a rotary evaporator to obtain an overall potassium loading of 1.92 wt.-%, which is the absolute amount incoporated in the potassium containing perovkites. The evaporation was carried out at 80 °C and 150 mbars. The sample was then allowed to dry overnight in a Memmet oven at 120 °C followed by calcination at 350 °C in air in a glass fluidized bed reactor for 5 hours, using a ramp rate of 2 °C/min. Lower loadings of 1.0 wt.-% and 0.5 wt.-% K were also prepared following the same procedure. The K impregnated $LaAlO_3$ were then used as support for the iron oxide nanoparticles following the procedure described in section 4.3.1.

4.3.3 Preparation of model catalyst using 3DOM perovskites

Incipient wetness impregnation [20] was used to deposit the iron precursor onto the 3DOM perovskites. The metal salt, 7.49 g $Fe(NO_3)_3 \cdot 9H_2O$, was dissolved in 30 ml of deionized water and then added to the 3DOM perovskite support to obtain a loading of 16 wt.-% Fe. The incipient wetness was achieved by saturating the dry support with the metal precursor solution until a paste formed. The volume of solution required to form a paste was noted. The catalyst was then dried in the rotary evaporator at 80 °C and 150 mbars. The remaining precursor solution was topped with deionized water to the volume used in the first impregnation step and the second impregnation is carried out with the dried material. After drying in the rotary evaporator, the sample was dried overnight in a Memmet at 120 °C. The catalyst was finally calcined at 300 °C in flowing air for 5 hours with a ramp rate of 2 °C/min.

4.4 Characterization of prepared materials

4.4.1 X-ray diffraction

Offline XRD analysis was performed on all the prepared samples to determine the species and phases present in the sample. The diffraction patterns were compared with known diffraction patterns listed in the International Centre for Diffraction Data (ICDD) Powder Diffraction File-2 (PDF-2) database. The diffraction patterns were acquired on a D8 Advance diffractometer (Bruker, Germany) equipped with a position-sensitive detector (LYNXEYE) in Bragg Brentano geometry with a Co anode in the 2θ range of 20−120° (1/d = 0.19−0.97 $Å^{-1}$) using a step size of 0.043° and with a time per step of 0.75 s. The total scan time amounts to 30 min.

4.4.2 Transmission electron microscopy

To determine the size distribution of the iron oxide nanoparticles and study the structure of the perovskite support samples, transmission electron microscopy (TEM) was used. For the supported material, TEM was also used to determine how well dispersed the nanoparticles were on the support. 100% ethanol was first added to the powder sample and the mixture was sonicated in an ultrasonic bath for 15 minutes in order to obtain a suspension. A droplet of the suspension was then transferred on to a carbon coated copper grid. The grids were allowed to air dry before analysis in a Tecnai F20 transmission electron microscope operated at 200 kV.

Scanning Transmission Electron Microscopy (STEM) was also used to characterize the perovskites. An Energy Dispersive X-ray Analyzer (EDX or EDA) was employed extensively to provide elemental identification and quantitative compositional information on the surface of perovskite samples. STEM EELS (electron energy loss spectroscopy) which allows the fine structure of ionization edges to be observed, was used for elemental mapping. These analyses were performed using a field emission FEI Tecnai F20 microscope, operated at 200 kV, and equipped with a high-angle annular dark-field (HAADF) detector for Z-contrast imaging. Before conducting any measurements, the powder samples under investigation were sonicated in 100% ethanol and the suspension supported onto lacey carbon coated copper grids (SPI Supplies, 200 mesh). TEM and STEM micrographs were analyzed using the freeware imageJ to obtain particle size distributions [21]. An attempt was made to measure at least 300 particles to ensure statistical relevance of the data. Selected samples of bulk perovskites were analyzed at the Centre for High-Resolution TEM at the Nelson Mandela university (NMU), in South Africa. The images were taken in a JEM-ARM200F microscope (Jeol) equipped with a field emission cathode and an integrated correction of the spherical aberrations of the objective and condenser lenses. The instrument is fitted with an advanced GIF electron spectrometer with dual EELS capabilities, as well as with an XMax 100 TLE high collection angle, ultra-sensitive detector (Oxford Instruments) for analysis by means of EDS.

4.4.3 Atomic absorption spectroscopy and inductively coupled plasma optical emission spectrometry

Atomic absorption spectroscopy (AAS) and inductively coupled plasma optical emission spectrometry (ICP-OES) were used to determine metal loadings and perovskite compositions. For AAS, the sample is first ground, and then 0.1 g is placed into a wide-mouthed 250 ml Erlenmeyer flask. The digestion of the

sample was carried out by adding 10 ml of a 4:1 HCl/HF mixture and bringing the mixture to boil, after which 10 ml of HNO_3 was added to the flask until the sample volume was reduced through evaporation to approximately 2 ml. 5 ml of $HClO_4$ was added and again boiled until approximately 2 ml of sample remained. At this point a white cloud was observed indicating that a reaction had taken place. The solution was allowed to cool before transferring the sample into a 100 ml volumetric flask and filled up to 100 ml with distilled water. The liquid sample was filtered through a Whatman No. 1 filter paper and submitted to the AAS spectrometer for analysis.

For the ICP-OES analysis, the samples were digested in 3 ml of HCl, 3 ml of HF and few drops of HNO_3 in a reactor containing bi-distilled water. The mixture was then heated to 130 °C, stirred for about an hour and then cooled under a jet of water. To make sure that there is no residue, 60 ml of H_3BO_3 was added under stirring. The solution was subsequently filtered and transferred to a volumetric flask. The solution was injected into a Varian OES 730 Series spectrometer. Elements could then be identified and quantified based on the standards available [22].

4.4.4 Brunauer-Emmett-Teller surface area measurement

N_2 physisorption analysis was conducted to determine the mass specific surface area and pore size distributions of both the bulk and 3DOM perovskites using a BET Micrometrics TriStar 3000.
0.5 g of sample was loaded into a glass tube and pre-treated to remove water. The sample was first kept at 90 °C for 1 hr and then heated to 350 °C at a constant heating rate of 10 °C/min, holding it for 4 hrs. The sample was cooled and transferred to a BET machine where it was further cooled to cryogenic temperature (-196 °C). Nitrogen was introduced to the sample in a series of precisely controlled pressures. As the pressure increased, the number of gas molecules adsorbed on the surface also increased. The equilibrated pressure (P) and the saturation pressure (P^0) are determined to obtain the relative pressure ratio (P/P^0) which is recorded, together with the quantity of gas adsorbed by the sample at each equilibrated pressure.

4.4.5 Temperature programmed reduction

Temperature programmed reduction (TPR) was used to determine the reduction behavior of the supported samples. The reduction was carried out in a U-type quartz reactor on a Micromeritics Auto Chem 2910 (Micromeritics Instrument Corp., USA) equipped with a thermal conductivity detector (TCD) to measure hydrogen consumption. 50 mg of a supported iron sample was first dried by flowing argon (10 ml

(NTP)/min) through the system and heating it to 110 °C (heating rate: 10 °C/min) and holding for 60 minutes. The system was then cooled to 60 °C. 5% hydrogen in argon (50 ml (NTP)/min) was flown through the sample and the system was heated to 900 °C at a heating rate of 5 °C/min.

4.4.6 X-ray absorption spectroscopy

X-ray absorption spectroscopy (XAS) experiments were performed at the Diamond Light Source, UK's national synchrotron science facility, located at the Harwell Science and Innovation Campus in Oxfordshire. Access to the B18 beamline was granted via the UK catalysis Hub's Block Access Group. The samples were bulk perovskites incorporated with potassium and/or manganese as prepared, after exposure to activation conditions used for reduction of FT iron catalyst (16 $ml \cdot min^{-1} \cdot g_{catalyst}^{-1}$ at 450 °C with a ramp rate of 2 $°C \cdot min^{-1}$ and held for 15 hrs) and after 48 hours under FTS conditions mentioned in chapter 4.5.2. The analysis was performed at the potassium and manganese K-edges and compared to references KO_2, $KHCO_3$, $KAlO_2$, K_2MnO_4 and $LaMnO_3$. All references were chosen based on their possible presence in the samples under investigation and the chemical nature of the potassium and manganese atom. For each sample, the average spectra of 3 scans was analyzed to improve the signal/noise ratio. The as prepared and pre-reduced samples were deposited onto sticky Kepton film prior to analysis. The spent samples are encased in wax and were analyzed as is. Data processing was performed using Athena from the Demeter software package [23].

4.4.7 *In situ* X-ray diffraction

The in house developed *in situ* XRD capillary cell [24,25] was used to monitor the bulk reduction and formation behavior of the selected supported γ-Fe_2O_3 nanoparticles under the following conditions. The reduction was conducted in a continuous H_2 flowrate 40 $ml \cdot min^{-1} \cdot g_{catalyst}^{-1}$ while heating the cell to 450 °C at 2 $°C \cdot min^{-1}$ and held for 15 hrs to simulate the offline model catalyst activation. Following reduction, the formation of carbide species was done simulating reaction conditions of the FTS in the continuous stirred tank reactor. The reduction temperature was subsequently reduced to 240 °C, and the catalyst exposed to a 2:1 mixture of H_2 and CO allowing the pressure to increase from atmospheric to the pressure of 13.5 bar. The catalyst was held at these conditions for 250 min at a space velocity of 383 $ml \cdot min^{-1} \cdot g_{catalyst}^{-1}$ while taking the scans at the narrow scan range of 1/d = 0.2948 to 0.6583 $Å^{-1}$ to reduce the amount of time per scan. The *in situ* XRD cell is attached to a laboratory XRD (Bruker D8 Advance) operated at 47 kV and 35 mA equipped with a molybdenum source (λ = 0.7107 Å) and a position sensitive detector (Bruker AXS

Vantec). The obtained diffraction patterns were evaluated against the reference patterns recorded in the ICDD PDF-2 and analyzed using Rietveld refinement techniques [26] available in the TOPAS 5 (BRUKER) software.

4.5 Fischer-Tropsch Synthesis Experiments

4.5.1 Experimental setup

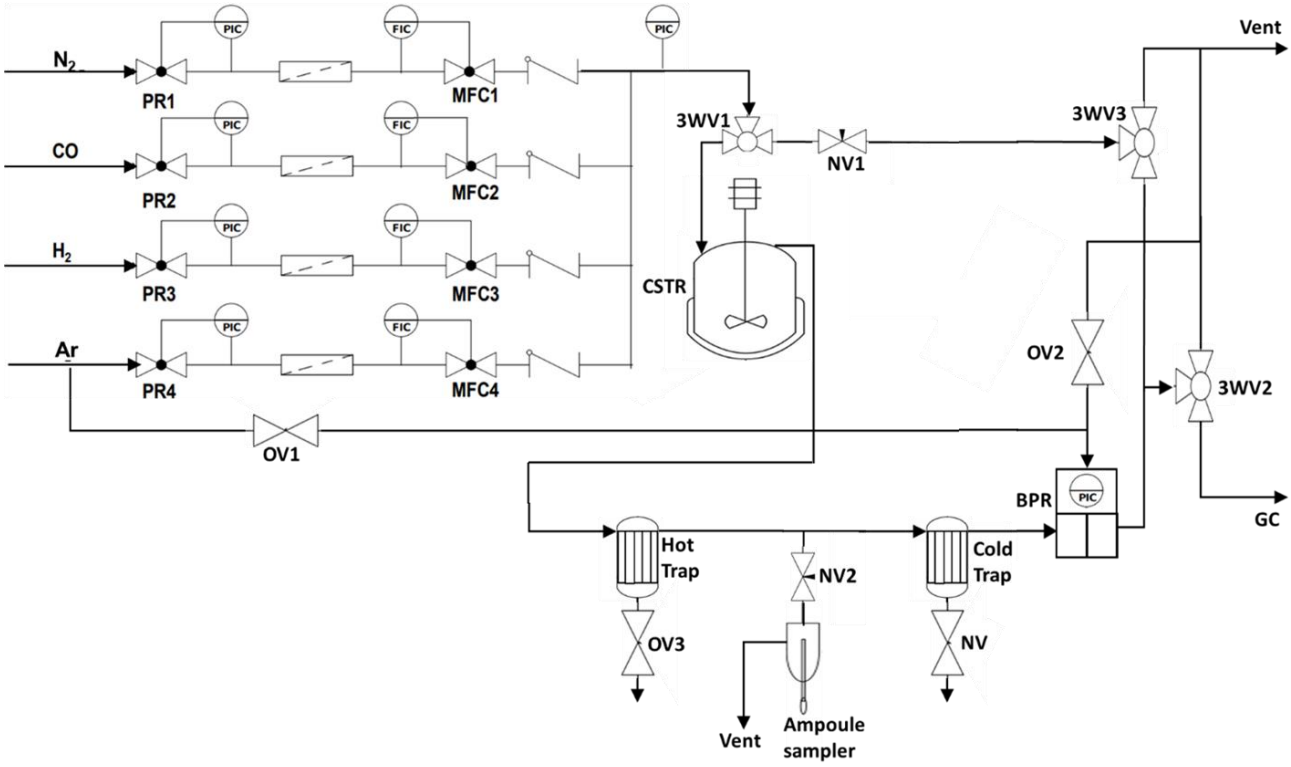

Figure 4-4: Experimental reactor set up. PR1-4: pressure regulators, MFC1-4: mass flow regulators/controllers, 3WV1-2: three-way valves, NV1-2: needle valve, BPR: backpressure regulator, PIC: pressure indicator and control, FIC: flow indicator control, CSTR: continuously stirred tank reactor, OV1-3: one way valve.

The schematic representation of the slurry reactor test unit used to carry out FT runs is shown in Figure 4-4. Before each FT run, the slurry type 600 ml continuous stirred tank reactor (CSTR), pre-loaded with wax

and reduced catalyst (see chapter 4.5.2 for details), was pressurized with argon through mass flow controller MFC4 and the temperature was ramped to 240 °C. The pressure of the system was controlled by a dome loaded back pressure regulator with Ar as pressurizing gas. During operation, syngas with some nitrogen as internal standard was fed to the reactor through mass flow controllers MFC1 to 3.

Liquid products were collected as wax from the hot trap and as mixture of water and lower hydrocarbon liquids in the cold trap. Gaseous samples were collected in pre-evacuated ampoules from the ampoule sampler [27].

4.5.2 Experimental procedure

5 g of supported iron oxide catalyst was activated or reduced *ex situ* in a tubular furnace. The temperature was increased to 450 °C using a heating ramp rate of 2 °C/min and the catalyst was kept at 450 °C for 15 hrs fluidized in a hydrogen flow of 80 ml/min. At the end of reduction process, the reduced catalyst was cooled to room temperature and the gas was changed to argon. Meanwhile, 50 g of wax (Sasol H, specifications in Table 4.1) was melted at 140 °C under a blanket of argon. The catalyst was carefully transferred into the wax, making sure to avoid any contact with air. After the molten wax was cooled to room temperature a wax pellet containing the reduced catalyst was obtained. This pellet was added to a 600 ml stainless steel CSTR pre-loaded with 300 g of molten wax at 140 °C and slowly flushed with argon. The reactor was then sealed, slowly pressurized with argon to 15 bar and heated to 240 °C at a stirring speed of 150 revolutions per minute (rpm).

Upon reaching the reaction pressure and temperature, the stirring speed was increased to 350 rpm and synthesis gas (H_2/CO = 2) with 10 vol.% of nitrogen, acting as internal standard for the gas chromatograph, was introduced to the reactor. The gaseous products after the hot and cold traps were analyzed online with a gas chromatograph (GC) fitted with a thermal conductivity detector (TCD) detector to determine the relative amounts of products and educts in the gas product stream to determine CO conversion and CO_2 and CH_4 selectivity (see chapter 4.6 for more details). The GC-TCD was programmed to take a sample every 10 minutes for the duration of the FT run. The system took three to four hours to reach steady state. Gaseous samples after the hot trap were collected in pre-evacuated ampoules every 24 hours of the 48 hours FT synthesis run [27]. The samples in the ampoules were analyzed off-line using a gas chromatograph equipped with a flame ionization detector (GC-FID).

Table 4-1: Sasol wax specifications [28].

Wax properties	Units	Specification	Typical values
Congealing point	°C	96 - 100	97
Color	Saybolt	+ 15 min	+ 22
Oil content	mass%	-	< 0.2
Molecular weight	Dalton	-	880
Brookfield viscosity at 135 °C	cP	6-10	8
Penetration at 25 °C	0.1 mm	1 max	1

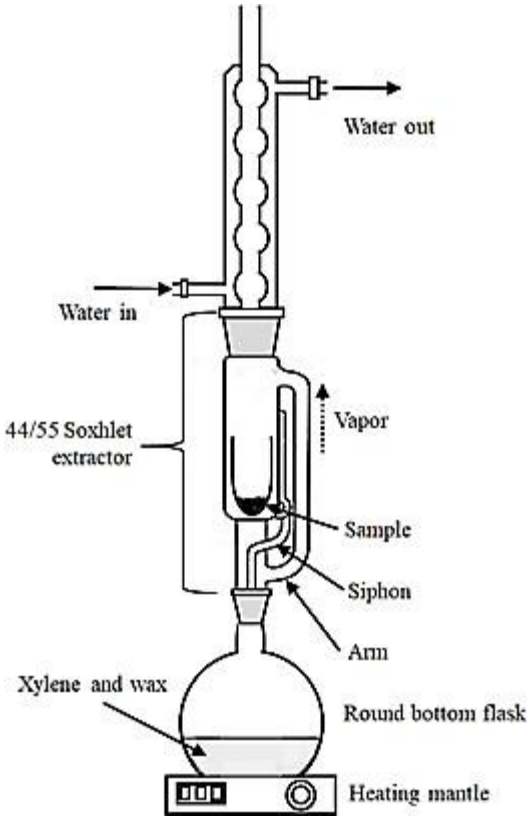

Figure 4-5: 1000 ml Glass Soxhlet Extraction set up.

At the end of the run, the gases were switched off, the reactor was cooled to 140 °C and the contents of the hot and cold traps removed. The reactor was depressurized, sending the gases to the vent. The spent catalyst was allowed to settle at the bottom of the reactor and the wax free of the catalyst was scooped out. In selected cases, parts of the wax encased catalyst was transferred to a Soxhlet extraction unit to remove any organics (see Figure 4-5). A round bottom flask was half filled with 500 ml of xylene and secured in a heating mantle. A 44/55 Soxhlet, in which a cellulose thimble containing the wax covered spent catalyst, was inserted on top of the flask. The set up was completed with a condenser placed on top of the Soxhlet, attached to a water inlet. The xylene was heated to boil (140 °C), at which point the vapor travelled up the bypass arm and was condensed into the Soxhlet. The unit was left to reflux for 4 days after which the sample was washed from the thimble into a beaker with ethanol and allowed to dry in the fume hood.

4.6 Product analysis

The tail gases were sampled in an Agilent Technologies 7820a GC-TCD with two parallel columns (column 1: Porapak Q 80/100 SST, column 2: MolSieve 5Å, 60/80 SST) fitted with a single-filament design that provides lower noise and higher sensitivity. The detector and oven are heated to 250 °C and 50 °C respectively, with a run time of 10 minutes. This allowed real time monitoring of the conversions and product yield. Conditions of the analysis are listed in Table 4-2. The GC is calibrated periodically using a standard calibration gas mix, with a known content of hydrogen, carbon monoxide, nitrogen, argon, methane and carbon dioxide. The response factors (f_i) for CH_4, CO and CO_2 were calculated using N_2 as an internal reference (see Equation 4.1).

$$\frac{n_i}{n_{N_2}} = f_i \frac{A_i}{A_{N_2}} \qquad 4.1$$

Where; f_i is the response factor for compound i.

n_i and n_{N_2} are the molar flow rates of compound i and N_2 respectively.

A_i and A_{N_2} are the areas in the TCD chromatogram of compound i and N_2 respectively.

The CO conversion can be calculated according to

$$X_{CO} = \frac{n_{CO,in} - n_{CO,out}}{n_{co,in}} \quad 4.2$$

Where; X_{CO} is the conversion of CO.

$n_{CO,in}$ and $n_{CO,out}$ are the molar flow rates of CO in the feed and tail gas respectively.

The methane selectivity (S_{CH_4}) and CO_2 selectivity (S_{CO_2}) were calculated according to

$$S_{CH_4} = \frac{n_{CH_4,out}}{n_{CO,in}.X_{CO}} \quad 4.3$$

$$S_{CO_2} = \frac{n_{CO_2,out}}{n_{CO,in}.X_{CO}} \quad 4.4$$

Where; $n_{CH_4,out}$ and $n_{CO_2,out}$ are the molar flows rates of CH_4 and CO_2 in tail gas respectively.

$n_{CO,in}$ is the molar flow rate of CO in the feed.

Table 4-2: Experimental conditions of GC-TCD Agilent Technologies 7820A.

Oven temperature	70 °C
Detector temperature	250 °C
Column 1	Porapak Q 80/100 SST
Column 2	MolSieve 5Å, 60/80 SST
Carrier gas	argon
Reference gas	argon
Reference flow	15 ml/min
Makeup flow	3 ml/ min
Analyzed gases	Column 1: N_2, CH_4, CO Column 2: CO_2

A GC with a flame ionization detector (FID) (Varian CP-3800 GC) was used for offline analysis of organic products in the gas phase under reaction conditions. The glass ampoules collected during the FT experimental run were broken at the tip and the sample collected in a GC syringe to be injected into the column injector.

The FID is carbon specific in its response. The signal intensity of hydrocarbons in the FID is proportional to the number of carbon atoms, however the response of all carbon atoms is not equal. For instance, carbon atoms bonded to an oxygen atom result in a weaker response. Kaiser [29] developed an incremental method of calculating the response factor by assigning every carbon-carbon bond a value of 1, a carbon-oxygen single-bond a value of 0.55 and a carbon-oxygen double bond is assigned a value of 0.

The response factor of a specific compound can be calculated according to

$$f_i = \frac{N_{C,i}}{N_{C(noO)} + 0.55(N_{C(CO)})} \qquad 4.5$$

Where; f_i is the response factor for compound i.

$N_{C,i}$ is the total number of carbon atoms.

$N_{C(noO)}$ is the number of carbon atoms not bonded to an oxygen atom.

$N_{C(CO)}$ is the number of carbon atoms with a single bond to oxygen.

To quantify the data collected, methane quantified in the online GC-TCD was used as the internal reference component. The quantity of compound i could thus be calculated on a molar basis according to

$$n_i = n_{CH_4} \frac{N_{C,CH_4}}{N_{C,i}} \cdot \frac{f_i . A_i}{f_{CH_4} . A_{CH_4}} \qquad 4.6$$

Where; n_i is the molar flow rate of compound i.

N_{C,CH_4} is the number of carbon atoms in methane (equal to 1).

$N_{C,i}$ is the number of carbon atoms in compound i.

A_i is the peak area of compound i in the FID chromatogram.

f_i is the response factor for compound i described in equation 4.5.

Using the calculated molar flow rates of reactants and products, the selectivity can be determined. The selectivity (S_i) can be determined according to

$$S_i = \frac{Y_i}{X_{CO}} \tag{4.7}$$

Where Y_i is the yield of compound i given by

$$Y_{i,C} = \frac{n_{i,out}}{n_{CO,in}} \tag{4.8}$$

On a carbon basis, the $S_{i,C}$ can be determined by

$$S_{i,C} = \frac{Y_{i,C}}{X_{CO}} \tag{4.9}$$

The selectivity of hydrocarbons in the C_{5+} range is calculated by

$$C_{5+} = 100 - \sum_{i=1}^{4} S_{C,i} \tag{4.10}$$

The chain growth probability between C_3 and C_8 can be determined according to

$$\alpha = 10^{\frac{\Delta \log(n_i)}{\Delta C_n}} \tag{4.11}$$

Where n_i is the molar flowrate of component 'i' C_n is the Carbon chain with 'n' chain length.

References

[1] M.P. Pechini US3330697A, (1967).

[2] U. Megha, K. Shijina, G. Varghese, Nanosized $LaCo_{0.6}Fe_{0.4}O_3$ perovskites synthesized by citrate sol gel auto combustion method, PAC 8 (2) (2014) 87–92.

[3] B. Gates, Y. Xia, Fabrication and Characterization of Chirped 3D Photonic Crystals, Advanced Materials 12 (18) (2000) 693–713.

[4] H. Míguez, F. Meseguer, C. López, F. López-Tejeira, J. Sánchez-Dehesa, Synthesis and Photonic Bandgap Characterization of Polymer Inverse Opals, Advanced Materials 13 (6) (2001) 393–396.

[5] A.D. Dinsmore, J.C. Crocker, A.G. Yodh, Self-assembly of colloidal crystals, Current Opinion in Colloid & Interface Science 3 (1) (1998) 5–11.

[6] Y. Xia, B. Gates, Y. Yin, Y. Lu, Monodispersed Colloidal Spheres: Old Materials with New Applications, Advanced Materials 12 (10) (2000).

[7] H. Arandiyan, Y. Wang, J. Scott, S. Mesgari, H. Dai, R. Amal, In Situ Exsolution of Bimetallic Rh–Ni Nanoalloys: A Highly Efficient Catalyst for CO_2 Methanation, ACS Applied Materials & Interfaces 10 (19) (2018) 16352–16357.

[8] A. Stein, F. Li, N.R. Denny, Morphological Control in Colloidal Crystal Templating of Inverse Opals, Hierarchical Structures, and Shaped Particles, Chemistry of Materials 20 (3) (2008) 649–666.

[9] A. Stein, B.E. Wilson, S.G. Rudisill, Design and functionality of colloidal-crystal-templated materials--chemical applications of inverse opals, Chemical Society Reviews 42 (7) (2013) 2763–2803.

[10] N.D. Petkovich, A. Stein, Controlling macro- and mesostructures with hierarchical porosity through combined hard and soft templating, Chemical Society Reviews 42 (9) (2013) 3721–3739.

[11] A. Stein, R.C. Schroden, Colloidal crystal templating of three-dimensionally ordered macroporous solids: Materials for photonics and beyond, Current Opinion in Solid State and Materials Science 5 (6) (2001) 553–564.

[12] C.I. Aguirre, E. Reguera, A. Stein, Tunable Colors in Opals and Inverse Opal Photonic Crystals, Advanced Functional Materials 20 (16) (2010) 2565–2578.

[13] M. Sadakane, W. Ueda, Three-Dimensionally Ordered Macroporous (3DOM) Perovskite Mixed Metal Oxides. In P. Granger, V.I. Parvulescu, S. Kaliaguine, W. Prellie, Perovskites and Related Mixed Oxides: Concepts and Applications (2015) 113–142.

[14] X.C. Yang, Y.L. Shang, Y.H. Li, J. Zhai, N.R. Foster, Y.X. Li, D. Zou, Y. Pu, Synthesis of Monodisperse Iron Oxide Nanoparticles without Surfactants, Journal of Nanomaterials 2014 (2) (2014) 1–5.

[15] Y. Pu, X. Tao, J. Zhai, J.F. Chen, Hydrothermal synthesis and magnetic properties of $Co_{0.2}Cu_{0.03}Fe_{2.77}O_4$ nanoparticles, Materials Research Bulletin 45 (5) (2010) 616–620.

[16] Y. Pu, X. Tao, J. Zhai, J.F. Chen, Synthesis and electromagnetic properties of microwave absorbing material: $Co_x(Cu_{0.5}Zn_{0.5})_{1-x}Fe_2O_4$ ($0<x<1$) nanoparticles, Materials Science and Engineering: B 176 (2) (2011) 163–166.

[17] Y. Pu, X. Tao, X. Zeng, Y. Le, J.F. Chen, Synthesis of Co–Cu–Zn doped Fe_3O_4 nanoparticles with tunable morphology and magnetic properties, Journal of Magnetism and Magnetic Materials 322 (2010) 1985–1990.

[18] Y. Pu, H. Zou, J.X. Wang, J. Zhai, N.R. Foster, J.F. Chen, Novel Sr–Zn–Co hexagonal ferrite nano-rods by wood-template chemical solution synthesis, Materials Letters 65 (14) (2011) 2213–2215.

[19] G. Ghosh, M.C. Drew, Comparison of analytical methods for extraction of chloride from plant tissue using36Cl as tracer, Plant and Soil 136 (2) (1991) 265–268.

[20] Y.J. Huang, J.A. Schwarz, The effect of catalyst preparation on catalytic activity: IV. The design of Ni/Al_2O_3 catalysts prepared by incipient wetness, Applied Catalysis 32 (1987) 59–70.

[21] C.A. Schneider, W.S. Rasband, K.W. Eliceiri, NIH Image to ImageJ: 25 years of image analysis, Nat. Methods 9 (7) (2012) 671–675.

[22] M.I. Sánchez de Rojas, M.P. de Luxán, M. Frías, Inductively coupled plasma emission spectrometry, materconstrucc 36 (202) (1986) 31–46.

[23] B. Ravel, M. Newville, Athena, Artemis, Hephaestus: data analysis for X-ray absorption spectroscopy using IFEFFIT, Journal of Synchrotron Radiation 12 (4) (2005) 537–541.

[24] N. Fischer, B. Clapham, T. Feltes, E. van Steen, M. Claeys, Size-dependent phase transformation of catalytically active nanoparticles captured in situ, Angewandte Chemie International Edition 53 (5) (2014) 1342–1345.

[25] N. Fischer, M. Claeys, Phase changes studied under *in situ* conditions—A novel cell, Catalysis Today 275 (2016) 149–154 .

[26] H.M. Rietveld, A profile refinement method for nuclear and magnetic structures, Journal of Applied Crystallography 2 (2) (1969) 65–71.

[27] H. Schulz, W. Boehringer, C. Kohl, N. Rahman, A. Will, DGMK Forschungsbericht 3 (1984) 320.

[28] Sasol, Sasolwax H1 Fischer-Tropsch Hard Wax for PVC Processing: Performace Chemicals Wax Division, (2016).

[29] R. Kaiser, Rentention indices in gas chromatography, Chromatographia 3 (8) (1970) 383–398.

[30] R.B. Anderson, Catalysis IV (1956) PH Emmett, Ed, Rheinhold Publishing Company, New York.

5 Results and discussion

5.1 Characterization of unsupported nanoparticles

Iron oxide nanoparticles were synthesized by the coprecipitation method outlined in section 4.2. The morphology and phase compositions of the nanoparticles was analyzed using X-ray diffraction (XRD) and transmission electron microscopy (TEM).

The obtained diffraction patterns were compared to the reference patterns for maghemite, hematite and magnetite available in the ICDD database. The presence of a pure maghemite (γ-Fe_2O_3) phase was concluded (see Figure 5-1). The crystal structure of maghemite and magnetite is very similar and just diverges by minor differences in the position of the reflexes. The identification of maghemite was aided by the reduction behavior observed in in-situ XRD (see Figure 5-14).

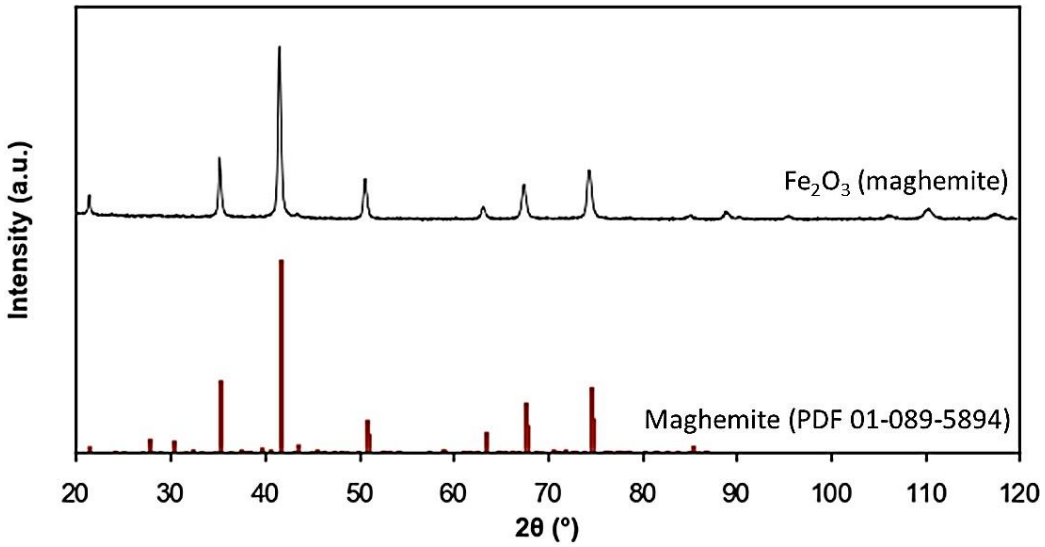

Figure 5-1: XRD diffraction pattern of unsupported γ-Fe_2O_3 particles and reference pattern for maghemite.

To confirm the success of the synthesis technique in yielding well defined iron oxide nanocrystallites, transmission electron microscopy was used. The obtained micrographs show that the obtained crystallites have a truncated spherical morphology with a mean crystallite size of 22 nm, which is outside the range in which a change in crystallite size has been reported to have an effect on the activity and selectivity in the FT reaction (see Figure 5-2) [1].

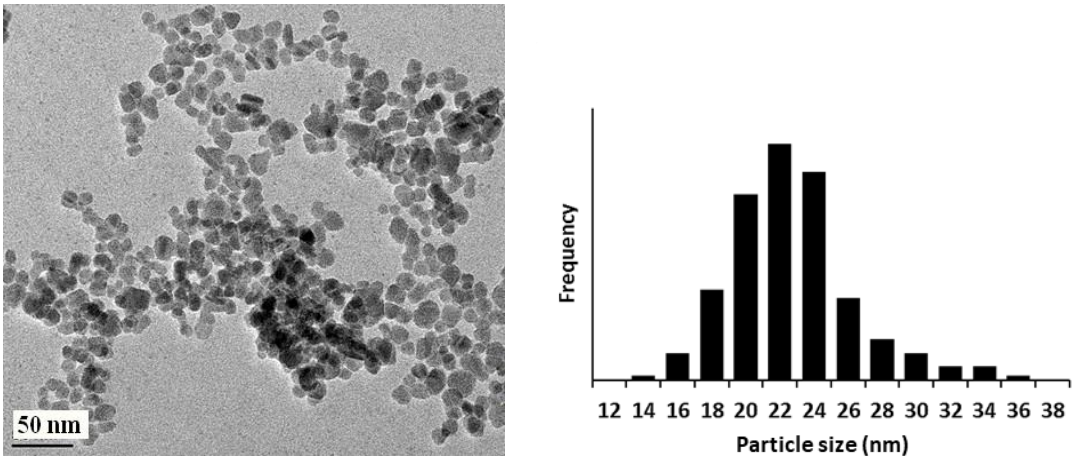

Figure 5-2: TEM micrographs and particle size distribution of the synthesized γ-Fe_2O_3 *nanoparticles.*

5.2 Characterization of perovskites

Several characterization techniques were employed to fully analyze the synthesized perovskites to make sure that the targeted phase, structure, and elemental compositions are achieved.

The XRD pattern of the $LaAlO_3$ sample shows that the sample is a pure perovskite with a rhombohedral structure (see Figure 5-3). The data is in good agreement with the reported reference diffraction peak positions ($LaAlO_3$ PDF 01-085-1071). With the partial substitution of the aluminum cation with manganese on the B site, the XRD patterns remain monophasic with rhombohedral symmetry (space group R-3m (166)). $LaMnO_3$ perovskites calcined in excess air have been reported to have a rhombohedral structure while calcination in N_2 leads to an orthorhombic structure [2,3]. The XRD peaks progressively shift to lower 2θ angle values with increasing amount of manganese due to a lattice expansion (interplanar distance), which increases the unit cell volume as the smaller Al^{3+} (0.670 Å) is replaced by the larger Mn^{3+} (0.785 Å), (see Table 5-1) [4,5]. The shift is a confirmation that the manganese cations have been successfully incorporated into the perovskite lattice [6]. Some diffraction reflexes associated to La_2O_3 are observed for the sample $LaMn_{0.6}Al_{0.4}O_3$ suggesting that not all La is forming part of the perovskite structure. The average crystallite size of the perovskites is estimated using Rietveld refinement. The results show that the crystallite sizes are markedly decreased with increasing Mn substitution (see Table 5-1).

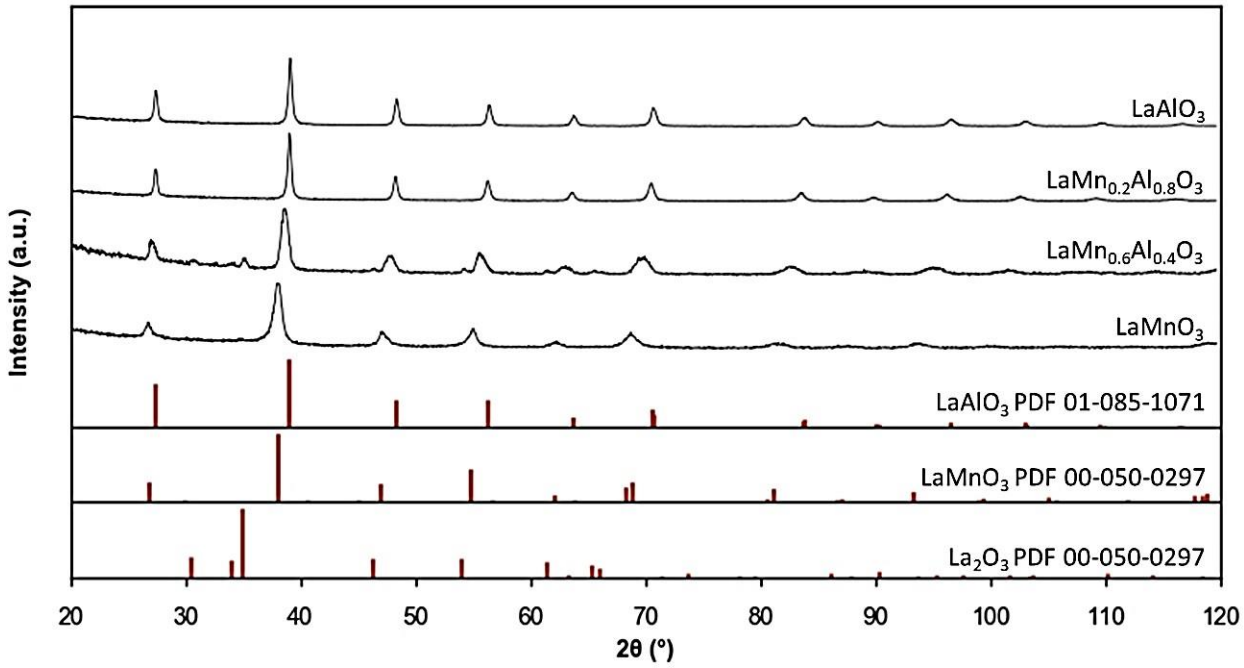

Figure 5-3: XRD diffraction patterns of prepared $LaAlO_3$, $LaMn_{0.2}Al_{0.8}O_3$, $LaMn_{0.6}Al_{0.4}O_3$ and $LaMnO_3$ and reference patterns of $LaAlO_3$, $LaMnO_3$ and La_2O_3.

Table 5-1: Average $LaMn_xAl_{1-x}O_3$ crystallite size and lattice parameter distance obtained from Rietveld refinement.

Sample	a [Å]	c [Å]	D [nm]
$LaAlO_3$	5.36	13.08	64.8
$LaMn_{0.2}Al_{0.8}O_3$	5.38	13.14	41.9
$LaMn_{0.6}Al_{0.4}O_3$	5.43	13.20	41.5
$LaMnO_3$	5.51	13.33	13.2

With the partial substitution of lanthanum with potassium in the structure of the $LaAlO_3$ perovskite, and further in the $LaMn_xAl_{1-x}O_3$ (x=0.2,0.6,1) perovskites lattice, the samples still retain the structure of the perovskite. Only $La_{0.9}K_{0.1}MnO_3$ showed traces of La_2O_3 (see Figure 5.4). Because the Goldschmidt ionic

radii of La^{3+} (0.122 nm) and K^{+} (0.133 nm) are not very different, substituting small amounts of K^{+} into the A-site of the perovskite is expected to have little effect on the crystalline phase and the degree of crystallinity of the perovskite [7]. As observed in the absence of K, the reflexes also systematically shift to lower 2θ angles with the addition of Mn due to the expected increase in cell dimension. Fang *et al*. [8] reported for a their $La_{1-x}K_xCo_{1-y}Mg_yO_3$ perovskites system (x=0 – 0.4; y=0 – 0.2), that the substitution of La^{3+} with K^{+} caused unstable occupancy of the La site by K^{+} leading to segregation cobalt in the oxide form, especially with no Mg substitution. The partial substitution of La^{3+} by K^{+} causes a charge imbalance within the perovskite, and oxygen vacancies are created as a charge compensation mechanism [9].

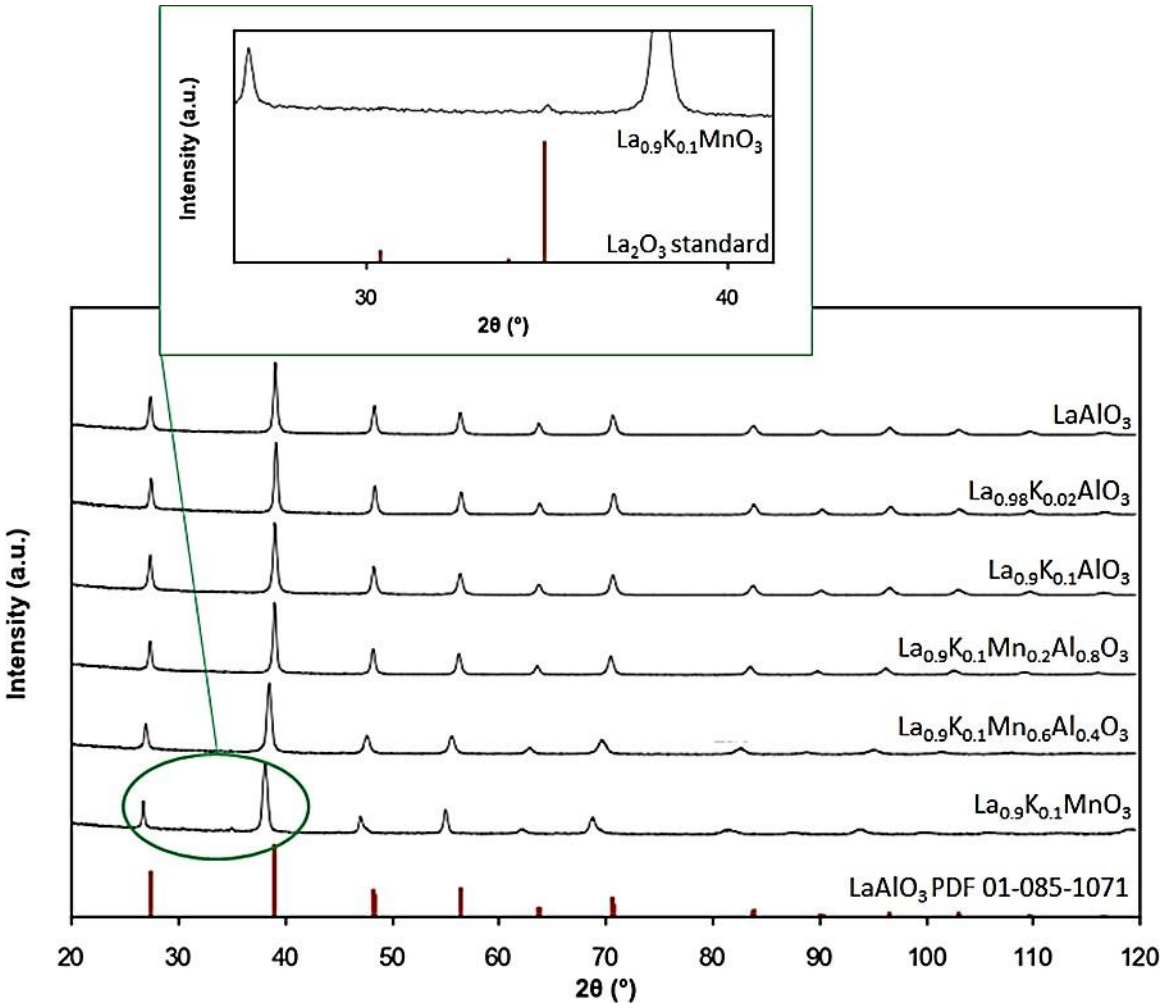

Figure 5-4: XRD diffraction patterns of $LaAlO_3$, $La_{0.98}K_{0.02}AlO_3$, $La_{0.9}K_{0.1}AlO_3$, $La_{0.9}K_{0.1}Mn_{0.2}Al_{0.8}O_3$, $La_{0.9}K_{0.1}Mn_{0.6}Al_{0.4}O_3$ and $La_{0.9}K_{0.1}MnO_3$ of the prepared samples and reference patterns of $LaAlO_3$ and La_2O_3.

The surface morphological and microstructural details of the prepared samples were obtained from TEM and SEM micrographs. The images show a porous material for both $LaAlO_3$ and $LaMn_{0.6}Al_{0.4}O_3$ samples with uneven shapes and sizes which may be a result of an uneven temperature during the combustion process. The TEM images of the other Mn containing samples are provided in Appendix B. $LaAlO_3$ has larger grains than the manganese substituted sample with pore diameters in the rage of 10-50 nm (see Figure 5-5). The pores increase with increasing manganese content but disappear at higher substitutions (80 mol. % Mn) as particles break into smaller nearly spherical grains, which are not dispersed but appear fused.

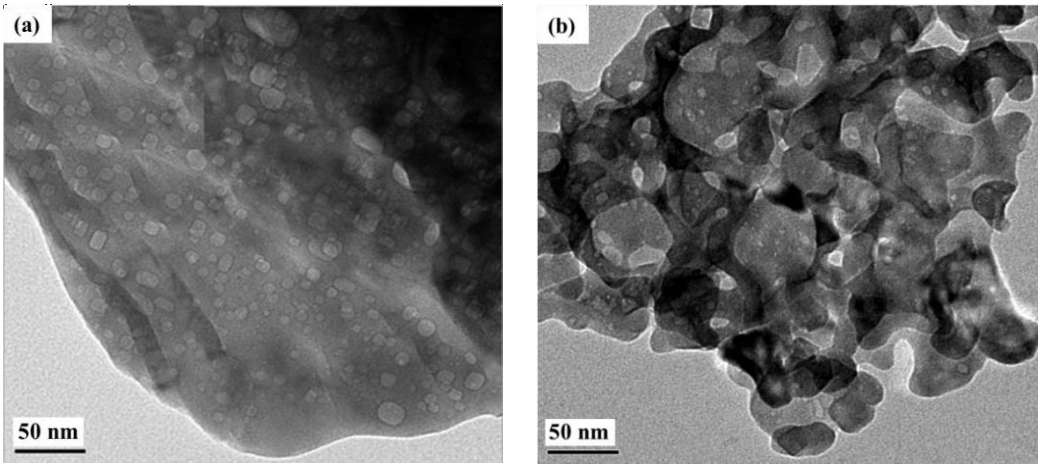

Figure 5-5: TEM micrographs of (a) $LaAlO_3$ and (b) $LaMn_{0.6}Al_{0.4}O_3$.

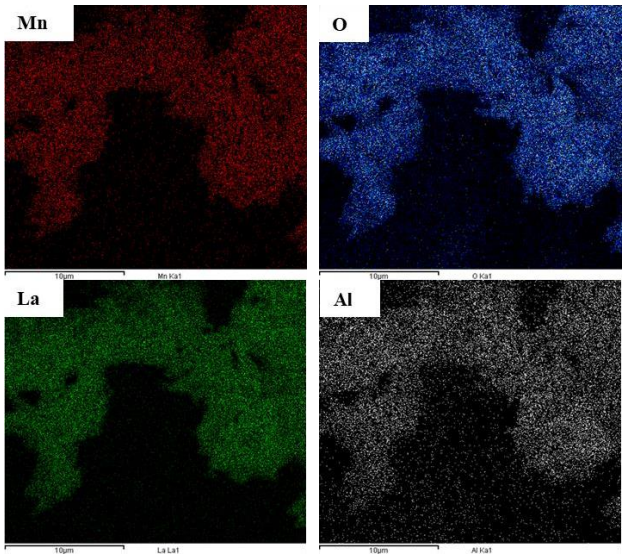

Figure 5-6: SEM EDS elemental mapping micrographs of $LaMn_{0.6}Al_{0.4}O_3$.

To confirm the homogeneity of elements in the samples, elemental mapping was performed using SEM-EDS analysis. The mapping revealed that the contained elements were distributed evenly in the structure of the perovskite (see Figure 5-6 and Appendix B). Compared to the XRD patterns in Figure 5-4 above, no evidence of La enrichment due to free La_2O_3 is evident besides for the sample $La_{0.9}K_{0.1}MnO_3$.

For the K containing samples, Energy Filtered Transmission Electron Microscopy (EF-TEM) was used to investigate the homogeneity of the samples. For $La_{0.9}K_{0.1}AlO_3$ all elements seem evenly distributed throughout the entire sample without any apparent enrichments (see Figure 5-7). This could mean that the 10 atom-% substitution of La with K on the A site is possible and that the K cation is fully incorporated in the perovskite structure or that K is highlight dispersed on the surface of the perovskite.

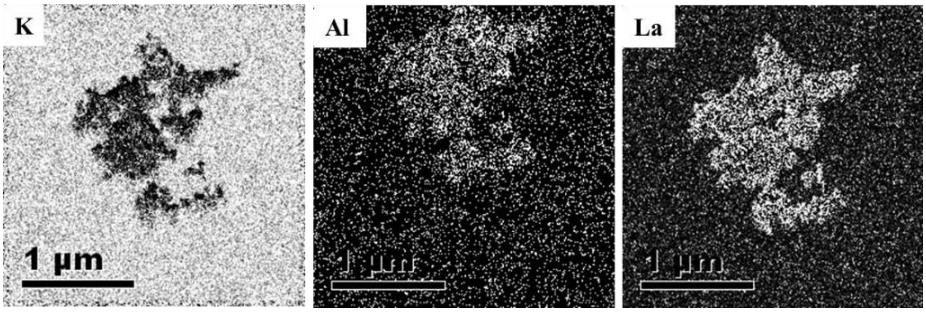

Figure 5-7: Energy Filtered Transmission Electron Microscopy micrographs of $La_{0.9}K_{0.1}AlO_3$ sample.

Higher potassium concentrations in the A site and impregnated potassium on $LaAlO_3$ were also investigated. Images a and b in Figure 5-8 represent the normal TEM images and images labelled K, La and Al are the elements present in a or b. It can be clearly seen that potassium compounds form a physical mixture with the perovskites for the potassium impregnated sample, distinctly showing areas of high potassium. The most probable forms of the potassium promoter are K_2O, KOH and K_2CO_3, rather than metallic potassium [10,11].

The K rich phase is present in rod-like grains with a length of > 1 µm and a thickness of approximately 20 nm. Similar rod-like structures (circled in red) were observed in the sample in which 20 atom-% of K was substituted in the A site of the $LaAlO_3$ perovskite, targeting a composition of $La_{0.8}K_{0.2}AlO_3$. However, these structures were also associated with increased aluminum content, suggesting that a potassium aluminate was formed during synthesis. It is apparent that an increase in potassium substitution in the A site beyond 10 atom-% is unfeasible. This is attributed to the structural distortion caused by the increased concentration of K^+ as well as the increase charge difference which Al^{3+} cannot compensate. Similar effects were found

in earlier research whereby elevated K substitution (> 10 atom-%) resulted in the B-site cation forming oxide structures external to the perovskite upon calcination [12–14]. Tsounis *et al*. [12] studied the change in chemical properties of $La_xK_{1-x}NiO_3$ (x = 0–0.3) using XPS analysis. They observed peaks believed to correspond to K-O group, which were likely due to K_2O formed during the sample calcination in air [15,16].

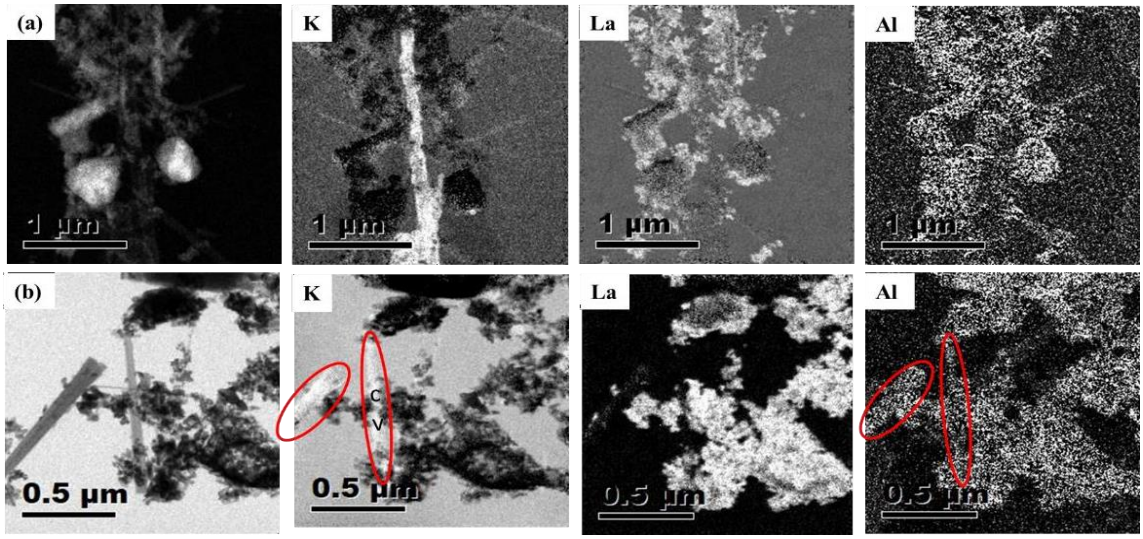

Figure 5-8: Energy-Filtering Transmission Electron Microscopy micrographs of (a) potassium impregnated on $LaAlO_3$ and (b) $La_{0.8}K_{0.2}AlO_3$.

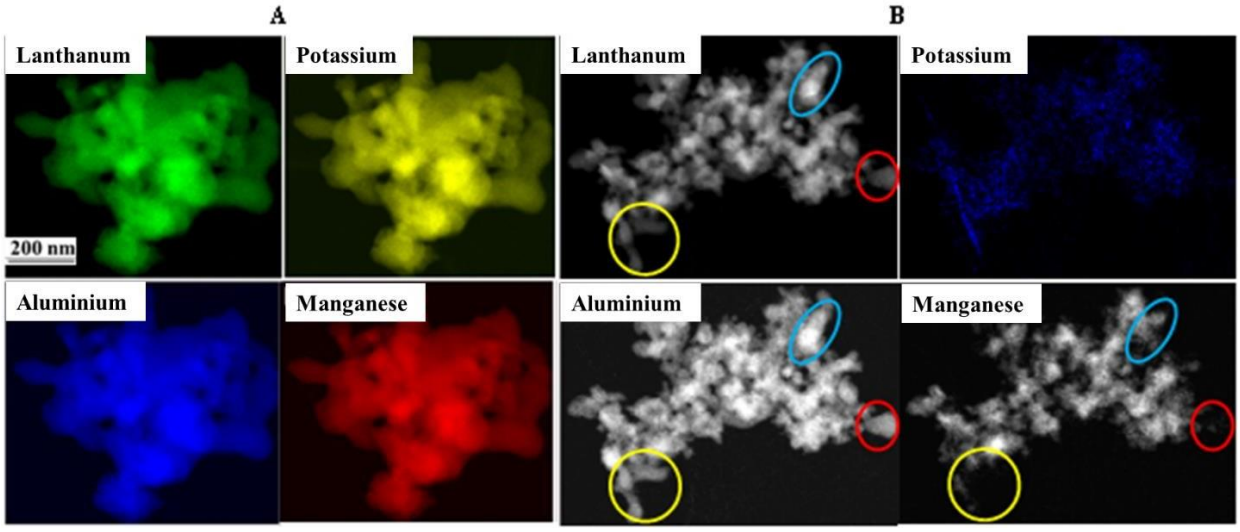

Figure 5-9: TEM EDS elemental mapping of A: $La_{0.9}K_{0.1}Mn_{0.2}Al_{0.8}O_3$ and B: $La_{0.9}K_{0.1}Mn_{0.6}Al_{0.4}O_3$ samples.

The purity and homogeneity of the perovskite samples was further analyzed using high resolution transmission electron microscopy (HRTEM). Figure 5-9 shows the elemental maps of $La_{0.9}K_{0.1}Mn_{0.2}Al_{0.8}O_3$. The results clearly confirm that the La, K, O, Al and Mn atoms are evenly distributed throughout the sample. The sample $La_{0.9}K_{0.1}Mn_{0.6}Al_{0.4}O_3$ was found to have manganese deficiencies in regions circled in Figure 5-9 B.

In an attempt to increase the surface area, three dimensionally ordered macroporous (3DOM) perovskites were prepared by impregnation of PMMA spheres with the precursor solution. It is reported that the pore diameter of the porous perovskite is smaller than the diameter of the PMMA spheres [17–19]. The spheres shrink when the temperature goes beyond their glass transition temperature with is typically in the range from 95−110 °C. Above this temperature the polymer spheres are completely destroyed as they change from being hard and brittle to being rubber [17–19]. SEM imaging of the 3DOM perovskite structures $La_{0.9}K_{0.1}AlO_3$ and $LaAlO_3$ containing an interconnected macroporous framework, show an average pore diameter of about 200 nm while the polymer spheres have a diameter of approximately 250 nm (see Figure 5-10). During calcination, heat control is crucial as the removal of PMMA spheres in air is an exothermic reaction that can lead to the collapse of the 3DOM structure. Zheng *et al*. [20] reported that the structural collapse is due to the crystallite size of samples growing rapidly with a spike in temperature. This was overcome by diluting the samples with silicon carbide and using increased air flow rates during calcination to quickly remove the generated heat. Sadakane *et al*. [21] proposed that the use of ethylene glycol in the perovskite synthesis further weakens the walls in the interspace between the spheres as the precursor solution is unable to completely fill the voids in the spheres because of its high viscosity.

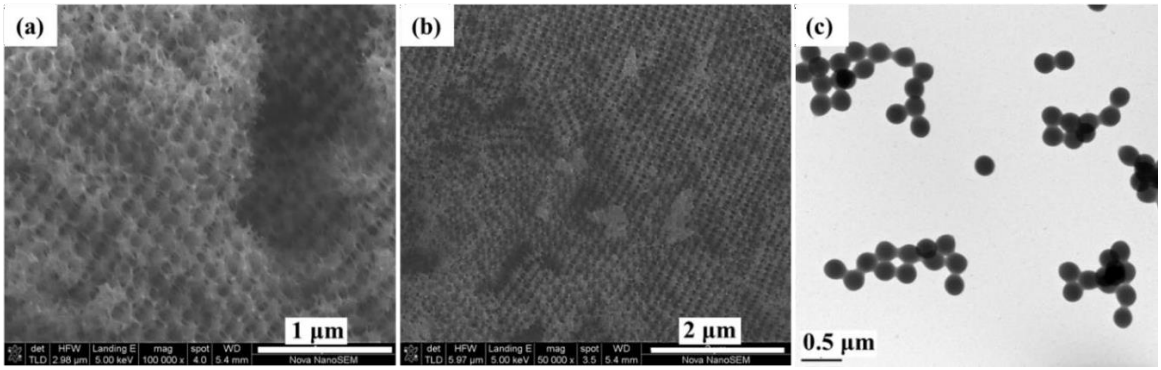

Figure 5-10: SEM micrographs of 3DOM (high surface area) perovskites, (a) $La_{0.9}K_{0.1}AlO_3$, (b) $LaAlO_3$ and (c) PMMA spheres.

Table 5-2: Specific BET area and ICP/AAS Elemental compositions of prepared samples with theoretical values.

Sample/Element	ICP/AAS wt.-%					Targeted wt.-%				S_{BET} (m^2 g^{-1})
	La	K	Al	Mn	Fe**	La	K	Al	Mn	support only
Fe-$LaAlO_3$	84.9	0.0	15.1	0.0	12.1	83.7	0.0	16.3	0.0	4.5
Fe-$La_{0.98}K_{0.02}AlO_3$	60.4	0.9	5.9	11.5	13.4	83.1	0.5	16.5	0.0	-
Fe-$La_{0.9}K_{0.1}AlO_3$	82.3	2.2	15.5	0.0	13.1	80.0	2.5	17.0	0.0	28.8
Fe-$La_{0.9}K_{0.1}Mn_{0.2}Al_{0.8}O_3$	79.7	1.5	13.7	5.1	13.6	77.0	2.0	13.0	7.0	20.5
Fe-$La_{0.9}K_{0.1}Mn_{0.6}Al_{0.4}O_3$	76.7	1.2	7.5	14.6	13.9	72.0	2.2	6.0	19.0	17.8
Fe-$La_{0.9}K_{0.1}MnO_3$	78.5	1.5	0.0	19.9	14.0	68.0	2.1	0.0	23.0	11.4
Fe-$LaMnO_3$	76.0	0.0	0.0	22.0	12.0	74.0	0.0	0.0	28.0	13.8
Fe2K-$LaAlO_3$	83.7	1.9	14.4	0.0	13.5	80.0	2.5	17.0	0.0	4.5
Fe1K-$LaAlO_3$	82.9	1.6	12.2	0.0	13.8	82.9	1.0	16.1	0.0	4.5
Fe0.5K-$LaAlO_3$	84.8	1.0	14.2	0.0	14.0	83.3	0.5	16.2	0.0	4.5
Fe-LaAlO3 3DOM*	83.5	0.0	16.4	0.0	12.2	83.7	0.0	16.3	0.0	10.9
Fe-$La_{0.9}K_{0.1}AlO_3$ 3DOM	78.9	3.0	18.5	0.0	13.3	80.0	2.5	17.0	0.0	34.7

Fe**: Iron oxide target loading = 15.0%

3DOM*: Three-dimensionally ordered macroporous

The elemental compositions of the as-prepared samples were determined by atomic absorption spectroscopy and inductively coupled plasma optical emission spectrometry. The results compiled in Table

5-2 demonstrate that the lanthanum and aluminum contents are close to the targeted values. This is often the case when the sample synthesis method does not include any separation step like crystallization or filtration [22]. Potassium and manganese contents are however lower than the theoretical values. Goldwasser *et al*. [23] report a similar trend for the composition of perovskites, and the assertion was made that the lower than expected K was due to the volatility of K_2O at elevated temperatures. The low Mn content could be due to the hygroscopic nature of the precursor (manganese nitrate), therefore leading to an underestimation of the measured mass of Mn during sample preparation.

A number of selected perovskite samples were analyzed with X-ray absorption spectroscopy in the near edge region (XANES) of the K and Mn K-edge to investigate the surface enrichment of K or Mn on the perovskites. The analysis was performed on two sets of samples; the as synthesized samples and the same samples treated in hydrogen fluidized bed at 450 °C, simulating the reduction procedure used to activate the iron FT catalysts.

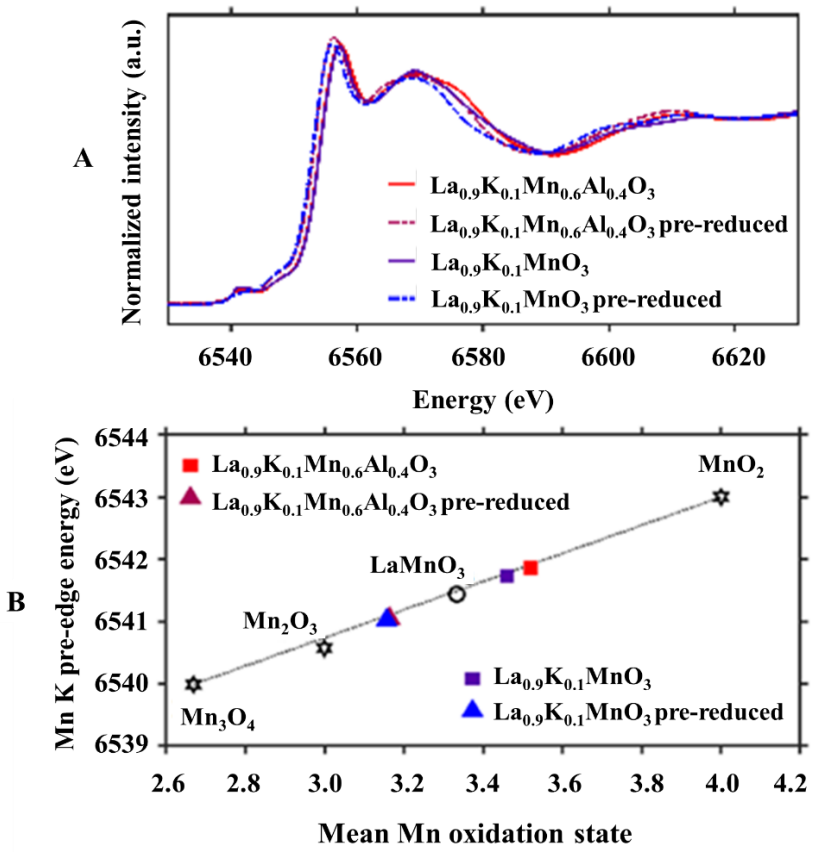

Figure 5-11: A: Mn K-edge XANES spectra of $La_{0.9}K_{0.1}Mn_{0.6}Al_{0.4}O_{3-\delta}$ and $La_{0.9}K_{0.1}MnO_{3-\delta}$ samples as synthesized and after reduction. B: Mn K pre-edge energies of $La_{0.9}K_{0.1}Mn_{0.6}Al_{0.4}O_3$ and $La_{0.9}K_{0.1}MnO_3$ samples as synthesized and after treatment in reductive atmospheres together with $LaMnO_3$, Mn_3O_4, Mn_2O_3 and MnO_2 references from literature as function of mean Mn oxidation state.

Mn K-edge XANES was used to confirm that the Mn species are representative of those found in the perovskite structure. Figure 5-11 A shows the $La_{0.9}K_{0.1}Mn_{0.6}Al_{0.4}O_3$ and $La_{0.9}K_{0.1}MnO_3$ as prepared and after exposure to hydrogen at 450 °C for 15 hrs. The spectra of these samples before and after reduction agrees with that of $LaMnO_3$ reported elsewhere [24–26]. However, from the summarized threshold energies (E_0) (see Table 5-3) it can be observed that there is a chemical shift to higher energies for the as synthesized $La_{0.9}K_{0.1}Mn_{0.6}Al_{0.4}O_3$ and $La_{0.9}K_{0.1}MnO_3$ samples and a shift to lower energies when these samples are reduced, with respect to $LaMnO_3$. These are due to higher oxidation states for the as prepared samples, possibly to compensate for the charge imbalance upon K incorporation into the $LaMnO_3$ and $LaMn_{0.6}Al_{0.4}O_3$ matrix. Upon reduction, the oxidation states decrease from 3.5 and 3.6 to the same value of 3.2 respectively (see Figure 5-11 B). The pre-reduced samples still maintain the general shape of the $LaMnO_3$ perovskite spectra.

Table 5-3: Threshold energies (E_0) for $LaMnO_3$ and the as synthesized and reduced $La_{0.9}K_{0.1}Mn_{0.6}Al_{0.4}O_3$ and $La_{0.9}K_{0.1}MnO_3$ samples.

Compound	E_0 (eV)
$La_{0.9}K_{0.1}MnO_3$ (not reduced)	6553.72
$La_{0.9}K_{0.1}MnO_3$ (reduced)	6552.60
$La_{0.9}K_{0.1}Mn_{0.6}Al_{0.4}O_3$ (not reduced)	6553.68
$La_{0.9}K_{0.1}Mn_{0.6}Al_{0.4}O_3$ (reduced)	6553.00
$LaMnO_3$	6553.59

To confirm the successful incorporation of potassium promoter into the perovskite by partial substitution of La with potassium, potassium K-edge XANES was used. The spectra of the potassium incorporated samples was compared against the spectra of the possible potassium compounds including a commonly present K_2CO_3 and a database of K standards (See Figure B. 5, Appendix B) [27,28]. Only the as synthesized $La_{0.9}K_{0.1}AlO_3$ XANES shows an indication of K_2CO_3 contributions to its spectra. Upon reduction these disappear. It is assumed that the reductive treatment results in partial oxygen removal in the perovskite, reducing the charge imbalance induced by the potassium incorporation, allowing all potassium species to be incorporated into the crystallographic lattice. In the presence of Mn in the B site of the

perovskite, the flexibility of oxidation state provides sufficient buffer for the charge imbalance even in the calcined state.

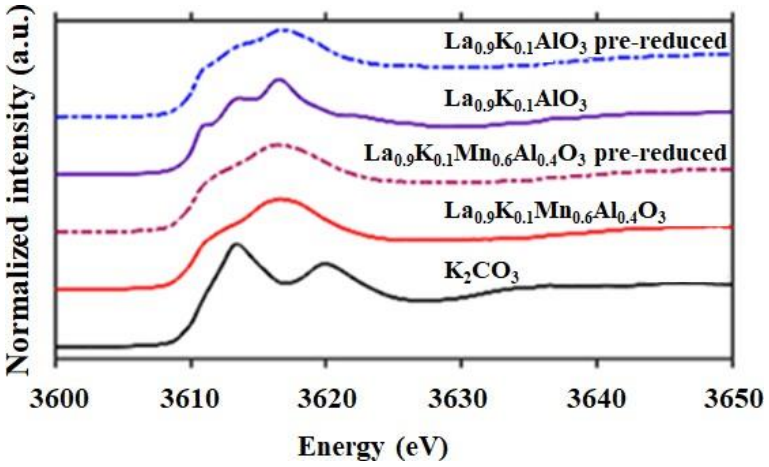

Figure 5-12: Potassium K-edge XANES spectra of $La_{0.9}K_{0.1}Mn_{0.6}Al_{0.4}O_3$ and $La_{0.9}K_{0.1}AlO_3$ samples as synthesized and after treatment in reducing conditions and of the K_2CO_3 reference.

The reducibility of the model catalysts, simulating catalyst activation in the Fischer-Tropsch synthesis, was studied using H_2-TPR. The samples were heated in a diluted hydrogen stream (5% H_2 in Argon) from 60 to 900 °C, recording the hydrogen consumption as a function of temperature. The XRD results discussed previously show that the iron oxide is present on the supports as a γ-Fe_2O_3. H_2-TPR results of maghemite in the work of Mou *et al*. [29] and Mogorosi *et al*. [30] showed that the reduction of γ-Fe_2O_3 to Fe proceeds in three sequential steps. Generally, the hydrogen peak centered at around 350 °C is attributed to the surface lattice oxygen, while the peaks and around 620 and 780 °C are attributed to the bulk lattice oxygen [31]. First γ-Fe_2O_3 reduces to Fe_3O_4, Fe_3O_4 reduces to FeO and then finally FeO reduces to metallic iron (Fe) [32–34]. The H_2-TPR experiment is therefore expected to have three peaks with a peak area ratio of 3:2:3 due to the number of moles of Fe oxide reduced (see eqn. 5.1–5.2), especially when the reduction temperature increases beyond 570 °C [33,35,36]:

$$3Fe_2O_3 + H_2 \rightarrow 2Fe_3O_4 + H_2O \quad (5.1)$$

$$Fe_3O_4 + H_2 \rightarrow 3FeO + H_2O \quad (5.2)$$

$$FeO + H_2 \rightarrow Fe + H_2O \quad (5.3)$$

Below 570 °C, the reduction only takes place in a two-step process with magnetite reducing directly to metallic iron [37]. However, Pineau *et al*. [38] reported that the presence of wüstite (FeO) has been detected in the temperature range 450–570 °C, but it is unstable [39], especially without a support which works as a stabilizer [40,41]. The exact peak position of the individual reduction steps may vary depending on the catalyst support used and experimental conditions (heating rate, reducing gas composition, etc.).

Similar to other supported iron catalysts [42,43], there is no reduction observed at temperatures below 250 °C except for the unsupported γ-Fe_2O_3 (see Figure 5-13). The unsupported nanoparticles start reducing at 238 °C, reaching maximum hydrogen consumption at 332 °C. Its second peak starts at 388 °C and strongly overlaps with the third peak, resulting in a broad peak with two shoulders reaching maxima at 596 °C and 817 °C for the second and third reduction events respectively. These peaks are very broad indicating that the second and third reduction steps are rather slow.

For the supported catalysts, the onset of reduction, in the temperature range of 250-300 °C, is due to the reduction of γ-Fe_2O_3 to typically Fe_3O_4. The peaks in this range appear at different temperatures depending on the support material, i.e., composition of the perovskite support. The onset of reduction for the Fe-$LaAlO_3$ is recorded at 290 °C, higher than the unsupported nanoparticles probably because of metal support interactions and decreased mobility of surface oxygen species. It is important to note that although the second peak also starts at a higher temperature (435 °C) when compared to the unsupported sample, it is centered at the same temperature (596 °C). The same behavior is observed on the third peak (817 °C). Beyond the third the peak is another shoulder indicative of the fourth peak which is possibly the partial reduction of the support. If perovskite reduction plays a role in the lower temperature hydrogen consumption events could not be excluded.

Upon addition of potassium into the $LaAlO_3$ matrix, the onset of reduction for the Fe-$La_{0.9}K_{0.1}AlO_3$ catalyst appears at a lower temperature of 270 °C. Of note is also the fact that the presence of potassium lowers the temperature of reduction of Fe_3O_4 to FeO from 596 to 580 °C when comparing the peak maxima. For this catalyst, the third and the fourth reduction event are completely convoluted resulting in one broad peak centered at 817 °C, same as the third reduction step of Fe-$LaAlO_3$. Thus, the presence of potassium in the support does not reduce the high temperature required for the deep reduction of metallic Fe to be achieved. On conventional supported catalysts impregnated with potassium, potassium either retarded the reduction to Fe_3O_4, shifting the reduction temperature to higher temperatures, or had no effect [44–46].

The presence of Mn resulted in the Fe-$LaMn_{0.2}Al_{0.8}O_3$ catalyst exhibiting a significant decrease in the reduction temperature of iron species, showing that the addition of small quantities of Mn can enhance the reduction of iron oxides [47]. The inception of reduction is at the temperature of 260 °C reaching a

maximum at 344 °C. The first peak contains a shoulder at 378 °C, signifying two overlapping reduction events. The subsequent peaks are completely merged showing shoulders at 500 °C and 600 °C, indicating a substantial peak shift to lower reduction temperatures. It is worth noting that hydrogen consumption has decreased in the presence of manganese when compared with the Fe-$LaAlO_3$ catalyst. Even though the onset of reduction is at the lower temperature, the reduction takes place very slowly. Chern *et al*. [48] observed the formation of manganowüstite in the reduction of a manganese containing catalyst, that prevented some iron species from complete reduction to Fe. The reduction profiles of the samples with complete substitution of Al with Mn, are quite different from the lower manganese or the promoter free catalysts. It is also observed that the reduction peaks associated with the reduction of $Fe_3O_4 \rightarrow FeO$ and $FeO \rightarrow Fe$ are more distinguishable and less intense when compared to the Fe-$LaMn_{0.2}Al_{0.8}O_3$ catalyst. This suggests that a high manganese content retards the full reduction to metallic Fe [49].

Addition of small amounts of both manganese and potassium (Fe-$La_{0.9}K_{0.1}Mn_{0.2}Al_{0.8}O_3$) leads to almost complete suppression of the first reduction peak. The first reduction peak of Fe-$LaMn_{0.2}Al_{0.8}O_3$ catalysts is also suppressed although not to the same extend, showing decreased hydrogen consumption. The same behavior is observed with increasing levels of Mn while keeping K constant (Fe-$La_{0.9}K_{0.1}Mn_{0.6}Al_{0.4}O_3$). The significant difference is seen for the Fe-$La_{0.9}K_{0.1}MnO_3$ catalyst with more prominent peaks showing increased hydrogen consumption. The Mn containing catalysts noticeably show a broad first peak. Li *et al*. [50] explained that any MnO formed during reduction migrates to the surface and encapsulates FeO preventing it from further reduction [51–53]. Manganese is also reported to have a tendency of inhibiting hydrogen chemisorption [54], explaining the reduced hydrogen consumption on the Mn containing samples. In summary, the structure of the reduction profiles of all manganese containing catalysts point to the presence, partly to a superposition, of various reduction reactions.

The impregnated catalyst Fe-$2KLaAlO_3$ shows the inception of H_2 consumption around the temperature of 300 °C and slowly reduce with increasing temperature, reaching a maximum at 400 °C (see Figure 5-13). The second and third peak are smaller than the first peak, indicating that the reduction of FeO to Fe is suppressed due to high promoter content. The fourth peak is also visible under the shoulder at 760 °C, and possibly associated to the reduction of the support. All the supported catalysts show four peaks, with three belonging to the reduction of maghemite, while the fourth peak is the reduction of the support or metal support complex.

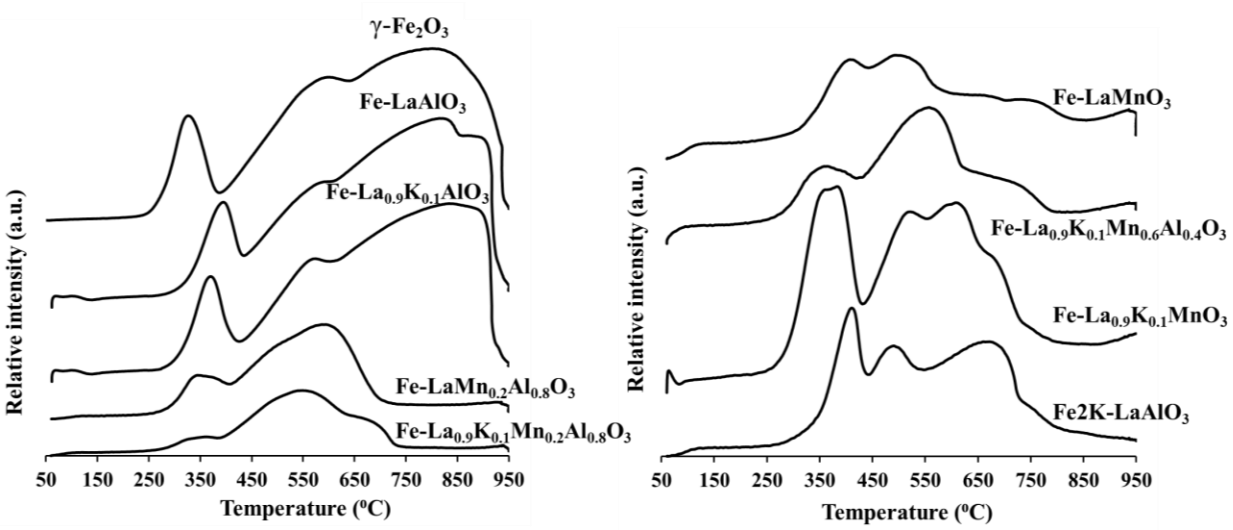

Figure 5-13: TPR traces of the calcined model catalysts.

To better understand the TPR profiles of the iron oxide on the prepared perovskites supports and investigate the role of potassium and manganese, three of the catalysts described above were further analyzed with *in situ* XRD (Fe-$LaAlO_3$, Fe-$La_{0.9}K_{0.1}AlO_3$ and Fe-$La_{0.9}K_{0.1}Mn_{0.2}Al_{0.8}O_3$). An in house developed *in situ* XRD cell was used to analyze the catalysts and the results are presented in Figure 5-14. The reduction and carburization conditions used for activating and testing the model catalysts in the reduction rig and slurry reactor were simulated. In the iron oxide supported on $LaAlO_3$ (see Figure 5-14 A), γ-Fe_2O_3 starts reducing to Fe_3O_4 at 260 °C reaching completion within minutes. The sample is reduced directly to metallic α-Fe from 400 °C onwards without the formation of wüstite, probably due to the low reduction temperature of below 570 °C [37]. With the partial substitution of lanthanum with potassium (10 atom-%) on the A-site of the perovskites, the reducibility of γ-Fe_2O_3 is improved by lowering the onset of reduction temperature to 180 °C, however, the reduction to metallic α-Fe is not affected in agreement with the trend observed from the TPR results and reported in literature [55].

Additional substitution of Al with 20 atom-% manganese, resulted in an increase of the reduction temperature from maghemite to magnetite compared to the promoter free sample, which could be attributed to a poorer hydrogen chemisorption in the presence of manganese [54]. The reduction of Fe_3O_4 to α-Fe is not affected. Following the reductive treatment, the samples were exposed to a mixture of hydrogen and carbon monoxide (H_2/CO=2) at a temperature of 240 °C to simulate Fischer-Tropsch conditions.

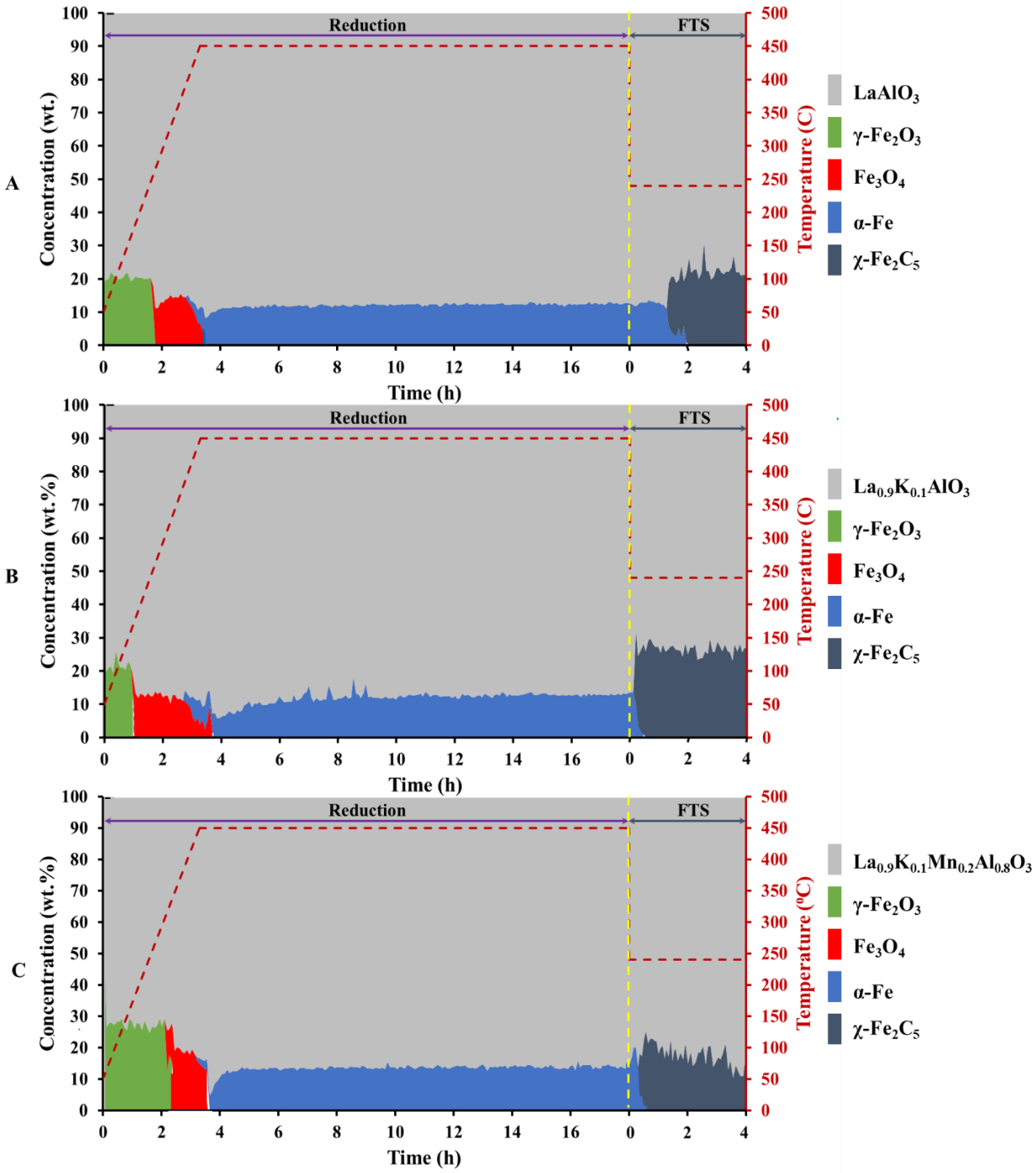

Figure 5-14: Percentage composition of model catalysts during reduction in hydrogen over 18 hrs followed by carburization under FTS conditions for 4 hrs. A: Fe-$LaAlO_3$, B: Fe-$La_{0.9}K_{0.1}AlO_3$ and C: Fe-$La_{0.9}K_{0.1}Mn_{0.2}Al_{0.8}O_3$.

The catalyst supported on the $LaAlO_3$ perovskite shows first signs of carburization after 75 minutes on stream and requires a further 40 minutes for a complete conversion of α-Fe to χ-Fe_2C_5 (Hägg carbide). Upon incorporation of potassium in the perovskite structure ($La_{0.9}K_{0.1}AlO_3$), the rate of carburization is significantly enhanced, achieving full phase conversion after only 20 minutes. For conventional catalyst promotion, it is widely reported that potassium improves carburization of the iron catalysts through a donation of electron density from the potassium metal to the iron phase selectively enhancing CO over H_2 adsorption and weakening the carbon oxygen bond [56–58]. This shows that potassium incorporated in the perovskite can directly influence the formation of the catalytically active phase. The presence of Mn does not show any significant enhancement or suppression of the carburization.

5.3 Catalytic performance in FT reaction

All the prepared perovskite samples were used as supports for the maghemite nanoparticles and tested in a 600 ml slurry reactor for a period of 48 hrs under FTS conditions. The reaction temperature and pressure were 240 °C and 15 bar respectively with a gas hourly space velocity of 2.4 L/(h·g_{cat}) referred to here as the original space velocity (SV_{org}). A maghemite loading of 20 wt.-%, which translates to 15 wt.-% Fe^0, was targeted (see Table 5-2 for actual loadings achieved). Traditional supports such as Al_2O_3, SiO_2, TiO_2 and ZrO_2 were tested under the same conditions as benchmark. The reported CO conversion and products selectivity were recorded after 48 hrs on stream. CO conversion and selectivity as function of time are provided in Appendix C (see Figure C.1–C.7).

The promoter free catalyst Fe-$LaAlO_3$ reached a CO conversion of 44.4% while the benchmark catalysts Fe-Al_2O_3, Fe-ZrO_2, Fe-SiO_2 and Fe-TiO_2 yielded conversions of 45.8, 36.3, 22.3 and 10.4% respectively (see Figure 5-15). The significantly lower activity of the TiO_2 supported catalyst could be the result of active phase encapsulation by partially reduced titania species as has been reported in related systems [59]. The iron nanoparticles supported on $LaAlO_3$ and Al_2O_3 show very comparable conversion levels. The product composition of these two catalysts is also similar, with slight differences in the olefin to paraffin (O/P) ratio and the calculated chain growth probability (α). At the lower conversion levels of the SiO_2 and ZrO_2 supported catalysts, a lower CO_2 selectivity was measured, compared to both $LaAlO_3$ and Al_2O_3 supported catalysts. The hydrocarbon fraction is of a slightly heavier slate, which for Fe-SiO_2 mostly manifests in an increased C_2–C_4 fraction, while Fe-ZrO_2 produces a higher concentration of C_{5+} product. The olefinicity, a measure of secondary hydrogenation activity, is hardly distinguishable from Fe-$LaAlO_3$. The very similar

catalytic performance of Fe-$LaAlO_3$ and the benchmark catalysts, with the exception of Fe-TiO_2, suggests that the unsubstituted perovskite merely acts as a support and does not influence the activity of the catalyst.

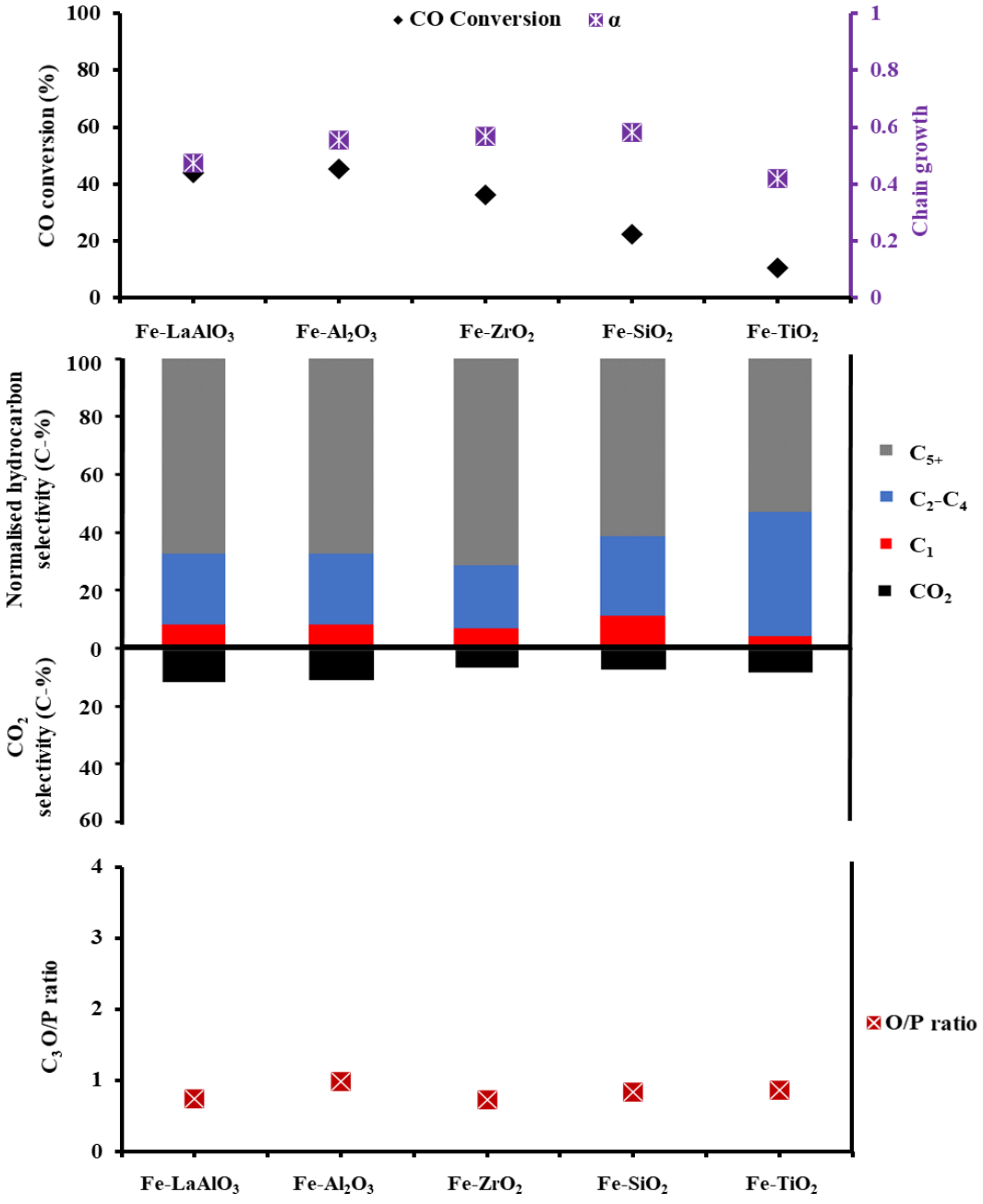

Figure 5-15: Catalytic performance of Fe-$LaAlO_3$, Fe-Al_2O_3, Fe-ZrO_2, Fe-SiO_2 and Fe-TiO_2 at the original space velocity (SV_{org}) after 48 hrs TOS. Top chart displays CO conversion and chain growth probability (α). Middle bar chart depicts the normalized CH_4, C_2–C_4, C_{5+} selectivity (hydrocarbon fraction in the product stream) and CO_2 selectivity. Bottom chart represents C_3-olefin to C_3-paraffin ratio (O/P).

A partial substitution of the aluminum cation on the B-site with 20 atom-% manganese as a promoter does not show any improvement in catalyst activity. The CO conversion for Fe-$LaMn_{0.2}Al_{0.8}O_3$ levels off at 38.7% at the end of the 48 hr FT run, 6% points lower than the unmodified Fe-$LaAlO_3$ (see Figure 5-16). The selectivity towards CO_2 and CH_4 is somewhat suppressed by the incorporation of manganese. The CO_2 selectivity decreases by 1.8 C-% points from about 12.7 C-% for Fe-$LaAlO_3$ to 10.9 C-% for Fe-$LaMn_{0.2}Al_{0.8}O_3$. Similarly, selectivity towards CH_4 is slightly decreased from 8.1 to 7.5 C-%. The enhanced chain growth is manifested in a smaller fraction of C_2–C_4 and a slightly increased C_{5+} selectivity. The O/P ratio is unaffected.

Further substitution of aluminum with manganese significantly decreases the activity of the catalysts by about 50%. In parallel, a significant increase in water gas shift activity is observed, i.e. the selectivity to CO_2 increases to approximately 20 C-% of all carbon containing products. Amongst hydrocarbons, a shift to a lighter product slate (C_2–C_4 fraction) is observed. The shift to light hydrocarbons (C_2–C_4) at higher levels of Mn was also previously reported by Tingzhen *et al*. [50] and Barrault *et al*. [60].

Classic promotion with small amounts of manganese either via impregnation or precipitation is reported to increase the rates of reduction and carburization of the catalysts by maintaining the structural integrity thereby preventing agglomeration during hydrogen reduction [50,51,61]. The suppressing effect of low levels of manganese on CH_4 selectivity and a slight shift to heavy hydrocarbons was reported by Barrault *et al*. [62]. This is reported to be due to the increased surface basicity of the catalyst [63]. The presence of manganese enhances the surface basicity which in turn selectively improves CO dissociative adsorption over that of H_2 to facilitate chain growth. At higher contents of manganese, CO_2-TPD studies of Yang *et al*. [64] indicated that the surface basicity decreased due to manganese enrichment on the surface, affecting the chain growth and blocking active sites. The observed shift of hydrocarbon selectivity to lighter hydrocarbons at higher levels of Mn is also reported elsewhere in literature [50,65].

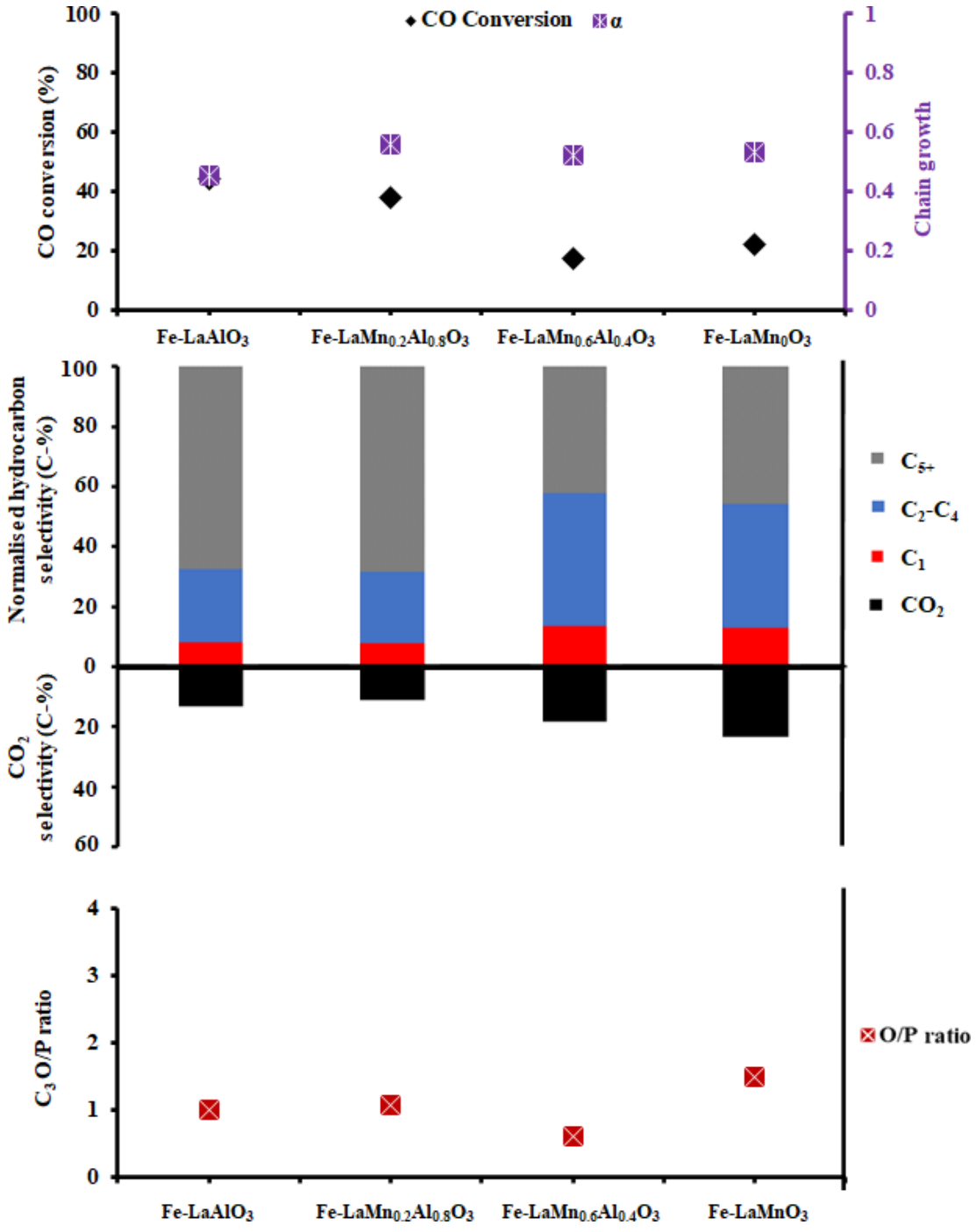

Figure 5-16: Catalytic performance of Fe-$LaAlO_3$, Fe-$LaMn_{0.2}Al_{0.8}O_3$, Fe-$LaMn_{0.6}Al_{0.4}O_3$ and Fe-$LaMnO_3$ at the original space velocity (SV_{org}) after 48 hrs TOS. Top chart displays CO conversion and chain growth probability (α). Middle bar chat depicts the normalized CH_4, C_2–C_4, C_{5+} selectivity (hydrocarbon fraction in the product stream) and CO_2 selectivity. Bottom chart represents C_3-olefin to C_3-paraffin ratio (O/P).

Potassium incorporation (10 atom-%) into the perovskite support by partial substitution of lanthanum with potassium was observed to enhance the rate of carburization of metallic iron to Hägg iron carbide via *in situ* XRD, which has been widely reported to be the active phase for CO activation and C-C chain growth in the FT synthesis [66–69]. The Fe-$La_{0.9}K_{0.1}AlO_3$ catalyst shows a substantial increase in CO conversion to 75.8% compared to 44.6% in the absence of K (see Figure 5-17). A comparable enhancement of CO conversion is observed in the presence of an additional small amount of Mn in the B site of the perovskite structure (Fe-$La_{0.9}K_{0.1}Mn_{0.2}Al_{0.8}O_3$). Further increases in Mn content, result in sharp decreases in CO conversion, below the unpromoted reference catalyst. Product selectivity, especially in complex reaction networks such as the FT synthesis, is generally a function of conversion, therefore the selectivity of different catalysts should be compared at similar conversion levels. To allow for comparison with the other catalysts tested in this study, the CO conversion of Fe-$La_{0.9}K_{0.1}AlO_3$ and Fe-$La_{0.9}K_{0.1}Mn_{0.2}Al_{0.8}O_3$ was adjusted by increasing the space velocity by a factor of 3.75. The new high space velocity is termed $3.75 \cdot SV_{org}$.

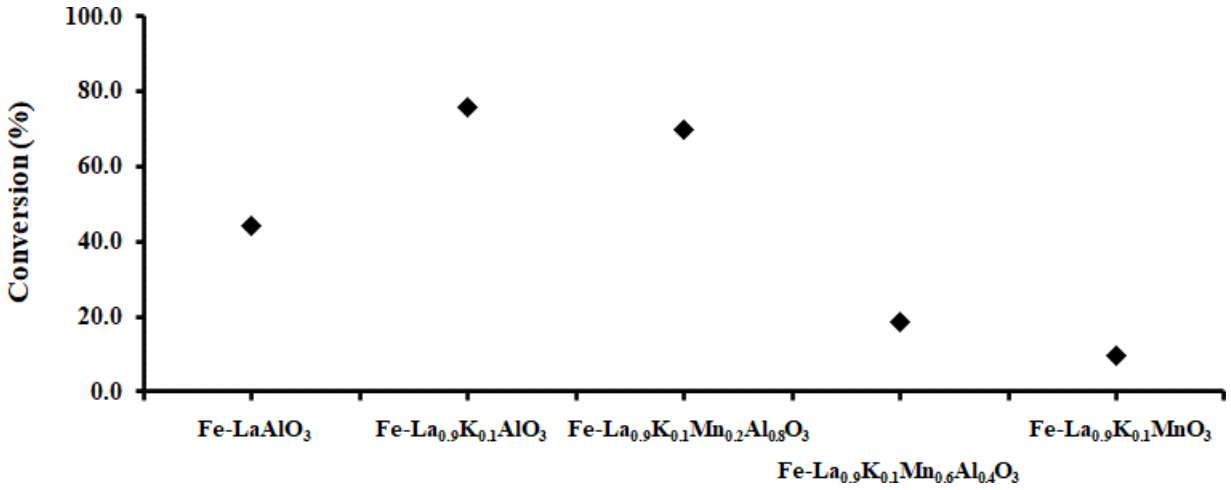

Figure 5-17: CO conversion of Fe-$LaAlO_3$, Fe-$La_{0.9}K_{0.1}AlO_3$, Fe-$La_{0.9}K_{0.1}Mn_{0.2}Al_{0.8}O_3$, Fe-$La_{0.9}K_{0.1}Mn_{0.6}Al_{0.4}O_3$ and Fe-$La_{0.9}K_{0.1}MnO_3$ at original space velocity at original space velocity (SV_{org}).

The increase of space velocity reduced the CO conversion of Fe-$La_{0.9}K_{0.1}AlO_3$ and Fe- $La_{0.9}K_{0.1}Mn_{0.2}Al_{0.8}O_3$ to 34.0 and 30.0% respectively (see Figure 5-18), still representing a much-enhanced rate of CO conversion but at a similar overall conversion level allowing for selectivity comparisons. Fe-$La_{0.9}K_{0.1}AlO_3$ shows a slight increase in CO_2 selectivity (from 12.7 to 15.6 C-%), which suggests a moderate enhancement of the water gas shift reaction. In parallel the methane selectivity is reduced in favor of the C_{5+} selectivity resulting in an increased chain growth probability. The olefinicity of the hydrocarbon product is drastically increased

from 0.7 to 3.2 in the C_3 product suggesting a reduced hydrogenation efficiency of primarily formed olefins. All these effects have previously been reported for K promotion in iron-based FT catalysts. The presence of the lowest studied concentration of Mn in the perovskite further improves the product composition. The CO_2 selectivity, i.e. the WGS reaction, is less enhanced representing only 14% of the product bound carbon. The methane selectivity is even lower compared to Fe-$La_{0.9}K_{0.1}AlO_3$ and the product slate shifts towards the C_{5+} hydrocarbons now comprising 75.7% of the carbon bound in the hydrocarbon product. The olefin to paraffin ratio is not affected by the additional presence of Mn. Potassium and manganese are frequently used to improve olefin selectivity [70,71].

Besides the previously discussed detrimental effect on activity, the increase of Mn content also does not improve the product composition. The WGS activity is enhanced, resulting in 40 to 45% of all product carbon to be bound in CO_2. At the same time the methane selectivity increases, even above the levels of Fe-$LaAlO_3$ and the hydrocarbon product spectrum shifts towards the C_2–C_4 fraction. The olefinicity is further enhanced reaching values of 3.6 and 3.9 for the C_3 fraction. Mn in particular has been reported to reduce the secondary hydrogenation probability of C=C bonds leading to an increased selectivity towards olefins [50,72].

Tao *et al.* [64] observed for coprecipitated Fe/Mn/K catalysts an increase in the catalyst activity with increasing manganese content up to a certain maximum. Further addition of Mn decreases the activity supposedly because higher levels of manganese (above 6.0 wt.-%) stabilize Fe^{3+} and Fe^{2+} irons and inhibit the carburization of the catalyst in syngas. In the present study, the employed concentrations of Mn did not enhance activity and TPR results showed that the presence of manganese in the perovskite matrix hinders the reduction of the iron phase, potentially affecting the number of active sites under reaction conditions. Lower levels of Mn substitution of Al should be investigated. It is important to note that in the here developed empowered support materials the effect of Mn is limited to an electronic promotion due to its incorporation in the perovskite matrix. Previously observed structural promotion through stabilization of iron crystallites against sintering can be excluded [50,73].

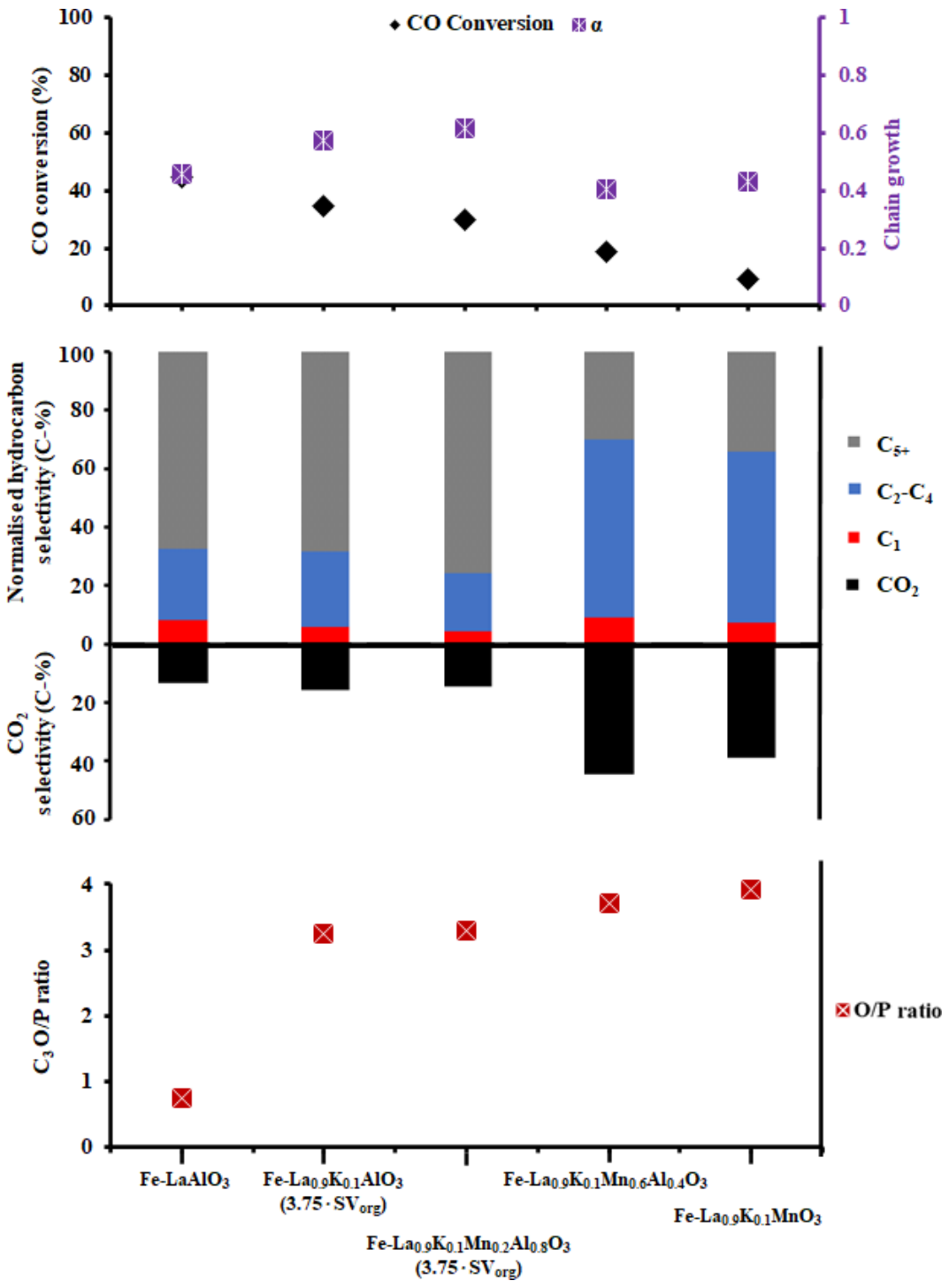

Figure 5-18: Catalytic performance of Fe-$LaAlO_3$, Fe-$La_{0.9}K_{0.1}Mn_{0.6}Al_{0.4}O_3$ and Fe-$La_{0.9}K_{0.1}MnO_3$ at the original space velocity (SV_{org}) and Fe-$La_{0.9}K_{0.1}AlO_3$ and Fe-$La_{0.9}K_{0.1}Mn_{0.2}Al_{0.8}O_3$ at high space velocity (3.75 ·SV_{org}) after 48 hrs TOS. Top chart displays CO conversion and chain growth probability (α). Middle bar chat depicts the normalized CH_4, C_2–C_4, C_{5+} selectivity (hydrocarbon fraction in the product stream) and CO_2 selectivity. Bottom chart represents C_3-olefin to C_3-paraffin ratio (O/P).

The effect of promotion by potassium incorporation into the $LaAlO_3$ perovskite matrix was compared with the traditional potassium promotion achieved via impregnation of $LaAlO_3$ with potassium nitrate. Because the amount of potassium promoter exposed on the surface termination of the perovskite and in contact with the iron/iron carbide nanoparticles is not known and is less than the absolute amount of potassium in the perovskite, three different promoter concentrations, namely 0.5, 1 and 2 wt.-%, were prepared (termed Fe-0.5K$LaAlO_3$, Fe-1K$LaAlO_3$ and Fe-2K$LaAlO_3$ respectively). A potassium loading of 2 wt.-% equates to the absolute amount of potassium incorporated into $La_{0.9}K_{0.1}AlO_3$.

Fe-0.5K$LaAlO_3$, Fe-1K$LaAlO_3$ showed elevated CO conversions at the original space velocity, similar to Fe-$La_{0.9}K_{0.1}AlO_3$ and Fe-$La_{0.9}K_{0.1}Mn_{0.2}Al_{0.8}O_3$ and were therefore re-evaluated at a space velocity increased by a factor of 3.75 to achieve iso-conversion (see Figure 5-19). At these conditions, the product composition of the catalysts with promoter incorporation into the perovskite matrix and the samples with impregnated potassium are markedly different. Compared to Fe-$La_{0.9}K_{0.1}AlO_3$ and Fe-$La_{0.9}K_{0.1}Mn_{0.2}Al_{0.8}O_3$, the samples with classic promoter deposition show a heavier product slate, i.e. lower methane and C_2–C_4 selectivity at an increased C_{5+} fraction. Within the hydrocarbons, the olefin content is comparable with O/P ratios of the C_3 fraction of 3.2, 3.4, 2.9 and 3.2 for the Fe-$La_{0.9}K_{0.1}AlO_3$, Fe-$La_{0.9}K_{0.1}Mn_{0.2}Al_{0.8}O_3$, Fe-0.5K$LaAlO_3$ and Fe-1K$LaAlO_3$ respectively. However, in parallel with the enhancement of the FT selectivity the impregnated potassium also enhanced the water gas shift activity significantly. While the CO_2 selectivity of Fe-$La_{0.9}K_{0.1}AlO_3$ and Fe-$La_{0.9}K_{0.1}Mn_{0.2}Al_{0.8}O_3$ only increased by 22 and 10% respectively when compared to Fe-$LaAlO_3$, the potassium impregnation resulted in an increase of 86 and 69% for the 0.5 and 1 wt.-% K loading. This results in an overall higher undesired C_1 product selectivity of the impregnated samples. It appears, that at the given conditions, potassium incorporated into the perovskite matrix selectively promotes the FTS without enhancing the WGS to the same extent. Such a deconvolution is not possible with conventional promoter impregnation.

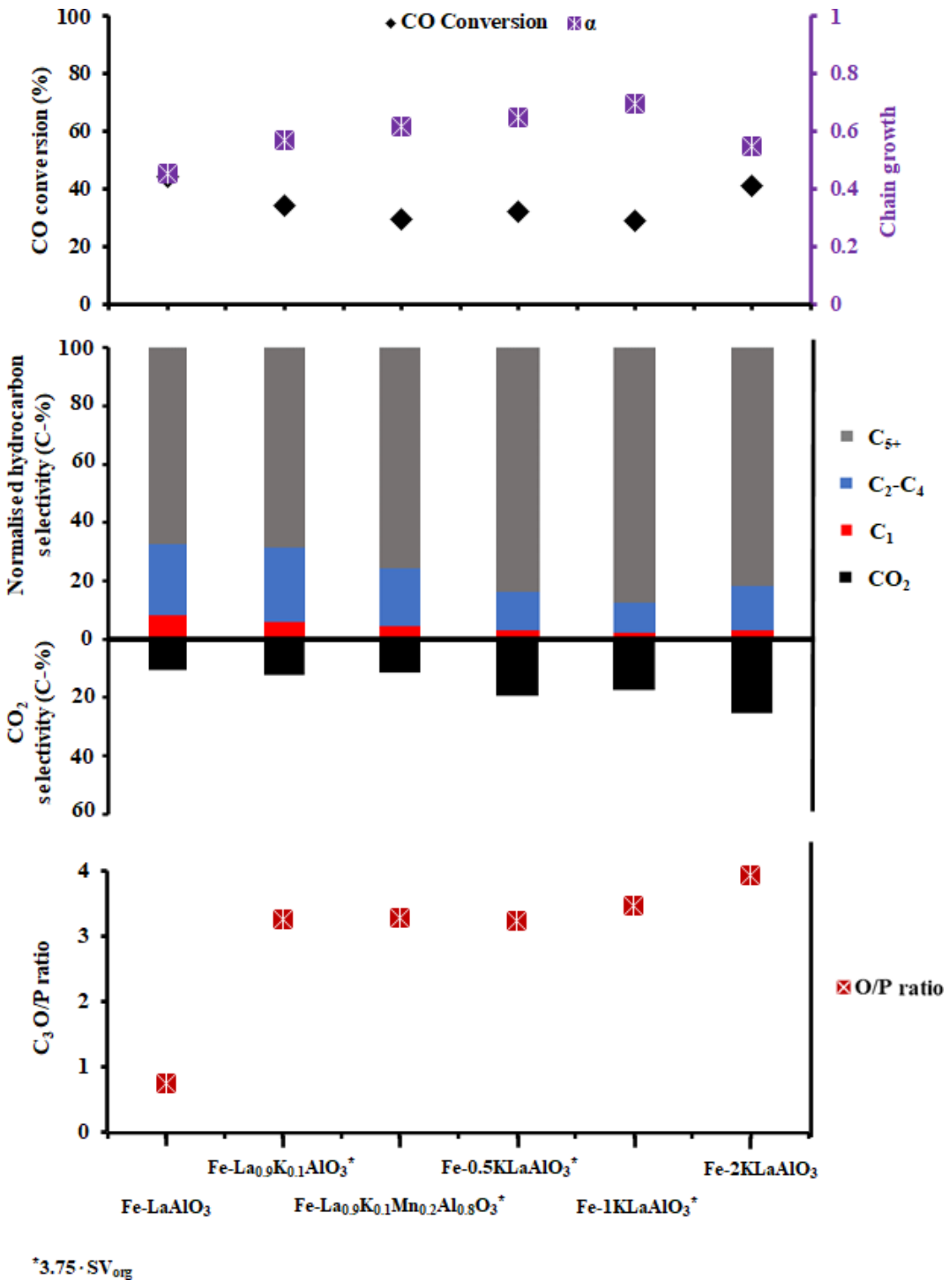

Figure 5-19: Catalytic performance of Fe-2KLaAlO$_3$ at the original space velocity (SV$_{org}$) and Fe-LaAlO$_3$, Fe-La$_{0.9}$K$_{0.1}$AlO$_3$, Fe-La$_{0.9}$K$_{0.1}$Mn$_{0.2}$Al$_{0.8}$O$_3$, Fe-0.5KLaAlO$_3$ and Fe-1KLaAlO$_3$ at the high space velocity (3.75 ·SV$_{org}$) after 48 hrs TOS. Top chart displays CO conversion and chain growth probability (α). Middle bar chat depicts the normalized CH$_4$, C$_2$–C$_4$, C$_{5+}$ selectivity (hydrocarbon fraction in the product stream) and CO$_2$ selectivity. Bottom chart represents C$_3$-olefin to C$_3$-paraffin ratio (O/P).

The spent catalysts were collected at the end of the 48 hrs FT run and subjected to a four-day extraction of wax using xylene. The samples were subsequently washed with ethanol and dried overnight. The XRD patterns of the spent Fe-$LaAlO_3$ and Fe-$La_{0.9}K_{0.1}Mn_{0.2}Al_{0.8}O_3$ catalysts run at the original space velocity show that the perovskite structure is not destroyed (see Figure 5.18). The promoter free catalyst consists of the Hägg carbide phase with about 6 wt.-% metallic iron and some magnetite. The promoted catalyst does not show any presence of metallic iron but consists mainly of Hägg carbide phase and traces of Fe_3O_4. These results further confirm the earlier discussion enhanced carburization in the presence of K (see Figure 5-14). The presence and amount of carbide in the spent catalysts also supports the stability of the catalysts also evidenced by the relatively constant CO conversion throughout the 48 hrs FT synthesis run (see Figure C. 1 - 5).

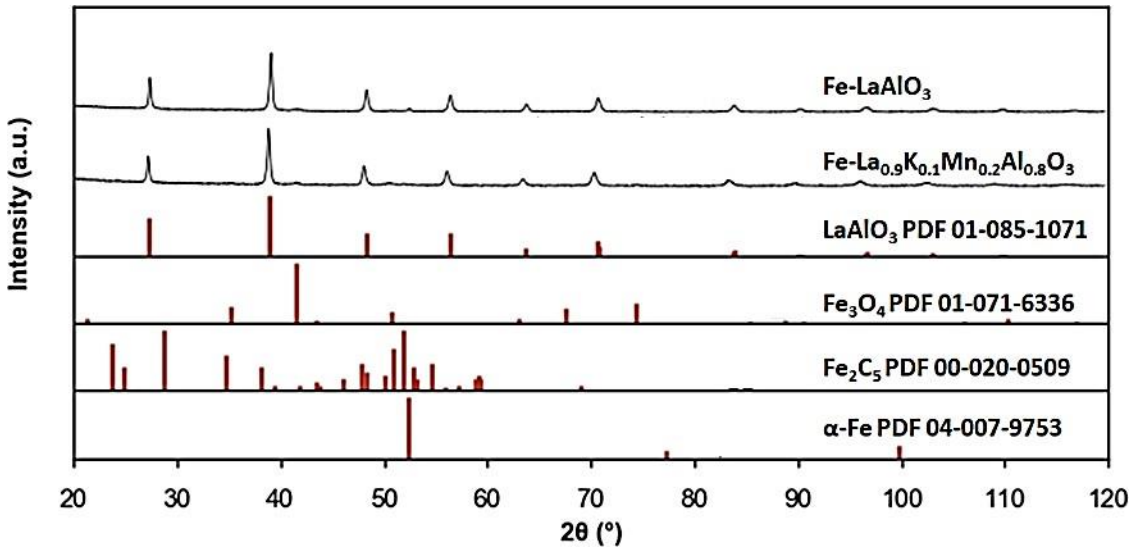

Figure 5-20: XRD diffraction patterns of spent Fe-$LaAlO_3$, and Fe-$La_{0.9}K_{0.1}Mn_{0.2}Al_{0.8}O_3$, and reference patterns of $LaAlO_3$, Fe_3O_4, Fe_2C_5 and α-Fe.

Elemental analysis of spent catalyst entrapped in wax also compared well with the composition of the fresh samples, excluding significant loss of promoters through leaching (see Table 5-3).

Table 5-4: ICP/AAS Elemental compositions of prepared samples, spent samples and their theoretical values.

Sample/Element	Fresh Catalyst ICP/AAS wt.-%				Spent Catalyst ICP/AAS wt.-%				Theoretical wt.-%			
	La	**K**	**Al**	**Mn**	**La**	**K**	**Al**	**Mn**	**La**	**K**	**Al**	**Mn**
Fe-$La_{0.9}K_{0.1}AlO_3$	82.3	2.2	15.5	0.0	81.5	1.9	16.7	0.0	80.0	2.5	17.0	0.0
Fe-$La_{0.9}K_{0.1}Mn_{0.2}Al_{0.8}O_3$	79.7	1.5	13.7	5.1	71.1	1.7	22.6	4.7	77.0	2.0	13.0	7.0

All previously discussed catalysts containing potassium incorporated into the perovskite matrix targeted a 10 atom-% occupancy of the A site with potassium. It was shown that higher potassium loadings (20 atom-%) did result in external potassium enriched structures, probably due to the charge imbalance which cannot be compensated by Al^{3+} rather than the ionic radius of K^+. It can however not be claimed that the successfully synthesized Fe-$La_{0.9}K_{0.1}Mn_yAl_{1-y}O_3$ (with y = 0 and 0.2) represents the ideal potassium concentration. A measurement of potassium exposed on the surface terminations of the perovskite is challenging and its amount directly correlates with surface area. It is also unclear if only surface exposed potassium contributes to the observed promotional effect or if subsurface species play a role and if so to what depth.

To shed some initial light on these questions two additional samples were prepared, a bulk Fe-$La_{1-x}K_xAlO_3$ with x = 0.02 and a 3DOM perovskite with the stoichiometry of x = 0 and 0.1. The elevated surface area of the 3DOM samples also allowed for an incipient wetness impregnation of the iron precursor, instead of the complicated and not scalable approach to deposit pre-prepared nanoparticles.

When exposed to the FT conditions at the original space velocity the Fe-$La_{0.98}K_{0.02}AlO_3$ catalyst also shows high levels of CO conversion comparable to Fe-$La_{0.9}K_{0.1}Mn_yAl_{1-y}O_3$ (with y = 0 and 0.2) (see Figure 5-21). At a lower water gas shift activity (CO_2 selectivity) the hydrocarbon product is heavier, with a higher selectivity of C_{5+} hydrocarbons. While elevated in comparison to Fe-$LaAlO_3$, at a different conversion level, the O/P ratio of the C_3 fraction is lower at the reduced K content (2.3 vs 3.2 to 3.4 in the C_3 fraction). These results support the assumption that the promoter concentration in the new class of empowered supports can further be tuned and optimized, specifically for the reaction conditions of interest.

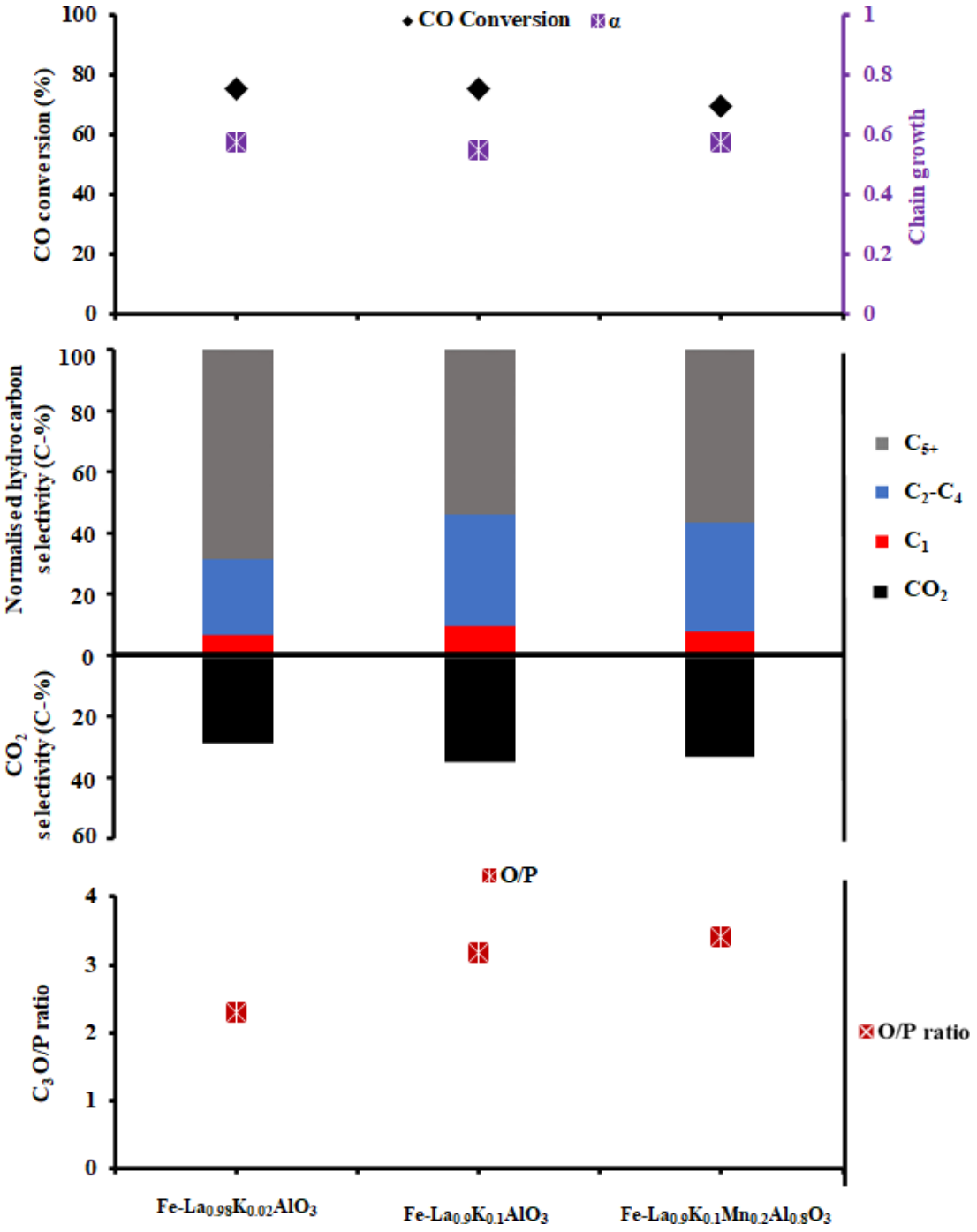

Figure 5-21: Catalytic performance of Fe-$La_{0.98}K_{0.02}AlO_3$, Fe-$La_{0.9}K_{0.1}AlO_3$ and Fe-$La_{0.9}K_{0.1}Mn_{0.2}Al_{0.8}O_3$ at the original space velocity (SV_{org}) after 48 hrs TOS. Top chart displays CO conversion and chain growth probability (α). Middle bar chat depicts the normalized CH_4, C_2–C_4, C_{5+} selectivity (hydrocarbon fraction in the product stream) and CO_2 selectivity. Bottom chart represents C_3-olefin to C_3-paraffin ratio (O/P).

Due to the fundamentally different synthesis techniques applied, the catalytic performance data of the 3DOM catalyst could not be directly compared to the previously discussed bulk perovskite-based catalysts. However, it is evident that the CO conversion levels achieved are lower at the original space velocity than was observed even for Fe-$LaAlO_3$. The incorporation of K in the 3DOM perovskite matrix, while resulting in an increased surface area (see Table 5-2), did not enhance the FT activity (see Figure 5-22). The product composition however is radically affected. In the potassium bearing sample the water gas shift activity is suppressed, reducing CO_2 selectivity from 22 to just under 4 C-%. In parallel, the chain growth probability increases dramatically from 0.61 to 0.86, reducing the fraction of C_1-C_4 hydrocarbons in the hydrocarbon pool from 42.8 to 5.8 C-%. The olefin to paraffin ratio of the C_3 fraction drops slightly (1.9 to 1.6) but this effect might be related to the drop in C_3 product yield. In the C_6 fraction, as representative of the C_{5+} product group, the O/P ratio of the potassium free 3DOM catalyst is 1.5 vs. 1.7 in the presence of potassium. The reason for the differing promotional effects in the 3DOM samples compared to the bulk samples is at this stage unknown and requires further studies. It could in part be the result of the different iron deposition strategies.

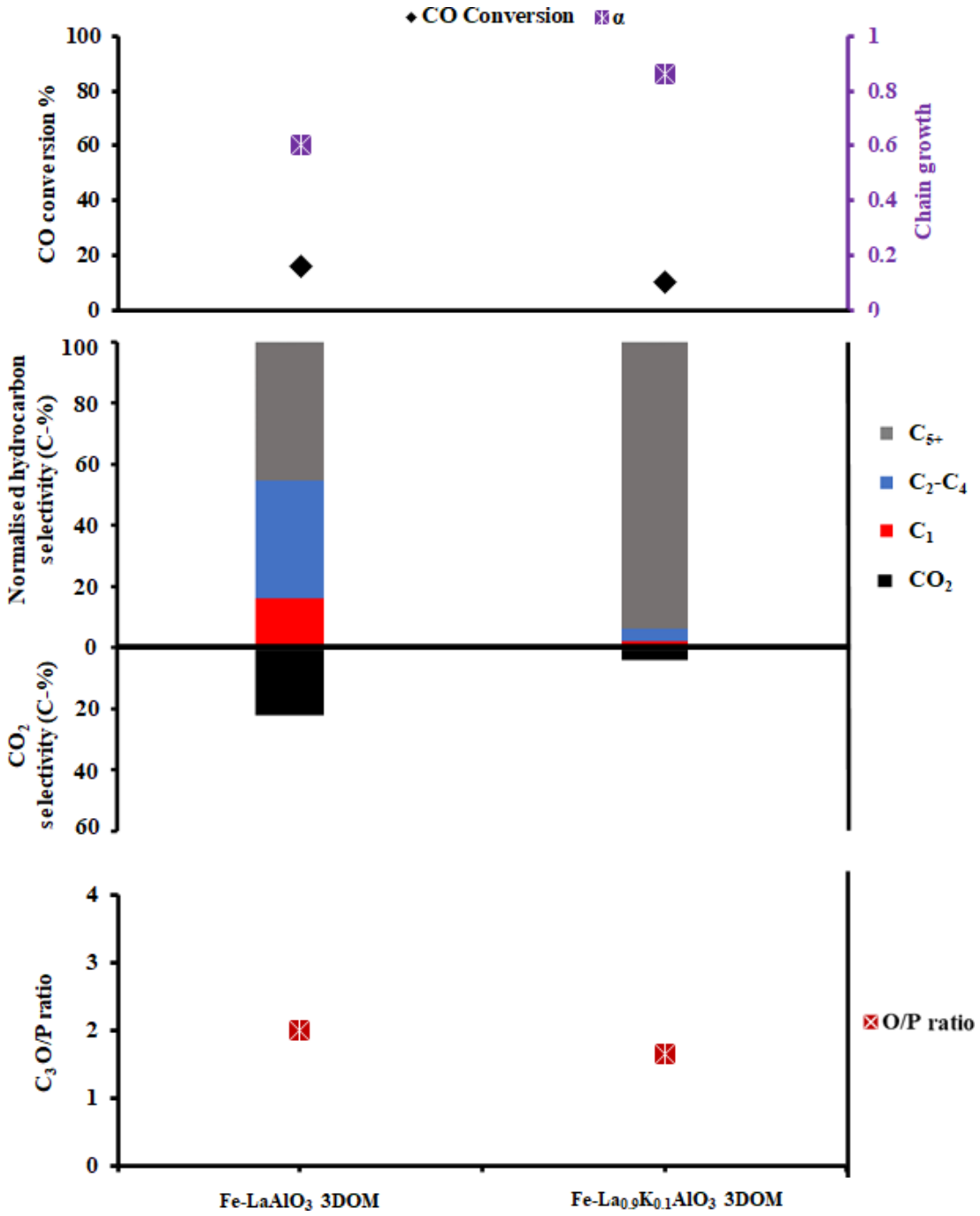

Figure 5-22: Catalytic performance of the three-dimensionally ordered mesoporous Fe-$LaAlO_3$ and Fe-$La_{0.9}K_{0.1}AlO_3$ at the original space velocity (SV_{org}) after 48 hrs TOS. Top chart displays CO conversion and chain growth probability (α). Middle bar chat depicts the normalized CH_4, C_2–C_4, C_{5+} selectivity (hydrocarbon fraction in the product stream) and CO_2 selectivity. Bottom chart represents C_3-olefin to C_3-paraffin ratio (O/P).

References

[1] N. Fischer, E. van Steen, M. Claeys, Preparation of supported nano-sized cobalt oxide and fcc cobalt crystallites, Catalysis Today 171 (1) (2011) 174–179.

[2] P. Norby, I.G.K. Andersen, E.K. Andersen, N. Andersen, The Crystal Structure of Lanthanum Manganate (iii), $LaMnO_3$, at Room Temperature and at 1273 K Under N_2, Journal of Solid-State Chemistry 119 (1995) 191–196.

[3] J.B. Elemans, B. van Laar, K.R. van der Veen, B.O. Loopstra, The crystallographic and magnetic structures of $La_{1-x}Ba_xMn_{1-x}Me_xO_3$ (Me= Mn or Ti), Journal of Solid-State Chemistry 3 (2) (1971) 238–242.

[4] R.D. Shannon, Revised effective ionic radii and systematic studies of interatomic distances in halides and chalcogenides, Acta Crystallographica Section A 32 (5) (1976) 751–767.

[5] WebElements, https://www.webelements.com, accessed July 2021.

[6] Y.Z. Fang, Y. Liu, L.H. Zhang, $LaFeO_3$-supported nano Co-Cu catalysts for higher alcohol synthesis from syngas, Applied Catalysis A: General 397 (1) (2011) 183–191.

[7] J.F. Shackelford, W. Alexander, CRC Materials Science and Engineering Handbook, 3rd ed., CRC Press LLC, United States of America, (2001).

[8] S. Fang, L. Wang, Z. Sun, N. Feng, C. Shen, P. Lin, H. Wan, G. Guan, Catalytic removal of diesel soot particulates over K and Mg substituted $La_{1-x}K_xCo_{1-y}Mg_yO_3$ perovskite oxides, Catalysis Communications 49 (2014) 15–19.

[9] J. Hueso, A. Caballero, M. Ocana, A. Gonzalezelipe, Reactivity of lanthanum substituted cobaltites toward carbon particles, Journal of Catalysis 257 (2) (2008) 334–344.

[10] Z. Tian, C. Wang, Z. Si, L. Ma, L. Chen, Q. Liu, Q. Zhang, H. Huang, Fischer-Tropsch synthesis to light olefins over iron-based catalysts supported on KMnO4 modified activated carbon by a facile method, Applied Catalysis A: General 541 (2017) 50–59.

[11] J. Xie, J. Yang, A.I. Dugulan, A. Holmen, D. Chen, K.P. de Jong, M.J. Louwerse, Size and Promoter Effects in Supported Iron Fischer-Tropsch Catalysts: Insights from Experiment and Theory, ACS Catalysis 6 (5) (2016) 3147–3157.

[12] C. Tsounis, Y. Wang, H. Arandiyan, R.J. Wong, C.Y. Toe, R. Amal, J. Scott, Tuning the Selectivity of $LaNiO_3$ Perovskites for CO_2 Hydrogenation through Potassium Substitution, Catalysts 10 (4) (2020) 409.

[13] N. Feng, C. Chen, J. Meng, Y. Wu, G. Liu, L. Wang, H. Wan, G. Guan, Facile synthesis of three-dimensionally ordered macroporous silicon-doped $La_{0.8}K_{0.2}CoO_3$ perovskite catalysts for soot combustion, Catalysis Science & Technology 6 (21) (2016) 7718–7728.

[14] J. Xu, J. Liu, Z. Zhao, C. Xu, J. Zheng, A. Duan, G. Jiang, Easy synthesis of three-dimensionally ordered macroporous $La_{1-x}K_xCoO_3$ catalysts and their high activities for the catalytic combustion of soot, Journal of Catalysis 282 (1) (2011) 1–12.

[15] T. Maneerung, K. Hidajat, S. Kawi, K-doped $LaNiO_3$ perovskite for high-temperature water-gas shift of reformate gas: Role of potassium on suppressing methanation, International Journal of Hydrogen Energy 42 (15) (2017) 9840–9857.

[16] A. Miyakoshi, A. Ueno, M. Ichikawa, XPS and TPD characterization of manganese-substituted iron–potassium oxide catalysts which are selective for dehydrogenation of ethylbenzene into styrene, Applied Catalysis A: General 219 (1-2) (2001) 249–258.

[17] M. Sadakane, C. Takahashi, N. Kato, H. Ogihara, Y. Nodasaka, Y. Doi, Y. Hinatsu, W. Ueda, Three-Dimensionally Ordered Macroporous (3DOM) Materials of Spinel-Type Mixed Iron Oxides. Synthesis, Structural Characterization, and Formation Mechanism of Inverse Opals with a Skeleton Structure, Bulletin of the Chemical Society of Japan 80 (2007) 677–685.

[18] A. Stein, R.C. Schroden, Colloidal crystal templating of three-dimensionally ordered macroporous solids: Materials for photonics and beyond, Current Opinion in Solid State and Materials Science 5 (6) (2001) 553–564.

[19] P. Nagpal, D. Josephson, N. Denny, J. DeWilde, D. Norris, A. Stein, Fabrication of carbon/refractory metal nanocomposites as thermally stable metallic photonic crystals, Journal of Materials Chemistry 21 (29) (2011) 10836-10843.

[20] Y. Zheng, Y. Wei, K. Li, X. Zhu, H. Wang, Y. Wang, Chemical-looping steam methane reforming over macroporous CeO_2–ZrO_2 solid solution: Effect of calcination temperature, International Journal of Hydrogen Energy 39 (25) (2014) 13361–13368.

[21] M. Sadakane, W. Ueda, Three-Dimensionally Ordered Macroporous (3DOM) Perovskite Mixed Metal Oxides, in: (2015) 113–142.

[22] L. Bedel, A.C. Roger, C. Estournes, A. Kiennemann, Co^0 from partial reduction of La(Co,Fe)O_3 perovskites for Fischer-Tropsch synthesis, Catalysis Today 85 (2) (2003) 207–218.

[23] M.R. Goldwasser, V.E. Dorantes, M.J. Pérez-Zurita, P.R. Sojo, M.L. Cubeiro, E. Pietri, F. González-Jiménez, Y.N. Lee, D. Moronta, Modified iron perovskites as catalysts precursors for the conversion of syngas to low molecular weight alkenes, Journal of Molecular Catalysis A: Chemical 193 (1) (2003) 227–236.

[24] G. Subıas, J. Garcıa, M.G. Proietti, J. Blasco, X-ray-absorption near-edge spectroscopy and circular magnetic X-ray dichroism at the Mn K edge of magnetoresistive manganites, Physics Reviews. B 56 (13) (1997) 8183–8191.

[25] V. Celorrio, L. Calvillo, G. Granozzi, A.E. Russell, D.J. Fermin, $AMnO_3$ (A = Sr, La, Ca, Y) Perovskite Oxides as Oxygen Reduction Electrocatalysts, Topics in Catalysis 61 (3) (2018) 154–161.

[26] V. Celorrio, L. Calvillo, C.A.M. van den Bosch, G. Granozzi, A. Aguadero, A.E. Russell, D.J. Fermín, Mean Intrinsic Activity of Single Mn Sites at $LaMnO_3$ Nanoparticles Towards the Oxygen Reduction Reaction, ChemElectroChem 5 (20) (2018) 3044–3051.

[27] G. Jacobs, V.R.R. Pendyala, M. Martinelli, W.D. Shafer, M.K. Gnanamani, S. Khalid, A. MacLennan, Y. Hu, B.H. Davis, Fischer-Tropsch Synthesis: XANES Spectra of Potassium in Promoted Precipitated Iron Catalysts as a Function of Time On-stream, Catalysis Letters 147 (8) (2017) 1861–1870.

[28] C.J. Davies, A. Mayer, J. Gabb, J.M. Walls, V. Degirmenci, P.B.J. Thompson, G. Cibin, S. Golunski, S.A. Kondrat, Operando potassium K-edge X-ray absorption spectroscopy: Investigating potassium catalysts during soot oxidation, Physical Chemistry Chemical Physics 22 (34) (2020) 18976–18988.

[29] X. Mou, X. Wei, Y. Li, W. Shen, Tuning crystal-phase and shape of Fe_2O_3 nanoparticles for catalytic applications, CrystEngComm 14 (16) (2012) 5107–5120.

[30] R.P. Mogorosi, N. Fischer, M. Claeys, E. van Steen, Strong-metal–support interaction by molecular design: Fe–silicate interactions in Fischer-Tropsch catalysts, Journal of Catalysis 289 (2012) 140–150.

[31] J. Yu, Z. Si, L. Chen, X. Wu, D. Weng, Selective catalytic reduction of NO_x by ammonia over phosphate-containing $Ce_{0.75}Zr_{0.25}O_2$ solids, Applied Catalysis B: Environmental 163 (2015) 223–232.

[32] W.K. Jóźwiak, T.P. Maniecki, P. Mierczyński, K. Bawolak, W. Maniukiewicz, Reduction study of iron-alumina binary oxide $Fe_{2-x}Al_xO_3$, Polish Journal of Chemistry 83 (12) (2009) 2153–2162.

[33] W.K. Jozwiak, E. Kaczmarek, T.P. Maniecki, W. Ignaczak, W. Maniukiewicz, Reduction behavior of iron oxides in hydrogen and carbon monoxide atmospheres, Applied Catalysis A: General 326 (1) (2007) 17–27.

[34] P. Mierczynski, B. Dawid, W. Maniukiewicz, M. Mosinska, M. Zakrzewski, R. Ciesielski, A. Kedziora, S. Dubkov, D. Gromov, J. Rogowski, I. Witonska, M.I. Szynkowska, T. Maniecki, Fischer-Tropsch synthesis over various $Fe/Al_2O_3–Cr_2O_3$ catalysts, Reaction Kinetics, Mechanisms and Catalysis 124 (2) (2018) 545–561.

[35] Y. Jin, A.K. Datye, Phase transformations in iron Fischer-Tropsch catalysts during temperature-programmed reduction, Journal of Catalysis 196 (1) (2000) 8–17.

[36] D.B. Bukur, C. Sivaraj, Supported iron catalysts for slurry phase Fischer-Tropsch synthesis, Applied Catalysis A: General 231 (1-2) (2002) 201–214.

[37] V.P. Romanov, L.F. Checherskaya, P.A. Tatsienko, Peculiarities of wustite formed below 570 °C, physica status solidi (a) 15 (2) (1973) 721–724.

[38] A. Pineau, N. Kanari, I. Gaballah, Kinetics of reduction of iron oxides by H_2: Part I: Low temperature reduction of hematite, Thermochimica Acta 447 (1) (2006) 89–100.

[39] J. Huebler, in: Iron Ore Reduction, Proceedings of the Symposium on Electrothermics and Metallurgy Division. Chicago, May 1960, Pergamon Press, New York, The Electrochemistry Society (1962) 41–48.

[40] A.J.H.M. Kock, H.M. Fortuin, J.W. Geus, The reduction behavior of supported iron catalysts in hydrogen or carbon monoxide atmospheres, Journal of Catalysis 96 (1) (1985) 261–275.

[41] Y. Yang, H. Xiang, L. Tian, H. Wang, C. Zhang, Z. Tao, Y. Xu, B. Zhong, Y.W. Li, Structure and Fischer-Tropsch performance of iron manganese catalyst incorporated with SiO_2, Applied Catalysis A-general 284 (2005) 105–122.

[42] X.J. Wang, J. Renn, J. Spencer, C. Ratnasamy, Y. Cai, A Novel Method for Measuring Active Sites of Fe_3O_4 for WGS Reaction, Topics in Catalysis 56 (18) (2013) 1899–1905.

[43] R. Xu, P. Vengsarkar, D. Roe, C. Roberts, Fischer-Tropsch Synthesis Performance of Supported Nano-Iron Catalysts Synthesized By a Gas-Expanded Liquid Deposition Technique, Energy Fuels 31 (4) (2017) 4343-4352.

[44] J. Li, X. Cheng, C. Zhang, Q. Chang, J. Wang, X. Wang, Z. Lv, W. Dong, Y. Yang, Y. Li, Effect of alkalis on iron-based Fischer-Tropsch synthesis catalysts: Alkali-FeO_x interaction, reduction, and catalytic performance, Applied Catalysis A: General 528 (2016) 131–141.

[45] H. Xiong, M.A. Motchelaho, M. Moyo, L.L. Jewell, N.J. Coville, Effect of Group I alkali metal promoters on Fe/CNT catalysts in Fischer-Tropsch synthesis, Fuel 150 (2015) 687–696.

[46] N. Fischer, R. Henkel, B. Hettel, M. Iglesias, G. Schaub, M. Claeys, Hydrocarbons via CO_2 Hydrogenation Over Iron Catalysts: The Effect of Potassium on Structure and Performance, Catalysis Letters 146 (2) (2016) 509–517.

[47] B. Shi, Z. Zhang, Y. Liu, J. Su, X. Liu, X. Li, J. Wang, M. Zhu, Z. Yang, J. Xu, Y.F. Han, Promotional effect of Mn-doping on the structure and performance of spinel ferrite microspheres for CO hydrogenation, Journal of Catalysis 381 (2020) 150–162.

[48] J.F. Lee, W.S. Chern, M.D. Lee, T.Y. Dong, Hydrogenation of carbon dioxide on iron catalysts doubly promoted with manganese and potassium, The Canadian Journal of Chemical Engineering 70 (3) (1992) 511–515.

[49] Z. Yang, Z. Zhang, Y. Liu, X. Ding, J. Zhang, J. Xu, Y. Han, Tuning direct CO hydrogenation reaction over Fe-Mn bimetallic catalysts toward light olefins: Effects of Mn promotion, Applied Catalysis B: Environmental 285 (2021) 119815.

[50] T. Li, Y. Yang, C. Zhang, X. An, H. Wan, Z. Tao, H. Xiang, Y. Li, F. Yi, B. Xu, Effect of manganese on an iron-based Fischer-Tropsch synthesis catalyst prepared from ferrous sulfate, Fuel 86 (7) (2007) 921–928.

[51] T. Grzybek, H. Papp, N. Baerns, Fe/Mn oxide catalysts for Fischer-Tropsch synthesis: Part V XPS surface characterization of calcined and reduced samples, Applied Catalysis 29 (2) (1987) 335–350.

[52] K.M. Kreitman, M. Baerns, J.B. Butt, Manganese-oxide-supported iron Fischer-Tropsch synthesis catalysts: Physical and catalytic characterization, Journal of Catalysis 105 (2) (1987) 319–334.

[53] I.S.C. Hughes, J.O.H. Newman, G.C. Bond, The characterization of unsupported iron and manganese-promoted iron catalysts by X-ray photoelectron spectroscopy and temperature-programmed reduction, Applied Catalysis 30 (2) (1987) 303–311.

[54] K.B. Jensen, F.E. Massoth, Studies on iron-manganese oxide carbon monoxide catalysts: II. Carburization and catalytic activity, Journal of Catalysis 92 (1) (1985) 109–118.

[55] M. Jiang, N. Koizumi, M. Yamada, Characterization of potassium-promoted iron–manganese catalysts by insitu diffuse reflectance FTIR using NO, CO and CO+H_2 as probes, Applied Catalysis A: General 204 (1) (2000) 49–58.

[56] E. de Smit, A.M. Beale, S. Nikitenko, B.M. Weckhuysen, Local and long-range order in promoted iron-based Fischer-Tropsch catalysts: A combined in situ X-ray absorption spectroscopy/wide angle X-ray scattering study, Journal of Catalysis 262 (2) (2009) 244–256.

[57] S. Li, W. Ding, G.D. Meitzner, E. Iglesia, Spectroscopic and Transient Kinetic Studies of Site Requirements in Iron-Catalyzed Fischer−Tropsch Synthesis, The Journal of Physical Chemistry B 106 (1) (2002) 85–91.

[58] H. Jung, W.J. Thomson, Dynamic X-ray diffraction study of an unsupported iron catalyst in Fischer-Tropsch synthesis, Journal of Catalysis 134 (2) (1992) 654–667.

[59] M. Wolf, E.K. Gibson, E.J. Olivier, J.H. Neethling, C.R.A. Catlow, N. Fischer, M. Claeys, Water-Induced Formation of Cobalt-Support Compounds under Simulated High Conversion Fischer-Tropsch Environment, ACS Catalysis 9 (6) (2019) 4902–4918.

[60] J. Barrault, C. Forquy, V. Perrichon, Effects of manganese oxide and sulphate on olefin selectivity of iron supported catalysts in the Fischer-Tropsch reaction, Applied Catalysis 5 (1) (1983) 119–125.

[61] M. Dad, H.O.A. Fredriksson, J. van de Loosdrecht, P.C. Thüne, J.W. Niemantsverdriet, Stabilization of iron by manganese promoters in uniform bimetallic FeMn Fischer-Tropsch model catalysts prepared from colloidal nanoparticles, Catalysis, Structure & Reactivity 1 (2) (2015) 101–109.

[62] J. Barrault, C. Forquy, V. Perrichon, Effects of manganese oxide and sulphate on olefin selectivity of iron supported catalysts in the Fischer-Tropsch reaction, Applied Catalysis 5 (1) (1983) 119–125.

[63] M.E. Dry, G.J. Oosthuizen, The correlation between catalyst surface basicity and hydrocarbon selectivity in the Fischer-Tropsch synthesis, Journal of Catalysis 11 (1) (1968) 18–24.

[64] Z. Tao, Y. Yang, H. Wan, T. Li, X. An, H. Xiang, Y. Li, Effect of manganese on a potassium-promoted iron-based Fischer-Tropsch synthesis catalyst, Catalysis Letters 114 (3) (2007) 161–168.

[65] C. Wang, Q. Wang, X. Sun, L. Xu, CO Hydrogenation to Light Alkenes Over Mn/Fe CatalystsPrepared by Coprecipitation and Sol-gel Methods, Catalysis Letters 105 (1) (2005) 93–101.

[66] S.Y. Hong, D.H. Chun, J.I. Yang, H. Jung, H.T. Lee, S. Hong, S. Jang, J.T. Lim, C.S. Kim, J.C. Park, A new synthesis of carbon encapsulated Fe_5C_2 nanoparticles for high-temperature Fischer-Tropsch synthesis, Nanoscale 7 (40) (2015) 16616–16620.

[67] C. Yang, H. Zhao, Y. Hou, D. Ma, Fe_5C_2 nanoparticles: A facile bromide-induced synthesis and as an active phase for Fischer-Tropsch synthesis, Journal of the American Chemical Society 134 (38) (2012) 15814–15821.

[68] A.M. Saib, D.J. Moodley, Im Ciobîcă, M.M. Hauman, B.H. Sigwebela, C.J. Weststrate, J.W. Niemantsverdriet, J. van de Loosdrecht, Fundamental understanding of deactivation and regeneration of cobalt Fischer-Tropsch synthesis catalysts, Catalysis Today 154 (3-4) (2010) 271–282.

[69] J. Cheng, P. Hu, P. Ellis, S. French, G. Kelly, C.M. Lok, Density functional theory study of iron and cobalt carbides for Fischer− Tropsch synthesis, The Journal of Physical Chemistry C 114 (2) (2010) 1085–1093.

[70] W. Gong, R.P. Ye, J. Ding, T. Wang, X. Shi, C.K. Russell, J. Tang, E.G. Eddings, Y. Zhang, M. Fan, Effect of copper on highly effective Fe-Mn based catalysts during production of light olefins via Fischer-Tropsch process with low CO_2 emission, Applied Catalysis B: Environmental 278 (2020) 119302.

[71] Z. Yang, X. Pan, J. Wang, X. Bao, FeN particles confined inside CNT for light olefin synthesis from syngas: Effects of Mn and K additives, Catalysis Today 186 (1) (2012) 121–127.

[72] Y. Liu, J.F. Chen, J. Bao, Y. Zhang, Manganese-modified Fe_3O_4 microsphere catalyst with effective active phase of forming light olefins from syngas, ACS Catalysis 5 (6) (2015) 3905–3909.

[73] A. Campos, N. Lohitharn, A. Roy, E. Lotero, J.G. Goodwin, J.J. Spivey, An activity and XANES study of Mn-promoted, Fe-based Fischer-Tropsch catalysts, Applied Catalysis A: General 375 (1) (2010) 12–16.

6 Conclusions

The present study presents the synthesis of $LaAlO_3$ (ABO_3) with a successful partial replacement of lanthanum with potassium (10 atom-%) on the A site, and aluminum with manganese (20-100 atom-%) on the B site. The success of the synthesis is determined by characterization to ascertain the incorporation of the promoters into the matrix of the $LaAlO_3$ perovskite. The perovskites are used as carriers for γ-Fe_2O_3 nanoparticles, and the promoting capability of these model catalysts is tested in the Fischer-Tropsch synthesis followed by characterization of the spent catalysts. The study can essentially be divided into two sections, i.e., the synthesis and the testing of the model catalysts.

One of the major objectives of this study was the preparation of the model catalyst. A series of $La_{1-x}K_xMn_yAl_{1-y}O_3$, with x = 0 and 0.1 and y = 0, 0.2, 0.6 and 1, perovskites were synthesized by a modified Pichini method [1] which is essentially a citrate sol gel auto combustion method [2]. It involves the polyesterification of citric acid and ethylene glycol to easily synthesize the porous perovskites while giving good control of the product stoichiometry. Very little work has been described in literature on attempts to synthesis perovskites with potassium promoter partially replacing lanthanum, but no attempt was made to investigate if the potassium is successfully incorporated into the perovskite matrix. A series of characterization techniques including XRD, ICP/AAS, EDS-STEM and XANES were used. XRD was used to confirm the formation of the perovskite structure. ICP/AAS analysis techniques were used to confirm the overall composition with the content of potassium and manganese somewhat lower than targeted composition. EDS-STEM and XANES were used to confirm that no potassium or manganese was enriched on the surface of the perovskite when exposed to reaction conditions. Monodispersed iron oxide nanoparticles are prepared by a co-precipitation method in which the precipitation of the iron compounds is achieved by employing NaOH and NH_3OH. This process allows for the synthesis of iron oxide nanoparticles without the use of a any organic solvents, organic metal salts, or surfactants. The obtained nanoparticles were successfully supported on the perovskite carriers via an ultrasonic mixing technique [3].

The Fischer-Tropsch synthesis was carried out in a 600 ml continuous stirred tank reactor (240 °C, 15 bar pressure, a H_2:CO ratio of 2 with 10 vol.-% N_2 as internal standard, and two different space velocities to achieve iso-conversion. The iron supported on the promoter free perovskite $LaAlO_3$ compares well with the iron supported on conventional supports (SiO_2, Al_2O_3, ZrO_2 and TiO_2), especially alumina, confirming that the $LaAlO_3$ support does not influence the catalytic performance. Low levels of manganese (20 atom-%) resulted in a drop in CO conversion and no significant change was observed in product selectivity. CO conversion was decreased by further addition of manganese with an increased C_2–C_4 selectivity and water

gas shift activity. There are a number of manganese rich catalysts documented in literature, with the reports highlighting in particular a promotion of the C_2–C_4 hydrocarbon fraction and an increased resistance against deactivation [4–6]. The TPR results obtained for the manganese rich perovskite samples also showed a suppression of reduction, which could be the origin of the lower activity. An increase in CO_2 formation at high levels of manganese has also been observed and reported before [7].

Partial substitution of lanthanum with 10 atom-% potassium in the $LaAlO_3$ and $LaMn_{0.2}Al_{0.8}O_3$ perovskites lead to a significant increase in CO conversion (from 44.5 to 75.7% and from 37.8 to 69.7%). This could be the result of an increased rate of carburization under FT conditions as evidenced by *in situ* XRD. In the presence of higher contents of manganese, the potassium did not result in an activity enhancement. Comparable elevated conversion levels were also obtained when 0.5 and 1 wt.-% potassium was impregnated onto $LaAlO_3$. The catalysts with elevated conversion were re-evaluated at an elevated space velocity yielding conversion levels comparable with the unpromoted catalysts, to allow for a fair comparison of selectivity. The product spectrum obtained for Fe-$La_{0.9}K_{0.1}AlO_3$ contains an overall lower fraction of undesired C_1 products at a slightly reduced chain growth probability compared to the samples promoted via impregnation. Especially apparent is the lower CO_2 selectivity, i.e. WGS activity. The combined effect of potassium and manganese in Fe-$La_{0.9}K_{0.1}Mn_{0.2}Al_{0.8}O_3$ shows a further increase of the C_{5+} hydrocarbons in the product spectrum at an even lower CH_4 and CO_2 selectivity. All potassium containing samples yielded a highly olefinic product suggesting a reduced hydrogenation activity. No changes in composition, crystal phase and potassium speciation were detected in the spent samples after 48 hrs under FT conditions suggesting that the prepared perovskite materials are stable under the chosen reaction conditions.

A single experiment with lower concentration of potassium in the $LaAlO_3$ perovskite (2 atom-%) also yielded a more active catalyst. In comparison to Fe-$La_{0.9}K_{0.1}AlO_3$ and Fe-$La_{0.9}K_{0.1}Mn_{0.2}Al_{0.8}O_3$ the measured product composition was even more favorable with a reduced methane and CO_2 selectivity and an increased chain growth probability. This is clear evidence that the ideal promoter concentration incorporated into the perovskite matrix has not been identified and requires more detailed experimentation.

A common downside of perovskite materials is their low surface area making them unfavorable for use as catalyst supports. Using PMMA spheres as templates, $LaAlO_3$ and $La_{0.9}K_{0.1}AlO_3$ were successfully re-prepared with higher BET surface areas. This increase allowed for iron deposition via incipient wetness impregnation, a scalable synthesis technique. While the overall conversion of these materials was lower than previously observed, and the potassium in the perovskite did not result in an enhanced CO conversion, its effect on selectivity is remarkable. The formation CO_2, methane and even C_2–C_4 is all but suppressed,

increasing the measured chain growth probability from 0.61 to 0.85. The lack of activity enhancement is not understood at this stage but might be related to the different iron deposition process.

References

[1] M.P. Pechini US3330697A, (1967).

[2] U. Megha, K. Shijina, G. Varghese, Nanosized $LaCo_{0.6}Fe_{0.4}O_3$ perovskites synthesized by citrate sol gel auto combustion method, PAC 8 (2) (2014) 87–92.

[3] X.C. Yang, Y.L. Shang, Y.H. Li, J. Zhai, N.R. Foster, Y.X. Li, D. Zou, Y. Pu, Synthesis of Monodisperse Iron Oxide Nanoparticles without Surfactants, Journal of Nanomaterials 2014 (2) (2014) 1–5.

[4] T. Li, Y. Yang, C. Zhang, X. An, H. Wan, Z. Tao, H. Xiang, Y. Li, F. Yi, B. Xu, Effect of manganese on an iron-based Fischer-Tropsch synthesis catalyst prepared from ferrous sulfate, Fuel 86 (7) (2007) 921–928.

[5] Z. Tao, Y. Yang, H. Wan, T. Li, X. An, H. Xiang, Y. Li, Effect of manganese on a potassium-promoted iron-based Fischer-Tropsch synthesis catalyst, Catalysis Letters 114 (3) (2007) 161–168.

[6] J. Barrault, C. Forquy, V. Perrichon, Effects of manganese oxide and sulphate on olefin selectivity of iron supported catalysts in the Fischer-Tropsch reaction, Applied Catalysis 5 (1) (1983) 119–125.

[7] T. Riedel, M. Claeys, H. Schulz, G. Schaub, S.S. Nam, K.W. Jun, M.J. Choi, G. Kishan, K.W. Lee, Comparative study of Fischer-Tropsch synthesis with H_2/CO and H_2/CO_2 syngas using Fe- and Co-based catalysts, Applied Catalysis A: General 186 (1999) 201–213.

7 Recommendations

While this study successfully showed that the FT synthesis can be enhanced by potassium incorporated in a perovskite structure, surpassing conventional potassium promotion, there are still several opportunities to further improve the developed systems and as well as the need to gather more understanding of the prevailing processes.

- With the confirmation that the incorporated potassium can provide the chemical and electronic effects similar to those known for conventional promoters [1–3], the versality of the perovskite to accommodate a large number of elements can be exploited by changing the composition of the parent perovskite ($LaAlO_3$). For instance, a replacement of aluminum in the B-site with for example titanium could increase the maximum uptake of potassium owing to titanium's flexibility to balance the overall charge of the system.
- The bulk perovskite samples used in the present study exhibit a very low surface area ($LaAlO_3$: 4.5 m^2g^{-1}). While an attempt was made to improve this, it was not satisfactorily explored. There are several synthesis techniques reported to improve the surface area of perovskites through soft, colloidal or hard templating [4–9]. A higher surface area is a key characteristic of a catalyst support and would allow more common active phase deposition techniques.
- Improved XANES and XAFS studies at synchrotron facilities on the promoted perovskite samples and thorough analysis of the data can help to better understand the environments and local structures of the elements (promoters) introduced into the parent perovskite matrix.
- It is crucial to understand the surface composition of the perovskite materials especially for quantifying the amount of promoter element that is exposed on the surface. Low energy ion scattering (LEIS) has been demonstrated as tool to probe the surface terminations of perovskites and could be applied to the materials developed in the present work [10–12].
- It is believed that the potassium is homogenously distributed throughout the perovskite structure. As such, some of the promoter in the bulk is likely not contributing to the observed promotional effect. Density functional theory (DFT) calculations could share light on the actual workings of the potassium in the perovskite matrix and to what distance from the surface the promoter still influences the electronic properties of the active phase.
- The morphology of the iron nanoparticles (crystallite size and shape) is well known to influence the performance of a FT catalyst [13–15]. At the same time the interaction of the iron species with the potassium in the perovskite surface is critical. It is possible that an optimum crystallite size

exits that allows intimate contact between the iron nanoparticles and the without suffering from deteriorating performance due to structure sensitivity.

- The design of the empowered supports shows very interesting and promising results in the Fischer-Tropsch synthesis. It is believed that this concept can also be transferred to other catalytic processes of industrial relevance.

References

[1] M. Amoyal, R. Vidruk-Nehemya, M. Landau, M. Herskowitz, Effect of potassium on the active phases of Fe catalysts for carbon dioxide conversion to liquid fuels through hydrogenation, Journal of Catalysis 348 (2017) 29–39.

[2] L. Gavrilović, J. Save, E.A. Blekkan, The effect of potassium on cobalt-based Fischer-Tropsch catalysts with different cobalt particle sizes, Catalysts 9 (4) (2019) 351.

[3] Z. Paál, G. Ertl, S.B. Lee, Interactions of potassium, oxygen and nitrogen with polycrystalline iron surfaces, Applications of Surface Science 8 (3) (1981) 231–249.

[4] R.K.C.D. Lima, M.S. Batista, M. Wallau, E.A. Sanches, Y.P. Mascarenhas, E.A. Urquieta-González, High specific surface area LaFeCo perovskites—Synthesis by nanocasting and catalytic behavior in the reduction of NO with CO, Applied Catalysis B: Environmental 90 (3) (2009) 441–450.

[5] Y. Wang, J. Ren, Y. Wang, F. Zhang, X. Liu, Y. Guo, G. Lu, Nanocasted Synthesis of Mesoporous $LaCoO_3$ Perovskite with Extremely High Surface Area and Excellent Activity in Methane Combustion, J. Phys. Chem. C 112 (39) (2008) 15293–15298.

[6] A.G. Margellou, I.T. Papadas, D.E. Petrakis, G.S. Armatas, Development of enhanced surface area LaFeO3 perovskites using amino acids as templating agents, Materials Research Bulletin 83 (2016) 491–501.

[7] Y. Meng, D. Gu, F. Zhang, Y. Shi, H. Yang, Z. Li, C. Yu, B. Tu, D. Zhao, Ordered mesoporous polymers and homologous carbon frameworks: Amphiphilic surfactant templating and direct transformation, Angewandte Chemie International Edition 44 (43) (2005) 7053–7059.

[8] Y. Jiao, D. Han, L. Liu, L. Ji, G. Guo, J. Hu, D. Yang, A. Dong, Highly ordered mesoporous few-layer graphene frameworks enabled by Fe_3O_4 nanocrystal superlattices, Angewandte Chemie 127 (19) (2015) 5819–5823.

[9] L. Zhang, L. Jin, B. Liu, J. He, Templated Growth of Crystalline Mesoporous Materials: From Soft/Hard Templates to Colloidal Templates, Frontiers in Chemistry 7 (2019) 22.

[10] F. Polo-Garzon, Z. Wu, Acid–base catalysis over perovskites: A review, Journal of Materials Chemistry A 6 (7) (2018) 2877–2894.

[11] E. Symianakis, D. Malko, E. Ahmad, A.S. Mamede, J.F. Paul, N. Harrison, A. Kucernak, Electrochemical Characterization and Quantified Surface Termination Obtained by Low Energy Ion Scattering and X-ray Photoelectron Spectroscopy of Orthorhombic and Rhombohedral $LaMnO_3$ Powders, The Journal of Physical Chemistry C 119 (22) (2015) 12209–12217.

[12] T. Maneerung, K. Hidajat, S. Kawi, K-doped $LaNiO_3$ perovskite for high-temperature water-gas shift of reformate gas: Role of potassium on suppressing methanation, International Journal of Hydrogen Energy 42 (15) (2017) 9840–9857.

[13] G.L. Bezemer, J.H. Bitter, H.P.C.E. Kuipers, H. Oosterbeek, J.E. Holewijn, X. Xu, F. Kapteijn, A.J. van Dillen, K.P. de Jong, Cobalt particle size effects in the Fischer-Tropsch reaction studied with carbon nanofiber supported catalysts, Journal of the American Chemical Society 128 (12) (2006) 3956–3964.

[14] N. Fischer, B. Clapham, T. Feltes, E. van Steen, M. Claeys, Size-dependent phase transformation of catalytically active nanoparticles captured in situ, Angewandte Chemie International Edition 53 (5) (2014) 1342–1345.

[15] N. Fischer, E. van Steen, M. Claeys, Preparation of supported nano-sized cobalt oxide and fcc cobalt crystallites, Catalysis Today 171 (1) (2011) 174–179.

Appendices

Appendix A – GC TCD and GC-FID

Table 7.0-1: GC-FID operating settings

Model: GC-Model Varian 3900				
Detector		Flame ionization detector(FID)		
Detector temperature				200 °C
temperature				200 °C
Split ratio				7
Column				
Column pressure				1.72 bar
Flame gas	H_2			30 ml/min
Makeup gas	N_2			25 ml/min
Air flow				300 ml/min
Temperature program		Ramp (°C/min)	Step (°C)	Time (min)
		-	-55	1.5
		9	0	0
		4	100	1
		4	200	2
		10	280	5
		20	150	-
Total time				80 min
Coolant				CO_2 (liquid)

Table 7.0-2: TCD Calibration

Calibration to N_2

Gas mix	Comp. (%)	A1	A2	A3	A4	A5	Average	f(N_2)
H_2	39.7	21744.2	21738.4	21736.2	21735.3	21739.9	21738.8	9.3
CO_2	9.7	794.5	799.6	800.0	800.1	799.4	798.7	1.4
N_2	4.9	287.6	287.0	287.5	287.3	287.5	287.4	1.0
CH_4	15.3	3449.2	3434.0	3431.3	3451.1	3448.0	3442.7	3.8
CO	19.9	1137.9	1137.5	1139.6	1138.4	1141.5	1139.0	1.0

Appendix B – Characterization

TEM micrographs

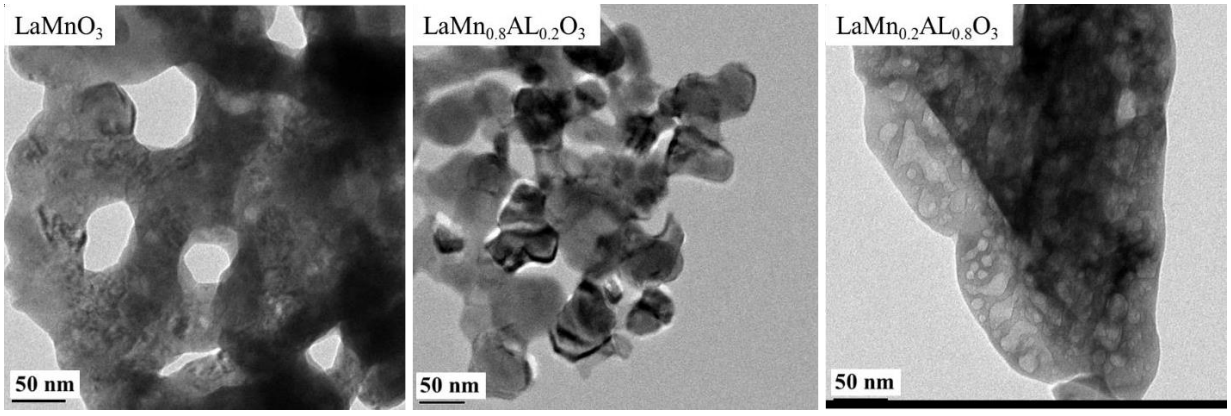

Figure B. 1: TEM micrographs of Mn doped perovskites

SEM Elemental mapping micrographs

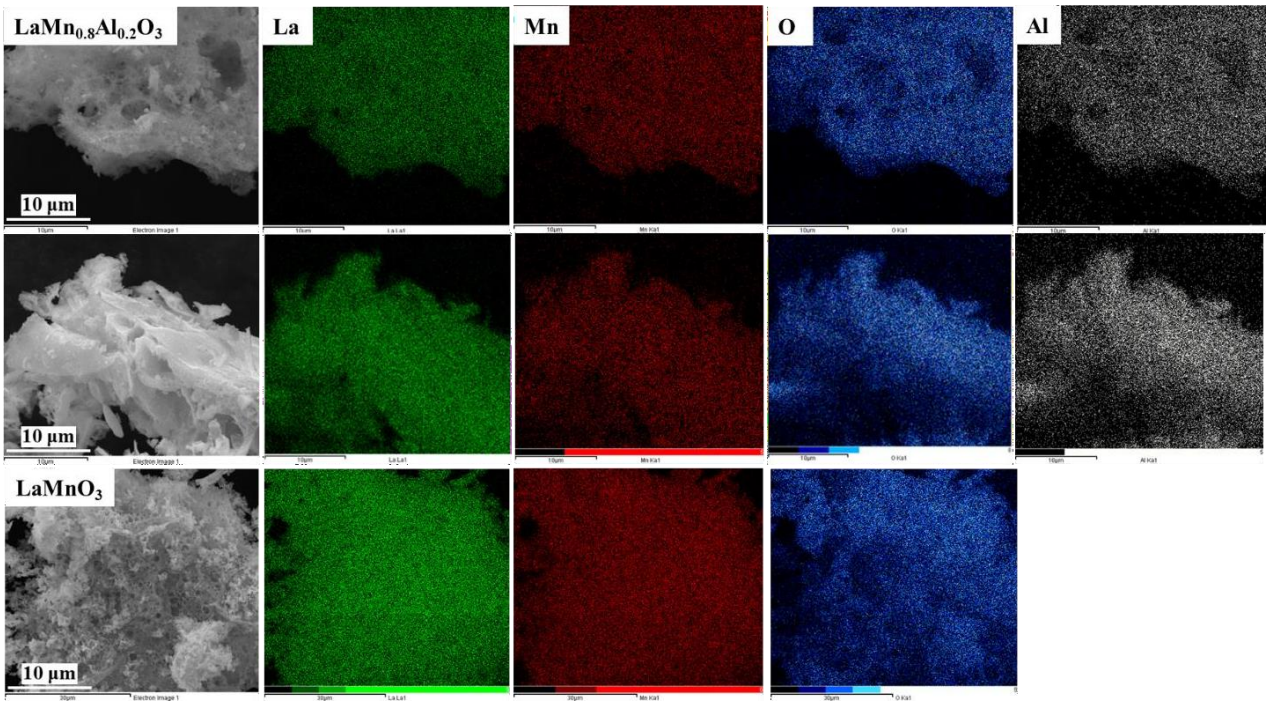

Figure B. 2: SEM elemental mapping of the prepared perovskites

EFTEM micrographs

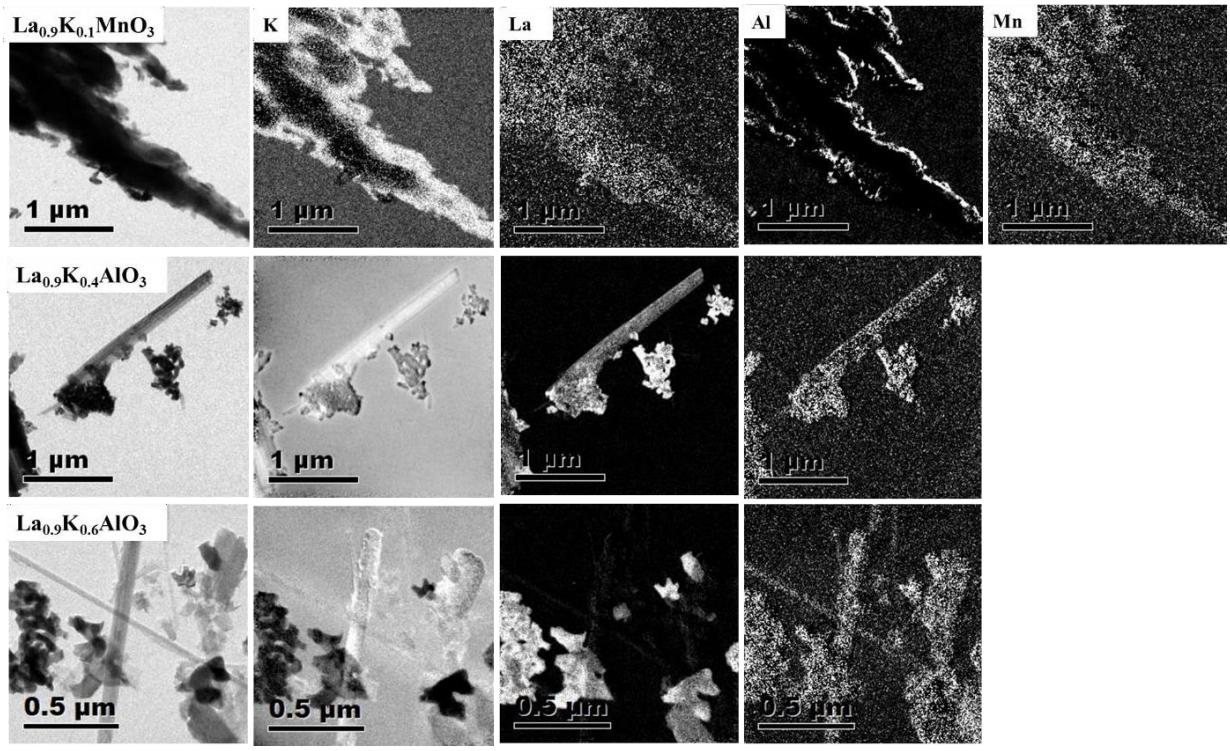

Figure B. 3: Energy-filtered transmission electron microscopy (EFTEM) of doped perovskites

HRTEM elemental mapping

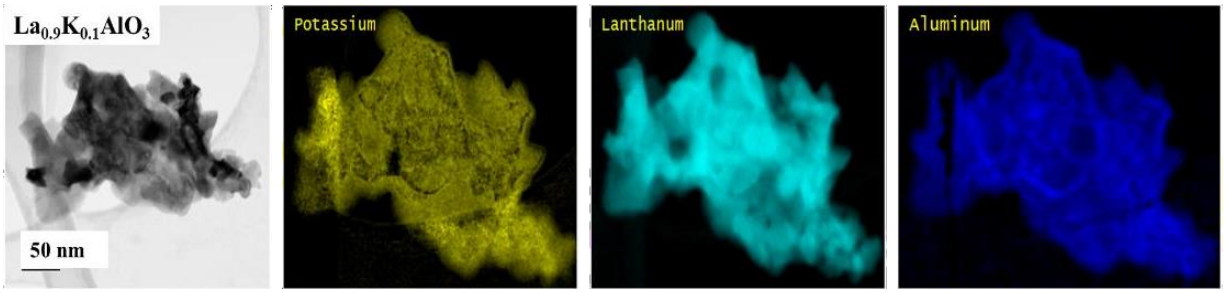

Figure B. 4: High-resolution transmission electron microscopy (HRTEM) of doped perovskites

Table B. 1: ICP and AAS elemental analysis

Sample/Element	ICP/AAS wt. frac.					Theoretical wt. frac.			
	La	**K**	**Al**	**Mn**	**Fe**	**La**	**K**	**Al**	**Mn**
Fe-$La_{0.9}K_{0.1}AlO_3$ (3.75SV)	0.817	0.019	0.164	0.000	13.40	0.800	0.025	0.170	0.000
Fe-$La_{0.9}K_{0.1}Mn_{0.2}Al_{0.8}O_3$ (High & Low SV)	0.797	0.015	0.137	0.051	13.60	0.770	0.024	0.130	0.070
Fe1K-$LaAlO_4$ (High & Low SV)	0.848	0.010	0.142	0.000	13.00	0.800	0.010	0.170	0.000
Fe0.5K-$LaAlO_5$ (High & Low SV)	0.829	0.016	0.122	0.046	14.00	0.800	0.005	0.170	0.000
Fe-$LaMn_{0.2}Al_{0.8}O_3$	0.817	0.000	0.130	0.053	12.80	0.810	0.000	0.130	0.066
$LaMn_{0.4}Al_{0.6}O_3$	0.823	0.000	0.091	0.086		0.780	0.000	0.090	0.120
$LaMn_{0.6}Al_{0.4}O_3$	0.814	0.000	0.054	0.132	13.30	0.760	0.000	0.060	0.180
Fe-$LaMn_{0.8}Al_{0.2}O_3$	0.812	0.000	0.043	0.145	12.10	0.740	0.000	0.020	0.240
Fe-$La_{0.9}K_{0.1}AlO_3$ 3DOM	0.837	0.018	0.145	0	13.30	0.8	0.025	0.170	0.000
Fe-$LaAlO_3$ 3DOM	0.835	0.001	0.164	0	12.20	0.84	0.000	0.160	0.000
$FeSiO_2$					13.90				
$FeZrO_2$					12.30				
$FeAl_2O_3$					14.00				
$FeTiO_2$					13.50				

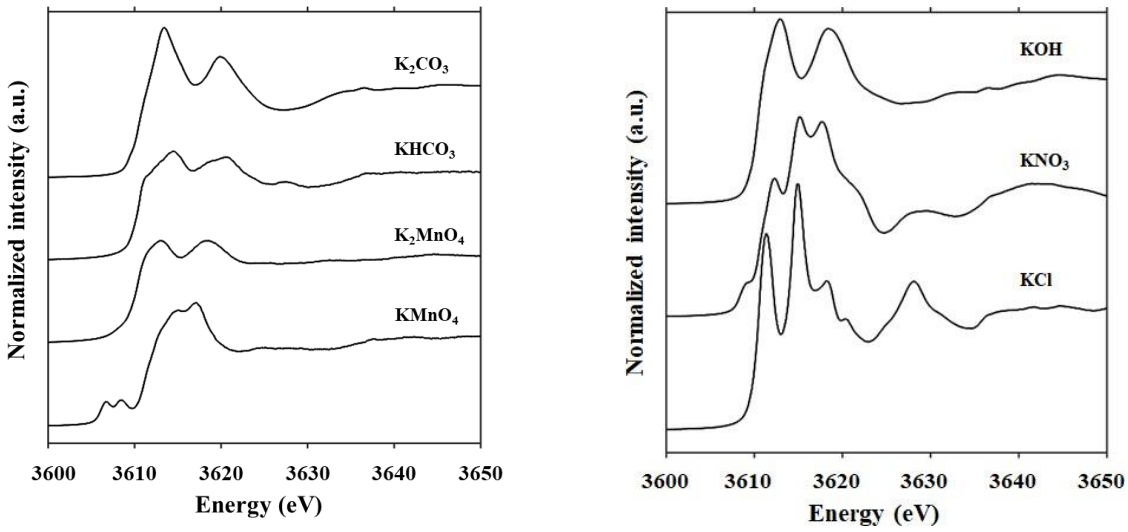

Figure B. 5: XANES of the potassium K-edge selected standards.

Appendix C – Activity

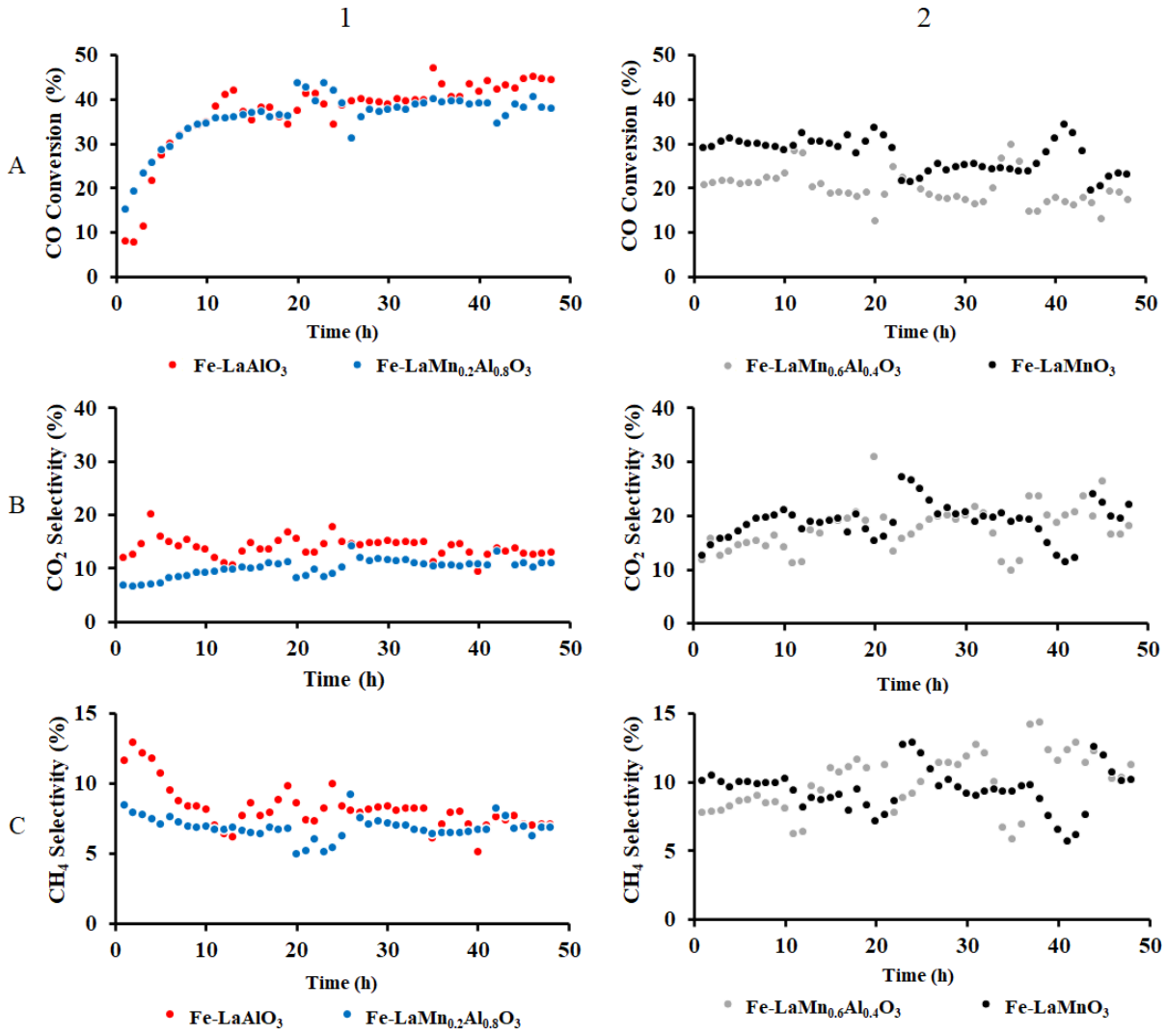

Figure C. 1: CO conversion, CO_2 and CH_4 selectivity for the Fe-$LaAlO_3$, Fe-$LaMn_{0.2}Al_{0.8}O_3$, Fe-$LaMn_{0.6}Al_{0.4}O_3$ and Fe-$LaMnO_3$ model catalysts at original space velocity (SV_{org}).

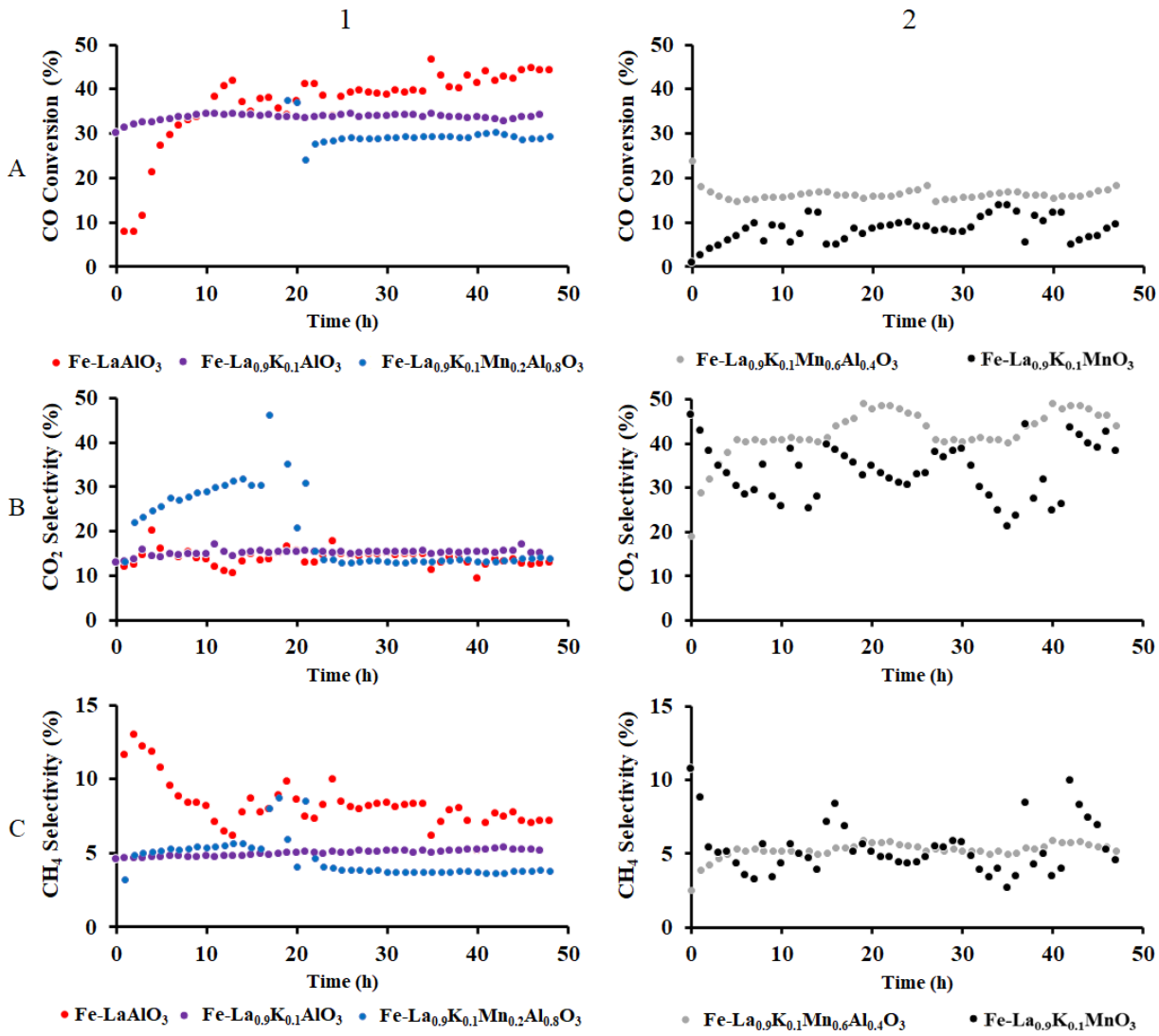

Figure C. 2: CO conversion, CO_2 and CH_4 selectivity for the Fe-$LaAlO_3$, Fe-$La_{0.9}K_{0.1}AlO_3$ ($3.75SV_{org}$), Fe-$La_{0.9}K_{0.1}Mn_{0.2}Al_{0.8}O_3$ ($3.75SV_{org}$), Fe-$La_{0.9}K_{0.1}Mn_{0.6}Al_{0.4}O_3$ and Fe-$La_{0.9}K_{0.1}MnO_3$ model catalysts.

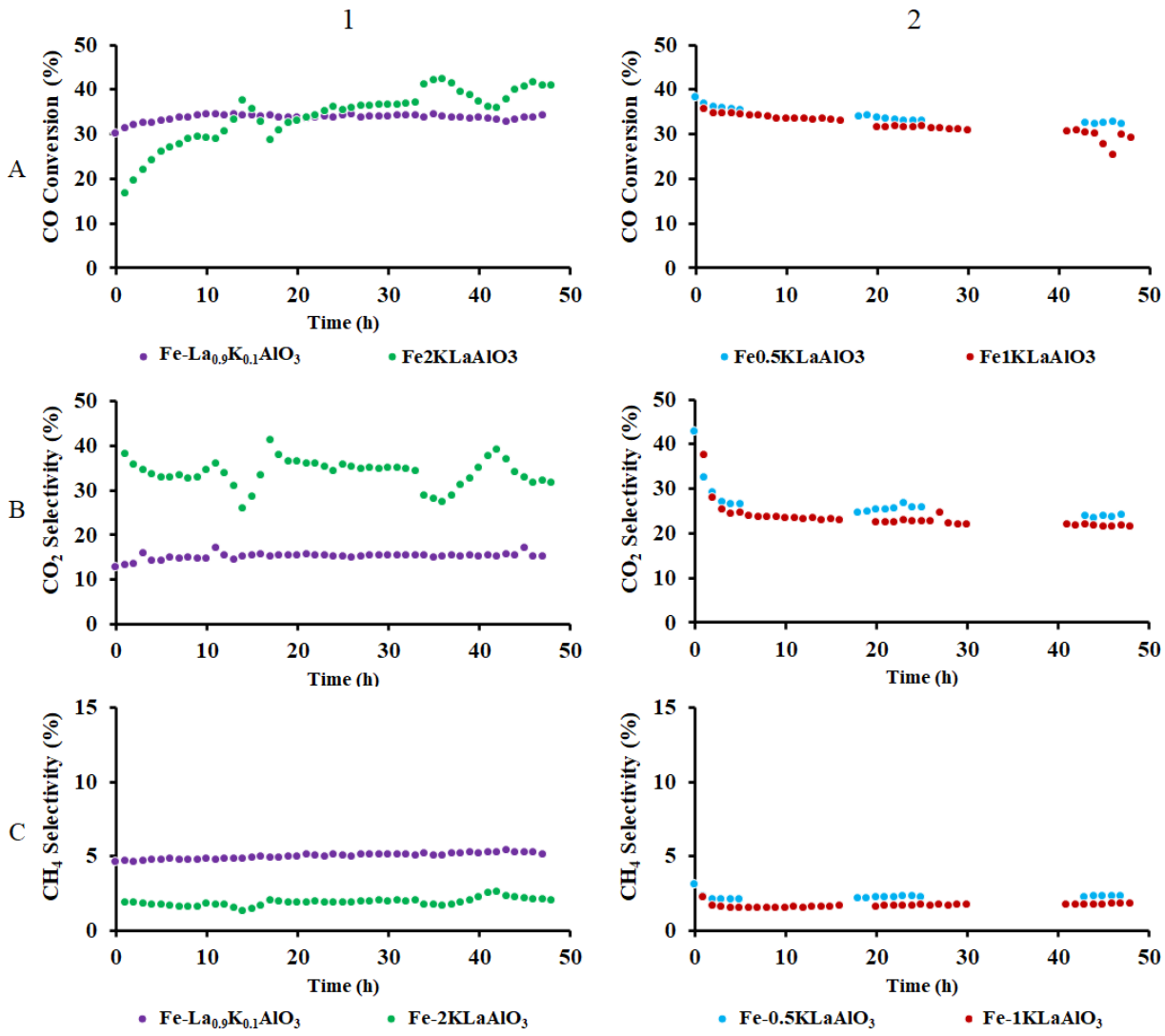

Figure C. 3: CO conversion, CO_2 and CH_4 selectivity for the Fe-$La_{0.9}K_{0.1}AlO_3$ (3.75SV_{org}), Fe-2KLaAlO$_3$ (SV_{org}), Fe-0.5KLaAlO$_3$ (3.75SVorg) and Fe-1KLaAlO$_3$ (3.75SV_{org}) model catalysts.

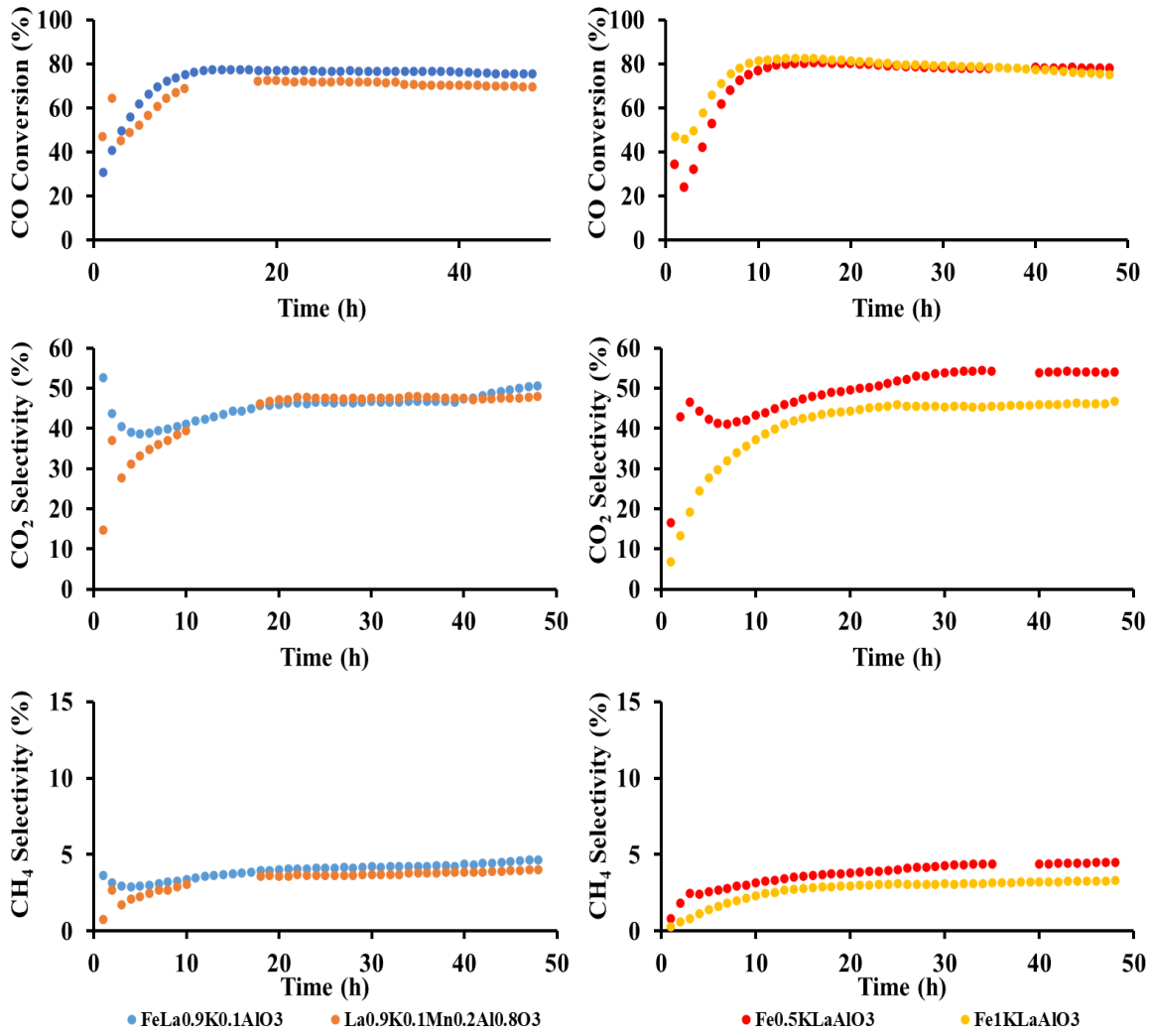

Figure C. 4: CO conversion, CO_2 and CH_4 selectivity for the Fe-$La_{0.9}K_{0.1}AlO_3$, Fe-$La_{0.9}K_{0.1}Mn_{0.2}Al_{0.8}O_3$, Fe-0.5KLaAl$O_3$ and Fe-1KLaAlO_3 model catalysts at original space velocity.

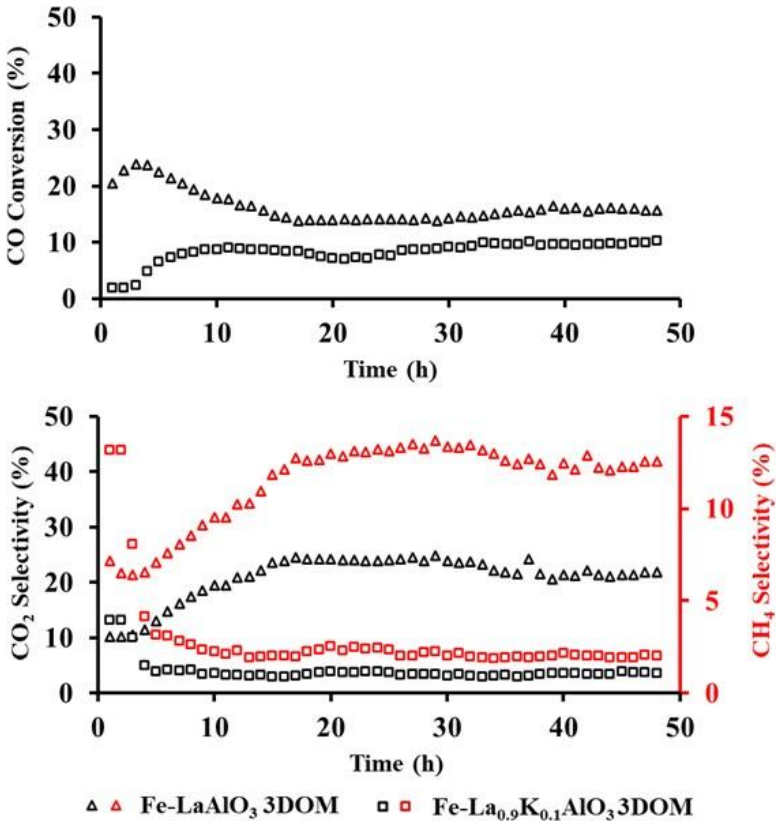

Figure C. 5: CO conversion, CO_2 and CH_4 selectivity for the three-dimensionally ordered mesoporous Fe-$LaAlO_3$ and Fe-$La_{0.9}K_{0.1}AlO_3$ model catalysts at original space velocity (SV_{org}).

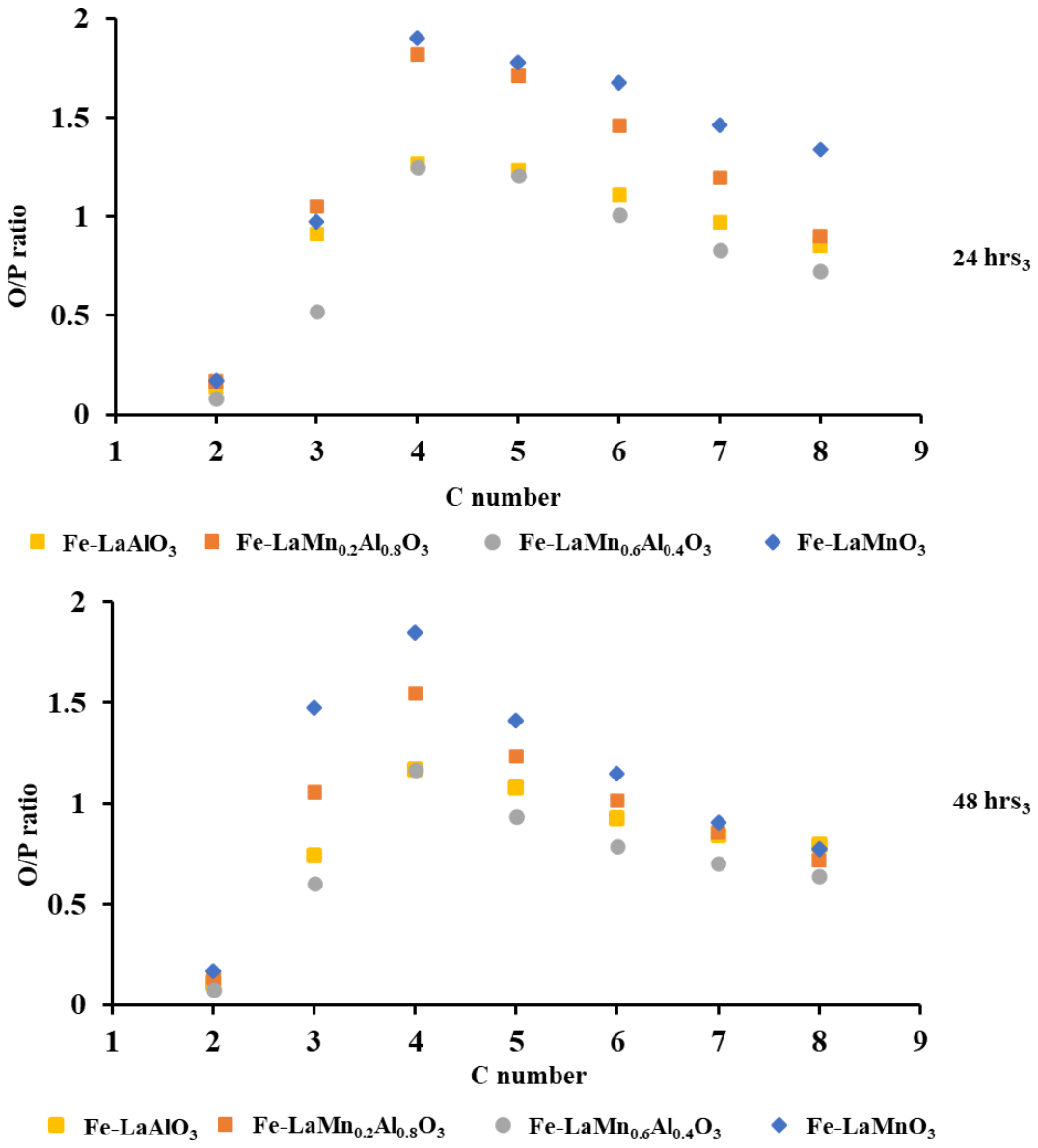

Figure C. 6: The variation of olefins to paraffins ratio as a function of Mn content in the perovskite support at 12 hrs intervals (24 and 48 hrs on stream).

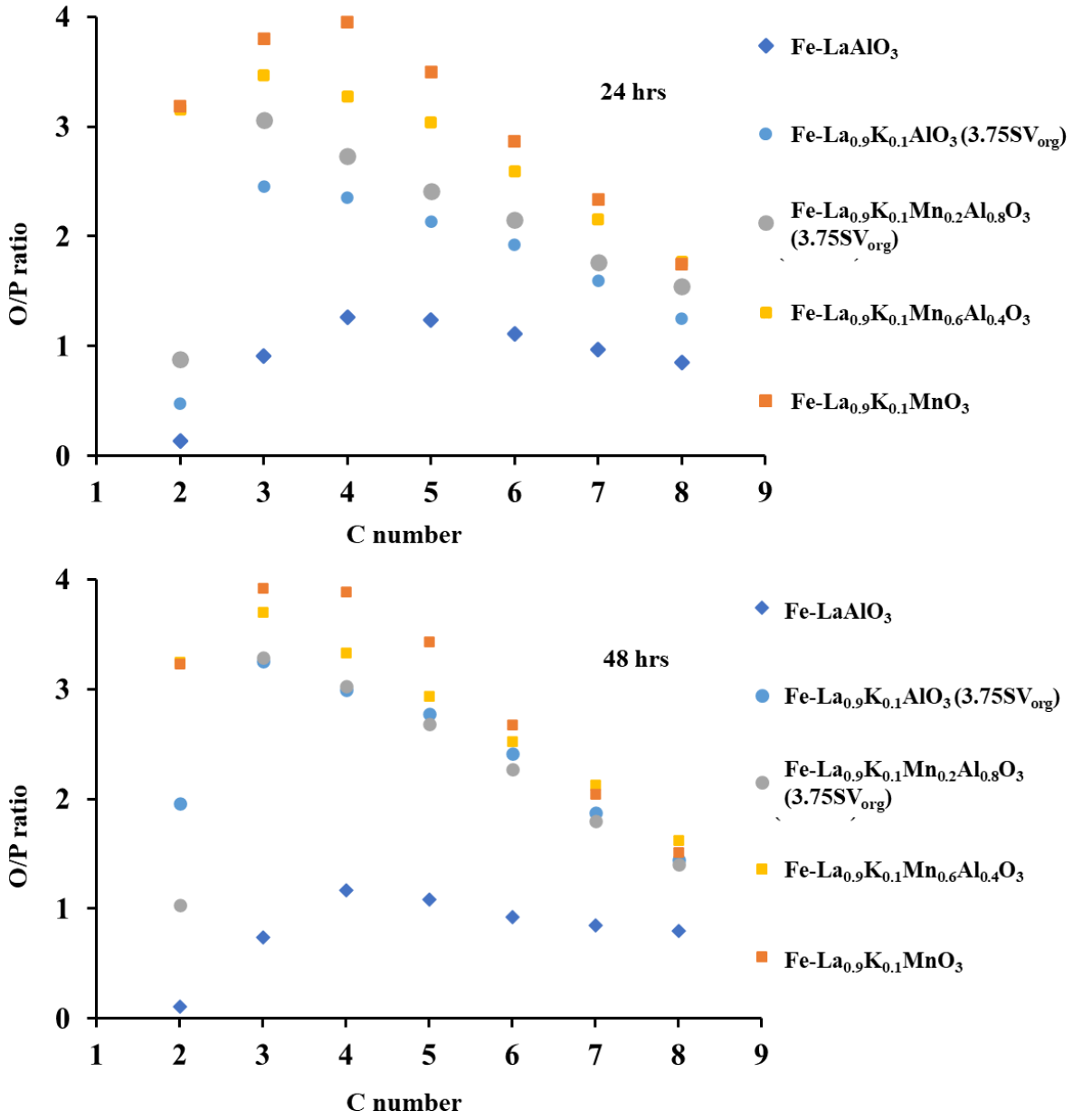

Figure C. 7: The variation of olefins to paraffins ratio as a function of Mn content in the potassium (0.1 mol.%) doped perovskites at 12 hrs intervals (24 and 48 hrs on stream).